Thèse de doctorat

Université de Lille

Unité de recherche : Institut d'électronique de microélectronique et de nanotechnologie
(IEMN – UMR 5820)

Soutenue le 16/12/2022
Par

Mahdi Ghazal

Titre:

Interfacing Neurons with Organic Nanoelectronics: From Passive Microelectrodes to Organic Electrochemical Transistors

Interfacer les Neurones avec la Nanoélectronique Organique : Des Microélectrodes Passives aux Transistors Électrochimiques Organiques

Spécialité: Electronique, microélectronique, nanoélectronique et micro-ondes

Jury :

Président du jury :

- Mme. Virginie HOEL, Professeure, *IEMN – CNRS*

Rapporteurs :

- Mr. Benoit CHARLOT, Directeur de recherche, *IES – CNRS*
- Mr. Christian BERGAUD, Directeur de recherche, *LAAS – CNRS*

Examinateurs :

- Mr. Urs FREY, PhD, *Maxwell Biosystems*
- Mme. Sophie HALLIEZ, Maîtresse de conférences, *Université de Lille*

Directeur de thèse: Mr. Yannick COFFINIER, Directeur de recherche, *IEMN – CNRS*

Co-Directeur de thèse: Mr. Fabien ALIBART, Directeur de recherche, *IEMN – CNRS*

Co-encadrant de thèse: Mr. Sebastien PECQUEUR, Chargé de recherche, *IEMN - CNRS*

Acknowledgement

During this journey, so many people have contributed in many different ways to realize this important achievement.

I would like to express my sincere gratitude to my PhD defense jury members. First of all, Dr. Benoit Charlot and Dr. Christian Bergaud, thank you for agreeing to review my thesis and for the time you have dedicated to it. I would also like to thank Dr. Urs Frey for accepting to be part of my jury, and I would like to renew my thanks for your valuable insights at our recent meetings. I would like to thank Dr.Sophie Halliez for being on the jury and also for her great contribution to my thesis's biological part. Prof. Virginie Hoel, thanks a lot for accepting the role as President of my jury and thank you for the advice and suggestions.

A special "Thank you" to my thesis supervisor. Dr. Fabien Alibart, first, thank you for accepting me in your IONOS project way back in 2019 as an intern and giving me your trust. You have provided me with fundamental insights and directed me in moments of indecision. Without your patience and reassuring guidance, it would certainly have been more difficult to extricate me from the pitfalls of the PhD. Not only, thank you for giving me a good example of professional leadership. The second special "Thank you" to my other supervisor, Dr. Yannick Coffinier. You supervised me and even shared with me doing multiple experiments and opened for me multiple collaborations. Besides your fruitful professional supervision, I will always cherish your funny and bright personality and your never-intrusive support. The third special "Thank you" is to my co-supervisor Dr. Sebastien Pecqueur. You have helped me on so many occasions, from my master's studies to this last day, that I cannot count. During our amazing discussions, you have opened for me the most important doors of my professional and scientific life, and your advice has been my sincerest.

I would also like to thank the past and present members of the IEMN-NCM group for welcoming me at the beginning of my experience in research and that have contributed in different manners especially Dr. Stephane Lenfant and Dr. David Geurin. Additionally, it is my honor to be the first student or member at IONOS project and hence I would like to show appreciation to the IONOS project past and present colleagues, especially Kamila, Corentin, Ankush, Anna, Michel, Alexis and Mona.

I also deeply thank the members of the LilNeuroCog especially, Dr. Pierre Yger, Dr. Sophie Halliez and Camille Lefebvre for the cell culture and bio-experiments that added a huge value to my results. Additionally, I would like to thank Dr. Sebastien Janel and Dr. Nicolas Barois from Institut Pasteur for the great collaboration.

My lovely thanks to Madelaine Audero. We were both PhD students, lovers and friends pushing each other through happiness and sadness. You were a great support to me when I passed through very tough periods in my journey. Thank you for your pure heart, love and infinite support.

I would like to thanks my friends in France and Lebanon. I want to express my limitless thanks to my childhood friends and cousins, the three "Mohammad"s, Fadel, Ali, Abbass and especially Zeinab (Zizi). You were always in my heart during this entire journey. I will not forget to thank my friends in France, Ahmad, Aida, Jad and Ahmad for our amazing moments in Paris. Additionally, I want to thank my friend Ali Abboud for passing the best moments here at IEMN and Lille and our infinite laughs that erased the sadness of the north weather. My cousins in France and Belguim, Ali and Hisham, I would like to express my limitless thank to your support, without you I guess I won't pass many obstacles.

Finally, I want to thank my support system, my Family. Thank you because you always trusted me and gave me everything you can for me to succeed. I guess I can never pay back what you did for me with all your love, kindness, and patience. I want to really show my gratefulness to my sister Mona and my brothers Hassan and Ali. It's my honor that you always look to me as your idol in life and professional career. I want to tell you that without this I will not continue and fight to achieve what I did. For my mom, I cannot literally find any word to explain the thanks to you. You gave me love support and me since the day one. If I have a single good character in me, it is because of you. You were always supporting me in my sadness to make it happiness with your love magic. If you read this, you are the only one know what I mean and how much I love you. Last but not least, to my idol and the one who taught me everything in this life, to the one who I was very happy to fulfill his dream, to the one who inherit me patience and persistence, to my dad, I would like to gift you this thesis as a sign of thank.

Abstract

Electrophysiology is the science that studies the electrical properties of electrogenic cells and tissues to characterize their functionality, excitability, and interconnectivity as a network. In the quest for cracking the neural code, changing the way our technologies work to record and stimulate brain's electrophysiology is essential. Unlocking bottlenecks in neuroprosthesis of artificial implants or electrostimulation of brain for chronical diseases curing, this goal is shared by many research initiatives worldwide: BRAIN initiative in the US, Human Brain Project in EU, the MIND project in Japan and the China Brain Initiative to name a few. Brain recording is done at many levels: with non-invasive or invasive devices, allowing either intracellular or extracellular recordings. Microelectrode arrays (MEA) for both *in vivo* and *in vitro* experiments offer the best compromise between information density (about a ms / tens of µm) and size (100+ cells recorded simultaneously). However, passive MEA suffers from a low signal-to-noise ratio (SNR), screening the detection of many biological events. In this work, transistors are studied as an alternative to MEA as an active device featuring on-site signal amplification. Thanks to their specific iono-electronic coupling, Organic Electrochemical Transistors (OECT) lead to improve signal transduction between biology and electronics. The materials involved are also a more biocompatible and conformal interface that can enhance neuron adhesion. In this manuscript, we will address different approaches from the circuit and device level problematic down to the materials' and try to address on the coupling between nanotechnology and neurons.

Particularly, EDOT electropolymerization is studied here to tune material's post-fabrication to optimize the cell/electrode interface. Combined with optical imaging and spike sorting, such enhanced recordings of 2D neural cultures allowed finer estimation of somas' position, opening possibilities to understand the neuron-electrode coupling better. For further optimization, the use of a synthetic monomer shown even higher coupling and performances compared to EDOT for *in vitro* extracellular recordings, with SNR values close to state-of-art 3D microelectrodes', allowing lower costs and complexity in their microfabrication process. Transferred on OECT for adapting sensing, electropolymerization showed to be a versatile technique to tune their transconductance and impedance independently, on-demand, to match different sensing requirements and adapt the operation speed and noise of OECT: crucial requirements for electrophysiology. Finally, the microscopic nature of the neuron-OECT were studied to give a physical explanation of the interface for having a firm basis for the systematic optimization of OECT. The advantages and drawbacks of using OECT for *in vitro* neural recordings are discussed based on the recordings obtained in this work, addressing both material and device levels for future instrument integration and impact at the circuitry level.

Novel materials, processes, and concepts of this study address the neuron/sensor interface issue. By enhancing/improving the recording's quality, this work contributes to a better understanding of the interaction at the neuron-microelectronic and biomolecules-nanostructures levels, leading to new fundamental discoveries while interfacing and computing the brain's electrical activity.

Résumé

L'électrophysiologie est la science qui étudie les propriétés électriques des cellules et des tissus électrogéniques, afin de caractériser leur fonctionnalité, leur excitabilité et leur interconnectivité en tant que réseau. Dans la quête pour déchiffrer le code neuronal, il est essentiel de changer la façon dont nos technologies fonctionnent pour enregistrer et stimuler l'électrophysiologie du cerveau. Débloquer les goulots d'étranglement dans les neuroprothèses d'implants artificiels ou l'électrostimulation du cerveau pour la guérison des maladies chroniques, cet objectif est partagé par de nombreuses initiatives de recherche dans le monde : l'initiative BRAIN aux États-Unis, le Human Brain Project dans l'UE, le projet MIND au Japon et la China Brain Initiative pour ne citer qu'eux. L'enregistrement cérébral se fait à plusieurs niveaux : avec des dispositifs non invasifs ou invasifs, permettant des enregistrements intracellulaires ou extracellulaires. Les réseaux de microélectrodes (MEA) pour les expériences in vivo et in vitro offrent un compromis entre la densité d'informations (environ une ms / dizaines de µm) et la taille (plus de 100 cellules). Cependant, le MEA passif souffre d'un faible rapport signal/bruit (SNR), filtrant la détection de nombreux événements biologiques. Dans ce travail, les transistors sont étudiés comme une alternative au MEA en tant que dispositif actif avec amplification de signal sur site. Grâce à leur couplage iono-électronique, les Transistors Electrochimiques Organiques (OECT) permettent d'améliorer la transduction du signal entre la biologie et l'électronique. Les matériaux impliqués sont également des interfaces plus biocompatibles et conformes qui peuvent améliorer l'adhésion des neurones. Dans ce manuscrit, nous aborderons différentes approches allant de la problématique au niveau des circuits et des dispositifs jusqu'aux matériaux et tenterons d'aborder le couplage entre la nanotechnologie et les neurones.

En particulier, l'électropolymérisation EDOT est étudiée ici pour ajuster la post-fabrication du matériau afin d'optimiser l'interface cellule/électrode. Combinés à l'imagerie optique et au Spike-Sorting, ces enregistrements améliorés de cultures neuronales 2D ont permis une estimation plus fine de la position des somas, ouvrant des possibilités pour mieux comprendre le couplage neurone-électrode. Pour une optimisation ultérieure, l'utilisation d'un monomère synthétique a montré un couplage et des

performances encore plus élevés par rapport à l'EDOT pour les enregistrements extracellulaires in vitro, avec des valeurs SNR proches des microélectrodes 3D, permettant de réduire les coûts et la complexité de leur processus de microfabrication. Transféré sur OECT pour adapter la détection, l'électropolymérisation s'est révélée être une technique polyvalente pour régler indépendamment leur transconductance et leur impédance, à la demande, pour répondre aux différentes exigences de détection et adapter la vitesse de fonctionnement et le bruit de l'OECT : des exigences cruciales pour l'électrophysiologie. Enfin, la nature microscopique du neurone-OECT a été étudiée pour donner une explication physique de l'interface pour avoir une base solide pour l'optimisation systématique de l'OECT. Les avantages et les inconvénients de l'utilisation de l'OECT pour les enregistrements neuronaux in vitro sont discutés sur la base des enregistrements obtenus dans ce travail, en abordant à la fois les niveaux de matériel et de dispositif pour l'intégration future de l'instrument et l'impact au niveau des circuits.

Les nouveaux matériaux, processus et concepts de cette étude abordent la question de l'interface neurone/capteur. En renforçant la qualité de l’enregistrement, ce travail contribue à une meilleure compréhension de l’interaction aux niveaux neurone-microélectronique et biomolécules-nanostructures, menant à de nouvelles découvertes fondamentales tout en interfaçant l’activité électrique du cerveau.

Table of Content

Chapter I. Introduction and General Context

Brains and computers both work electrically. In the 18th century, Luigi Galvani introduced electrophysiology by establishing the electrical coupling of inorganic conductors and electroactive tissue. Now, after tens of years of development in electrophysiological devices, our ability to interface with the brain has made tremendous progresses leading to better understanding its functioning. Finding new solutions in brain machine-interface (BMI) implants for artificial neuroprosthesis to aid paralyzed people or for electrostimulation to treat brain diseases, is now boosted by technological breakthrough companies such as Neuralink, sustained by worldwide and large-scale research projects from the US (BRAIN), EU (HBP flagship), Japan (MIND), and more recently, the China Brain Initiative.

A wide range of the neuronal signals have been discovered, from whole brain activity to slow network oscillations of small populations down to spiking activity of individual neurons. Microelectrode Array (MEA) has been considered the most popular tool for both *in vivo* and *in vitro* extracellular recording from neurons. It offers a great compromise between the spatio-temporal resolution (1ms/tens of µm) and surface coverage (i.e. thousands of cells recorded simultaneously) by detecting both single spike activity and Local Field Potentials. Standard sensing consists of capacitive coupling between the microelectrode surface and the active neurons transducing the ionic current into electronic current. We may envision such interface by far more complex interactions, right at the level of neurons and microelectronic devices (circuitry and device level) or even at the level of biomolecules and nanostructures (bio-nano interface and material level). In one hand, passive microelectrodes are currently further optimized by developing surface modification and structuration by finding the right materials and geometries that maintain higher affinity with neurons to improve the neuron-electrode interface coupling and, thus, the quality of the recordings. For example, 3D-shaped microelectrodes increase the contact area between the neuron and the electrode, which maintains a very high coupling with neurons leading to high-quality recordings. One potential direction for optimizing MEA is to address the device and circuitry problematic level by relying on the development of active sensors that have enhanced performances and additional features with respect to standard passive microelectrodes. Active microelectronics such as transistors embedded at close vicinity from the neurons are now maintaining additional aspects such as local amplification of the signal to improve signal-to-noise ratio by limiting capacitive noise and filtering that can compress the signal.

Recently, the use of conductive organic polymers such as PEDOT:PSS in standard passive and active devices is blooming. For passive MEA, PEDOT:PSS is used for coating microelectrodes due to its good biocompatibility and low impedance that can enhance the coupling with neurons. In addition to its advantages, and although it offers very low microfabrication complexity, its breakthrough is constrained by the performance of the currently available PEDOT-based microelectrodes. As an alternative, Organic Electrochemical Transistors based on this PEDOT:PSS materials have been used to demonstrate state of the art performances for *in vivo* brain recording, EEG, ECoG, ECG, and *in vitro* recordings from cardiac cells. This technology shifts the basic measurement's principle since here the recording results from ions penetrating the material and tuning its conductivity via (de)doping (bulk effect) and is not based anymore on capacitive coupling across an interface (surface effect) such as in Field Effect Transistor (FET) technology. For *in vitro* recordings from neurons, OECTs have been shown as a proof of concept; however, the development of electrical and morphological characterizations, theoretical concepts and experimental methods with neurons is in great need to explore the capability of OECTs in interfacing neurons.

The issue is an elucidation of the biophysical mechanism on the level of nanometers, micrometers (material level) and millimeter (circuitry and device level), and the development of advanced technological microelectronic devices and active materials combined with experimental and theoretical studies are a key solution for this issue. If we succeed in this endeavor, we shall be able to fabricate reliable iono-electronic devices to solve problems in molecular biology and medicine and contribute to information technology and BMI to enhance our understanding of the brain.

Chapter I of my manuscript will present an overview of the aspects related to this work, starting from the understanding of the brain and the generation of neural electrical signal. Later, a brief state-of-the-art of the electrophysiological approaches was introduced. Then we will focus on the use of passive MEA *in vitro* for extracellular recording from neurons by discussing its operational principle and the impact of the electrode impedance and the seal resistance on the quality of the recordings, pointing out the importance of the material choice such as PEDOT:PSS for MEA recordings. Active sensing aspect using OECT has been presented, discussing its operational principle, materials, important parameters, and challenges for its uses in extracellular recording from neurons. **Chapter II** provides an overview and a description of the materials, equipment and experiments used in this work to achieve the research objectives.

Once given the basis to contextualize this work, the results chapter of the manuscript will answer two main questions:

1) **Material level: how to improve planar classical MEA by addressing the bio-nano interface?**
2) **Device and circuit level: how does addressing active electrodes (OECT) will improve electrophysiology/cell interfacing?**

For this purpose, based on using conductive organic polymer materials, the work conducted during my PhD considered new devices and material engineering techniques for addressing different approaches from circuit and device level problematic down to the material level problematic and trying to answer the coupling between nanotechnology and neurons. **Chapter III**, showed how using EDOT electropolymerization to tune post-fabrication materials could optimize the cell/electrode interface microelectrodes. Using such enhanced recordings of 2D neural cultures combined with optical imaging and spike sorting, we dealt with the bio variability issue by accurately estimating the positions of the somas, opening new possibilities to understand the neuron-electrode coupling better. **In Chapter IV,** we went further by proposing new synthesized polymer-based microelectrodes that showed higher coupling, superior performances and signal-to-noise ratio (SNR) to state-of-art PEDOT microelectrodes for *in vitro* extracellular recordings from neurons. Such SNR values were close to that of state-of-art 3D morphological microelectrodes with lower cost and less complex fabricated microelectrodes. **In Chapter V,** based on the same principle of using electropolymerization as a post-microfabrication engineering technique, we try to address this solution at the device and circuit level by adding more functionalities than passive electrodes with OECT. We exploit the strategy of adaptive sensing by using OECT, where both transconductance and impedance are tunable and can be modified on demand to match different sensing requirements. The versatility of the electropolymerization technique is exploited to adjust post-fabrication the operation speed and noise of OECT, which are crucial requirements for electrophysiology. **In chapter VI**, we performed electrical, optical and theoretical experiments to study the neuron-OECT interaction at the microscopic scale and circuitry level. The combination of these experiments gave us solid knowledge about interfacing OECT with neurons, which are essential for implementing/optimizing OECTs. To my knowledge, we showed for the first time preliminary results of in vitro recordings from neurons using OECT, discussing its advantages, limitations, and challenges at the material and device level. These preliminary findings are critical for integrating OECTs with neurons at the circuitry level in its future uses and applications.

In the final chapter, **conclusions and future perspectives**, the main results achieved during this PhD will be summarized, and novel directions of our research work will be introduced for the short and long-term periods.

1. Brain and Neurons

1.1 The brain

The nervous system is the control center of the body that is responsible for directing its voluntary movement and is the space of our consciousness, personality, learning, and memory. Along with the endocrine system, the nervous system regulates many aspects of homeostasis, including respiratory rate, blood pressure, body temperature, the sleep/wake cycle, and blood pH.

The nervous system is divided anatomically into two major systems: the central nervous system (CNS) and the peripheral nervous system (PNS) as shown in Figure 1.1. The CNS is composed of the **brain** and the spinal cord that are responsible of information processing and control. The PNS connects the CNS to every other part of the body (e.g., organs) by carrying signals from and into the CNS through nerves. As part of the CNS, the brain is responsible for the bidirectional communication of information with the rest of the body. The brain receives, processes, and sends the signals sensed by the PNS (sounds, cognitive functions, sensations …).

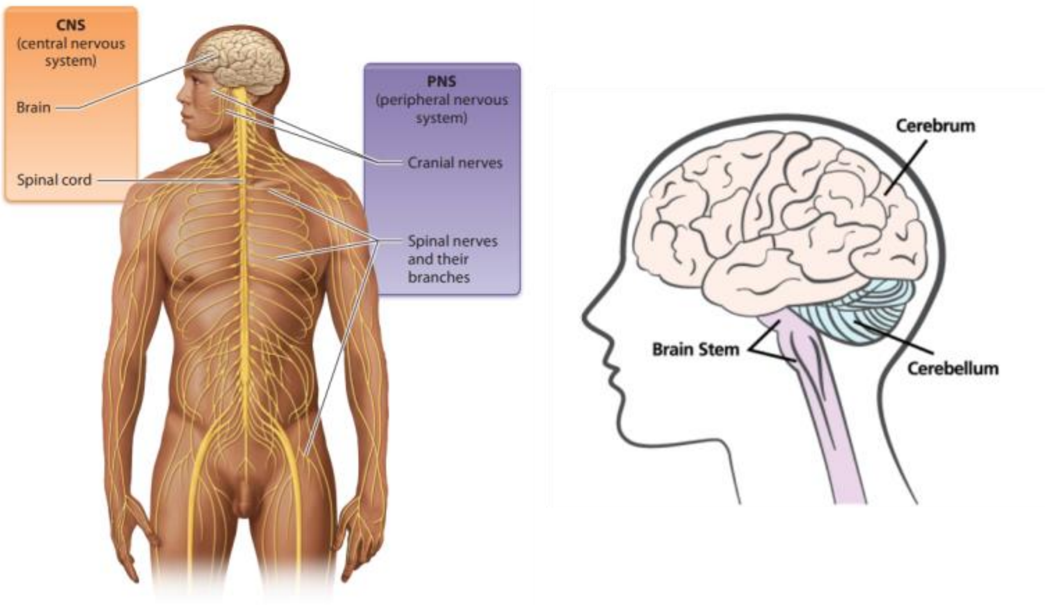

Figure 1.1 (a) Structure of the nervous system [1]. (b) the three main parts of the brain [2]

The brain is the organ enclosed and protected by the skull. In an adult, the brain weighs approximately 1.4 kg of gelatinous mass of fat and protein. It mainly consists in three regions (Figure 1.1): cerebrum, cerebellum and brainstem where each one controls specific tasks:

- Cerebrum: It is the largest section that controls high functions such as learning, reasoning, and speech, plus interpreting senses like sight and hearing.
- Cerebellum: It is the second largest part of the brain, which is located under the Cerebrum. The cerebellum is responsible for coordinating muscle movements, particurarly those that help maintain the body's balance and posture.
- Brainstem: It lies under the Cerebellum and anchors the brain to the spinal cord. It carries out several vital and automatic functions such as cardiac activity, respiration, digestion, and sleep.

These main parts of the brain work in synchrony to ensure body functions are fully operational.

1.2 Neurons

The brain consists of billions of highly specialized cells called neurons that work as messengers that transfer information between the brain and the rest of the body. The neurons are electrically excitable cells that transfer information between each other as electrical impulses. There are three functional classes of neurons: **afferent neurons** (carry information from the periphery towards the CNS), which are considered as sensory neurons since they carry information from sensory receptors (such as the tongue, the eyes,…) to the brain. **Efferent neurons** (carry information away from the CNS), which are considered as motor neurons since they carry motor information, such as speaking and running, from the brain to the organs and muscles. **Inter-neurons** are situated between sensory and motor neurons that receive information from one neuron and transmit it to other neurons.

.

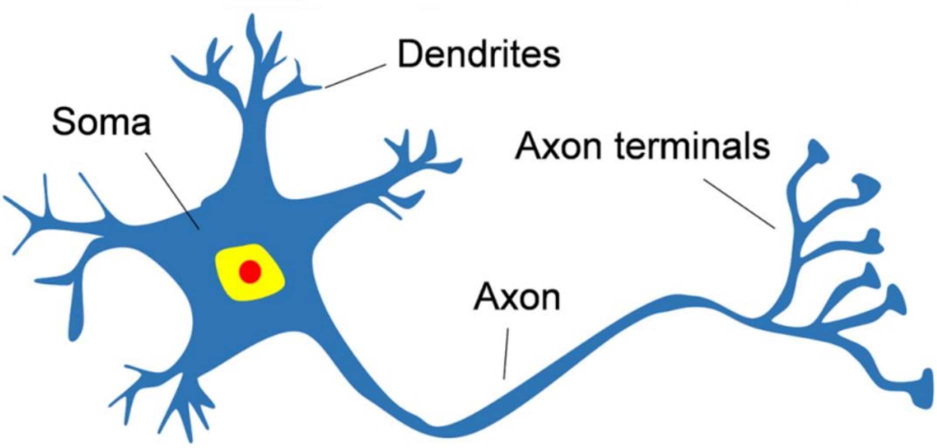

Figure 1.2 Typical structure of a neuron [3]

There are several structural types and physical appearances of neurons, but generally, they have the same parts (Figure 1.2). The typical structure of the neurons consists of three essential parts that allow for the transmission of the electrical signal:

- **Dentrites**: A small tree branched extensions of the neuron that are responsible for receiving the activity of other neurons and transferring the signal as electrical impulses to the cell body (the soma).
- **The cell body (soma)**: It is the wider piece of the cell that contains the nucleus, which contains the DNA or genetic material of the cell. The soma takes all the information from the dendrites and sends it to the next part of the neuron, which is called the axon
- **Axon**: The axon receives the impulses from the soma and transmits them away from the cell body towards the synaptic terminals. The electrical impulses transmission along the axons progress at different speeds depending on the diameter of the axon and the insulation of myelin sheaths. Myelin sheaths are insulated wrappers made up of glial cells that cover the axons and are designed to speed up neuronal transmission.

The transmission of the electrical neuronal signal is directed by an event called Action Potential (AP). several ions, including Sodium (Na^+), Potassium (K^+), and Chloride (Cl), are unequally distributed between the inside and the outside of the neuron cell. When the neuron is at rest (not sending a signal), the concentration of Na^+ ions is higher outside the cell than inside, while the relative concentration of the K^+ ions is the opposite, with more ions inside the cell than outside. The difference in concentration of ions between the inside and the outside of the cell cause a potential difference across the neuron's membrane called the membrane potential. At rest, the neuronal membrane has a resting potential of approximately -70 mV, with a negatively charged inner cell compared to its outer. As ions move through the channel crossing one side of the membrane to the other side, they cause a change in the membrane potential from its resting potential (-70 mV). Once the cell membrane reaches the threshold voltage of about -50 mV, the voltage-gated Na^+ channels open, causing the influx of Na^+ into the cell. As positive Sodium enters the cell, the membrane potential becomes less negative approaches + 30 mV; this process is called depolarization. After reaching 30 mV, the Sodium voltage-gated channels are inactivated, and the Potassium channels opens. The flux of potassium outside of the neuron causes repolarization of the membrane potential back to -70 mV. This biophysical event of depolarization of the neuron's membrane potential followed by a repolarization is called an AP (Figure 1.3).

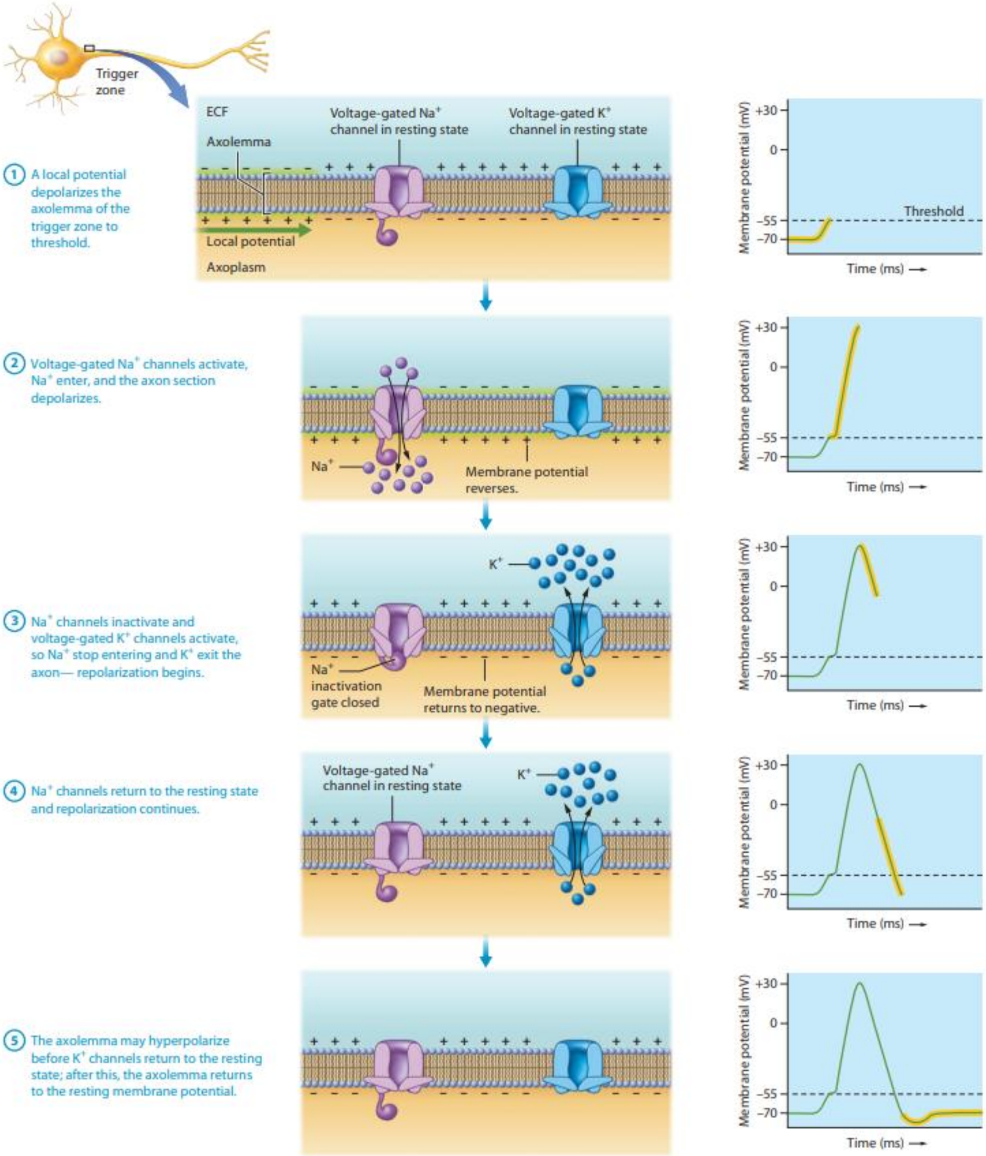

Figure 1.3 Events of an Action Potential (AP) [1]

We discussed previously the electrical activity that happens within a single neuron (AP). Neurons communicate with each other through synapses. Synapses are biological junctions between two neurons that allows the propagation of AP through an electrochemical process by transmitting electricity (*electrical synapses*) or releasing chemicals (*chemical synapses*).

- **Electrical synapses:** In electrical synapses, the impulse is transmitted from the neuron's terminal (presynaptic membrane) to the membrane of the adjacent neuron (postsynaptic membrane) in the form of an ionic current. In such synapses, presynaptic and postsynaptic membranes are joined by membrane pores called gap junctions (2-4 nm cleft size). The ionic charge can flow from one neuron to another as if they are sharing a common membrane allowing the AP propagates from cell to cell. The electrical synapses provide faster transmission than the chemical synapses (Figure 1.4a).

- **Chemical synapses:** When an AP reaches the presynaptic terminal, a depolarization event occurs and the voltage-gated calcium channels at the presynaptic terminal open, leading to the influx of calcium cations into the neuron. This results in the release of neurotransmitters across the synaptic cleft of 20-40 nm in size (Figure 1.4b). Consequently, the neurotransmitters exert their effect at the membrane of the adjacent neuron (postsynaptic membrane) by binding to its receptors. The receptors then open a channel enabling the influx of sodium ions into the postsynaptic neuron. If this leads to surpassing the threshold potential of the postsynaptic neuron, an AP is triggered (transformation of the chemical signal into an electrical signal in the postsynaptic neuron). The remaining neurotransmitters at the postsynaptic site are reabsorbed into the presynaptic neuron and recycled either directly or following its cleavage in the synaptic cleft.

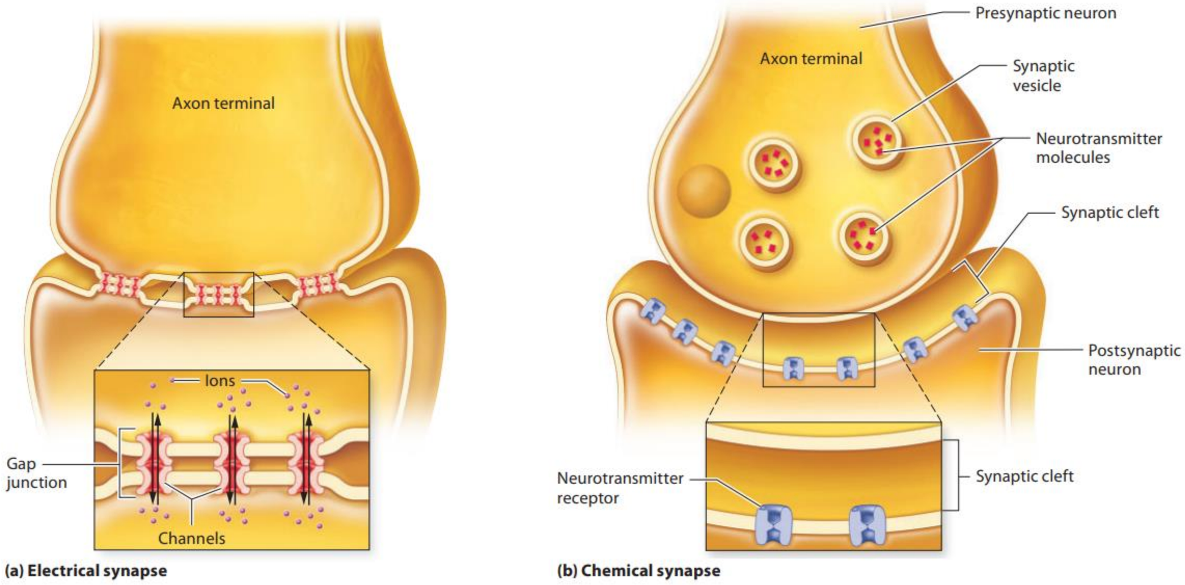

Figure 1.4 Structures of electrical and chemical synapses [1]

2. Electrophysiology and Neural Interface

Electrophysiology is a scientific discipline that studies the electrical properties of biological cells and tissues by investigating the voltage or the ionic current change in electroactive cells such as neurons. In the quest of communicating with the human brain, electrophysiology plays a great role in changing the way we interact with computer/machine technology [4], and it expands our capabilities to treat neuronal problems. From the applicative side of brain-machine interface (BMI), this revolution initiates lots of promising results in the advancement of neuroprosthesis for arms and legs replacement [5], artificial sensors for audition [6], and vision [7] in addition to brain disease treatment via brain stimulation [8] (Figure 1.5). These applications are sustained by large-scale research projects such as the BRAIN initiative in US, Human Brain Project in EU, the MIND project in Japan and the China Brain Initiative, and more are expected in the coming decades.

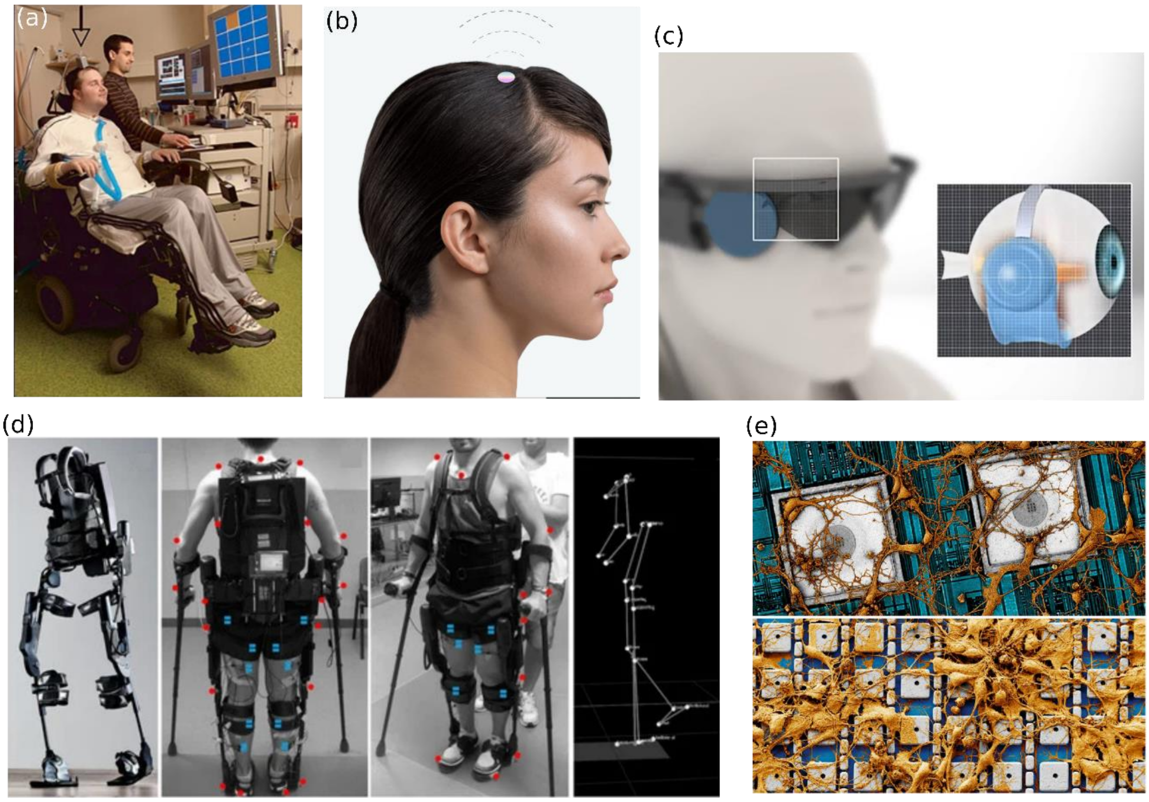

Figure 1.5 Brain Machine Interface applications. (a) The BrainGate sensor (arrowhead) for neural control of prosthetic devices by a human with tetraplegia [5]. (b) Schematic displaying the implantable chip of the breakthrough Elon Musk's company « NeuraLink » that aims to help people with paralysis to regain independence through the control of computers [4]. (c) Artificial vision device [7]. (d) Exoskeleton device for gait rehabilation [9]. (d) Rat neurons on top of neuromorphic electronic device based on copying and pasting the brain functionality. Presented from an innovative project lunched recently by Harvard University and Samsung Electronics [10].

There are different types of electrical signals that can be recorded from the brain. Two main broad types of brain electrical activity are spikes (APs) and field potential (FP) [11]. Spikes or APs was previously introduced, which are signals originate from a single neuron that is electrically excited. It can also occur that neurons are excited simultaneously, resulting in multiunit activity. FPs are more complex than spikes as these contain information of all transmembrane currents of a small population of neurons, varying in size, frequency and spatial distribution. FPs are both signals and signs [12] of underlying neural processes that generally reflect brain states, such as stages of sleep or alertness or higher cognitive processes. FPs contain two major subgroups: (i) repetitive neural activity called rhythmic signals, which originates from the synchronized activity of a large number of neurons and results in oscillation with different amplitude (10 µV to 100 µV), frequency and shape. The frequency band of rhythmic signals are divided into delta (δ: ~0.2–3.5 Hz), theta (θ: ~4–7.5 Hz), alpha (α: ~8–13 Hz), beta (β: ~14–30Hz), gamma (γ: ~30–90 Hz) and high frequencies (>90 Hz)[13]. (ii) Another subgroup is the event-related potentials (ERPs): Large potential shifts induced, for example, by an external event in a large neuronal group (time-locked event).

There are two methods of electrophysiology: Intracellular and extracellular recordings:

- Intracellular recording technique is a single-unit recording method that is used to study the physiology of a single cell. By inserting a patch clamp or microelectrode inside the cell, the intracellularly recorded potential relies on the comparison between the intracellular and the extracellular environment giving information about APs or postsynaptic potentials. The main advantage of intracellular recording systems is that they exhibit very good electrical coupling with the cell and provide an accurate readout of the entire dynamic range of voltages generated by cells without distorting the readout over time [14].
- Extracellular recording technique involves studying the ionic current in the extracellular matrix of a single cell or a group of neighboring cells or tissues without any necessity for getting within the tissue or cell and damaging its membrane (operational principal and extracellular space is explained more in details in next section).

APs or spikes are considered important carriers of information in the nervous system or brain. Neurophysiologists study the neuronal signal information at the level of spikes from a single cell up to a population of spiking neurons. For example, there is an impressive amount of information carried by spiking activity in the retina. The retina receives and compute visual scenes and sends it as an output to various downstream brain regions in the form of neuronal spikes for further computation [15,16]. Thus, in visual neuroprosthesis applications they consider the neuronal spikes as their neuronal signal of interest where several achievement have been done reporting visual computation models that use spikes to analyze natural scenes that include static images and dynamic videos [15]. Additionally, single cell activity in the motor cortex also gives information about few body movements such as hand velocity that can be extracted from parietal and frontal neuron spiking [11]. While investigating spikes activity has been a central of focus in some research, lately it is well known that information processing through the brain or neural network is a collective effect from population of neurons rather than from individual ones. Mostly, communicating with the brain for several and main applications requires recording activity from thousands of neurons in parallel (FPs). For example, there are several BCI systems rely on sensorimotor rhythms (SMR) signal. SMRs corresponds to rhythms signals of FPs that are recorded over sensorimotor areas (i.e. µ-rhythm and β-rhythm) and allow anatomically specific voluntary regulations. Thus, recording FPs opened a lot of opportunity for neuronal-rehabilitation, clinical diagnoses (i.e., Epilepsy), and communication and control (curser movement, game applications, control of external devices …etc.) applications [17]. To this end, several approaches allowing for recording/stimulating large numbers of neurons have been proposed. The extracellular recorded FP has been referred to as Electroencephalography (EEG) when recorded from the scalp, as Electrocorticogram (ECoG) when recorded by subdural grid electrodes on the cortical surface, and as the local field potential (LFP) when recorded by microelectrodes at more local locations of the brain. EEG experiments can detect only a large portion of the brain on the macroscopic level of neurophysiology with attenuated electrical activity recorded due to the high resistivity of the skull. This experiment provide a practical tool to monitor whole brain activity (Figure 1.6). For ECoG, it is an invasive recording technique where it bypasses the resistivity of the skull leading to higher temporal (5 ms) and spatial resolution (1 cm) recordings than scalp EEG (Figure 1.6). These techniques investigate the role of specific brain regions in different body functions, and help to diagnose neurological disorders.

Lately, neuroscience has seen the development of the use of **microelectrode arrays (MEA)** in neurophysiology for both *in vivo* and *in vitro* characterizations. This technology offers a good compromise between the spatio-temporal resolution (around 1 ms and down to tens of µm) and surface coverage (more than 100 cells can be recorded simultaneously). MEAs record LFP signals simultaneously with spikes differentiated by different band-pass filtering [18]. For example, LFPs reside within the 1 — 200Hz frequency band, whereas extracellular spiking associated with single-unit neuronal firing resides within the 300 — 3000 Hz band. Using MEAs yields the most informative signal for studying cortical electrophysiology due to the ability to record a wide-band signal (direct current to 40 KHz) which contains both APs and other membrane potential fluctuations in a small neural network (Figure 1.6).

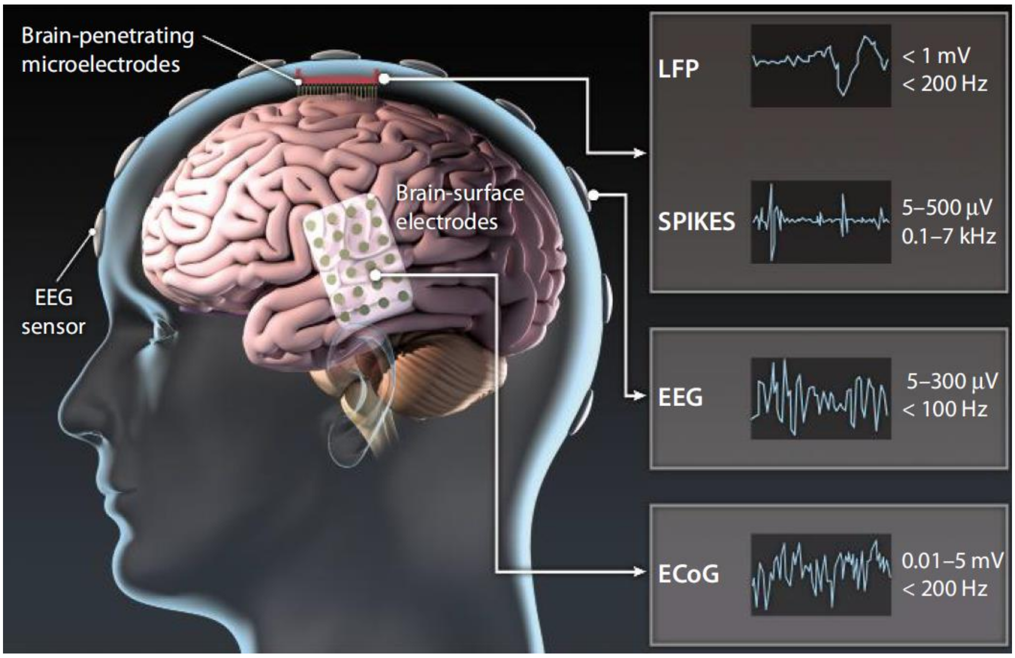

Figure 1.6 Different kinds of brain signals can be recorded from several levels with noninvasive and invasive neurophysiological recording devices [18].

In the following, we will explain the use of planar MEA for *in vitro* extracellular recordings from 2D neural culture. We will investigate the specific sensor requirements to achieve better coupling with neurons and, thus, higher quality of recordings.

3. *In vitro* extracellular recordings by Microelectrode Array (MEA)

Organoids, brain slices, and 2D neural networks cultured on top of a chip containing an array of sensors offer an exceptional tool for studying fundamental neuroscience concepts. Typically, planar MEAs that gather multiple in-plane microelectrodes patterned on a substrate (usually glass or silicon) acts as an interface that connects cells to electronic circuitry to record their activity.

Compared to *in vivo* experiments, *in vitro* testing for both research and medical applications a provides more effective platform in terms of cost, time consumption, and ethical issues in a well-controlled environment [19]. Biological testing of medical devices that relies mostly on animal models has been a central focus of most research. However, as scientific knowledge advances our understanding of basic mechanisms, preference should be given to *in vitro* models – a point backed by the International Organization for Standardization (ISO): "*In vitro test methods, which are appropriately validated, reasonably and practically available, reliable and reproducible shall be considered for use in preference to in vivo tests.*" (ISO 10993-1, 2009) [19]

For example, M. Chiappalone and her colleagues used an *in vitro* model to demonstrate neuromorphic prosthesis to restore bidirectional interaction between two neuronal populations that have been functionally disconnected by creating a focal lesion [20]. In their work, they showed that despite the technological progress, *in vivo* models still have bottleneck in these applications, such as the technical challenges to reproduce focal lesions faithfully (due to their complexity), and low controllability in distinguishing the actual effect of the adopted electrical therapy from the complex activity of the brain. Therefore, reducing neuronal systems *in vitro* to test neuroprosthetic devices may be advantageous.

Additionally, 2D cultured neural networks and brain slices are used to monitor information processing in defined neural networks, model and understand neurological diseases (stroke, epilepsy, Alzheimer), and investigating brain learning processes and memory developments. For example, in a study published in *Nature Neuroscience* done by teams from University of Lausanne and University of Lille (Neuroscience and Cognition institute, Inserm), they showed results that were crucial for understanding the Alzheimer's disease mechanisms and underlining the essential role of astrocytes in hippocampal function [21]. These results were obtained with accurate and high statistics due to the reproducibility, low time consumption, and well-controlled environments of the experiments supported by the *in vitro* platform (i.e. *in vitro* electrophysiology, calcium imaging … etc.).

2D neural culture is an interesting platform for modeling and understanding the electrical interaction between neurons and sensors. The first electrical models used to understand the operating principle of sensing neurons by microelectrodes [22] or other sensing technology such as transistors [23] were demonstrated based on *in vitro* experiments. The *in vitro* experiments gave more flexibility to position/localize neurons near sensors, reducing the complexity of understanding the neuron-sensor interface [23]. Starting demonstrating such models directly with *in vivo* experiments will add more bottlenecks due to the uncontrollable environment and the complexity of the neural network compared to the *in vitro* neural culture. Such understanding of the sensing mechanism and neuron interface by *in vitro* platform is essential for testing and validating new materials or sensing technologies that would be proposed in the future before trying it directly in *in vivo* applications.

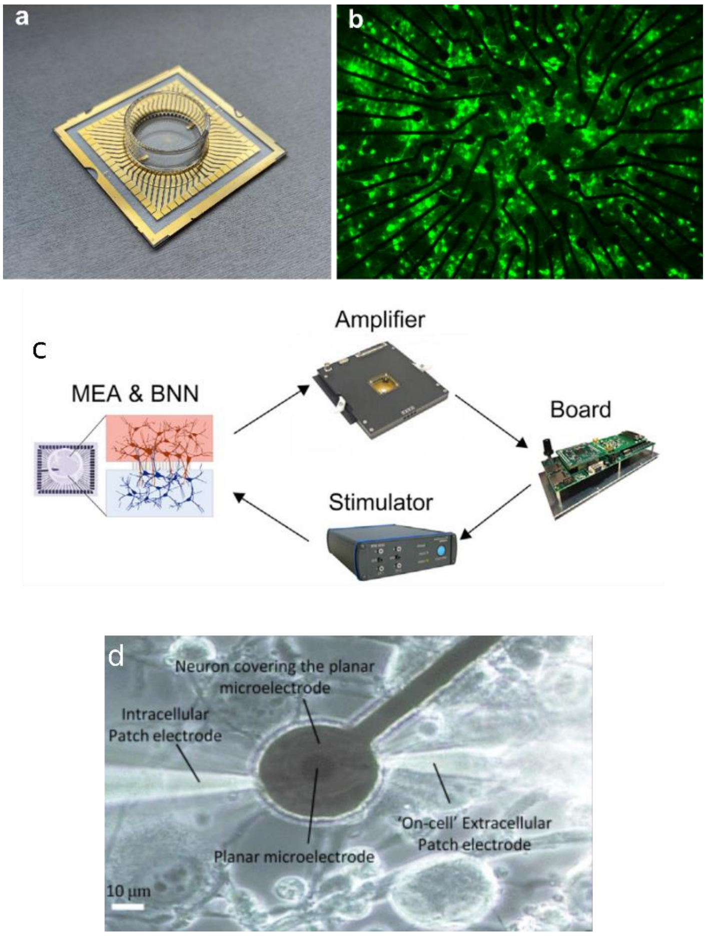

Figure 1.7 (a) Photo of a glass MEA chip with gold microelectrodes. (b) Live-imaging of primary cortical neurons on top of the MEA shown in (a), after 14 days in vitro (DIV14). (c) Schematic representation of the main elements of the setup used for the use of in vitro system (MEA) for interfacing a biological neural network (BNN) and neuromorphic neuroprosthesis [20]. (d) a microscopic image of a neuron cultured in vitro on top of a planar microelectrode on a MEA interfacing simultaneously to intracellular and "on-cell" extracellular patch electrodes. This shows how they used in vitro systems to understand the neuron-sensor interface [22].

Although *in vitro* cultures offer a useful tool for complex neurological investigations, yet it is still difficult to mimic the *in vivo* neuronal environments making it still far from the real-life biological conditions.

3.1 Extracellular space and operational principle

The extracellular potential due to a synaptic event is determined by the full distribution of neuron's membrane ionic current sources and sinks based on the volume conductor theory, i.e., Kirchhoff's current law or charge conservation and Ohm's law [24] (Figure 1.8a). The extracellular electric field is the superposition of all ionic processes, from fast action potentials to the slowest fluctuations in glia [25]. It does not matter if the synapses are chemical or electrical or whether action potentials occur in cell bodies, axons, or dendrites [24]. Thus, any transmembrane current, irrespective of its origin, leads to an intracellular as well as an extracellular voltage deflection.

A microelectrode can detect the extracellular field and its changes across close and nearby neurons. The effect of the membrane current on the electric field and the difference in the waveforms of the signal detected at differently located microelectrodes in the neuronal tissue is due to how each neuronal source linearly sums up (Figure 1.8) with source contributions weighted inversely to their distance. Maxwell's equations of electromagnetism were rewritten with appropriate Laplace boundary conditions, such that for a single point current source, the following equation can be proposed for the potential at an electrode assuming a homogenous and isotropic extracellular medium [26]:

$$V_e = \frac{I}{4\pi\sigma r}$$

Where I is the point current, σ is the conductivity of the medium, and r is the distance between the point source and the recording electrode. Accordingly, as explained in previous parts, the intracellular APs are with an amplitude of tens of millivolts detected with direct access inside the neuron (patch clamp), whereas, the extracellular APs are usually hundreds of microvolts up to a few millivolts detected by electrodes at the vicinity (~100µm) of the spike origin due to the distance and extracellular space effect.

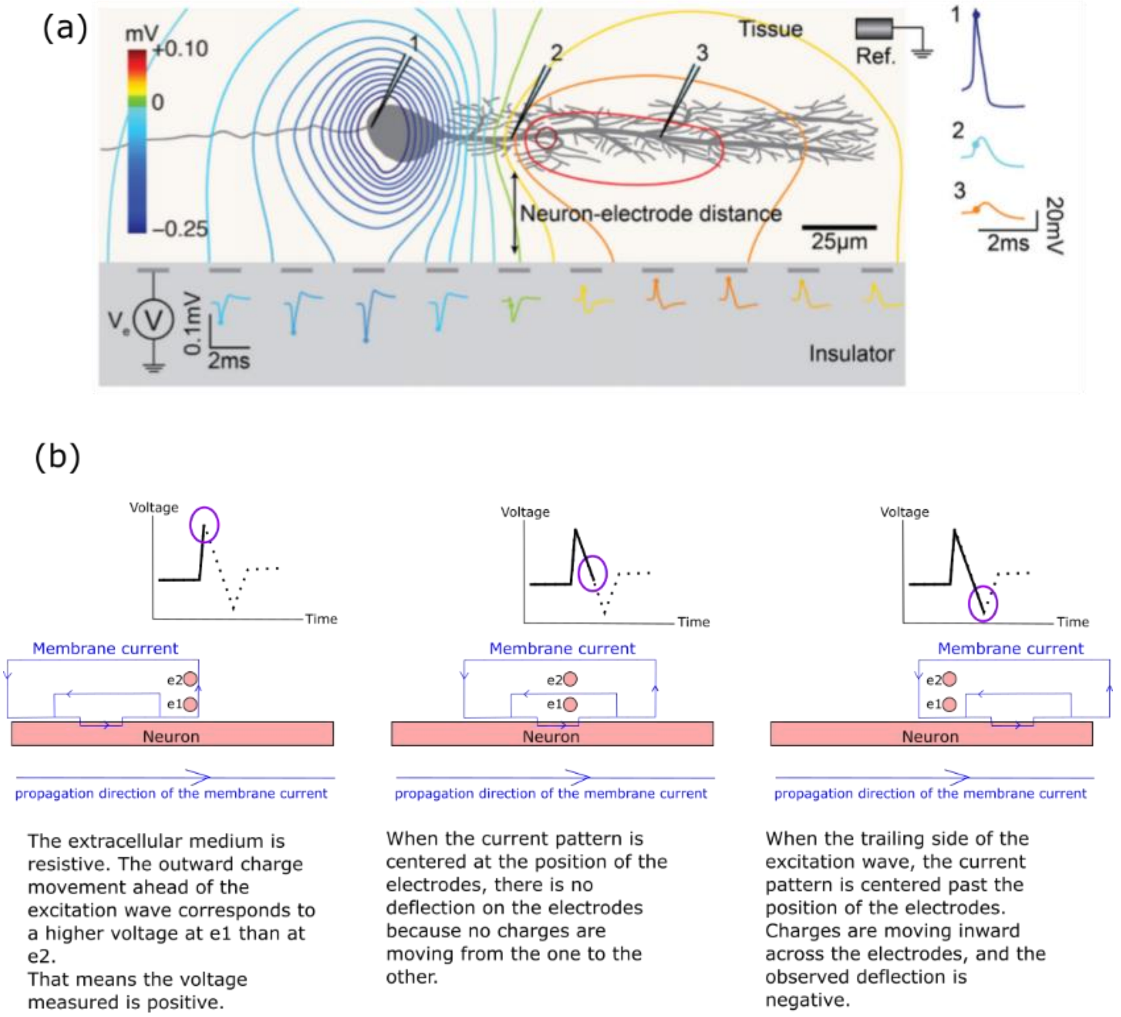

The extracellular medium is resistive. The outward charge movement ahead of the excitation wave corresponds to a higher voltage at e1 than at e2.
That means the voltage measured is positive.

When the current pattern is centered at the position of the electrodes, there is no deflection on the electrodes because no charges are moving from the one to the other.

When the trailing side of the excitation wave, the current pattern is centered past the position of the electrodes. Charges are moving inward across the electrodes, and the observed deflection is negative.

Figure 1.8 (a) Schematic showing the neuron electrode interface in the presence of extracellular ionic current. The distance is affecting the shape and amplitude of the electrodes (adapted from [26]). (b) Schematic showing the effect of electrode position on shape of the recorded signal

As shown in Figure 1.8a and b, the orientation and distance between the cell and the sensing electrode is the main parameter for identifying the amplitude and shape of the signals. This makes it possible to estimate this distance after the extracellular recordings using MEA. Approaches for MEA signal processing and analysis (i.e. Spike Sorting) will be the only way to identify which neuron fires on which electrode. Such methods will help us understanding more the organization of the neural network that is a crucial approach for several electrophysiological applications.

3.2 Analog electrical circuit of the Neuron/Electrode interface

The relevance of the interaction between electronics and neurons was well understood in the cell-electrode model interface was proposed in figure 1.9 [14,22,23]. Referring to the figure, the neuron-electrode system is composed of three domains:

- Neuron (blue), is divided into a junctional membrane that faces the sensing microelectrode (R_j and C_j), and a non-junctional membrane that faces the extracellular medium (R_{nj} and C_{nj}).
- Cleft formed at the adhesion site between the surface of the electrode and the plasma membrane of the neuron. This cleft formed the seal resistance (R_{seal})
- The impedance of the sensing microelectrode: R_e and C_e are the resistance and capacitance, respectively, of a simplified model of the electric double layer that forms at the electrode-electrolyte interface. The electrode is coupled to an amplifier (yellow) before transmitting the recordings into measurement setups.

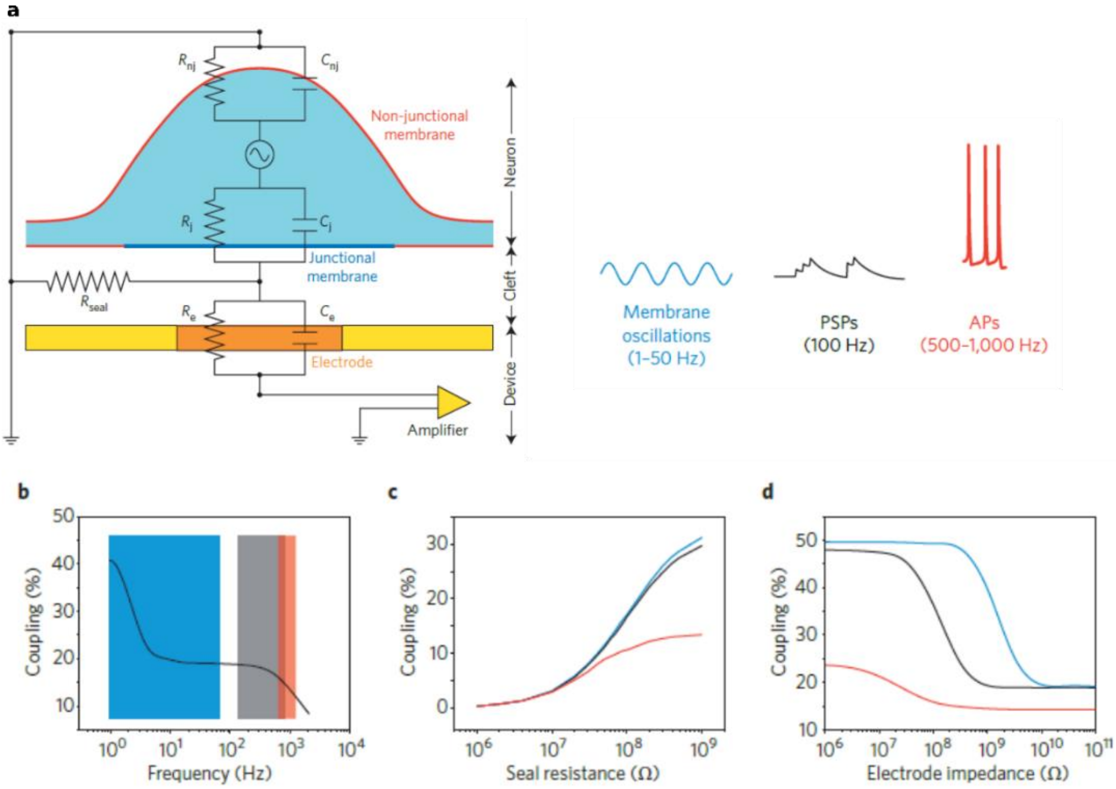

Figure 1.9 Neuron/electrode interface. (a) Left: schematic showing the analog electrical circuit of the neuron/electrode interface. Right: An illustration showing the different type of recorded signals such as low-frequency signals representing membrane oscillations, medium frequencies representing postsynaptic potentials (PSPs) and fast frequencies representing APs. The electrical coupling coefficient of the neuron/electrode as function of (a) type (frequency) of the signal, (b) seal resistance (b) and the electrode's impedance. Figure adapted from [14].

Different from the schematic in Figure 1.8b, most of the MEA applications are in unipolar sensing setup where the voltage measured on each of the local sensing electrodes is compared to a global reference electrode (zero or fixed potential) that is not affected by any electrical activity coming from the cells due to its very far distance. This makes the distance between the neuron and the sensing microelectrode the parameter that directly affects the amplitude of the detected signal.

R_{seal} signifies the quality of affinity between the neuron and the sensing electrode. The better affinity (closer distance) will lead to higher R_{seal} values that will also decrease the leak of the ionic current from the interface out to the medium. This parameter is the most impacting one in determining the efficiency of the neuron-electrode electrical coupling, and thus, the quality of the recordings. To this end, three-dimensional (3D) structured microelectrodes were used to increase R_{seal} by increasing the area of contact between neurons and electrodes due to the engulfment of the 3D microelectrode by the neuron leading into very high signal-to-noise (SNR) ratio of the recordings [27–29]. Some examples of proposed 3D microelectrodes-based MEAs were vertical nanowire probes MEA [30], gold mushroom microelectrodes [28] and gold nanowires [31] (Figure 1.10). Another strategy was to functionalize metallic microelectrodes with biomolecules such as proteins and lipid layers to enhance the adhesion and contact with cells [32–34].

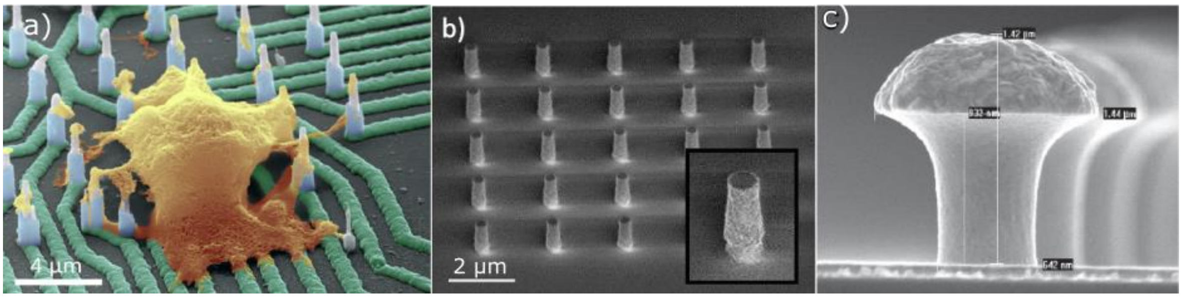

Figure 1.10 Different type of 3D structured MEA. a) Colorized SEM image of neuron on top of nanowires [31]. b) Vertical nanowire probes MEA [30]. c) Gold mushroom shaped microelectrode [28].

Another factor that affects the neuron/electrode electrical coupling is the impedance of the microelectrode. Impedance is a measure that is often presented when characterizing electrodes for neuronal applications and can be loosely defined as resistance to alternating currents [35]. The current of the neurons and electronic devices are fundamentally different: For neurons, it is formed by ions in solution, whereas the latter is formed by electrons in solid-state metals and semiconductors. At the electrode/electrolyte interface, signal transduction of charge carriers from ions in the electrolyte to electrons in the electrode occurs. Two primary mechanisms of charge transfer can occur at this interface, faradaic and capacitive (non-faradaic) reactions. Faradaic mechanisms involve the transfer of electrons at the electrode/electrolyte interface and generally occur when a charge is applied to an electrode resulting in potentials that exceed the threshold for reduction/oxidation (redox) reactions [35]. Capacitive mechanisms dominate in recording electrodes and involve the redistribution of charged chemical species in the electrolyte creating an electric double layer at the interface [35]. The change in local ionic concentrations associated with neuronal electrical activity alters the composition of the electric double layer and ultimately the voltage seen by the microelectrode. Hence, increasing the capacitance of the electrode by lowering its impedance is important for improving the electro-chemical properties of microelectrodes. One reason for decreasing impedance also is to contribute to a lower noise content. This can be seen from the relation between the noise content and the electrode impedance which is given by $V_{noise} = \sqrt{4kTBR_{tot}}$, where k is the Boltzmann constant, T is the temperature in degrees kelvin, B is the frequency bandwidth and R_{tot} is the real part of the total electrode impedance. Another major reason to decrease electrode impedance (Z_e) is to reduce attenuation due to $\frac{Electrode\ impedance}{Effective\ Amplifier\ impedance}$ ratio. The effective amplifier input impedance (Z_a) is connected in series to Z_e, which includes the actual input impedance of the amplifier (Z_a') and the shunt resistance and capacitance to ground outside the amplifier. To limit the influence of the input amplifiers on the measured voltage, they are designed to have high Z'_a (above 10 MΩ at 1 KHz) [36]. The shunt capacitance is the combination of all capacitances from wires from electrolyte to the amplifier, and the parasitic capacitance from metallic electrodes to the electrolytes. This shunt capacitance reduces the effective amplifier input impedance (Z_a), especially at higher frequencies [36]. Hence, the $\frac{Z_e}{Z_a}$ is important such that if the electrode impedance is low enough, it will reduce the influence of shunt capacitance to the recorded signal [26,36]. In consequence, various material and surface modifications such as carbon nanotubes [37,38], diamond coating [39], gold nano-structures [40] and spongy platinum coatings [41,42] have been used to increase the surface area of the commonly used planar metallic microelectrodes (i.e. Au, TiN) and decreasing its impedance (Figure 1.11).

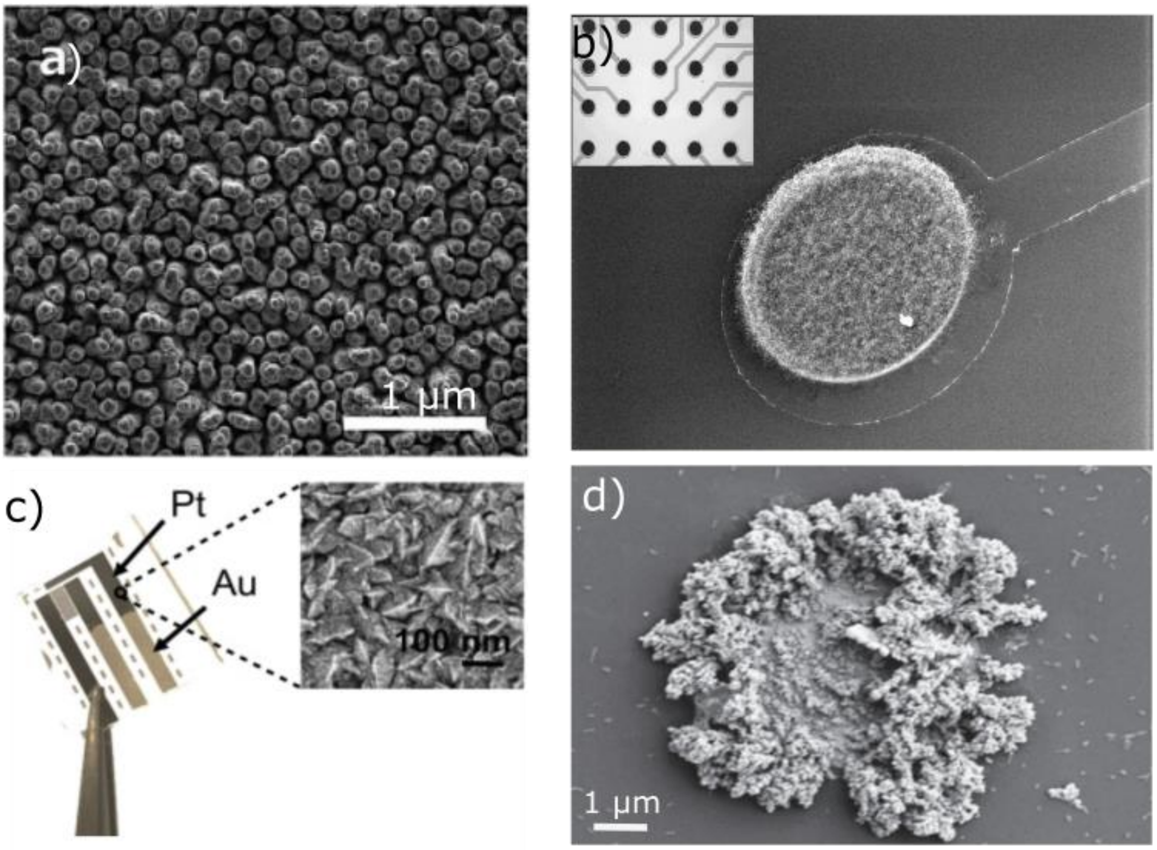

Figure 1.11 (a) Carbon nanotubes covered with diamond microelectrode [39]. (b) Carbon nanotube based microelectrodes [43]. (c) nanostructure platinum (Pt) microelectrodes [42]. (d) Gold nanostructure microelectrode.

Despite the importance of the electrode impedance parameter and the past research that focused on decreasing its value to enhance the recordings, still, the effect of the seal resistance has more impact on the coupling coefficient and the quality of the recording. Looking at the graphs in Figure 1.9d, we can see that the relative increase in the coupling (%) started to be in steady state when the electrode impedance started to be less than a cut-off impedance value. This curve shows that all electrode impedance values below Z_e =10 M Ω (which is the case in most of the MEA materials) will have the same effect on coupling (%) if they have same values for the other parameters (i.e. R_{seal}) also. However, by looking at the curve in Figure 1.9c, we can see that there is no cut-off seal resistance value, such that the more we increase R_{seal}, the more we still improve the recording. Therefore, any material or geometrical engineering technique used to optimize the impedance of an electrode with Z_e <10 M Ω, it will not enhance the coupling (%) more unless it is also increasing R_{seal} (maintaining better affinity with the neurons). This hypothesis is supported by the results summarized from [14] shown in Table 1.1. As we can see, the higher coupling coefficient % values achieved are in the cases where there are higher values of R_{seal} regardless of the electrode's impedance value. For example, planar MEAs (4th case) have Z_e values lower by 3 to 4 orders of magnitudes from that of VNEA (3rd case) but still maintain a maximum coupling coefficient of 1% which is much lower than that of VNEA (30 %). The reason behind that is that just two orders of magnitudes of difference in the R_{seal} values, made VNEA maintain a coupling coefficient higher by 30 times.

Table 1.1 Electrical and methodological specifications of different available techniques for recording from neurons. This table is adapted from [14]

Technology	**R_{seal} (Ω)**	**Electrode impedance (Ω)**	**Maximum AP (mV)**	**Coupling coefficient %**	**Ref.**
Patch-clamp electrodes	$>10^9$	10^6	100 mV	100%	[44]
Gold mushroom shaped MEA	10^8	10^{11}	25 mV	~50 %	[28]
Vertical nanowire electrode arrays (VNEA)	10^8	$\sim10^8$	4 mV	~30 %	[45]
Planar MEAs	10^6	$10^4 - 10^5$	<1	0.1-1 %	[39,41,46–48]

In this manuscript also, we will put forward solutions to enhance the surface/cell affinity (improve R_{seal}) and thus the quality of the extracellular recordings of planar MEAs by improving its electrode material instead of fabricating complicated, expensive, and time consuming 3D microelectrodes. For that, the use of conductive polymers is an interesting key solution. Our results showed that microelectrodes with same impedance values (kHz range) could maintain different quality of recording due to the R_{seal} enhancement **(*chapter IV*)**.

3.3 The use of organic polymers (PEDOT:PSS) in MEA

Conducting Polymers (CPs) consist of conjugated carbons chain with alternating single and double bonds that are responsible for their electrical and optical behavior due to the highly delocalized π-electrons.

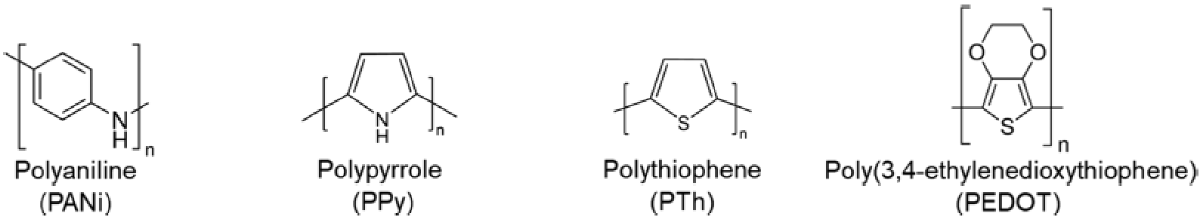

Figure 1.12 Chemical structure for the common conducting polymers used for *in vitro* bioelectronic applications [49]

Recently the use of CP has emerged as a coating material for optimizing the performance of microelectrodes for *in vitro* recording applications due to its advantages (Figure 1.13) such as:

Biocompatibility. The similarities between CPs, proteins, and natural tissues with their elements and long-chain architecture leads to the reasonable conclusion that CPs are better representations of living tissue response compared with metals, for example [50]. The biocompatible property of CPs as a coating material enhances the affinity between the neuron and the electrode, leading to better quality and long term recordings [49,51]. However, the biocompatibility of CPs cannot be universally defined because depending on the cell type and its environment, they can elicit different biological responses. Various biochemical studies are dedicated to improve the level of biocompatibility for CPs [52–54].

Mechanical properties. The mechanical matching between the electrode and the cell is crucial for *in vitro* recording to maintain a softer mechanical environment for the cell to survive at the interface. The soft and low mechanical stiffness (low Young Modulus values) of the CPs compared to metals, is adapted to biological environments. In addition to that, their mechanical flexibility property provides them the capability to be used in implantable or wearable devices [55].

Mixed conduction (ionic and electronic) and low impedance. The ability of CPs to conduct both ionic and electronic currents is one of the most important properties of CPs that makes them increasingly used for bioelectronics applications. When they are biased in an aqueous electrolyte, ions move from the electrolyte into the bulk of the material to compensate electronic charges [56]. Accordingly, extracellular ionic currents originating from biological activity affects the electronic properties of CPs directly when in contact with neurons [49]. The mix of electrical conductivity and ion permeability for these materials tends to increase the electrochemical surface area of the microelectrodes and reduce their impedance which is an important for the recordings, as explained in the previous sections [57,58]. The effect of the electrochemical surface area on the impedance of the electrode, among other parameters, is shown when coating microelectrodes with electroactive materials, i.e. the rougher/more porous the coating the lower the impedance [35].

Versatility in chemical modification. Many studies show chemical modification of polymers to enhance its biocompatibility or interaction with neurons [59]. The high degree of freedom for the use sidechain-engineering techniques to tune the chemical properties of these materials paves the way for a very interesting scientific direction for the use of CPs (***Chapter IV***).

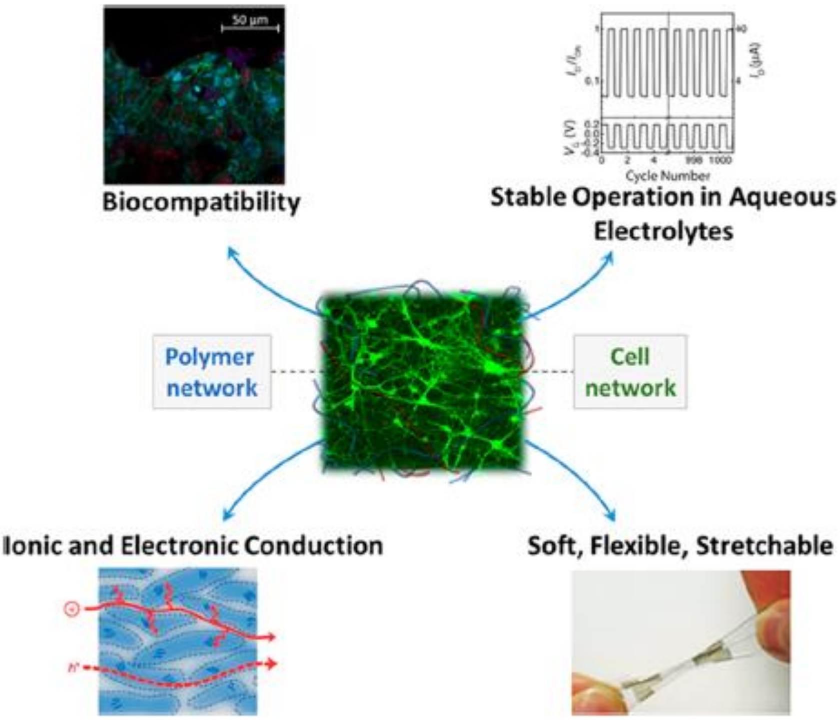

Figure 1.13 Schematic showing some of the essential propoerties of CPs for *in vitro* bioelectronics [49]

3.3.1 The Case of PEDOT:PSS

Poly(3,4-ethylenedioxythiophene) doped with poly(styrene sulfonate) (PEDOT:PSS) is a CP mixture of two ionomers: PEDOT is the p-type semiconducting conjugated polymer that carries positive charges (conduct holes in the form of polarons), and negatively charged sulfonate groups of PSS that stabilize electrostatically the PEDOT. It has been investigated that PSS does not homogeneously scatter into the PEDOT matrix, rather it forms nanometric domains [49]. PEDOT is a large gap organic semiconductor with a negligible intrinsic free charge density. Upon blending with PSS, the high acidity of the sulfonate part allows the release of a proton. The negative charge of PSS gets neutralized by the breaking of a double bond on the PEDOT chain i.e, the formation of a free hole. The free charge concentration (the concentration of SO_3^- also) reaches high values up to$10^{19} - 10^{21}\ cm^{-3}$. The PEDOT:PSS structure is based on random interactions between polymer chains due to the delocalization of positive charges in PEDOT and the different spacing of charges in PEDOT and PSS, this model called scrambled-egg arrangement. This results in a gel polymer network composed of aqueous gel particles and a solid state content depends on the ratio between PEDOT and PSS. This ratio changes the physical properties of the film such as the conductivity, sheet resistance, solute content, surface roughness, and the Young modulus value [60]. The ratio of PEDOT to PSS has a direct impact on the conductivity because it defines the density of charge transporting PEDOT chains. The PEDOT:PSS is produced commercially in industrial scale (Heraeus gmbH [61]). The addition of solvents, enhancing agents (3-glycidoxypropyltrimethoxysilane (GOPS)), and the alteration of pH can modify the conductivity of polymers. Conductivity of commercial PEDOT:PSS polymer can reach 1000 S/cm [61] making it an interesting option as a coating conductive material (coating passive microelectrodes)

In aqueous solutions, when electrically addressed (active bioelectronics), hydrated cations disrupt the electrostatic polaron SO_3^- bonds between the PEDOT backbone and PSS, respectively, leading into dedoping PEDOT:PSS. As shown in the schematic of figure 1.14, PEDOT chains are then deformed, the hole transport pathway is disrupted, and consequently, the hole conductivity of the material is reduced. The conductivity modulation is the main operation principle of PEDOT:PSS-based active bioelectronic devices that will be reported more in details in *Chapter I, part 3*. The bulk interaction between ions and holes leads to high capacitance values. Rivnay et al. discovered that there is a linear relationship between the capacitance and the volume of the film, revealing a volumetric capacitance of $C^* = 39\ F/cm^3$[62]. Volkov et al. showed that the electrical double layers formed along with the with interfaces between nanoscaled PEDOT-rich and PSS-rich interconnected grains form the main contribution to the capacitance of PEDOT:PSS [63].

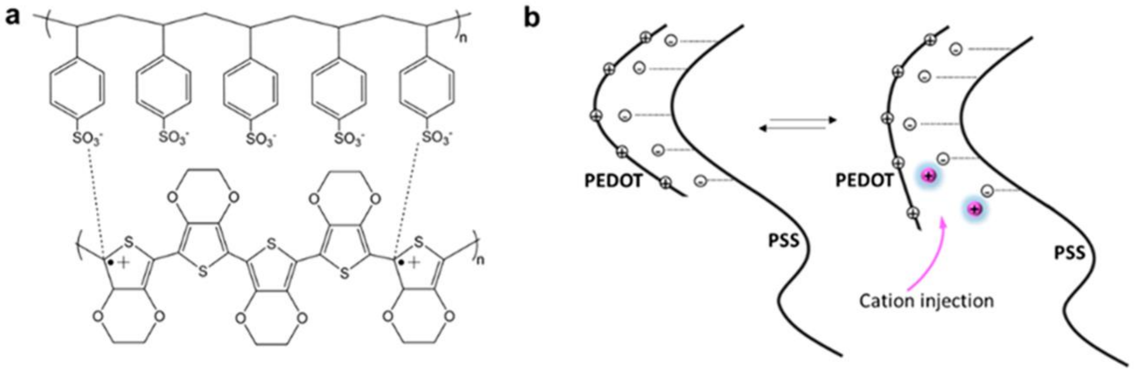

Figure 1.14 (a) PEDOT:PSS chemical structure. (b) Schematic showing the dedoping of PEDOT:PSS with cations from an electrolyte. Adapted from [49]

Recently, the use of PEDOT:PSS to coat microelectrodes has been considered for optimizing its performances in bio-sensing due to its ease of processing, commercial availabilities and high conductivity, in addition to the CPs beneficial properties that have been mentioned previously. PEDOT:PSS is of particular interest since it can be used to implement very low electrical impedance through its volumetric capacitance. Increasing the thin film thickness increase linearly the effective capacitance of the electrode and is used to improve the signal transmission [48,55,57]. As mentioned in previous section, the main parameter that enhance recording is the R_{seal}. In most of the reported work for using PEDOT:PSS for electrophysiology, they concentrated in their work more on optimizing impedance rather than seeking for the R_{seal} parameter [46,48,57,58,64,65]. Although a lot of studies reported PEDOT:PPS based microelectrodes with very low impedance values down to ~20 KΩ [46,57,64,66] (Figure 1.15d), however, the SNR ratio, coupling coefficient, and the quality of the *in vitro* extracellular recordings from the neurons by using PEDOT:PSS microelectrodes is still limited compared to SNR ratio that have been reached by 3D microelectrodes with high R_{seal} . Given this scenario, there is a great need to improve the coupling between neurons and PEDOT:PSS microelectrodes to reach higher performances. PEDOT:PSS shows good biocompatibility [52,55] and soft mechanical property (low Young modulus) [67] that matches the neuron coupling requirements. In contrast to the 3D microelectrodes, PEDOT:PSS coatings in microelectrodes are generally thin film structures leading to less mechanical tension between electrodes and neurons and good conformal adhesion. These aspects could be used and investigated to improve the seal resistance by increasing the cell/electrode affinity. Fortunately, CPs offer high versatility through side-chain engineering to chemically modify them such as incorporating bioactive species [68–70]. There are several reasons for incorporating bioactive species in the electrode material that could be of interest for *in vitro* extracellular recording from neurons. One important reason, it involves in immobilizing molecules on the surface of the microelectrode that can enhance and improve the attachment of neurons (increase R_{seal}) and decrease adverse immunological response (better biocompatibility). This significantly affects the quality of the recordings coming from these microelectrodes. However, the extent of using chemically functionalized PEDOT:PSS microelectrodes for *in vitro* extracellular neural recordings and investigating its effect on the quality of the signal is still unexplored widely. Accordingly, the next chapters use chemically synthesized EDOT for coating gold MEAs. I will report how this material will improve the neuron-electrode coupling (R_{seal}) leading into enhancement in the uses of PEDOT for neurosensing applications e.g. *in vitro* extracellular recordings from cortical neurons.

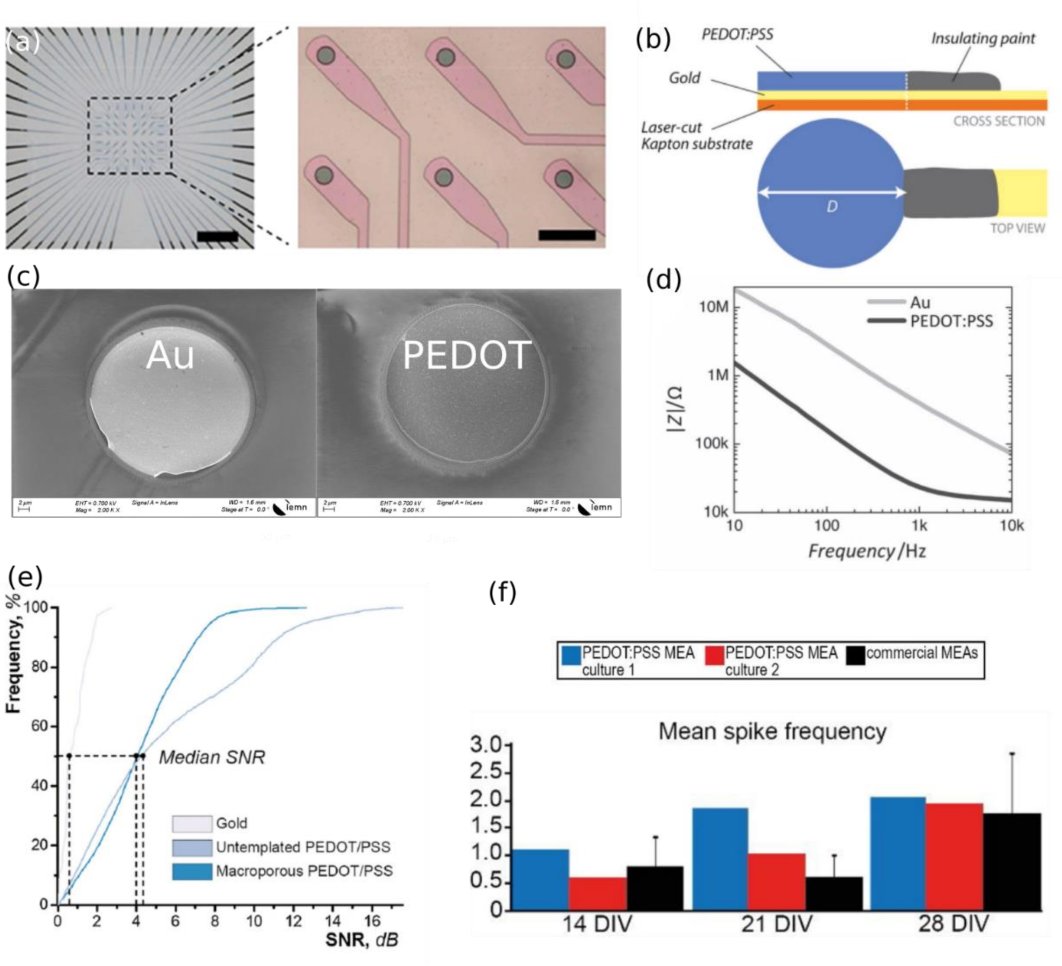

Figure 1.15 PEDOT:PSS MEAs. a) PEDOT:PSS based microelectrode array for simultaneous electrical and optical measurements of primary neuron cultures. Scale bards: left, 1cm; right: 100 µm. Adapted from [71] b) schematic showing the coating of PEDOT:PSS on top of flexible Kapton electrode [72]. c) SEM images showing coated PEDOT:PSS on top of bare gold microelectrode. Left: bare gold (Au) before coating, right: after coating PEDOT:PSS .d) Impedance modulus as function of frequency for gold and PEDOT:PSS electrode showing the notable lower impedance for PEDOT:PSS electrode [56]. e) Cumulative frequency plot showing the distribution of SNR for gold, PEDOT:PSS and macroporous PEDOT:PSS microelectrodes showing superior SNR values for PEDOT [64]. f) Mean spike frequency for two PEDOT:PSS base MEA (blue and red) and commercial TiN based MEA (black) at 14, 21 and 28 day in vitro (DIV) showing higher firing rate of the PEDOT:PSS MEA in comparison to the commercial one reassuring proper maturation of the neural network [57].

3.4 MEA signal processing; Spike Sorting

Indeed, in recent years, the development of microelectrode arrays (MEAs) for recording simultaneously the extracellularly electrical activities of single neurons up to large populations of neurons has been blooming [73]. The rationale for such an interest is that assuming one could record the activity of many neurons at the single-spike levels, the possibilities for brain-machine interfaces are tremendous [74–76]. In MEAs, it has been observed that one microelectrode can sense several number of cells or the electrical activity of one cell can be recorded by multiple microelectrodes [26]. Consequently, the analysis of the recorded signals from a large neuronal population of neurons using MEA is a crucial challenge to unravel how information is processed by the brain. To decode this neural activity and extract relevant information from the recordings obtained via these MEA, one needs to perform a post-processing step called spike sorting [77].

During spike sorting, the spikes detected from the extracellular traces are differentiated according to their spatio-temporal shapes (both in amplitude and time) in order to isolate the electrical activity of each individual neuron for a better understanding of the global dynamic of the neural network. The classic approach to spike sorting usually includes (1) filtering raw data, (2) spike detection, (3) feature extraction and (4) clustering (Figure 1.16). The raw signal is processed by filtering to separate APs from LFP by applying a band-pass filter from 300 to 3000 Hz. Spike detection is performed by amplitude thresholding to separate spikes from the baseline noise level. In most of the algorithms, the differentiation of the extracellular waveforms emitted by the individual neurons is usually performed via a clustering algorithm. The objective is to reduce the dimensionality of the waveforms to a so-called "feature space" in order to associate each spike (AP) to a specific neuron (Figure 1.16). In the literature, various dimensionality reduction techniques have been used to perform this projection, such as Principal Component Analysis [78], SVD [79], ICA [80]. All have in common required to be learned on a subset of the data, before application.

Recently, however, the question of bypassing such a feature extraction step has been brought up, especially in the context of *in vivo* nonstationary recordings, to tackle the problems of drifting tissues [81,82]. Indeed, the possibility to quickly get a raw estimate of the position of the cells obtained from the shapes of their extracellular waveforms would potentially ease the spike sorting procedures, and simplify the handling of physical drifts [83]. While, quite often, the localization of the neurons has been very naively estimated by several spike-sorting algorithms with a simple Center Of Mass (COM, see Methods) algorithm depending on their electrical signatures, more evolved algorithms have been proposed to infer such positions [84–86], taking into account some physical properties of the cells. Another localization spike-sorting algortihm could be is by considering cells behave as monopoles (Monopolar, see methods) [86,87]. Certainly, while appealing, the precision of these localization techniques has not been properly tested with ground truth recordings. Therefore, this is hard to know up to which extent such "estimated" positions could be used to properly estimate some true physical properties of the cells, such as for example drifts. Hence, *in vitro* 2D neuronal culture is a great alternative platform to understand better the spike-sorting performances (i.e. how accurate the algorithm in sorting spikes) due to its less degree of complexity compared to *in vivo* (i.e. no drift will occur, accuracy estimation will be easier). In upcoming chapters, we will compare how accurate such localization methods could be with *in vitro* recordings of neuronal cultures combined with optical imaging, and when the spacing between electrodes is not so dense. Indeed, it is well known that increasing the density of the recordings can help the spike sorting algorithms [78,88,89], but at the cost of more complicated analysis pipelines. Consequently, to enhance the quality of the recordings without increasing the density, we decided to test the use of electrodes made of conducting polymers such as PEDOT.

In our particular interest, being able to estimate accurately enough the positions of the somas from the extracellular signals might help in understanding better the coupling between the neuron and electrode and open new possibilities to investigate more the relationships between functional responses and morphologies of the cells. In the neuron-electrode interface and the extracellular space section, we identified the parameters that affect the quality of the recordings (i.e. neuron-electrode distance (R_{seal})). Identifying more accurately which cell has particular interaction with the measuring electrode could be a great methodology to follow for validating the parameter responsible for the improvement of the recording if new materials, microelectrodes or other technologies (i.e. transistors) are proposed. In our work, we will exploit the accurate spike-sorting algorithm as a tool to validate the performances of the new chemically synthesized polymer we used for coating MEAs. Being able to detect cells accurately, we support our hypothesis of the improvement in the affinity (higher R_{seal}) with neuron due to this polymer's chemical and morphological characteristics.

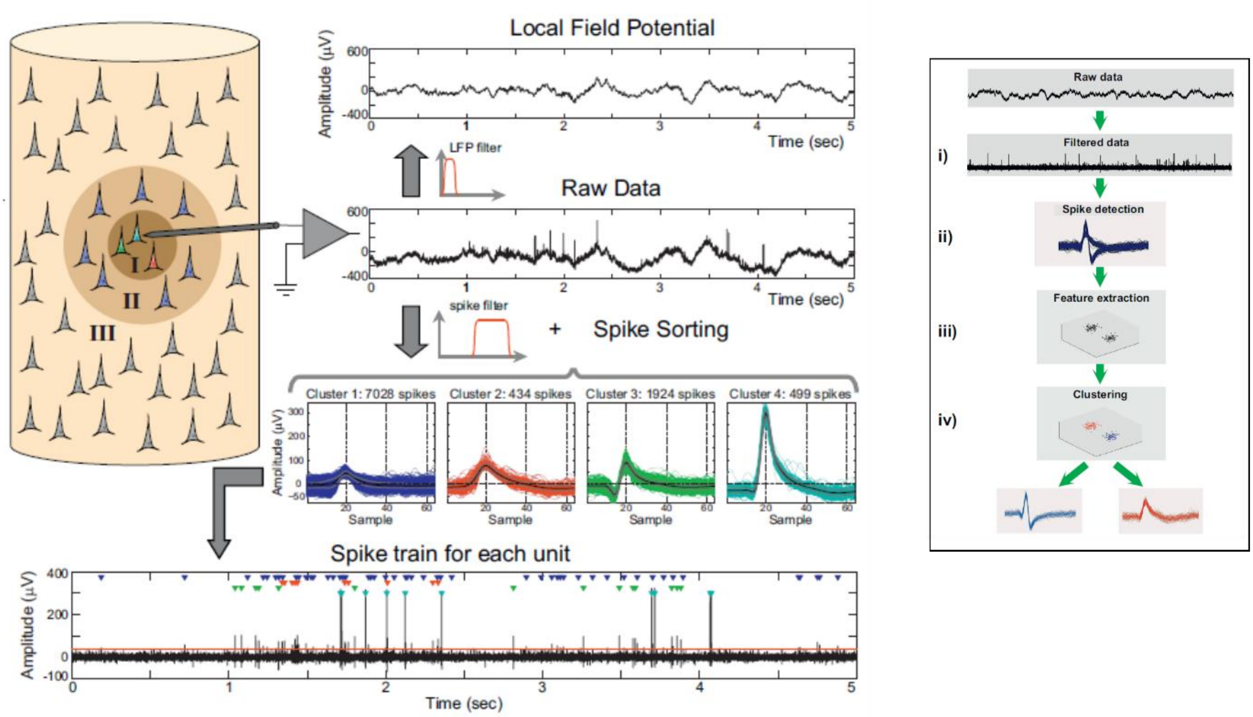

Figure 1.16 Spike sorting (Adapted from [90]). Example of raw data extracellular recording from the human entorhinal cortex. Within the filtered data between 300 and 3000 Hz there is a superposition of several effects. Neurons in Zone I are less than 50 µm away from the electrode, in Zone II between 50 µm and 140 µm away from the electrode and Zone III is more than 140 µm away from the electrode. We can see how spike sorting is clustering the spikes and is assigning each spike to a cluster depending on each amplitude and shape. Inset: schematic showing the basic steps for spike sorting.

4. Active Sensors: Organic Electrochemical Transistor (OECT).

In the previous part, I discussed passive microelectrode arrays. Although we pointed out to the need for material, and geometrical optimization of MEA to find the ideal parameters for interfacing the brain, still the present development in its fabrication process technology, electronics and signal processing make it a qualified technology to be commercially available and widely used in electrophysiology.

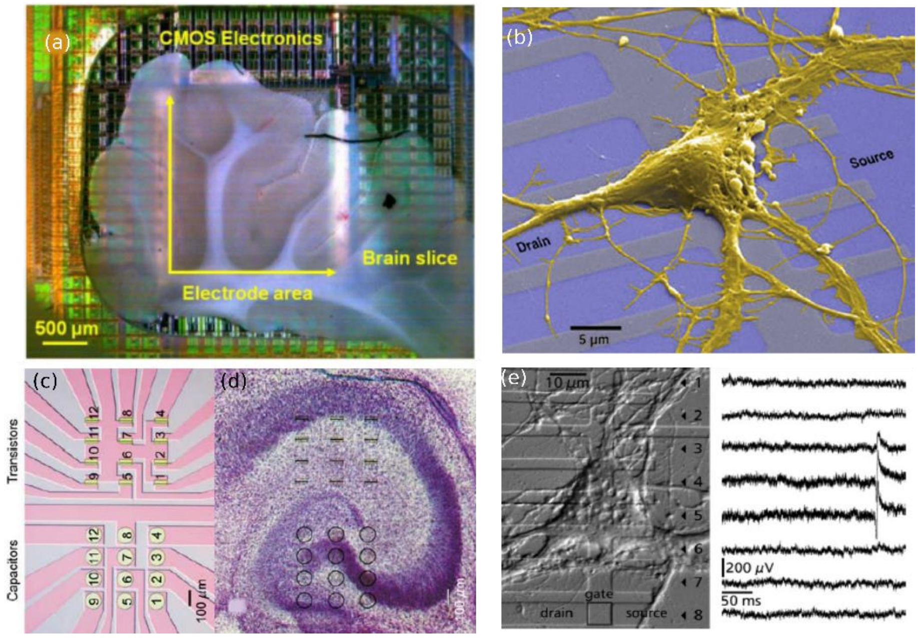

Figure 1.17 Interfacing neurons with active electronics. (a) Acute cerebellar brain slice (parasagittal cut) placed on a CMOS high-density electrode chip for measurements aimed for signal condition at the interface [91]. (b) Nerve cell from rat brain silicon chip contains field-effect transistors [92]. (c) Schematic of cross-section view of a chip containing capacitors and transistors aimed for (d) interfacing hippocampus slice culture [93]. (e) Micrograph of nerve cell on linear array of FETs and its extracellular recordings [92].

A major technological advance would be to use arrays with active electrodes. Active array composed of circuitry capabilities, such as amplifiers or filter units, which are integrated within or with the electrodes on the same substrate. Two important advantages of using active arrays (i) *connectivity*; larger number of sensors can be used (i.e. on-chip multiplexing architecture [91]); and then, more significantly, (ii) ***signal quality***; the signal is conditioned onsite at the interface due to its dedicated circuitry units (i.e. filters, amplifiers).

(i) Conventional passive MEAs usually contain tens of microelectrodes (i.e. 64 electrodes Multichannel System MEA), with each electrode requiring a connection to the external circuitry. This may add parasitic capacitance that can attenuate the small signals. Several studies reported the use of complementary semiconductor-metal-oxide (CMOS)-based active microelectrodes [73,91,94]. These CMOS MEAs offer large numbers of microelectrodes, up to approximately 26000 (i.e. MaxWell Biosystems MEAs), with the necessary on-chip circuitry. Addressing on-chip circuitry such as multiplexers will provide a very important asset of having high transducer density which cannot be realized with passive MEA simply (thousands of electrical connections on millimeter-size chips is impossible. Compact designs of the entire measurement platform within the chip area are also possible through implementing the circuit blocks on the integrated circuits (IC) or transistors. These minimized measurement system areas would be significantly beneficial, e.g., for implanted *in vivo* neural recording [95].

(ii) On-chip microelectronics provided by CMOS or transistor technology translate into improved system capability, which can be dedicated to crucial and challenging tasks in brain machine interface, information technology, and medical applications. Due to the analog nature of biological signals, integrating high-performance transistor-based sensors with analog circuits is crucial for improving the performances of neural interfaces. In the case of relatively low SNR recordings, the signal of interest will be smaller than the noise leading to difficulty analyzing data. Having transistors that can amplify and pre-process signals at the interface is crucial for ensuring that weak neuronal signals are faithfully recorded, which will reduce energy spent on post-processing data approaches. For example, the ionic currents coming from the neurons are small in the range of nA and need to be amplified through differential systems. This certainly will add pick-up electrical noise coming from the lead lines running from the electrolyte to the signal conditioning circuity that will get amplified with the signal. In active sensing using a transistor, the distance between the neuron and the amplifier (transistor) is micrometers far. Looking at the schematic shown in Figure 1.18, when comparing the SNR of the active transducing amplifier with the SNR of an electrode, the SNR of the transistor will theoretically always be higher than that of MEA since the noise of the lead lines was not amplified. This has been verified in a study [96] where they reported higher SNR values of the electrophysiological signal recorded from a transistor (32 dB) compared with electrodes (26 dB). Active sensors have also some additional functionality, such as analog-to-digital conversion (ADC) [91], on-chip spike detection [97], and versatile device calibration [26,91]. On-chip ADC means that the active sensors produce output signals that can be easily processed and transferred without compromising their information content [91]. For spike detection applications, work has been done to establish an optimal filtering method using an active array for the simultaneous detection and classification of neuronal APs [97]. This technique showed an interesting solution to solve the problem of overlapping spikes and the use of redundant data for the detection and classification of spikes which leads into an efficient real-time spike sorting approach. In the next chapters, we will show how bottom-up device engineering technique can be exploited to calibrate transistor to a matched filter for detecting specific artificial spikes, i.e. high frequency spikes rather than low frequency ones (filtering and spike detection).

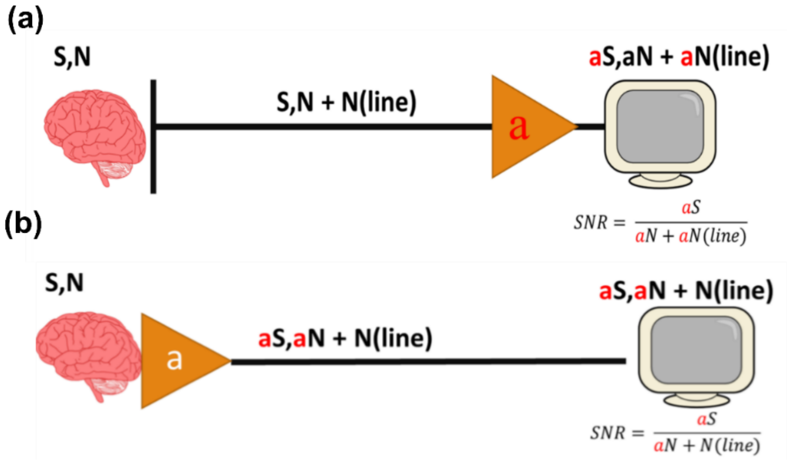

Figure 1.18 Schematics explaining the SNR of recordings by using (a) MEAs and (b) transistors. S: signal, N: noise and a: amplification.

The first recording from living tissue using a transistor device was performed in 1976 by Bergveld et al. [98], who measured the electrical signals from muscle fibers. The next landmark in using FET technology for *in vitro* recording from isolated neurons was set by Fromherz et al. in 1991 using leech neurons interfaced with silicon FETs.

Typically, the transistor is a three-terminal device (source, drain and gate terminals) that forms a switch-like structure that allows for a large modulation in its source-drain output current upon a small gate potential variation . Hence, they are described as voltage-controlled current source amplifiers. The substrate of a FET is a p-doped semiconductor (i.e. Silicon (Si)), which contains two highly doped regions that are source (S) and drain (D). The highly doped regions (S and D) are isolated from the substrate by p-n junctions. By applying a positive potential across the gate, the negative mobile electronic charges will accumulate near the dielectric with the interface leading to field-effect doping of the semiconductor channel (output drain current modulation by gate voltage). The slope of the drain current modulation by gate voltage represents the transconductance (gm) which describes the sensitivity of the transistor to the voltage changes across the gate. In accumulation regime, the transconductance (gm) and sensitivity (S) of a FET is [99]:

$$S = \frac{\partial I_{DS}/\partial V_{LG}}{V_{DS}} = \frac{g_m}{V_{DS}} = \mu . C_{ox}\frac{W}{L} ; \quad gm = \mu . C_{ox}\frac{W}{L} V_{DS}$$

With gm the FET transconductance, I_{DS} and V_{DS} the drain source current and voltage, V_{LG} the gate voltage, μ the charge carriers mobility, C_{ox} is the gate oxide capacitance per unit area. According to the equantions above, the FET sensitivity is directly dependent on the semiconductor channel material (mobility), the gate dielectric, and the dimension of the transistor (W/L ratio).

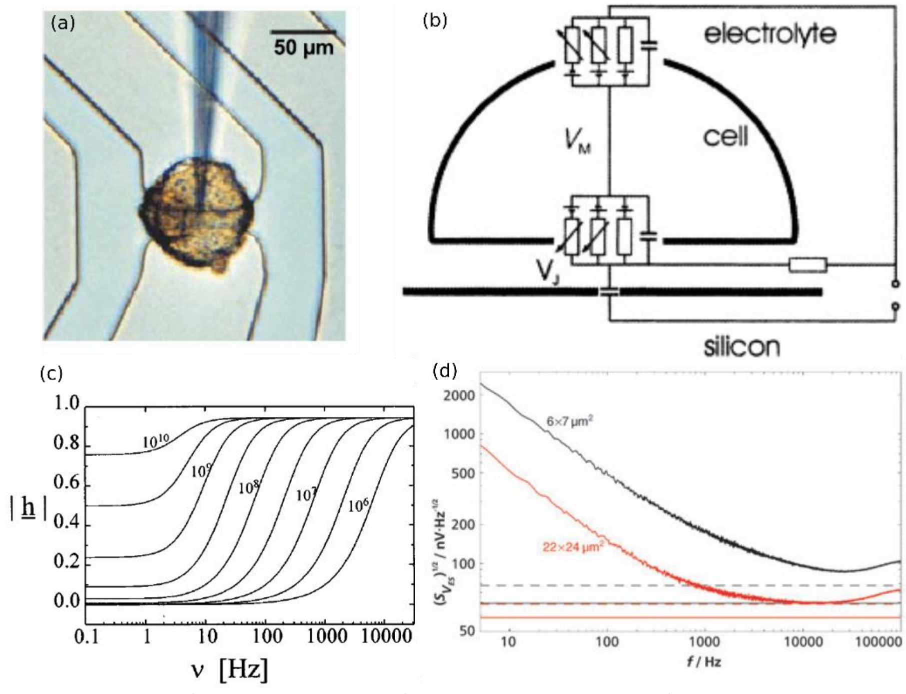

Figure 1.19 (a) Microscopic image of the leech neuron interfaced with FET. (a) Circuit of the neuron-Si junction. Global capacitances and resistances describe the oxide, membrane and electrolyte film. voltage-dependent ion conductances are considered in the contact and in the free membrane. V_M is the voltage in the cell and V_J is the extracellular voltage in the seal junction with respect to the bath potential. (adapted from [100]). (c) simulation of transfer function (VJ/VM coupling) versus frequency with different seal resistance values. Higher seal resistance leading into higher coupling with broader bandwidth [101] (d) Square root of the spectral density of the gated-referred noise voltage between electrolyte and silicon for two different transistors with different geometry. We can see that larger transistor (red) has lower noise. The solid horizontal lines describe the thermal noise. The dashed lines are the thermal noise plus amplifier noise [102].

Following Fromherz later studies on this topic[23,93,103], he developed a simple model to describe the junction between cell and transistor. This model called the point contact model, combines the ohmic junction, voltage gated ion channels and capacitive junction (Figure 1.19). As already explained in the extracellular space section, the extracellular ionic current will flow across the seal resistance in the cleft, forming an extracellular voltage V_J . This voltage modulates the current across the transistor channel [100]. Thus, the transistor modulates the cell's electrical activity into a measurable current signal ΔI. The output measured current depends on the extracellular potential and transconductance as follows: $\Delta I = gm$. V_J (in biased configuration), revealing the great potential for device engineering of the transistor. By choosing the right materials and dimensions of the transistor's channel, the transconductance can be increased resulting in better amplification and higher SNR of the recordings. On the other hand, capacitive current flows through the insulating oxide when a changing voltage is applied to a highly doped region of the silicon beneath the neuron. It also gives rise to an extracellular voltage V_J beneath the cell which is determined by the capacitance and resistance of the cleft [100] . If it is sufficiently high, this extracellular stimulus affects the cell membrane that may lead to opening the voltage-controlled ion channels, and thus AP may be elicited [100]. Therefore, the extracellular voltage V_J (t) arises from a superposition of all capacitive and ionic currents in the interface. The shape and the signal of this resulting extracellular voltage (note: not the recorded output current) is controlled by the accumulation and depletion of ion conductance in the membrane and by the specific conductance of the junction. Which is represented by the effect of capacitive coupling, ohmic coupling, and the voltage-gated ion channels (will be explained more in detail in *Chapter VI*). It is worth here to mention that for all coupling types, the amplitude of V_J increases with the seal resistance (Rseal) [101] , which directly increases the ΔI recorded at the output. We can see in Figure 1.19c, that the coupling coeffient's bandwidth and amplitude increase with the seal resistance. Indeed, using transistors with materials that are highly biocompatible and maintain high affinity with the neurons in order to increase Rseal and thus higher SNR of the recordings (higher ΔI). The neuron-transistor junction may be the microscopic input of an electronic amplifier without the interference of the stray capacitance and electrolyte-metal contact [102]. Low frequency noise in FETs is caused by electron tunneling between silicon and traps in the gate oxide [102]. Fromherz showed that the power density of the low-frequency noise is inversely proportional to the gate area and the C_{ox} of the transistor (Figure 1.19)[102]. This has been validated with *in vitro* neuronal recording where larger transistors showed 3 times lower RMS noise value. Increasing the WL yielded a low noise level, but the chances for a good match of neuron and active area are low (neuron was not covering totally the transistor), making a tread off with Rseal. For that reason, Fromherz results favored the use of smaller transistors despite their higher noise (higher effect of Rseal). Finding devices or materials that can increase the transistor's capacitance without significantly increasing its active area dimensions is important for reducing noise without any loss in Rseal. In the contrary, there is another argument concerning the C_{ox} of the transistor that can limit our confidenc in increasing their values. Fromherz also reported that the V_J and V_M ($\frac{V_J}{V_M}$ ratio) coupling is inversely proportional to C_{ox} value. However, the frequency that defines this effect is also related to the seal resistance. Noting that what we record is a modulation in the current where the sensitivity of this modulation is represented by gm that is directly proportional to the C_{ox} value. Hence, several tread-off parameters has been presented, and finding devices with the optimal parameters is crucial. Active transistors with different geometries and materials, including graphene [99,104], Si nanowire [105,106], diamond [107] and 3D FETs [108–110] has been used for *in vivo* and *in vitro* electrophysiology applications. However, there is still a need to find devices and materials that can maintain higher gm, better compatibility and affinity (Rseal), and optimum values of capacitance.

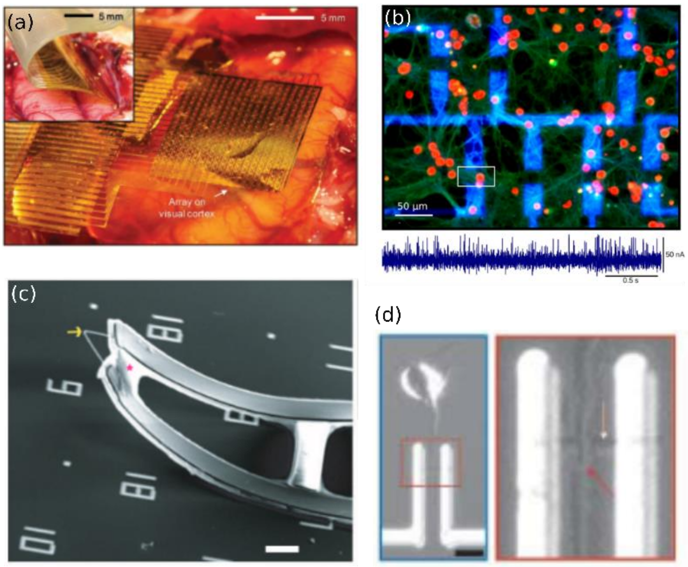

Figure 1.20 **Transistors with different materials and geormetries for electrophysiology and *in vitro* recordings. (a) A flexible, high-density active electrode array placed on the visual cortex [68]. *In vitro* neuron cell culture on top of graphene FET array. Inset showing recording from one transistor [99]. 3D FET transistor. Yellow arroy showing source and drain electrodes. Red star showing the channel [27]. Silicon nanowire transistor interfacing neuron [105]**

4.1 Organic Electrochemical Transistor (OECT)

Lately, the performance of organic bioelectronics, particularly organic electrochemical transistors (OECTs),have been identified as a promising device architecture to improve extracellular potentials recording in electroactive cells culture both *in vitro* and *in vivo*. In addition to unique properties of interest for electrophysiology such as biocompatibility and flexibility, OECTs operating principle is based on the transduction of ionic currents in the biological medium into electronic currents in the organic semiconductor (e.g. PEDOT:PSS) via electrochemical coupling

4.1.1 Operating Mechanism

Organic electrochemical transistor (OECT) belongs to the category of Electrolyte-Gated Organic Field-Effect Transistors or EGOFETs. The first OECT was demonstrated by the group of Mark Wrighton in the 80s [111]. An OECT consists of an organic semiconductor channel that is interfacing an electrolyte, in which the gate electrode is immersed (Figure 1.21). The source and drain metallic electrodes establish contact with the organic semiconductor channel. The operation principle of an OECT relies on the penetration of ions from the electrolyte into the organic film, thereby changing its doping state and hence its conductivity. The voltage across the gate (V_G) controls the injection of ions into the semiconductor channel and, therefore, its doping state. In standard operation, the source electrode is grounded, and a constant bias potential at the drain drives the flow of mobile holes or electrons (electronic current) through the channel between the source and drain. This channel current is the output current of the OECT (drain current,I_d), and therefore probes the doping state of the organic channel. Like MOSFETs and OFETs, OECTs work as a switch, where the input (gate voltage) controls the output (drain current). OECT operated in depletion and accumulation mode. In depletion mode, the semiconductor channel material is typically self-doped and conductive, where the application of V_G results in electrochemical de-doping which reduces the channel conductivity (Figure 1.21b). In accumulation mode, the material of the channel is poorly conductive and the application of V_G results into electrochemical doping which increases the channel conductivity (Figure 1.21c). A typical material used as a an active channel for OECTs is PEDOT:PSS. The PEDOT is a p-type doped (oxidized) semiconducting polymer, which results in having mobile holes that can move from one chain to another, leading in a hole current (output drain current) once the drain terminal is biased. On the other hand, the sulfonate anions of PSS work as a charge balance counter ions to compensate the PEDOT holes. The operation mechanism of PEDOT:PSS-based OECTS is in depletion mode. In the ON state, a hole current flows in the active channel without gate voltage applied. Once a positive voltage is applied, the anions in the electrolyte will move towards the gate electrode and for an electrical double layer at the gate/electrolyte interface. Concurrently, cations from the electrolyte are penetrating into the semiconductor channel, balancing the PSS anions and de-doping the PEDOT backbone. The number of holes (charge carriers) in the channel decreases leading into a drop in the drain output current, until the device reaches the OFF state at a specific voltage magnitude.

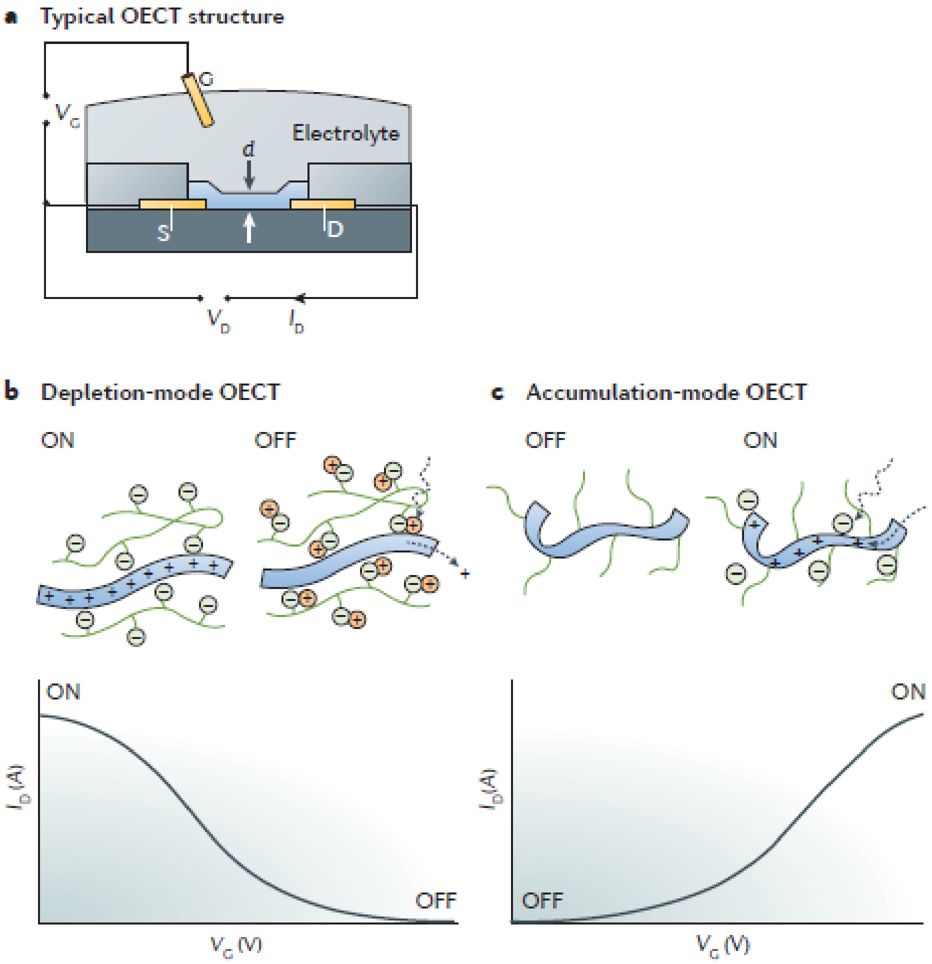

Figure 1.21 OECT's device physics and electrical characteristics (Adapted from [112]). (a) Schematic showing the typical strucutre of an OECT with drain (D), source (S), electrolyte and gate (G). (b) Transfer curve of depletion-mode OECT. When positive voltage is applied cations penetrate into the polymer to replace holes, moving. The OECT transitioning from OF to OFF state (closing the channel). (c) transfer curve of accumaltion-mode OECT. When negative gate voltage is applied, the holes accumulate and compensate injected anions. The transistor is ON.

4.1.2 The device model of OECTs

Bernards model: Steady-state behavior:

The behavior of OECT in depletion mode could be described with the model proposed by D. A. Bernards and G. G. Malliaras in 2007 (henceforth referred to as the “Bernards model”) [113]. The model leans heavily on the analogy with thin-fil transistor (i.e. MOSFET) behavior. The device model is shown in Figure 1.22, The channel of the transistor has a length L, a width W, and a thickness T. Here, the x-axis ranges from the edge of the source terminal at x = 0 to the edge of the drain terminal at x = L.

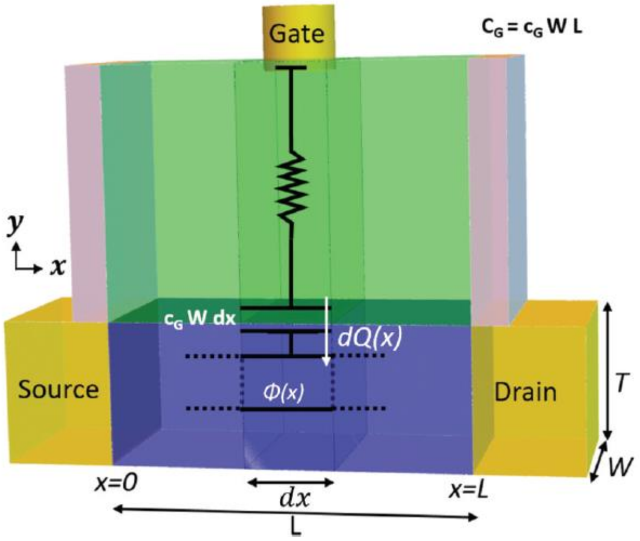

Figure 1.22 Schematic showing the coupling between the ionic and the electronic circuits that represents the Bernards model of OECT. L, is the length of the channel between source (x=0) and drain (x=L). T, channel thickness, channel potential $\emptyset(x)$, and dQ(x) is the total charge of the cations injected to the channel. Adapted from [114]

This model is defined by the combination of two circuits: ionic and electronic circuits. The electronic circuit represents the carrier (holes) movement in the organic semiconductor channel between the source and the drain. The ionic circuit is defined as the movement of the ions in the electrolyte and in the organic semiconducting channel. A resistor (R_E) and a capacitor (C_G) in series represent the ionic circuit. R_E describes the conductivity of the electrolyte and is a measure of its ionic strength while C_G accounts for polarization at the organic film-electrolyte and gate electrode-electrolyte interfaces. C_G is defined as the ratio of the charge of the injected ions per unit area $\frac{dQ(x)}{Wdx}$ to the voltage applied to the capacitor:

$$C_G = \frac{dQ(x)}{dxW}\frac{1}{V_G - \emptyset(x)} \qquad (1)$$

With $\emptyset(x)$ the potential along the semiconductor channel.

Eqn (1) assumes that no cations are injected into the channel without applying voltage across the gate capacitance. However, this assumption neglects charge accumulation at the electrolyte/channel interface. To consider these effects, a threshold voltage V_T, similar to the threshold voltage of field effect transistors can be defined. Hence, the charge dQ of the cations injected at x becomes:

$$dQ(x) = C_G . W . dx\left(V_G - V_T - \emptyset(x)\right) \qquad (2)$$

And the total cation’s charge that enter the semiconductor channel becomes:

$$Q = \int_0^L dQ(x)dx = C_G . W \int_0^L \left(V_G - V_T - \emptyset(x)\right)dx. \qquad (3)$$

The electronic circuit of an OECT is modeled using Ohms’s law:

$$J(x) = -e\mu p(x)\frac{dV(x)}{dx} \qquad (4)$$

Where J is the current flux, e is the elementary charge, μ is the hole mobility, $p(x)$ is the hole density along the channel.

Bernards and Malliaras anticipated that the ionic and the electronic systems are strongly coupled by an electrostatic de-doping process. In the case where V_G is positive with respect to the channel of the transistor (i.e. $V_G > V_T + \emptyset(x)$), the cations will penetrate into the semiconductor polymer. Hence, every penetrated cations replaces one free hole. The hole concentration p(x) along the semiconductor channel becomes:

$$p(x) = p_o\left(1 - \frac{dQ(x)}{ep_oWdxT}\right) \qquad (5)$$

Where p_o is the initial doping concentration inside the organic polymer.

To get the steady state current density $J(x)$, the hole concentration in eqn (4) is replaced by the one in eqn (5) and (2):

$$J(x) = e\mu p_o[1 - \frac{V_G - V_T - \emptyset(x)}{V_p}]\frac{d\emptyset(x)}{dx} \qquad (6)$$

Where $V_p = \frac{ep_oT}{C_G}$ is the pinch-off voltage of the transistor. V_p is a function of the device geometry, material and doping concentration.

Since the current density $J(x)$ has to be constant along the semiconductor channel, eqn (6) is integrated to obtain an analytical expression for the output drain current:

$$I_D = G[1 - \frac{V_G - V_T - \frac{V_D}{2}}{V_P}]V_D \qquad (7)$$

Where $G = e\mu p_o\frac{WT}{L}$ is the conductance of the transistor channel without applying V_G. This relation is true when the transistor is functioning it its linear regime (for $V_D > V_G - V_T - V_P$), i.e. the region where the channel is not fully depleted of holes.

In the case where the drain potential is too negative ($V_D < V_G - V_T - V_P$), the hole concentration in the channel drops to zero at the drain forming a highly resistive region until the drain current saturates. This regime identified as saturation regime and describes by the following equation:

$$I_D = -G\frac{\left[V_G - V_T - \frac{V_D}{2}\right]^2}{2V_P} = -G\frac{[V_D^{sat}]^2}{2V_p} = -\mu C_G\frac{W}{2L}[V_D^{sat}]^2 \qquad (8)$$

Where $V_D^{sat} = V_G - V_T - V_P$ is the drain voltage as function of V_G that determines the transition between saturation and linear regimes.

Bernards model: Transient behavior:

As already explained previously for the steady-state model, the transient behavior of OECTs is also defined by electronic and ionic systems.

The injection on cations and removal of hole at the source ($V_D > 0$) are the main effects that rules the transient behavior. Removal of the holes at the drain terminal occurred to compensate the increase in the net charge inside the organic film. To describe this behavior, the hole density and ionic current are assumed to be constants within the channel and they are equal to their average value. A simplified behavior is obtained by adding the current associated to the removal of holes due to the de-doping and the one from the Ohm's law of the electronic circuit:

$$J(t) = e\mu p(t)\frac{V_D}{L} + efL\frac{dp(t)}{dt} \qquad (9)$$

By using eqn (5), the transient current I(t) = J(t).W.T as defined in eqn (9) becomes:

$$I(t) = G\left[1 - \frac{Q(t)}{ep_o V}\right]V_D - f\frac{dQ(t)}{dt} \qquad (10)$$

Where Q(t) is the transient response of the ionic circuit and V = WTL is the volume of the semiconductor channel.

There are two cases in order to verify the transient response of an OECT, one is obtained by fixing the gate current $I_G = \frac{dQ}{dt} = \frac{Q}{t}$ or the other is by fixing the gate voltage. The first case is not a typical operating regime of an OECT but it is preferable to understand better the physics of the device. Fixing the gate current will fix the kinetics of the ionic circuit that gives the possibility to focus on the electronics circuit characteristics regardless the ionic one. By applying fix gate current for t>0, the drain current is described by:

$$I(t, I_G) = I_o - I_G(f + \frac{t}{\tau_e}) \qquad (11)$$

With $\tau_e = \frac{L^2}{\mu V_D}$ is the time constant of the electronic circuit and $I_o = G.V_D$ is the drain current in the absence of gate current (steady state current). One of the interesting utilizations of this regime is to extract the effective value of the mobility in the organic channel. Bernards and Malliaras have validated this where they used the extracted τ_e values and showed that these values similar to the ones in literature[113]

In the other case where a fix voltage is applied to the gate, the change in cations inside the semiconductor channel exhibits the characteristics of a charging capacitor:

$$Q(t) = Q_{ss}[1 - \exp(-t/\tau_i)] \qquad (12)$$

Where $\tau_i = R_E\, C_G$, is the capacitive charging time constant. In order to simplify the description, it is assumed that the voltage drop across the gate capacitor is averaged to $\Delta = V_G - \frac{1}{2}V_D$. Accordingly, the transient behavior of an OECT is described as follows:

$$I(t,V_G) = I_{ss}(V_g) + \Delta I_{ss}\left(1 - f\frac{\tau_e}{\tau_i}\right).\exp\left(-\frac{t}{\tau_i}\right) \qquad (13)$$

Where I_{ss} is the steady drain current for a fixed gate voltage. Depending on the values of τ_i and τ_e two different transient responses are identified when applying a gate voltage pulse: a monotonic decay ($\tau_i > f\tau_e$) or spike-and-recovery ($\tau_i < f\tau_e$) type responses. In the monotonic decay condition, the hole extraction process (electronic response) is very fast and it is negligible compared to the transient response (ionic response). This could be the case in small channel length OECTs or/and biasing with high drain voltage values. In spike-and-recovery response, the electronic response (hole extraction) is the dominant process which occurs with relatively slow time.

The response time of the OECT is determined by two parameters: τ_i and τ_e. The time constant of the ionic transport in the electrolyte τ_i is defined by the solution resistance and the ionic double layer. By using the Gouy-Chapman theory: $\tau_i \sim \frac{l}{{C_o}^{1/2}}$ (l is the length of the electrolyte and C_o is the ion concentration), this time constant can be linked with physical parameters of the OECT. For example, the device ionic response can be tuned by decreasing the distance l or by increasing the electrolyte concentration. Similarly, the eqn (13) is also influenced by the electronic time constant. Taking into consideration the ratio expression: $\frac{\tau_e}{\tau_i} \sim \frac{lL^2}{\mu V_d}$, the electronic transient response can be tuned by modulating the electrode postion, the channel length or the drain voltage value.

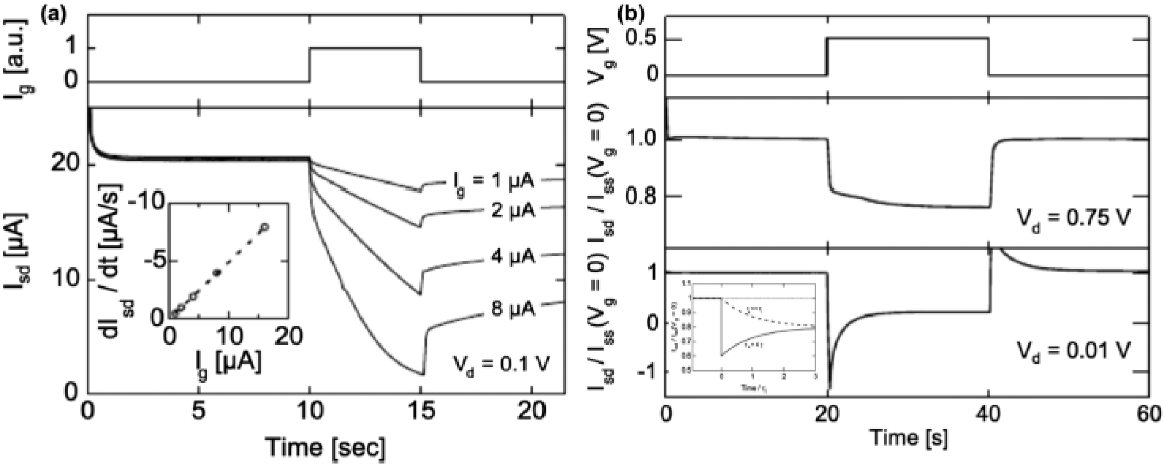

Figure 1.23 (a) Transient response of OECT under the application of a constant gate current. Inset: a graph showing the transient slope of drain current as function of gate predicting $\tau_e = 0.5\ s$. (b) Transient response of OECT under the application of a constant gate voltage. Inset: graph showing modeled drain current transient for a constant drain voltage with an arbitrary ΔI and fixed geometric factor (f = 1/2) showing two different possible characteristics responses. Adapted from [113]

4.1.3 OECT Performance Metric ($\mu.C^*$ product)

Historically, the transconductance (g_m) is considered the main figure of merit for OECTs which represents a measure of its ability to amplify an input signal[115]. Transconductance is calculated by the first derivative of the transfer curve $\frac{\partial I_D}{\partial V_G}$ (Figure 1.24). This is a particularly important parameter in which higher transconductance values lead into better sensitivity performances for OECTs. For example, biosensing applications use configurations such that the input voltage at the gate electrode is detected by measuring its effect on the output drain current. This means the amplitude of the output signal of an OECT is directly proportional to its transconductance.

As shown in the discussion of the Bernards model, the transconductance (g_m) at saturation regime and for depletion-mode becomes:

$$g_m = \left(\frac{W}{L}\right). d. \mu. C^*. (V_{th} - V_G) \qquad (14)$$

Where W, L and d are the channel width, length and thickness, respectively; μ is the charge-carrier mobility; C* is the capacitance per unit volume of the channel; and V_{th} is the threshold voltage. In this equation, the product d·C* replaces the capacitance per unit area of the MOS capacitor in FET transistors. In OECTs, the charges in the electrolyte penetrate throughout the bulk of the semiconductor channel and do not accumulate at the dielectric/channel interface. In OECTs, g_m scales with both the geometric factor (W, d and L) and material-dependent factor (mobility and volumetric capacitance; $\mu. C^*$ product). For example, with the same thickness of the channel ~100 nm, a typical organic FET (SiO2 layer) has C' with tens of nF cm^{-2} values [116], an electrolyte gated FET with electrical double layer capacitance C' of 1–10 µF cm^{-2} [117], however for an OECT the product of d·C* (capacitance per unit area) is 500 µF cm^{-2} [62]. This volumetric gating effect characteristic provide the OECTs with high transconductance values setting it apart from other transistor technologies in terms of amplification performances

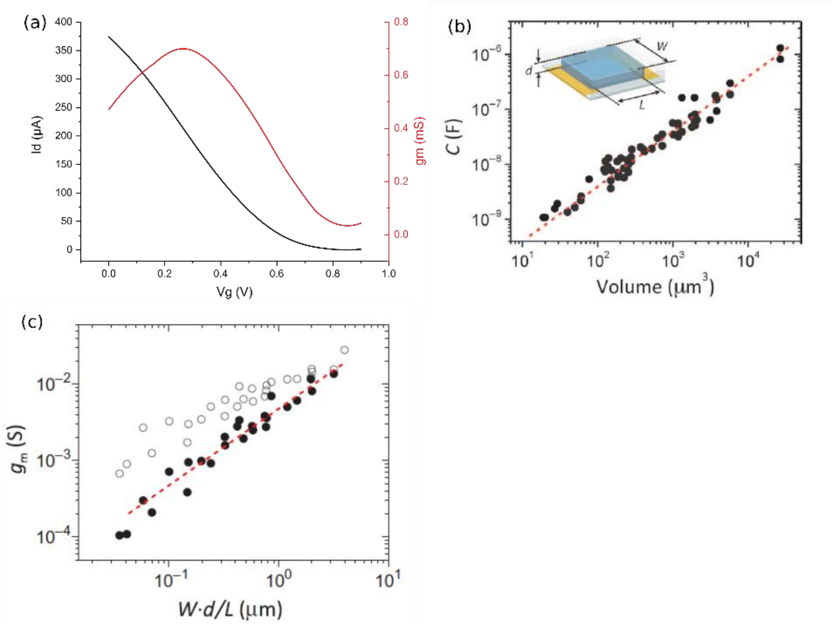

Figure 1.24 (a) Transfer curve and the extracted gm curve (first derivative of the transfer curve). (b) Graph showing th scale of the a PEDOT:PSS OECT capacitance with volume (W x L x d). (c) Scaling of transconductance with geometry (W.d/L). The line is linear fit to the gm at saturation (eqn (14)). (b) and (c) adapted from [62].

Tuning the device's geometry to increase the value of its $\frac{W}{L}$ ratio is a facile way to improve the device's transconductance [118]. However, several biological applications have constraints on the device's footmark [119]. Therefore, another commonly used approach to optimize transconductance through geometry is to increase the thickness of the OECT semiconductor channel [62]. Increasing the transconductance of OECTs through thickness increment comes at the cost of rather slow response times, therefore can limit the operating frequencies of an OECT but still can be used to implement transconductance equivalent or better than other materials i.e. graphene [120]. Alternative material design and engineering work have been made to increase the transconductance values by increasing the $\mu.C^*$product through either volumetric capacitance or electronic mobility tuning [121,122].

Materials design and engineering for OECTs

The semiconductor channel of OECTs is typically made of PEDOT:PSS. As explained in the previous part of this chapter, this material showed several advantages for its uses in *in vitro* neuronal recording applications. In OECTs, a lot of studies investigated the structure and electronic conductivity of this organic material [56,64,118,123,124]. Technically, it is rather simple to prepare PEDOT:PSS-based OECTs with a transconductance in the range of milliseimens and response time in the range of microseconds, which makes the performances of OECTs based on this polymer matching the requirements for several sensing applications. Despite the advantages of PEDOT:PSS and its attractive performances, this polymer faces some limitations. In term of electrical properties, the volume fraction of the PEDOT in the film is affected by the bulky structure of the PSS. Consequently, this affects directly the $\mu.C^*$product, which is the figure of merit to help the design of future channel materials for OECTs. A tightly packed and organized crystalline polymer morphology achieves high μ values, while high values of C^* relies on ionic mobility (volume fraction of PEDOT) within the polymer film. For this reason, recent works have used solution-phase chemical approaches to diversify the polymer structure by attaching and fine-tune the properties of the polymer material using side-chain and backbone engineering techniques. Here I present in summary some approaches used for side-chain and backbone engineering techniques. One approach was to remove PSS and instead attach other ionic groups directly on the thiophene backbone. For example, in depletion mode p-doped OECTs, some efforts demonstrated a conductor based on PEDOT with a pendant sulfonate group (PEDOT-S) [125] (Figure 1.25a). Mixing a semiconducting and conducting conjugated polyelectrolyte tune OECTs by balancing the stoichiometry of the channel [125]. Another alternative approach used is to use conjugated polymers with hydrophilic or ion-transporting side chains as a channel material. For example, a study shows OECTs with a channel made from poly(2-(3,3′-bis(2-(2-(2-methoxyethoxy) ethoxy)ethoxy)-[2,2′-bithiophen]-5-yl)thieno[3,2-b] thiophene) p(g2T-TT), a polythiophene with glycolated side chains (Figure 1.25b) [126]. This material eases the bulk doping and allows for efficient modulation of the channel's conductance (six times higher volumetric capacitance than PEDOT:PSS). This result inbetter transconductance values than OECTs with PEDOT:PSS channel with same device geometry [126]. Yet, relatively less efforts have been dedicated to optimize specifically the carrier mobility (μ) although it is a key parameter to improve the transcoductance or current modulation of an OECT. One reason could be that the carrier mobility is relatively hard to modify other than by molecular design and packing since it is considered as an intrinsic material property. A study demonstrated a highly ordered crystalline PEDOT:PSS microfiber structure as an OECT channel leading to large carrier mobility (12.9 $cm^2\ V^{-1}\ s^{-1}$) and $\mu.C^*$ product (1500 F $cm^{-1}\ V^{-1}\ s^{-1}$) [127] (Figure 1.25c). In this work, the scientists used a strain engineering technique to enhance the microstructure ordering in the PEDOT:PSS channel.

One technique of depositing PEDOT:PSS is by electropolymerization. The electropolymerization technique showed a high degree of control over the CP thickness, surface properties, and its ionic/electrical parameters [124,128] which makes it an interesting solution for bottom-up material co-integration. In this thesis, I will show how the iono-electornic coupling of OECTs can be finely tuned (in operando) post-microfabrication via the electropolymerization technique. Our technique can lead to a fine control of PEDOT microdomains organization, which directly affects the iono-electronic properties of OECTs. This approach improves the transconductance by 150% while reducing their variability by 60% in comparison with standard spin-coated OECTs. We further highlight how volumetric capacitance and effective mobility of PEDOT:polystyrene sulfonate influence distinctively the transconductance and impedance of OECTs. This strategy exploits the concept of adaptive sensing where both transconductance and impedance are tunable and can be modified on-demand to match different sensing requirements.

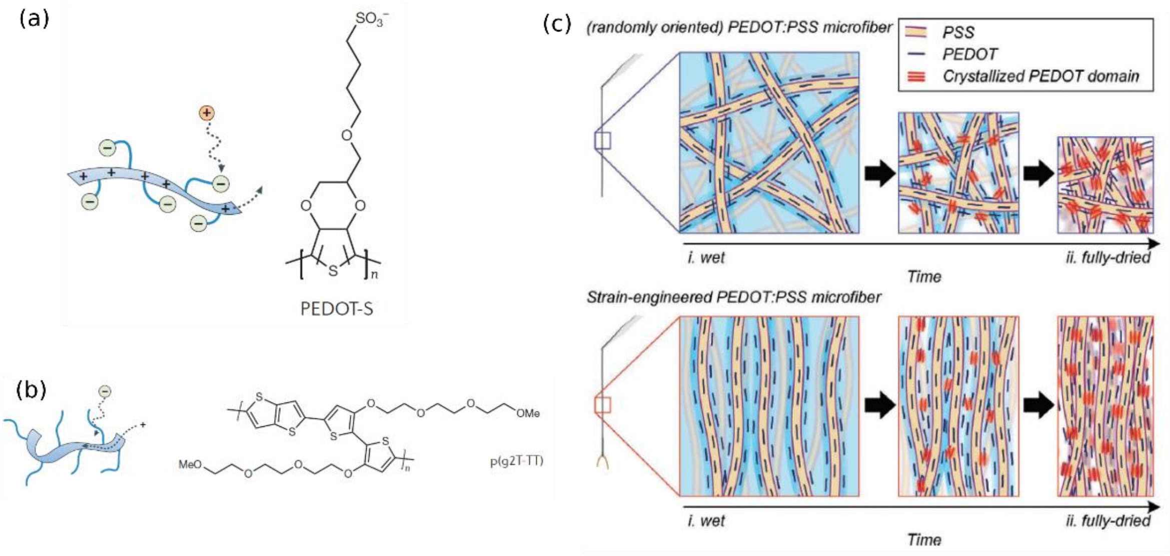

Figure 1.25 Examples on backbone and side-chain engineering of PEDOT:PSS. (a) conducting poly(4-(2,3-dihydrothieno[3,4-b][1,4]dioxin-2-yl-methoxy)-1-butanesulfonic acid) (PEDOT-S)(adapted from [118]). (b) Semiconducting polymers include p-type poly(2-(3,3´-bis(2-(2-(2-methoxyethoxy)ethoxy)ethoxy)-[2,2´-bithiophen]-5-yl)thieno[3,2-b]thiophene) (p(g2T-TT)) (adapted from [118]). (c) Schematic illustration of structural evolution of wet PEDOT/PSS chains during the drying process without and with applied stress in the proposed study of strain-engineered crystalline PEDOT:PSS microfibers (adapted from [127])

4.2 Organic Electrochemical Transistors (OECTs) and neural interface

As bio-sensors, OECTs offer very attractive solutions for converting ionic signals into electronic ones thanks to the unique property of organic mixed ionic-electronic conductors (OMIECs). Ionic concentration from an analyte or ionic currents from electroactive cells can be efficiently sensed/probed and amplified, thus making OECTs attractive sensors. Additionally, PEDOT:PSS based OECTs is an interesting choice for biosensensing applications due to its good biocompatibility, relatively high steady state performance and high sensitivity (high gm). OECTs have already been used in various bio-sensing applications such as biomolecular sensors (e.g. glucose[129], dopamine[130] DNA[131], lactate[132], and bacteria[133]), barrier tissue integrity sensors [134] and cell impedance sensors [135,136]. Malliaras and co-workers has firstly shown the merit of OECT for *in vivo* sensing with a highly conformable array consisting of multiple PEDOT:PSS OECTs (and several PEDOT:PSS passive electrodes) specifically designed for electrocorticography (ECoG) [96]. In this study, the authors were able to show superior SNR performances of OECTs comparing to PEDOT:PSS microelectrodes, and owing to local signal amplification. The direct contact between the oxide-free organic conducting channel and the tissue have been used to locally inject current and stimulate neurons in the spinal fluid. OECTs have shown promising results for other electrophysiological applications such as electro-oculogram (EOG) [137], EEG [137] and electrocardiogram (ECG) [138].

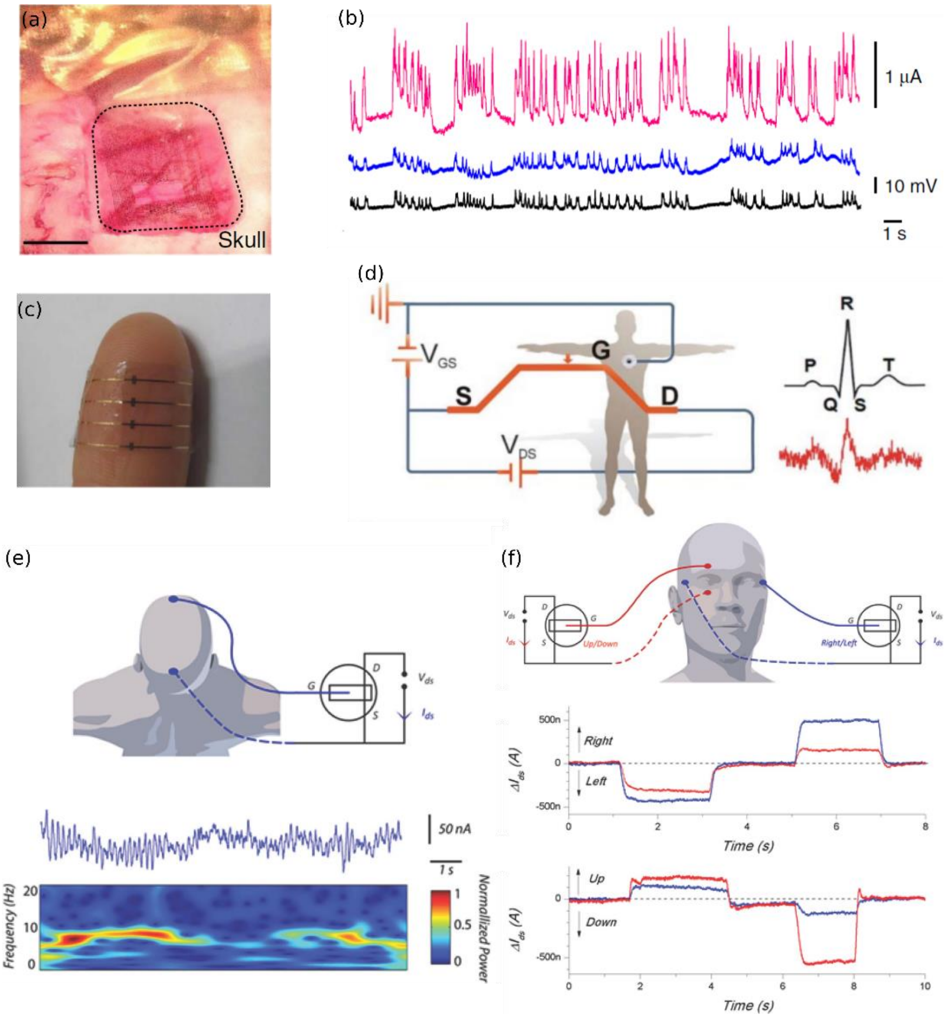

Figure 1.26 OECTs for *in vivo* and noninvasive electrophysiolocal applications. (a) Optical micrograph of the ECoG probe used by Malliaras and coworkers [96] for brain cortex ECoG (Scale bar, 1mm) and (b) its recordings from an OECT (pink), a PEDOT:PSS surface electrode (blue) and Iridium penetrating electrode (black). Notable higher SNR values of the OECT recordings compared to the electrodes. (c) photograph of the OECT attached to human skin used in (d) for ECG recordings operates in direct contact with the skin (c and d reproduced from [138]). (d) Schematic representing the use of OECT for EEG applications showing its recordings of spontaneous brain activity (top), alpha rhythm and associated time-frequency spectrogram (bottom)[137]. (e) Schematic representing the use of OECT for EOG applications showing its recordings [137].

Even with the remarkable uses of OECTs in electrophysiology (*in vivo* and noninvasive experiments) for clinical applications (Figure 1.26), still a very few work concerning *in vitro* extracellular recording applications have been developed so far. The first example of an *in vitro* extracellular recording by using OECT was reported by Yao *et al.* in 2015 [139] where they recorded electrical activity from cardiac cells (HL-1 cells). Following this work, several studies later reported more investigations and optimization of OECTs in its uses for *in vitro* recordings from cardiac tissues and cells [140–143] showing excellent signal-to-noise ratio recordings. In the work of Gu *et al.* in 2019 [141], the authors showed the ability to monitor and map the action potential propagation of both 2D and 3D structures of cardiac cells demonstrating the viability of the OECT technology for applications in medical health and pharmacological industries.

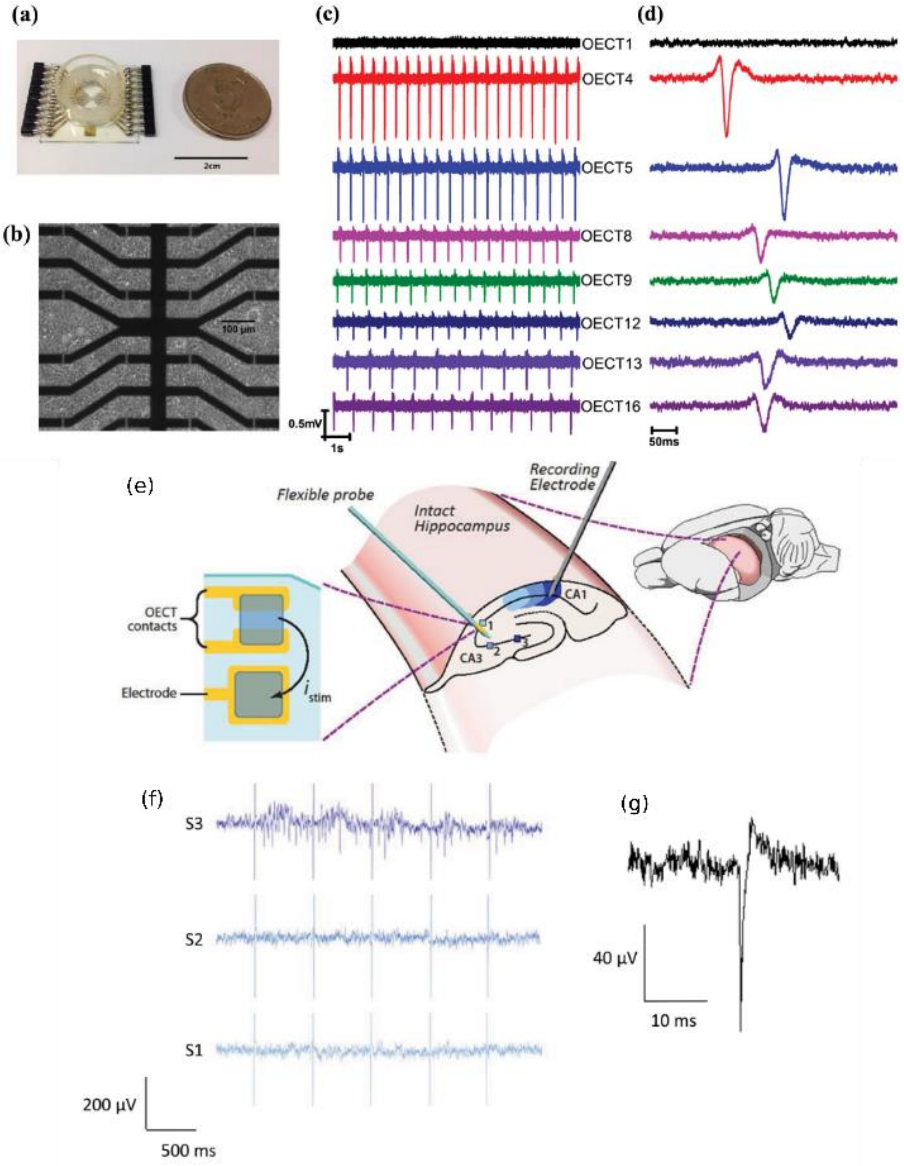

Figure 1.27 OECT for *in vitro* extracellular recordings. Photo showing the OECT array proposed by Yao et al. used for cardiac cell *in vitro* recording. (b) microscopic image of the HL-1 cell layer cultured on top of the OECT array. (c) Traces of spikes recorded by several OECTs from the same chip. (d) zoomed in traces showing the shape of single spikes corresponded to the signals shown in (c) (a,b and c reproduced from [139]). (e) schematic showing the OECT array on the probe proposed by Williamson et al. [144] that has been characterized in vitro with hippocampus preparations. (f)the response in the recorded section of CA1 evoked by the stimuli to site 3 (rightmost region of CA3). (g) zoomed trace showing the shape of single evoked spike in CA1. (e,f and g and reproduced from [144])

Contrary, the *in vitro* recording from neuron cells by using OECT has not been reported completely yet. OECT has been employed once for *in vitro* neural recording, however for testing experiment of a delaminating depth probe designed for *in vivo* applications [144]. Although this probe was designed for *in vivo* applications yet the biocompatibility of the material, recording and stimulation capability of this device was tested *in vitro* with hippocampus preparation. This study show just a very general proof of concept about interfacing OECT with neural culture *in vitro*. However, many more deep experiments, characterizations, and investigations for several parameters are missing to understand more the sensing mechanism of OECTs for *in vitro* recordings from neurons. Similar to what has been done by Fromherz (previous section), such experiments could give us more quantitative feedback about the effect of the cleft resistance, transconductance, capacitance and operating voltage of an OECT on the shape and the quality of recordings. In the case of OECT, there is no insulating dielectric as FETs in such the physics behind sensing that is valid for other transistors may not be right for the OECT case. As explained in previous sections, the electroactive signal coming from the neurons is created by the ion flux at the cell membrane. Theoretically, the ions in the electrolyte should penetrate the bulk of the polymer to change its conductivity; therefore, the ionic conductivity of the channel is related directly to the efficiency of this process revealing the importance of transconductance value in the sensing quality. Consequently, *chapter VI* will be dedicated to interfacing neurons with OECTs by performing electrical and material characterizations of OECTs *in-situ* while interfacing neural biological medium. Electrochemical impedance has been done while neurons are on top to aid in understanding the effect of the neural network on the electrochemical performance of the OECT. Electrical modeling extracted from these measurements reveal quantitatively the change of OECTs electrochemical parameters (impedance) after culturing neurons on top and how this can affect its sensing performances. DC electrical characterization also has been performed in-situ while interfacing neurons that helped identify the effective operating voltage during recording. These investigations lead us to a better understanding of OECTs behavior with neurons to exploit it for *in vitro* recordings.

Chapter II. Materials and Experimental Techniques

This chapter provides an overview and a description of the materials, equipment and experiments used in this work in order to achieve the research objectives.

1. Microfabrication

1.1 Organic Electrochemical Transistor (OECT) microfabrication

The OECT arrays are consists of glass slides (5*5 cm) which are patterned with gold metallic lines forming the sources and drains electrodes. PEDOT:PSS were coated forming the OECT channel between the source and the drain. The OECTs were insulated by parylene-C layer. The resulting W/L for OECTs was 30/12. The configuration of the contact pads and the size of the chip were compatible with commercial MEA-System (MEA, 2100-System, Headstage for two MEAs with 60 electrodes, Multi Channel Systems). While a detailed process with exact parameters are reported in Figure 2.1, a brief explanation is given below to guide the reader through the fabrication process with some additional remarks.

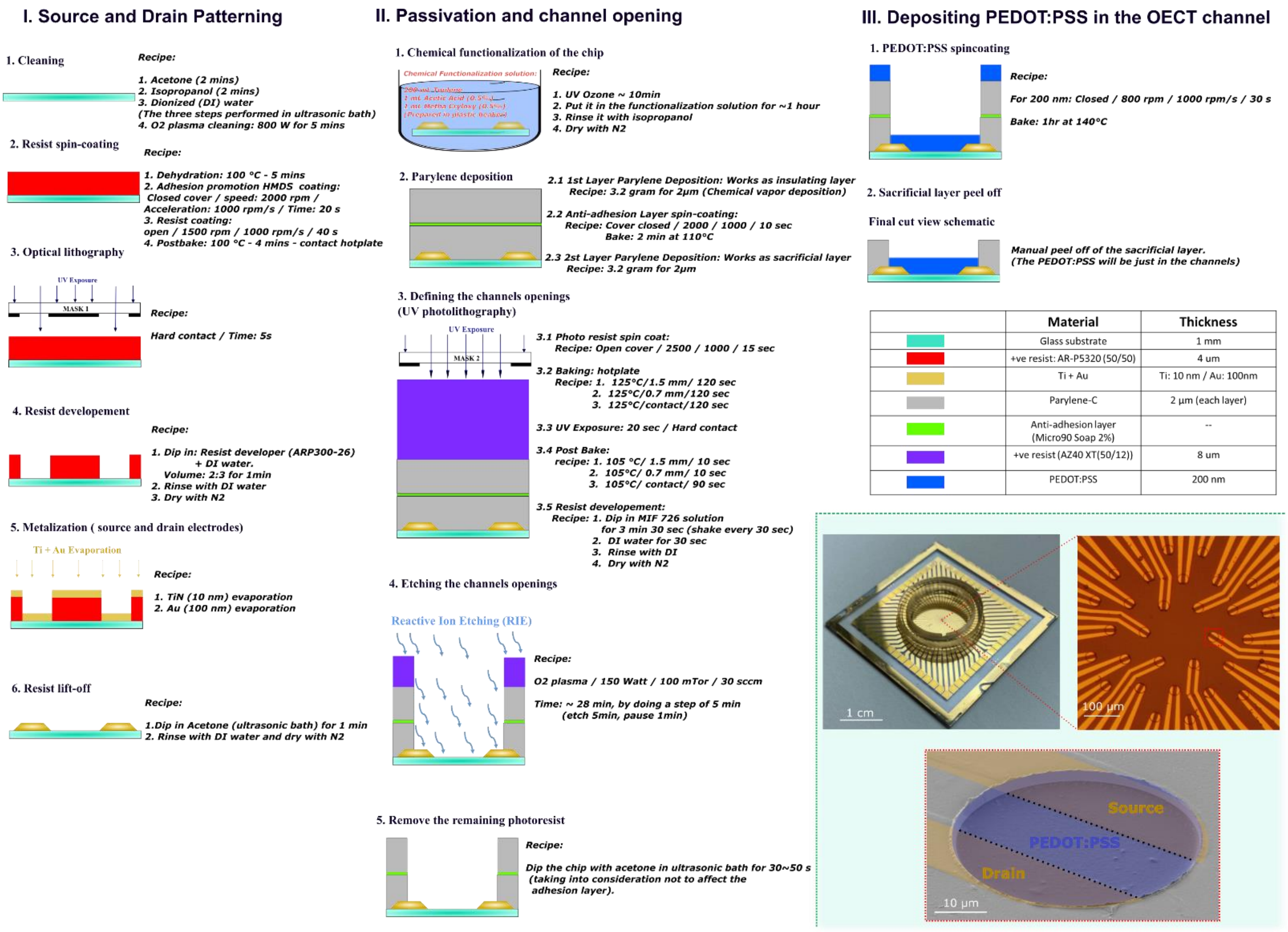

	Material	Thickness
🟦	Glass substrate	1 mm
🟥	+ve resist: AR-P5320 (50/50)	4 um
🟨	Ti + Au	Ti: 10 nm / Au: 100nm
⬜	Parylene-C	2 µm (each layer)
🟩	Anti-adhesion layer (Micro90 Soap 2%)	--
🟪	+ve resist (AZ40 XT(50/12))	8 um
🟦	PEDOT:PSS	200 nm

Figure 2.1 Microfabrication process of an OECT. Inset: Macroscopic, microscopic and SEM images of OECTs.

Firstly, the glass chips were cleaned by sonication acetone/isopropanol/deionized water (DI water) bath for 3 min each. The substrates were rinsed with DI water and dried with nitrogen gun. The metallic electrodes were patterned on the substrate using the AR-P5320 (50/50) positive photoresist. The resist is spin-coated, dehydrated by baking, exposed to UV light and developed in ARP300-26. To ensure a good adhesion of the metal on the substrate, Argon etching (200 V / 120 s) is performed which removes any photoresist residue within the pattern. During metallization, Titanuim Nitrate (TiN) is first evaporated with a thickness of 10 nm. TiN serves as adhesion promotor for the gold which is then evaporated with a thickness of 100 nm. Next, the chips are prepared for sonication for 30 seconds in an acetone bath for lift-off.

Before depositing the insulating layer on the chip, oxygen plasma treatment was performed followed by chemical functionalization bath for 1 hour to ensure a good adhesion of Parylene-C on the chip. Subsequently, the Parylene-C layer of the OECT chip was deposited. The thickness of the parylene layer is dependent on the amount of the Parylene-C dimer loaded for deposition, with 3.2 grams resulting in approximately a 2 µm thick layer. Before patterning and etching the insulation layer to open the connector pads and the transistors channels, a second sacrificial layer of Parylene-C is deposited (2 µm thick). Prior to this deposition, an anti-adhesion layer (2% soap) was spin-coated onto the substrates to ensure smooth final peel-off. The contact pads and the channels openings can subsequently be patterned using a viscous AZ40XT (50/12) resist as an etch mask. This resist allows for a thick and robust protective layer necessary to allow etching (reactive ion etching (RIE)) through the two paryelene layers to define a 30 µm diameter opening on top of the S and D contacts. The remaining resist is removed with acetone sonication bath.

Finally, the channels were coated with PEDOT:PSS as a organic semiconductor channel material. The prepared formulation of the deposited PEDOT:PSS is as follow: PEDOT:PSS solution (20 mL) (Clevios^{TM} PH1000, Heraeus) was mixed with ethylene glycol (5 mL), dodecyl benzene sulfonic acid (DBSA) (50 µL) and 1wt.% of (3-Glycidyloxypropyl)trimethoxysilane (GOPS). The prepared solution was spin-coated resulting in a 200 nm thick spin-coated PEDOT:PSS in between S and D contacts. The sacrificial layer is then peeled off. For cell culture purposes, a glass well was attached on top of the chip. The global common gate Ag/AgCl wire was molded manually to the glass well such that will dipped in the electrolyte. The images shown in the inset in Figure 2-1 shows an overview of the device. Each OECT array contains 30 OECT devices (60 microelectrode). The channel length between the S and D contacts is 12 µm. The spacing between two adjacent OECTs is 100 µm.

1.2 Microelectrode array (MEA) microfabrication

The microfabrication process of the MEA arrays was similar to the process of OECT arrays reported previously in details. However, for MEAs the opening of the microelectrodes were defined using one Parylene layer since no spin-coated PEDOT:PSS was deposited on top of the microelectrodes. Fifty-eight microelectrodes of 30 µm diameter and two reference electrodes of 1000 µm diameter were patterned on a glass substrate through conventional optical lithography and lift-off steps. A 2-µm thick parylene C layer was deposited as an insulating layer. Openings of the contact pads, microelectrodes and the two reference electrodes were defined by optical lithography combined with reactive-ion etching (RIE) step. The configuration of the contact pads, and of the internal reference electrode were compatible with commercial MEA-System (MEA, 2100-System, Headstage for two MEAs with 60 electrodes, Multi Channel Systems). The spacing between two adjacent microelectrodes is 100 µm. For cell culture purposes, a glass well was attached on top of the chip.

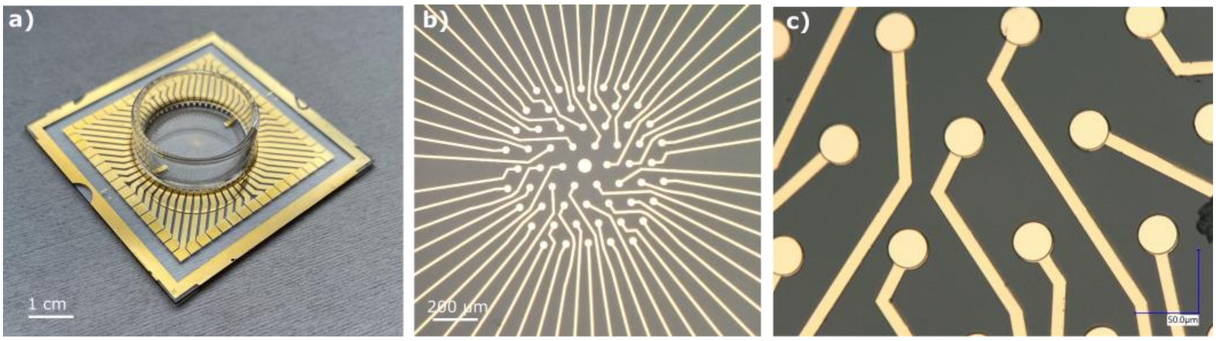

Figure 2.2 (a) image showing a MEA chip. (b-c) microscopic images showing the microelectrodes of an MEA

2. Electrical Characterizations

2.1 DC Electrical Characterization for OECTs

Keysight B1500A Semiconductor Device Analyzer of Precision Current-Voltage Analyzer Series is an all in one analyzer supporting IV, CV, pulse/dynamic IV and more, which is designed for semiconductor devices characterization. In our experiments, it is used for the DC electrical characterization of the OECT where it supply gate and drain voltage and measures the drain output current. It is used mainly to study the transfer and output curves of the OECTs. These curves are important to investigate its performance and functionality. The transistors were characterized using a PBS solution as the electrolyte. An Ag/AgCl wire was immersed in the electrolyte and used as the gate electrode. During bio experiments, the transistors were characterized using a cell culture medium with neuron cells as the electrolyte.

2.2 Electrochemical impedance spectroscopy (EIS)

Electrochemical impedance spectroscopy (EIS) is a powerful tool for the study of structure and electrical features of the electrochemical interface. The technique consists in measuring the current flowing in the electrochemical cell after probing it with a small ac-perturbation voltage (V_a) on top of the controlled DC polarization potential (V_{DC})over a range of frequencies. EIS is widely used as a standard characterization technique for many material systems and applications (corrosion, plating, batteries, fuel cells, etc.). For neurosensing applications, EIS has been used to electrically characterize the interface for various electrode materials and varying electrode sizes. In our experiments, All EIS measurements were performed with a Solartron Analytical (Ametek) impedance analyser from 1 MHz to 10 Hz in aqueous solution. All impedance measurements were done in the same electrical conditions (V_{DC} = 100mV and V_a = 20mV). ***For MEAs***, The 30-µm microelectrode was set as a working electrode (V_{IN}) and the in-plane gold reference electrode was set as V_{OUT}. ***For OECTs***, Source and drain as working electrode (V_{IN}) and grounded Ag/AgCl wire as reference electrode (V_{OUT}) dipped into the electrolyte.

In this work a model describing these physical processes was validated and extended to quantify the effect of material engineering techniques used and the effect of neurons and its culture on MEAs and OECTs. EIS Spectrum Analyser software [145] was used to perform circuit impedance modelling. The RC parameter fitting was manually optimized from the software by simultaneous comparison of the Nyquist plots, Bode's modulus, and Bode's phase plots.

3. Electropolymerization technique

3.1 For MEA

The conducting polymer was deposited on top of the gold microelectrodes by electropolymerization in an aqueous electrolyte containing 10 mM of 3,4-ethylenedioxythiophene (EDOT) and 100 mM of sodium poly(sodium-4-styrene sulfonate) (NaPSS). All chemicals were purchased from Sigma Aldrich. The microelectrode (30 µm) as working electrode (V_{IN}) and reference electrode (1000 µm) as counter electrode (V_{OUT}) dipped into the electrolyte. (Schematic and more details of the setup will be explained in *Chapter III*)

3.2 For OECT

Electropolymerization was done by potentiostatic configuration in an aqueous electrolyte containing 0.1 M of poly(sodium-4-styrene sulfonate) (NaPSS) and 0.01 M of 3,4-ethylenedioxythiophene (EDOT). All chemicals were purchased from Sigma Aldrich. Source and drain as working electrode (V_{IN}) and grounded Pt wire as counter electrode (V_{OUT}) dipped into the electrolyte. (Schematic and more details of the setup will be explained in *Chapter V*)

4. Monomer synthetization

The monomer synthetization was done by *Dr. David* Guérin.

Synthesis of EDOT-g_4 :

The synthesis of EDOT-g_4 monomer was performed following methods of literature[1] with slight differences.

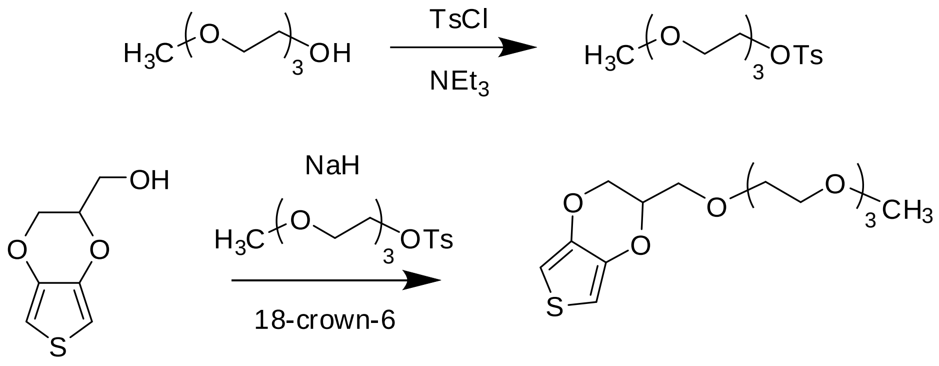

Materials. Starting compounds (triethylene glycol monomethyl ether, hydroxymethyl-EDOT), other reactants and solvents were all purchased from Merck. There were used without further purification. Dichloromethane (DCM) and anhydrous tetrahydrofurane (THF) were stored over 4 Å activated molecular sieves for at least 48 h before use.

Triethylene glycol monomethyl ether tosylate *(for short or 2-(2-(2-methoxyethoxy)ethoxy)ethyl p-toluenesulfonate).* Under inert atmosphere, to a stirring solution of triethylene glycol monomethylether (10 g, 60 mmol) and triethylamine (10 mL, 72 mmol) in 50 mL of dry DCM cooled at -5°C was added dropwise (over a periode of 1h30) a solution of tosyl chloride (14 g, 72 mmol) in dry DCM (20 mL). Medium was maintained at 0°C during TsCl addition then the reaction was allowed to warm to RT and stirred for 18h. Afterwards, the organic layer was washed with ice water (2x100 mL), with 1 M NaOH (100 mL), then again with ice water until neutral pH of the water phase, and dried over $MgSO_4$. After evaporation and drying under vacuum, the yellowish oil obtained was purified by column chromatography on silica gel, first with DCM/hexane (1:1) to eliminate an impurity then with DCM/acetone (1:1). The tosylate was obtained as a pale yellow oil (17.6 g, yield: 92 %). ^{1}H NMR (300 MHz, $CDCl_3$) δ(ppm) 7.79 (d, J = 8.3 Hz, 2H, ArH), 7.33 (d, J = 8.5 Hz, 2H, ArH), 4.17–4.14 (m, 2H, $-CH_2OTs$), 3.70–3.66 (m, 2H, $-\underline{CH_2}CH_2OTs$), 3.62–3.58 (m, 6H, $-O\underline{CH_2}\underline{CH_2}O\underline{CH_2}$-), 3.54–3.50 (m, 2H, $-\underline{CH_2}OCH_3$), 3.36 (s, 3H, $-OCH_3$), 2.44 (s, 3H, $ArCH_3$).

EDOT-g_4 *(for short or 2-2,5,8,11-tetraoxadodecyl-2,3-dihydrothieno[3,4-b][1,4]dioxine).* Under nitrogen atmosphere, a solution of hydroxymethyl-EDOT (500mg, 2.8 mmol) in dry THF (3 mL) was slowly added dropwise to a solution of sodium hydride (0.2 g, 4.9 mmol, 60% in mineral oil) with 18-crown-6 (25 mg) in dry THF (10 mL) at room temperature. The stirring was maintained for 4h before dropwise addition of a solution of triethylene glycol tosylate (1.54 g, 1.7 eq) in dry THF (3 mL). The stirring is continued at RT for 3 days under nitrogen, diluted with 5% NH_4Cl (50 mL), and treated with 0.5 mL of piperidine to remove the excess of tosylate. The product was extracted with ether (4x25 mL), washed with water (3x), dried with $MgSO_4$, then the solvent and piperidine were evaporated at 10 mbar.

---

[1] (a) I. F. Perepichka, M. Besbes, E. Levillain, M. Sallé, J. Roncali, *Chem. Mater.* **2002,** *14*, 449-457. (b) RMN de EDOT-g4 conforme à L. Cai, X. Liu, L. Wang, B. Liu, *Polym. Bull.* **2012**, *68,* 1857–1865. (c) J. Leira-Iglesias, A. Sorrenti, A. Sato, P. A. Dunne, T. M. Hermans, *Chem. Commun.*, **2016**, *52*, 9009-9012.

The crude product was purified by column chromatography on silica gel with DCM/acetone (90:10) as eluent yielding the desired compound as a colorless oil (530 mg, 59 %).

^{1}H NMR ($CDCl_3$, 300 MHz) δ(ppm) 6.32–6.31 (m, 2H, ArH), 4.33–4.30 (m, 1H, -$OCH_AH_BC\underline{H_C}(CH_2OR)O$-), 4.27–4.23 (m, 1H, -$OCH_A\underline{H_B}CH_C(CH_2OR)O$-), 4.09–4.02 (m, 1H, -$OC\underline{H_A}H_BCH_C(CH_2OR)O$-), 3.79–3.63 (m, 12H, -$C\underline{H_2}(O\underline{CH_2CH_2})_2O\underline{CH_2}$-), 3.53–3.56 (m, 2H, -$\underline{CH_2}OCH_3$), 3.37 (s, 3H, -$CH_3$).

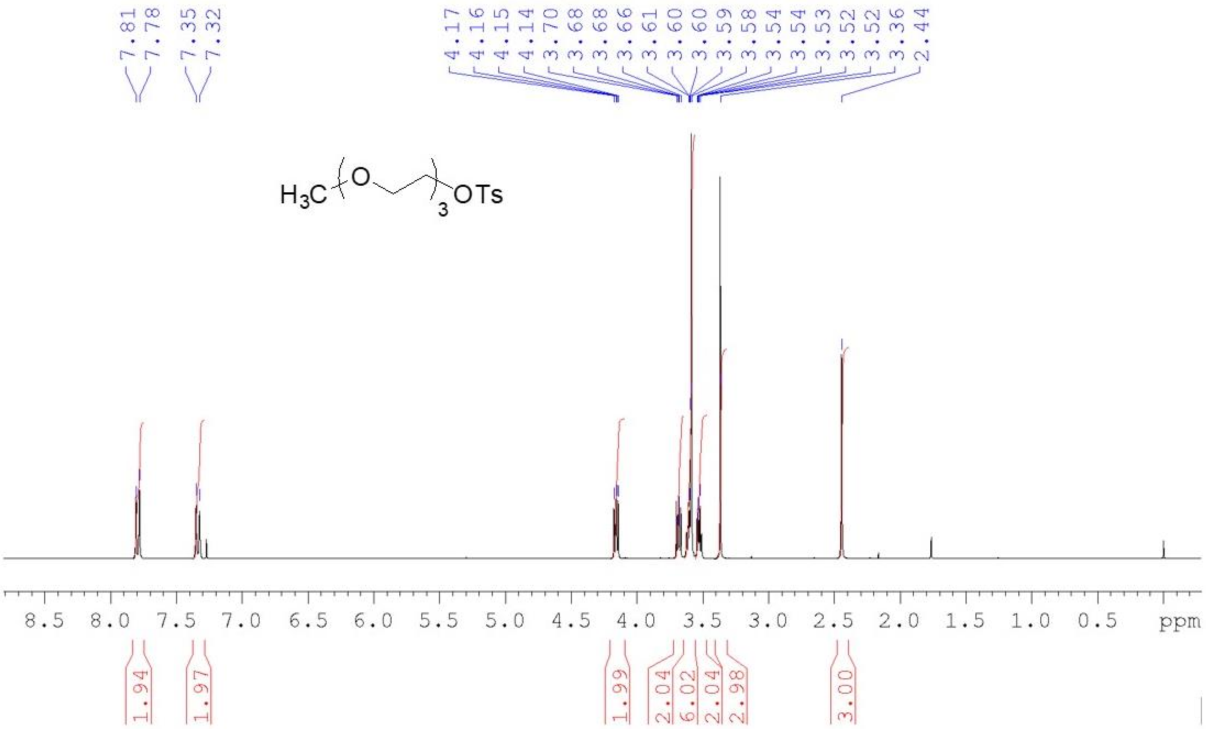

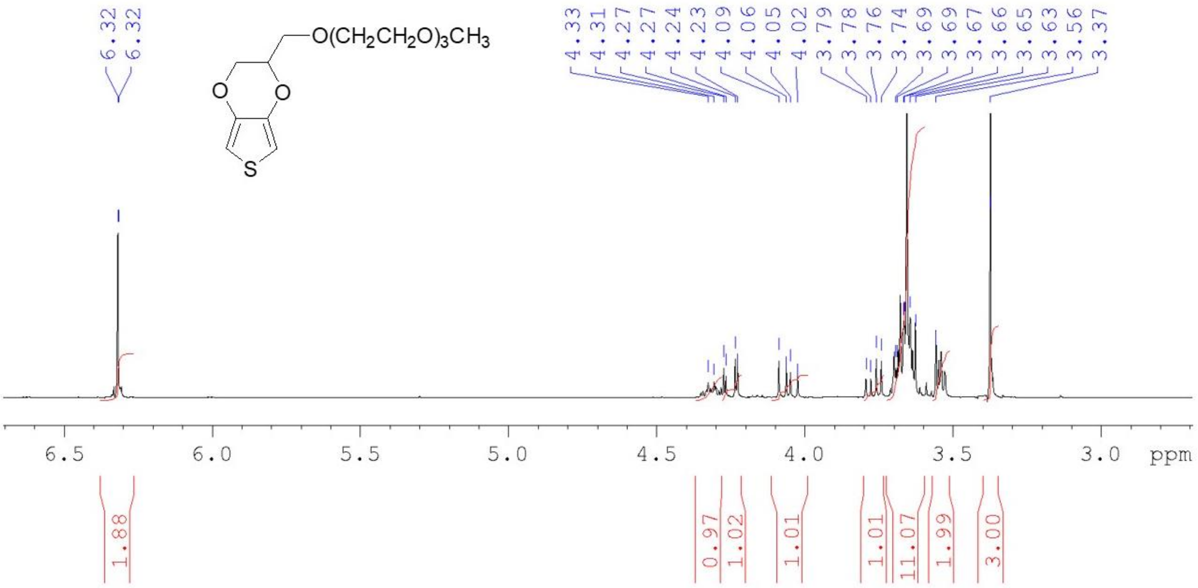

5. Optical and morphological characterizations

5.1 Atomic Force Microscopy (AFM)

AFM in air (*Chapter V*): ICON, Bruker atomic force microscopy (AFM), tapping and phase mode images taken in air atmosphere at room temperature ~ 293 K. We used Si cantilevers with a free oscillating frequency f_0 ~ 320 kHz and a spring constant k ~ 42 N/m. AFM images were treated with Gwyddion.[146]

AFM in Liquid (*Chapter III***):** AFM was performed on a JPK NanoWizard® III system mounted on a Zeiss Axio Observer.Z1 optical microscope. Imaging and mechanical characterization were performed in PBS buffer with a Brüker RFESP probe (3 N/m) in QI® mode with either a 20 nN threshold force and a 200 nm z-ramp (high-resolution imaging) or a 200 nN and 2 µm z-ramp (large view elasticity). Spring constant was calibrated prior to the experiment using the Sader method and the sharpness of the tip was verified after the experiment using scanning electron microscopy. Data were analyzed using the JPK DP software for zero-force topography, line profile, roughness, and elasticity with a cone indenter. Statistics show mean +/- standard deviation (SD). These experiments were performed in collaboration with *Dr. Sebastien Janel* at *Institute Pasteur De Lille*.

6. Scan Electron Microscopy (SEM)

SEM images were obtained using an electron microscope ULTRA 55 (Zeiss) equipped with a thermal field emission emitter with three different detectors: EsB detector with filter grid, high efficiency In-lens SE detector and Everhart-Thornley Secondary Electron Detector.

7. Raman Spectroscopy

A 473 nm excitation laser (~1 mW) focused with a 100× objective was used for confocal Raman spectroscopy measurements in air at room temperature. Raman data were treated with Labspec5 software provided by Bruker. A post-doc researcher colleague *Dr. Michel Daher Mansour* led the Raman spectroscopy experiments and data analysis.

8. Bio experiments

The Bio experiments were performed at Lille Neuroscience & Cognition Research Centre, University of Lille, INSERM U1172, Lille, France under the supervision of Dr. Sophie Halliez, member of the 'Alzheimer & tauopathies' team led by Dr. Luc Buée. The EOPS facility (PLBS UAR 2014 - US 41) took care of the animals.

8.1 Cell viability/metabolic activity assay and cytotoxicity/cell death assay

All the materials that were investigated for the biocompatibility experiments were deposited on glass coverslips. The coverslips then were inserted into 12-well cell culture plates (Corning, USA) then sterilized by UV exposure. The adhesion layer coating was performed with a mix of Poly-D-lysine (0.5 mg ml-1, Sigma) and laminin (10 µg ml-1, Sigma). The coating solution was applied for 2 hours at room temperature then washed using sterile water (Corning) and air-dried. Mouse primary cortical cells and cell culture medium were prepared as described above. In each well, 500000 viable cells were seeded in 1.5 ml culture medium (131500 cells/cm2). Cultures were kept in a cell incubator (ThermoScientific) at at 37°C in a 5% CO2 atmosphere. The culture medium was never changed but small amounts of fresh medium were added once a week to compensate medium evaporation (never more than 10% of the initial volume).

To assay metabolic activity/number of viable cells, cellular reduction of MTS tetrazolium into formazan was quantified using the CellTiter 96 Aq$_{\text{ueous}}$ One Solution Cell Proliferation Assay (Promega) following the manufacturer's instructions. Cells grown on regular glass coverslips were used as a reference meaning that their metabolic activity was set as the reference value (100%). The metabolic activity of the cells grown on the other surfaces was normalized against it. To assay cell death, the release of lactate dehydrogenase (LDH) into the cell medium was quantified using the CytoTox 96 Non-radioactive Cytotoxicity Assay (Promega) following the manufacturer's instructions. Maximum LDH release was determined by adding lysis solution (9% Triton X-100) to cells grown on regular glass coverslips. Significant differences between results obtained for cells grown on glass and results obtained for other samples with the different materials were examined using the nonparametric Mann-Whitney and Wilcoxon tests, and *p*-values <0.05 were considered significant.

8.2 Cell cultures on MEAs and OECTs

Mouse primary cortical cells were prepared from 15-days-old C57BL/6JRj mouse embryos as previously described [147]. The present experimental research has been performed with the approval of an ethical committee (agreement APAFIS#2264-2015101320441671 from CEEA75, Lille, France) and follows European guidelines for the use of animals. Gestating females (Janvier Labs) were housed in a temperature-controlled (20 - 22° C) room maintained on a 12 h day/night cycle with food and water provided *ad libitum*. The culture medium was made of Neurobasal (Gibco) supplemented with B-27 (Gibco), Antibiotic-Antimycotic (Gibco), and L-glutamine (Gibco). Before utilization, the MEAs/OECT arrays were sterilized by heating in water at 125°C for 30 minutes then it was kept in water. Before cell seeding, the MEAs were coated with an adhesion layer consisting of a mix of Poly-D-lysine (0.5 mg/ml, Sigma) and laminin (10 µg/ml, Sigma). The coating solution was applied for 30 minutes at room temperature and then washed using sterile water (Corning). For each MEA/OECT array, one drop of a cellular suspension at 4000 cells/µl in cell culture medium was seeded on the MEA recording area (120 000 cells). Ten minutes after plating, 1 ml of fresh medium was added and the MEA culture chambers were sealed with a removable hydrophobic semipermeable membrane cover (fluorinated ethylene-propylene, 12.5 microns thick, Multi-Channel Systems). Cultures were kept in a cell incubator (ThermoScientific) at 37°C in a 5% CO2 atmosphere. The culture medium was never changed but small amounts of fresh medium were added once a week to compensate for medium evaporation (never more than 10% of the initial volume).

8.3 *In vitro* extracellular setup for MEA Recording

In vitro recordings were performed using a MEA2100-system (Multi Channel Systems) experimental setup with a 60 channels headstage (Multi Channel Systems) that amplifies and digitizes the signals, an interface board (MCS-IFB, Multi Channel Systems). Connected with GUI on a computer for real-time monitoring, signal filtering, spike detection and recording by using the Multi Channel Experimenter software (Multi Channel Systems). A temperature controller (TC02, Multi Channel Systems) was used to keep the temperature of the cultures at 37°C during the recording (Figure 2.3). MEAs were kept 15 minutes into the experimental setup then recorded for 5 minutes.

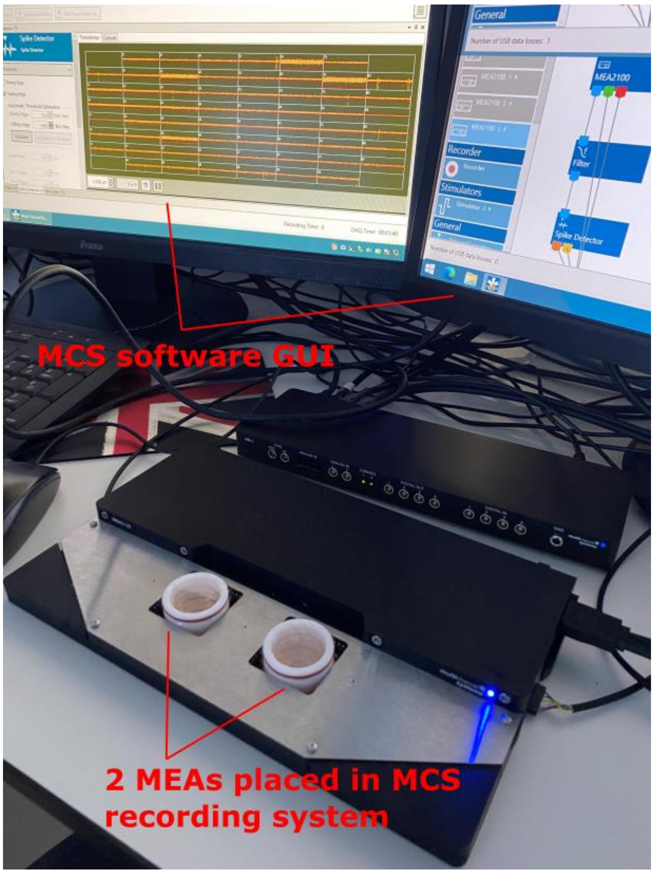

Figure 2.3 Image showing two MEAs has been recorded by MCS recording system

9 Processing and analysing the recorded biodata of MEAs

9.1 Spike and bursts analysis

The spiking and bursting events were detected through the Multi Channel Experimenter software by amplitude thresholding. A threshold was set for each recording electrode as 10 times the standard deviation of the baseline noise level after a software band pass filter from 200 Hz to 4 kHz. Then the recordings were exported to the NEX format using the Multi Channel DataManager software (Multi Channel Systems). All the analysis were done through the Neuroexplorer software (Nex Technologies). The analysis was performed over the total recording time of five minutes.

9.1 Spike Sorting

The spike sorting experiments were performed in collaboration with *Dr. Pierre Yger* from Institut de la Vision and Lille Neuroscience & Cognition Research Centre.

The raw extracellular recordings were processed with the SpyKING CIRCUS software [78], v1.1. Default parameters were used, and by default all the templates found by the softwares were kept for further analysis. The temporal width of the templates is fixed to 3ms. By default, every channel detects the peaks higher than 6 median absolute deviations of its noise level.

Signal-to-Noise ratio (SNR) calculation: First of all, all the raw data coming from the channels are high-pass filtered with a third order Butterworth filter with a 300 Hz cut-off frequency to analyze the spikes activity. A whitening is then performed to remove spurious spatial correlations between nearby recording electrodes. SNR was calculated for each electrode from its mean spike amplitude and the mean-absolute deviation (MAD) of its background after setting the threshold by 5xMAD. The analysis was performed over the total recording time of five minutes.

Estimation of the positions: To assess the putative positions of the somas, two methods are considered. The first one used a lot in the literature, is a straightforward center of mass estimation. More precisely, assuming that the neuron i has the waveform $w_i(t)$ defined on several channels $a \in \{1, .. n_{channels}\}$, we computed the peak-to-peak values $ptp_i(a)$ on every channel a. Since every channel has a physical position in the 2D space $\boldsymbol{p_a} = (\boldsymbol{x_a}, \boldsymbol{y_a})$, we can obtain, for every neuron i its barycenter or, its so-called Center of Mass (CoM_i) as

$$CoM_i = \frac{\sum_a \quad ptp_i(a).p_a}{\sum_a \quad ptp_i(a)}$$

The second method used in the paper is referred to as the monopole approximation. As has been done in [148] or [83], the idea is to consider the cell as a monopole and infer its position by triangulation given the amplitudes of the templates, perceived on all channels. More precisely, assuming the cell behaves as a monopole, we can exploit the fact that each spike is detectable on multiple channels a simultaneously: i.e., if the position of cell i is (x_i, y_i), we have multiple observations of the form

$$ptp_i(a) = \frac{k}{\sqrt{(x_a - x_i)^2 + (y_a - y_i)^2}}$$

Therefore, one can try to solve an optimization problem, and optimize the following cost function $\Phi(x_i, y_i, k)$, finding (x_i, y_i, k) in order to minimize

$$\Phi(x_i, y_i, k) = \sum_a \quad (ptp_i(a) - \frac{k}{\sqrt{(x_a - x_i)^2 + (y_a - y_i)^2}})^2$$

All cells are assumed to only have 2D coordinates, i.e. the depth is considered as fixed and equal for all neurons.

Synthetic templates: In order to benchmark how precise the localization of the soma can be for various methods, we generated synthetic templates via the MEArec software [148]. Using a standard neuronexus 32 channels probe layout, with a spacing of 100 µm between channels (to copy the spacing used in the real recordings), we generated 50 templates for 50 fake neurons at random positions. The extracellular waveforms of these cells are taken from a library (see [148]) of *in vivo* excitatory/inhibitory neurons.

10. In vitro recordings of OECTs

The "RHS2000 Intan 128ch" Stimulation/Recording controller is a system that allows users to record biopotential signals up to 128 channels and it can generate constant current stimulation pulses if needed through these channels. This device contains 4 ports (Figure 2-4 (a) labeled A-D) that provide connection points for the stim/record headstages where each headstage contains 16 or 32 channel amplifier chips. Each stim/record headstage contains: one or two RHS2116 amplifier chips. The RHS2116 amplifier chip is a complete bidirectional electrophysiology interface system that contains an array of stimulation/amplifier blocks and each channel includes a low-noise amplifier with programmable bandwidth. Intan Technologies provides an open source, multi-platform GUI software that controls the operation of recording or stimulating of all the input and output ports of the device. In our experiment, this device gave us the capability to measure multiple OECTs from different sites. This device measures bio-potentials from 50µv until 5mV directly from passive electrodes. While we are using OECTs with drain output current, some electronic setup was implemented to make this Intan device compatible with OECT array. This electronic setup was composed just from passive devices in order to achieve compatibility between OECT and Intan. The aim here is to implement a voltage divider circuit setup for each OECT in the array to get voltage outputs so it can be compatible for having measurements using this INTAN device. The REF pin of the headstage is shorted and connected to the ground of its amplifier [149], by connecting the REF pin to the ground of the circuit, the output voltage of each voltage divider setup at each electrode pin is represented in equations below:

$$V_{out} = R_l * I_d$$

$$\mathrm{V_{out}} = \left(\frac{\mathrm{R_l}}{\mathrm{R_l} + \mathrm{R_{OECT}}}\right)\mathrm{V_{DS}}$$

Where $\mathrm{R_l}$ is the load resistance and $\mathrm{V_{DS}}$ is the drain-source biasing voltage.

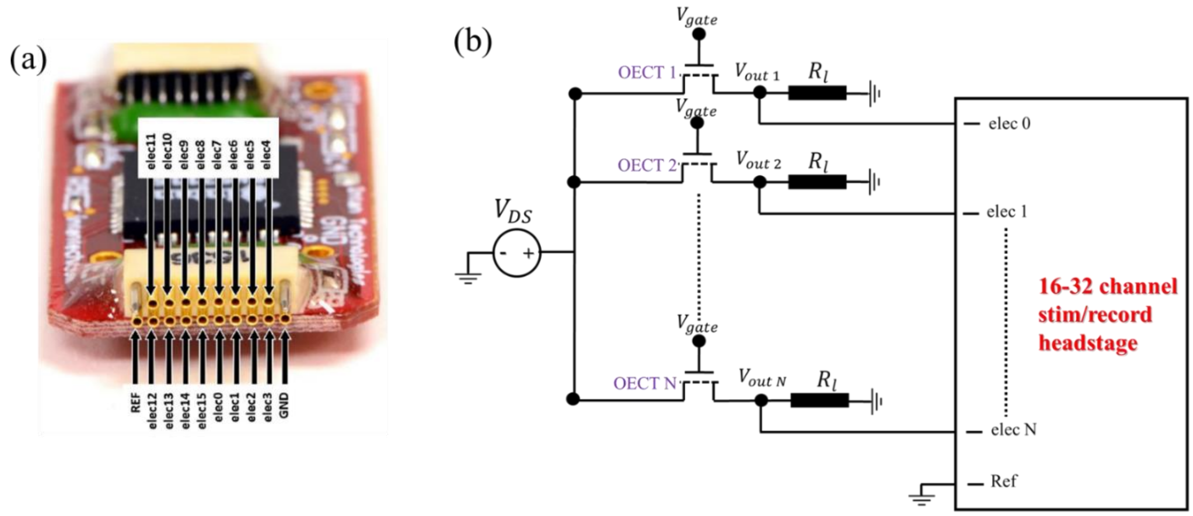

Figure 2.4 (a) Electrode connector pin diagram for stim/record INTAN headstage. (b) Schematic of the OECT array with voltage divider configuration

Chapter III. Electropolymerized conductive polymer on microelectrodes for enhanced cell electrical activities measurements and neuronal accurate localization

3.1 Introduction

As mentioned previously in *chapter I*, recently, the use of conducting polymers (CP) as PEDOT:PSS has emerged a lot for coating microelectrodes for biosensing due to its mixed ionic electronic conduction, biocompatibility, and low impedance. A lot of studies showed promising results for the use of PEDOT for coating the microelectrodes of MEA as a state of art and proof of concept in enhancing the signal-to-noise ratio (SNR) [150] and the quality of the recordings [151,152]. PEDOT:PSS coatings are patterned through several wet-coating techniques, such as spin-coating, drop-casting, ink-jet printing, or *via* electropolymerization [46,67,153]. Electropolymerization of PEDOT from EDOT monomers has been explored as a versatile post fabrication bottom-up material engineering technique [154]. Although this process is still not conventional in micro fabricating biosensor devices, it has been showing great impact on biosensors and its potential to adapt *in-operando* their properties according to the signal they sense [124]. The versatility of electropolymerization and its high degree of control over the CP thickness, surface properties, and ionic/electrical parameters [124,128] makes it an attractive solution for bottom-up material co-integration. In this chapter, we will intensively investigate the electropolymerization technique by *in-situ* electrochemical impedance spectroscopy measurements during deposition. This will give us more insights about the change in the physical parameters of the electrode before, during and after coating. We report the use of EDOT electropolymerization to tune post-fabrication material and geometrical parameters of passive microelectrodes for *in-vitro* extracellular recordings from neurons. The process optimizes the cell/electrode interface by decreasing its impedance and improving its affinity with neurons: results demonstrate an improved signal-to-noise ratio, good biocompatibility, and a higher number of neurons detected in comparison with gold electrodes from the same neural cultures. Then, by exploiting these high-performance MEAs, we investigated the possibility of accurately estimating the positions of the neurons solely from extracellular recordings by studying the correlation between electrical activity (obtained via spike sorting) and optical imaging (Fluorescent) of neural networks cultured on MEAs. Here, we used spike-sorting algorithms as a tool to check if the physical positions of the neurons could be reliably inferred from extracellular electrical recordings by MEAs. The rational goal behind that is to be able to better understand the organization of the 2D neural culture, which would help in understanding finer the coupling between the neuron and electrode..

3.2 Impedance gradual tuning through potentiodynamic electropolymerization

In the electropolymerization mechanism (Figure 3.1), when the voltage applied on the electrode reaches an oxidation potential, electron transfer oxidizes EDOT monomers and is coupled to form dimeric cations. Then, a process called deprotonation occurs to stabilize the formed dimeric cations. This dimer is oxidized, and a positively charged cationic group is later formed. When the deprotonation and coupling steps are repeated, the cationic group progressively forms a conjugate PEDOT chain. Simultaneously, the counter anion (A^-) enters the PEDOT chain as a dopant, maintaining charge balance. As shown in Figure 1, during the charge-discharge, PEDOT converts between oxidation and reduction state, associated with the doping and de-doping of counter anions. Hence, one interesting feature of electropolymerization is how this procedure affects the physical properties of the electrode material by playing with several conditions such as electrodeposition modes, parameters, and counter ions. The changes in the film’s electrochemical behavior are not only during deposition but also before and after coatings. Many studies use impedance spectroscopy to investigate the influence of the incorporated molecules on the electrochemical properties of the electrode after deposition. A general assumption is that the most important signal for neural communication is from 1 Hz up to the range KHz; however, it worth noting that the behaviors over the whole frequency range can give interesting clues to material composition, porosity, and permeability.

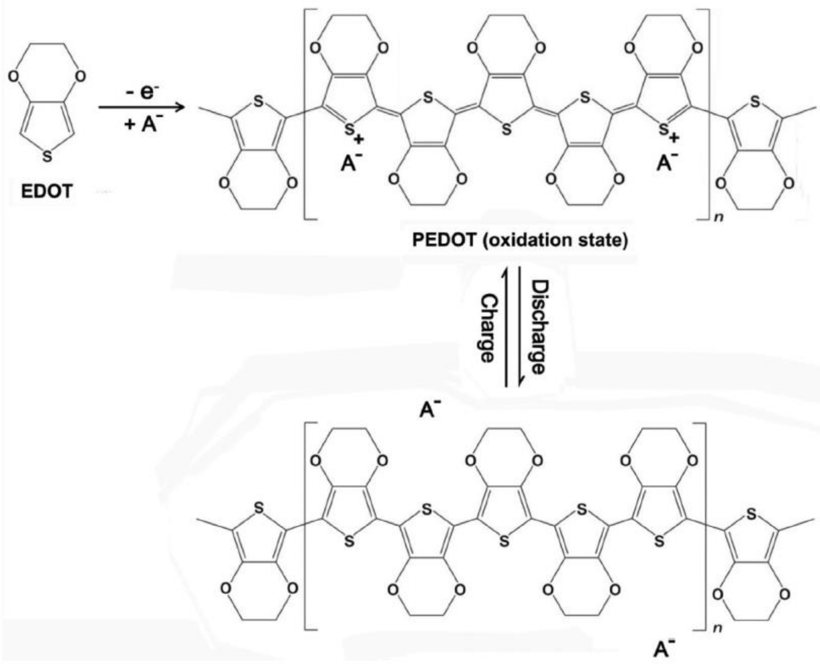

Figure 3.1 The electropolymerization of EDOT to PEDOT mechanism and the transition between oxidation-reduction states for PEDOT during the charge-discharge. A$^-$ represents counter anion (adapted from [155])

To get the insight of the physical and electrochemical properties of the PEDOT during the growth of polymer on top of the gold electrode, we performed *in-situ* electrochemical impedance spectroscopy (EIS) during the potentiodynamic electropolymerization experiment.

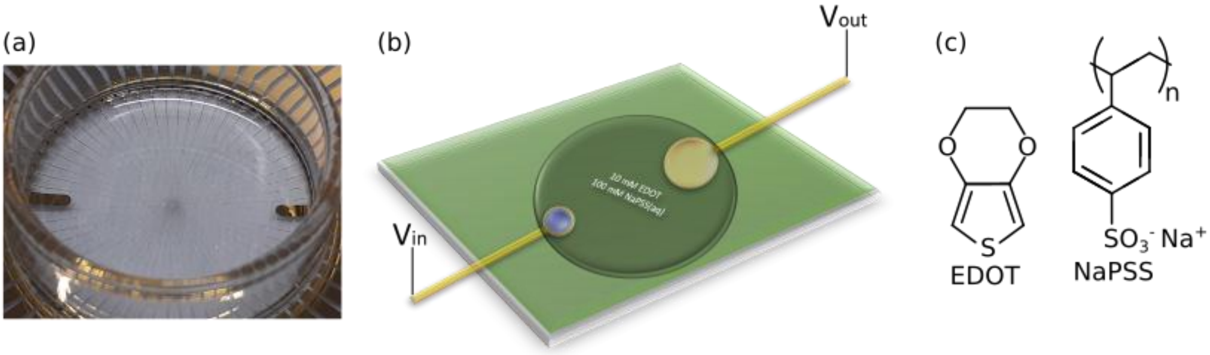

Figure 3.2 Electropolymerization setupe. (a) Photograph of the one-milliliter glass chamber for the *in vitro* cell culture and recording via 58 microelectrodes, plus 2 macro references away. (b) Electrochemical setup for electropolymerization technique and for impedance spectroscopy to characterize the impedance of the electrochemically modified electrodes, using the in-plane gold reference as output electrode. (c) Chemical structures of the components introduced in the electroactive electrolytes, comprising EDOT (left) and sodium polystyrene sulfonate used as a supporting electrolyte in water.

Figures 3.3a and b. show the Bode's modulus and Bode's phase plots of the impedance spectra measured from 1 Hz to 1 MHz with voltage ramp of the bias (V_{DC}) from 0 to 1.3 V with a scan rate of 1 mV/s in an aqueous electrolyte solution containing 10 mM of EDOT monomer and 100 mM of NaPSS (Figure 3.2c). We note that each spectrum was acquired while the bias was swept but with a rate of change sufficiently small with respect to the scan frequency to ensure consistency of the results. After exceeding the oxidation potential, the Bode's modulus graph shows a gradual decrease of the impedance modulus of the electrode with the gradual growth of the conducting monomer on top of gold surface. The value of the impedance modulus at 1 kHz changed from MΩ to kΩ range ending at 76.6 kΩ for a microelectrode upon reaching 1.3 V of electropolymerization potential. It is worth mentioning that such post-fabrication step allows improving the electrode impedance and could be applied to any electrodes without mean of additional and complicated micro-fabrication techniques. To analyse the change of the electrical and physical parameters of the electrode during electropolymerization, EIS modelling was systematically made according to the equivalent circuit shown in Figure 3.3c. The chosen model has been restricted to only five elements according to the complexity of the visualized spectra and the interpretation of the physical significance of each parameter corresponding to the dependency with ion concentration and electrode size and distance [156]. In such model, $C_{PSS/Au}$ is the reference electrode capacitance, r_{red} is the cathodic charge-transfer resistance on the reference electrode, R_e is the electrolyte resistance for the ion drift, R_{ox} is the anodic charge-transfer resistance on a micro-electrode, and CPE is a constant phase element referring to the charge/discharge on a micro-electrode. CPE is an electrochemical circuit element that describes the transient response of a linear element of admittance $1/Z = Q_0*(i\omega)^n$, with Q_0 the non-ideal capacitance, ω the pulsation and n a power factor. This implies that depending on the two factors n and Q_0, the CPE element can be defined as a pure resistor ($n = 0$) or as a pure capacitor ($n = 1$), but also other elements having both resistance and reactance showing ($Q_0 > 0$ and $0 < n < 1$). The evaluation of n is a strategy to quantitatively assess an electrode's Debye relaxation and deviation from this ideal law informing on the state of the energy levels (*i.e.* atomic level heterogeneity) and structure (*i.e.* roughness) of such electrode [157,158]. Notably, the extracted values for the EIS analysis under voltage ramp do not show modifications of the reference electrode capacitance ($C_{PSS/Au} = 10.9 \pm 0.3$ pF), reduction resistance ($r_{red} = 11 \pm 2$ kΩ), nor the electrolyte resistance ($R_e = 11 \pm 2$ kΩ) during electropolymerization. However, we monitored clear changes in the CPE exponent (n), the CPE capacitance (Q) and the anodic charge-transfer resistance (r_{ox}) with the gradual growth of PEDOT material on the electrode surface. Q increases from 0.1 nS·s $V_{DC} = 0.6$ V to 10 nS·s at 1.2 V, showing that the microelectrode specific capacitance increases by two orders of magnitudes thanks to electropolymerization, which testify on the volumic aspect for ion accumulation of electropolymerized PEDOT (ePEDOT). R_{ox} shows substantial decrease from 1 GΩ to 10 MΩ. Accurate value for R_{ox} when electropolymerization started is more difficult to extrapolate due to the change of regime from non-Faradaic to Faradaic, which limits the EIS modelling.

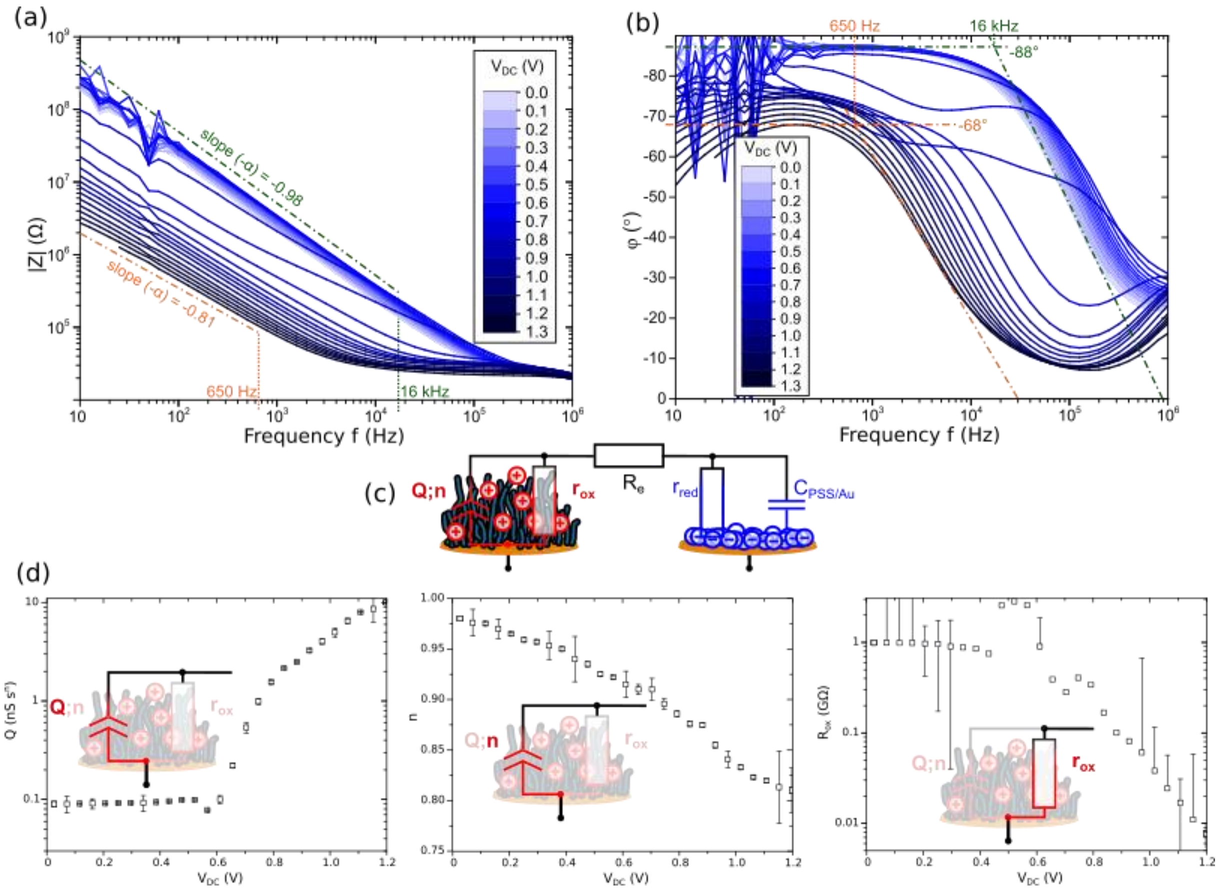

Figure 3.3 In-situ electropolymerization of 10 mM EDOT$_{(aq)}$ in 100 mM NaPSS$_{(aq)}$ upon voltage ramped impedance spectroscopy, displaying a gradual change in the impedance modulus (a) and phase (b) with the increase of the positive DC-component applied on the micro-electrode (Measurements and graph done by post-doc colleague Dr. Anna Susloparova). (c) Equivalent circuit that displays a first-level model for the impedance recorded through the micro-electrodes, and physical representation of the different elements involved in the model. (d) Electrochemical circuit element parameter evolution with the applied DC component during impedance spectroscopy, resulting from in-situ electropolymerization on micro-electrodes.

A monotonic change of the CPE index from ideal capacitor signature (n~1 at V_{DC} = 0 V) to a non-ideal capacitive response signature (n= 0.8 at V_{DC} = 1.2 V) during electropolymerization was occurred. It is worth to remark that, the monotonic decrease of the CPE index (n) started before the increase in Q, which suggests that the capacitance non-ideality is not exclusively attributed to the morphology of ePEDOT and diffusion limitations associated to its bulk charge. Indeed, experimental and theoretical models studies showed that the CPE exponent (n) tends to decrease with the surface roughness [159–161] by investigating the relationship between CPE model and the dimensions of fractals in porous and fractal electrodes[158,162]. On the other hand, there was a complete disagreement about this direct relationship between CPE and roughness of the electrode by revealing a very high values of the CPE exponent (>0.99) for a very rough material ball-milled Pt powder [163,164], proposing here the increase of the CPE exponent with roughness conversely to what mentioned previously. Furthermore, Kerner and Pajkossy [157,165] upgraded the level of investigation by disputing that the CPE behaviour tends to be more associated to the heterogeneity of the surface on the atomic scale together with the presence of some kinetic process (most probably with specific anion adsorption) rather than the geometric imperfection (larger than those on the atomic scale) represented by the roughness of the electrode. In previously reported work [165,166] , capacitance dispersion has been observed even with single crystalline electrodes, which have a perfect surfaces as a consequence of specific anion adsorption. Since the activation energies of the kinetic process on these surfaces has a particular distribution, this dispersion with energetically non-uniform surfaces is enhanced. That is, due to the exponential relationship between activation energy and rate coefficient, a relatively low distribution of the activation energy causes a broad distribution of the rate coefficients yielding more frequency dependence. Here, in our experimental impedance measurements and theoretical modelling we determined results that can support the assumption of Pajkossy and coworkers [157,167,168]. We showed that even before the start of the deposition of the polymer on top of gold, there was a monotonic decrease in the CPE element of the microelectrode. This CPE behaviour can be correlated to the atomic level heterogeneity of the surface rather than geometric change. This surface disorder can be due to the adhesion of molecules from the monomer electrolyte to the surface of the microelectrodes causing anion adsorption.

3.3 Effect of PEDOT coatings on cell activity measurement

In this section, we wanted to check if using EDOT electropolymerization to tune post-fabrication of the electrodes could help to boost the signal-to-noise ratio for the spikes recorded in the vicinity of the electrodes and the performance of cell detection. Here, the PEDOT coatings on top of the 30 µm microelectrodes have been deposited through potentiostatic electropolymerization by a correlation between voltage and time applied for forming a thin film coating on top of the gold micro-electrode. A 1.4 V_{IN} has been applied for 8 seconds on the working electrode while grounding the reference electrode resulting in coating 200 nm PEDOT thickness in the center and 500 nm thickness at the edges of the opening. For the potentiostatic electropolymerization, several V_{IN} values (above the oxidation potential (Figure 3.3a)) has been studied; however the chosen value (1.4 V) was able to coat the microelectrode with the desired thickness with less electropolymerization time. Figure 3.4b shows the Bode's modulus plot of the impedance spectra measured from 1 Hz to 1 MHz in an electrolyte containing Phosphate-buffered saline (PBS) solution for microelectrodes (n=10) before and after PEDOT coating. Thanks to the electropolymerization of PEDOT, notably, the value of the impedance modulus at 1 kHz changed from MΩ to kΩ range after depositing PEDOT on top of the gold microelectrodes (e.g. decreasing from 25 MΩ to 23 KΩ).

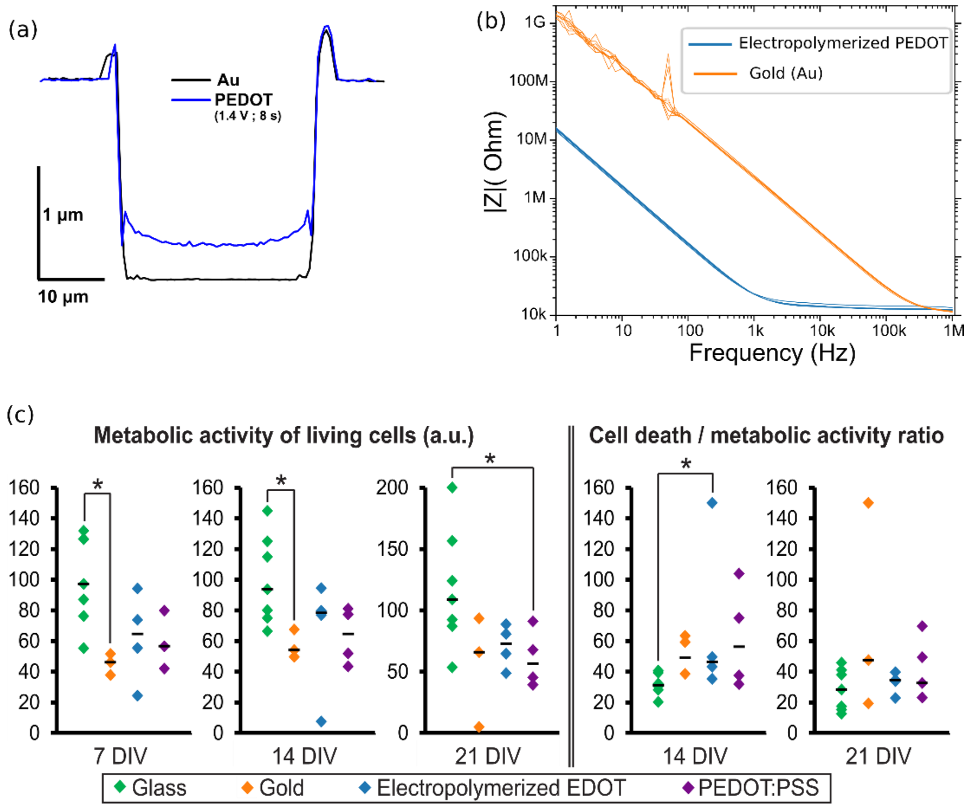

Figure 3.4 (a) Topology of a micro-electrode coated with electropolymerized PEDOT (1.4 V_{DC} for 8 seconds). (b) Bode plot cure showing the impedance modulus of both non-coated (gold) and coated electrodes (potentiostatic electropolymerized PEDOT). (c) Biocompatibility assessment of gold, electropolymerized PEDOT, commercial spin-coated PEDOT:PSS compared to glass biocompatibility (reference) through metabolic activity assays, cell death assays, and the ratio of cell death on metabolic activity. The differences between results obtained for cells grown on glass and results obtained from other materials were examined using the non-parametric Mann-Whitney and Wilcoxon tests (*:$p < 0.05$).

As explained in previous chapters, one of the parameters that affect the coupling between the neuron and electrode is its input impedance, which represents how much voltage drop it can maintain on its node such that the lower impedance (higher capacitance) the better recordings expected. Another important parameter for sensing is the seal resistance; henceforth, it signifies the degree of affinity between the neuron and the electrode. Accordingly, we studied the innocuity of the electropolymerized PEDOT material and compared it with several materials such as glass, gold, and commercial spin-coated PEDOT:PSS used in state-of-the-art (Figure 3.4c). This experiment is performed by measuring the living cell numbers (metabolic activity as a proxy for cell number) and death assays of cells cultured on top of the different materials. Rat cortical cells grown on gold, electropolymerized EDOT, and PEDOT:PSS were compared to cells grown on glass (control) after 7,14, and 21 days of culture *in vitro* (DIV). The mean metabolic activity of the cells grown on electropolymerized EDOT was not significantly different from that of glass at contrary with gold, for example. However, cell death was slightly increased after 2 weeks of culture compared to glass. It is worth to highlight the fact that the cells grown commercial spin-coated PEDOT:PSS exhibit a significantly lower mean metabolic activity from that of electropolymerized EDOT at DIV 7, 14 and 21. The cell death was also slightly lower at DIV 21 compared to spin-coated PEDOT:PSS. One hypothesis behind the enhanced biocompatibility of the electropolymerized EDOT compared to spin-coated PEDOT:PSS could be correlated to a possible slight cytotoxic effect induced by the additives used during the preparation of the latter, such as (3-Glycidyloxypropyl)trimethoxysilane (GOPS) cross linker used to improve film mechanical stability and adhesion to the substrate. For example, previous studies reported that using alternative cross linkers other than GOPS enhances the cytotoxicity of PEDOT:PSS films [169]. Taken together, this showed the low toxicity of electropolymerized EDOT coupled to a lower impedance in comparison to gold, thus demonstrating its superiority as microelectrode material.

Accordingly, thanks to the versatility of the electropolymerization technique we coated half of our MEA's electrode with electropolymerized PEDOT. As shown in Figure 3.5a, we coated the electrodes with random distribution to neglect the biological variability that could come from the cell growth heterogeneity. Here, we will be able to record the activity of the same neural network through microelectrodes with the two different materials giving us the ability to compare fairly the performances in cell detection.

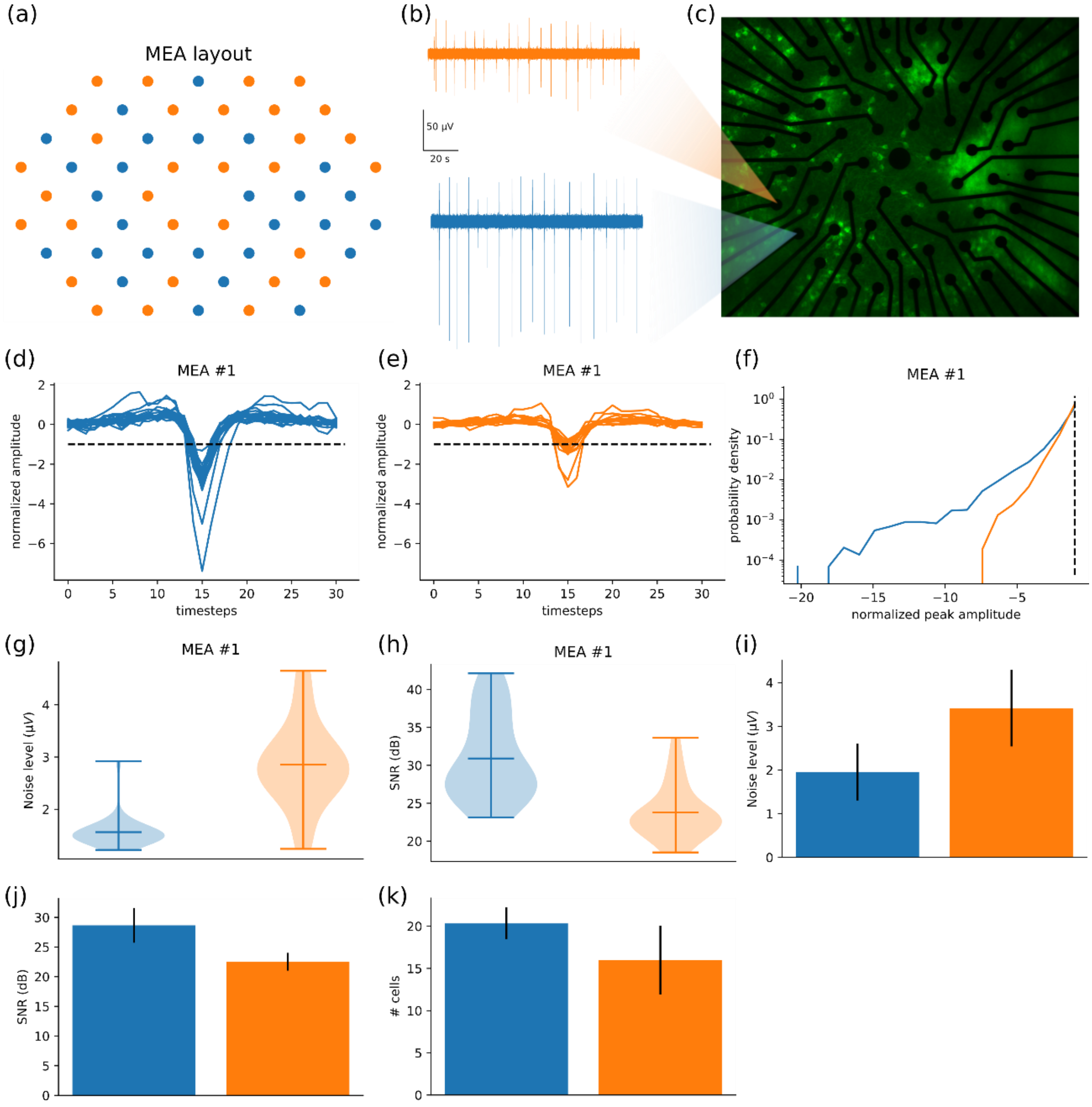

Figure 3.5 Effect of PEDOT coating on cell detection. (a) The layout of the MEA, and the patterning of the coated vs non-coated channels. (b) Time series showing spontaneous burst-spike activities of a neural culture at DIV21 from a gold electrode and coated ePEDOT electrode on the same MEA number 1.(c) Live-imaging of primary cortical neurons on top of the MEA, after 21 days in vitro (DIV21).Note that only live neurons are detected by the fluorescent probe we used. (d) Canonical waveforms obtained for spiking neurons, over coated channels, and. (e) non-coated channels of MEA number 1. (f) Probability density of the normalized peak amplitudes over all channels of MEA number 1, sorted by types (coated vs non-coated). (g) Violin plot chart showing the noise levels obtained over all channels of MEA number 1, sorted by types (coated vs non coated). (h) Violin plot chart showing the Signal to Noise ratio (SNR) over all channels of MEA number 1, sorted by types (coated vs non coated). Histograms showing the (i) noise levels and (j) SNR values obtained over all channels averaged over three different MEAs, sorted by types (coated vs non coated). Error bars show standard deviations (k) Histogram showing the number of cells detected after spike sorting whose template peaks are on coated or non-coated channels averaged three different MEAs (three different cell cultures). Error bars show standard deviations.

First, as shown in the graphs of figures 3.5g and h, the noise level and SNR of the recordings were calculated statistically on the gold and electropolymerized microelectrodes. Remarkably, the mean average SNR value of the recorded microelectrodes through ePEDOT (~ 30 dB) is higher by 50% than that from gold microelectrodes (~ 20 dB). For more statistical investigations, the SNR of the recordings was calculated for three different MEAs (Figures 3.5 i and j) with reproducible results showing both a global reduction of the noise (Figure 3.5i) and higher SNR values (Figure 3.5j) of coated electrodes compared to gold ones. Hence, the microelectrodes that record data with better SNR are likely to detect more spikes with low amplitudes, which is considered to be one of the challenging tasks in cell networkactivity measurement/characerization (*i.e.* spike sorting). To test this hypothesis, we performed spike sorting on the extracellular traces *via* a customized and dedicated software (Spyking-circus, see Methods in *chapter II*). The spike sorting experiments through Spyking-circus software have been performed by *Dr. Pierre Yger* in collaboration. As presented in the histogram in figure 3.5k, we show how these coated microelectrodes had the ability to detect a higher number of cells than gold microelectrodes from the same neural culture, recorded at the same time under the same conditions from three different MEAs (three different cell cultures). Noting that, for each MEA of these three MEAs, the number of the detecting cells by the coated channels was higher than that from the non-coated channels. Interestingly, by looking at Figure 3.5j and Figure 3.5, we see the relative difference in the values of SNR of the coated channels (40% higher) from non-coated is remarkably correlated to the relative difference between the number of cells detected from coated (~34% higher) and non-coated channels.

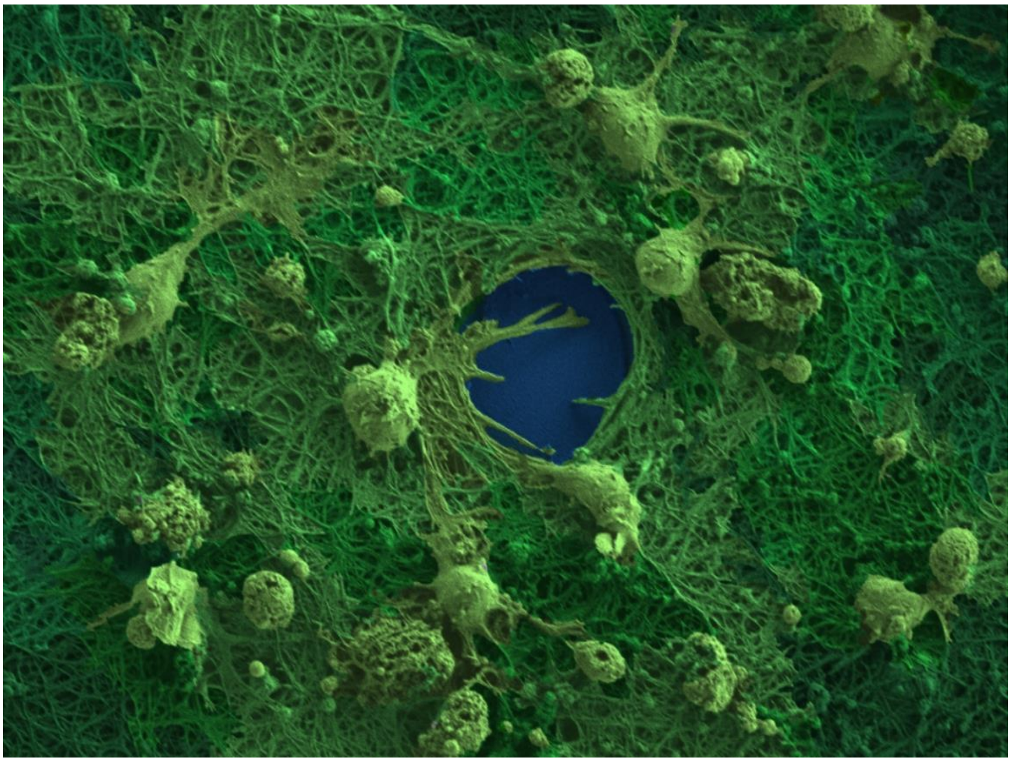

Figure 3.6 Colorized SEM image of neurons outgrowth around and on top of PEDOT microelectrode

3.4 Active neurons localization in 2D cell cultures by using high-performance electropolymerized microelectrode arrays correlated with optical imaging

The *in-vitro* extracellular recording results investigated in the previous section point out the effect of high-performant microelectrodes on cell electrical activity measurements. Here, we will use MEAs with fully PEDOT coated microelectrodes, and we will exploit its good-quality recordings and correlate it with optical imaging to localize active neurons accurately. While, quite often, the localization of the neurons has been very naively estimated by several spike-sorting algorithms with a simple Center Of Mass (COM) algorithm depending on their electrical signatures, more evolved algorithms have been proposed to infer such positions [84–86], taking into account some physical properties of the cells. In this part, we will try to estimate how precise such localization schemes could be in 2D cell cultures when considering that cells behave as monopoles [86,87].

3.4.1 Estimation of the positions from *in vitro* recordings

To first estimate how precise one could hope to be in estimating the putative position of a soma given its extracellular signature, we generated synthetic templates via the MEArec software [148]. The software comes with a built-in library of compartmental excitatory/inhibitory cells (mostly reconstructed from *in vivo* neurons) and while simulating them with the neuron software [170], it allows to get an as accurate as possible view of the extracellular potentials at various recording sites (see Methods). The position of the cell is first estimated via the classical Centre of Mass procedure (COM) (see Methods), or via a more complex method assuming that the soma behaves as a monopole (see Methods). Because the black line, in these two panels, shows how the normalized amplitudes should behave given the real (artificially generated) positions, we can notice that the monopolar estimation provides a much better estimation compared to the theoretical estimate (Figure 3.7a and b)

Now, we can apply the exact same analysis to some *in vitro* recordings performed on cell cultures. Figure 3.7c, and d shows the positions obtained after running our spike sorting software on a particular recording (DIV 21). The positions of the cells, given their Spatio-temporal extracellular signatures, are estimated either via COM or a monopolar estimation. Strikingly, one can note the fact that somas are much more likely to be close to recording channels with the second case. To establish if some positions are more “plausible” than others, we displayed, in Figure 3.7e and f the amplitudes of the templates as a function of the distances between the estimated cell’s position and the channels. The distribution looks more in line with the power law and thus is more realistic. This can be observed at the population levels when the same distributions are plotted over numerous recordings/tissues (see Figure 3.7e and f).

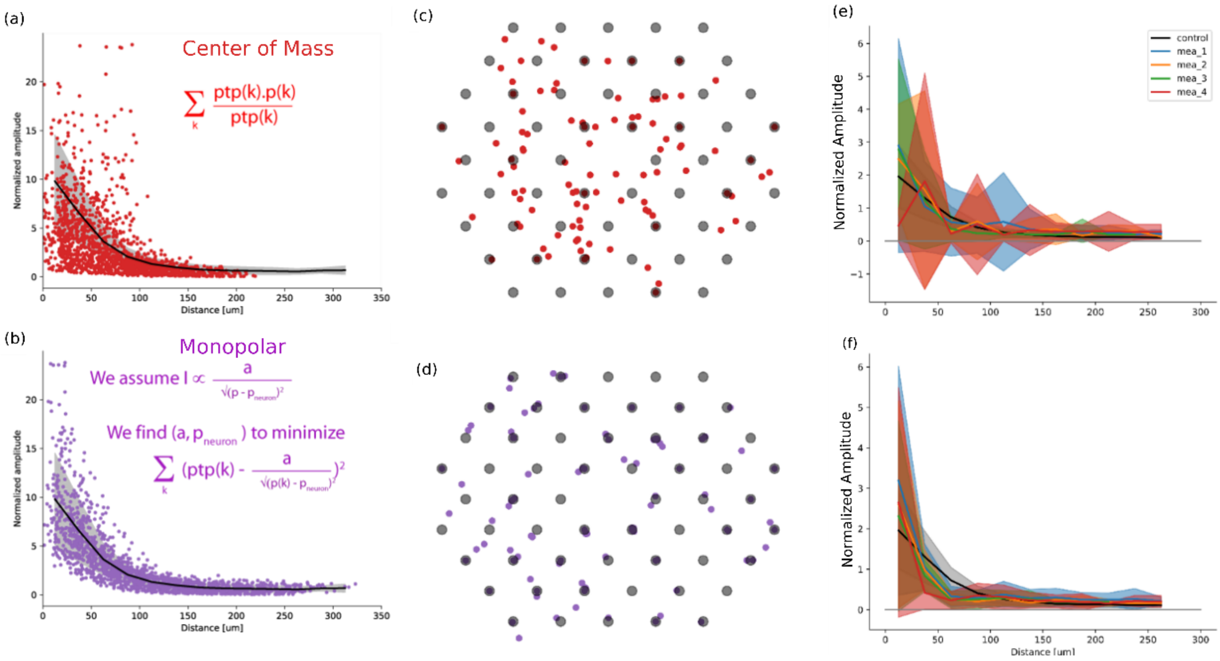

Figure 3.7 Estimation of the positions from *in vitro* recordings. (a) The layout of the MEAs, superimposed with the positions (estimated via the Center of Mass procedure) for all the templates discovered during spike sorting via Spyking-circus [78]. (b) Same as (a), but when positions are estimated via the monopolar estimation. (c) Maximum normalized amplitudes for all the MEAs templates, as a function of the distance between the cell positions when estimated via the center of Mass and the channel at which the extrema is obtained. (d) Same but when the position of the cells is estimated via a monopolar estimation. (e) Average errors between the estimated and the physical positions of the cells, when positions are estimated either via Center of Mass. (f) Same as (e) with the Monopolar estimation.

3.4.2 Validation of the positions from *in vitro* recordings

Finally, we wanted to check if the positions estimated via the monopolar estimation are good enough such that one could rely on them accurately. To test that, we used the fluorescent imaging available for all our recordings. As can be seen in Figure 3.8a, we have, for every *in vitro* recording, the estimated positions of our neurons found by spike sorting, superimposed on top of the MEA layout. Then, we also have the fluorescent images (see Methods) of all the living neurons that have been co-registered to the recording sites (see Figure 3.8b). Using a dedicated software (see Methods), we found the putative cell bodies from the fluorescent images, in order to know where real neurons are (Figure 3.8c).

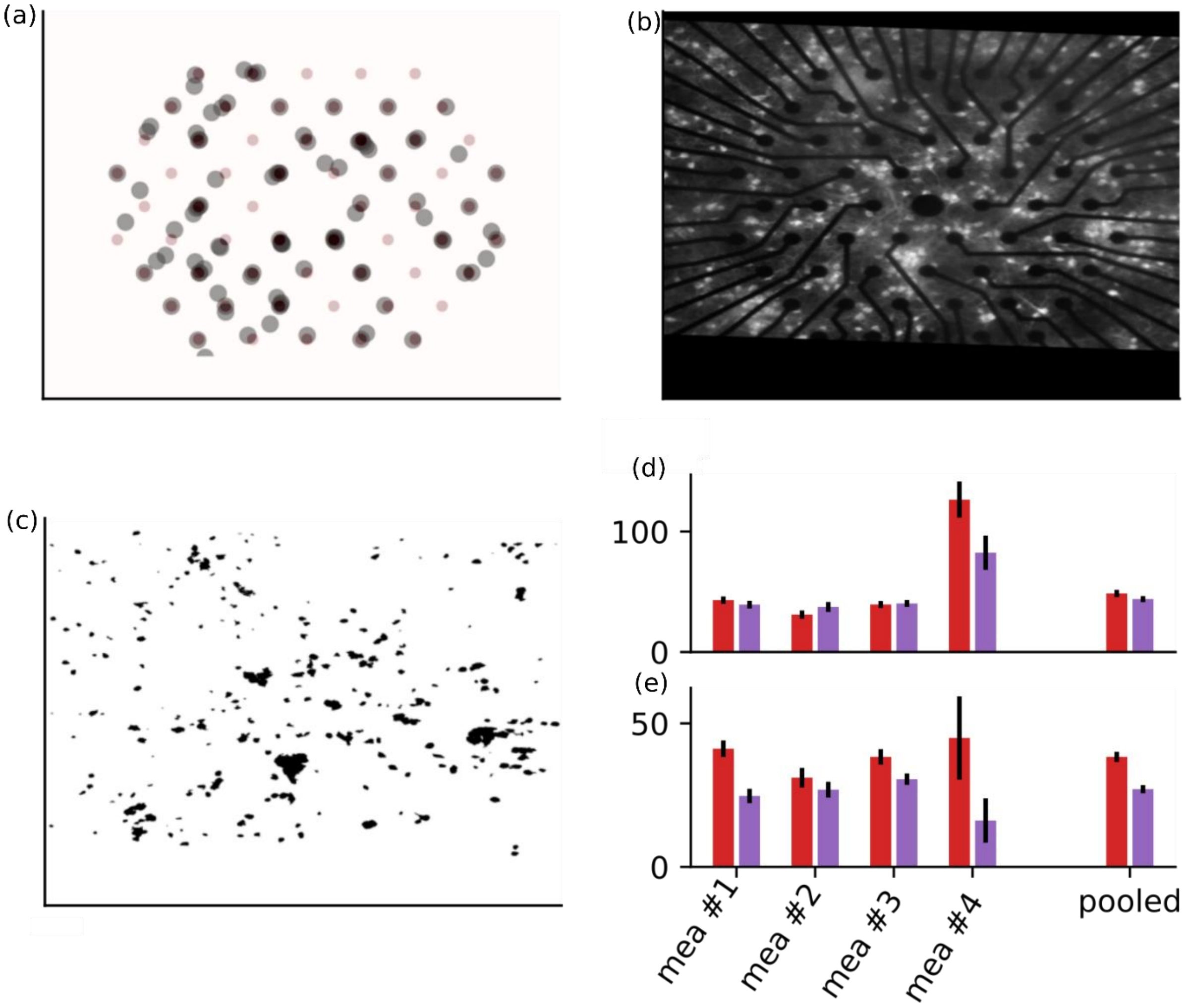

Figure 3.8 Validation of the positions from in-vitro recordings. (a) The layout of the MEAs, superimposed with the positions (estimated via the monopolar procedure) for all the templates discovered during spike sorting via Spyking-circus [78]. (b) The fluorescent image of the tissue (see Methods) co-registered to the MEA layout. (c) The cell bodies from B marked via CellPose (see Methods), to identify putative neurons in the recorded tissue. (d) Average distance (in µm) between the positions of the neurons estimated after spike sorting (either via COM (in red) or monopole (in purple)), for all individual recordings and for all pulled together. Error bars show standard deviations. (e) Same as in (d), but considering only the cells whose nearby match is less than 50 µm apart (to avoid bias of non-transparent electrodes).

Once this is achieved, we look at the probability distribution between the estimated positions of the cells and the one obtained from the fluorescent images. We iterated over all the available recordings, and with positions estimated either via the COM method or via the monopolar estimation. While we would like, ideally, to be able to directly establish a match between the estimated position of a cell and a cell body on the fluorescent images, we realized that it was impossible for several reasons. The first one is that, as we saw in Figure 3.7, even for synthetic recordings, the precision of the methods to estimate the position is only in the order of tens of microns. While at a first glimpse this number might seem pretty good (since this is the scale of the somas) it prevented us from establishing the matches: this is easy to find other cell bodies in the vicinity of our positions. In addition, because the cultures are not sparse enough, and/or the recorded neurons are not particularly tagged with particular dyes, we cannot have full certainty when it comes to identifying a match. Moreover, one other problem arose when looking at the data. Due to the opacity of the electrodes, the cells on top of them cannot be imaged (no fluorescent signal). This is problematic because, as shown in Figure 3.7a when the positions are estimated via the monopolar estimation procedure, numerous somas are close if not on top of the recording sites, which cannot be quantified. One proposed solution to solve the latter issue was performing SEM imaging to scan the neurons on top of the electrodes (not imaged by fluorescent). The idea was to superposition of the fluorescent imaging, SEM and the MEA layout superimposed with the estimated positions to target the blind spots on top of the microelectrodes (as shown in Figure 8c but also to SEM imaging). We performed SEM images by scanning all the MEAs with a square window of 400-µm side by targeting around 15 microelectrodes per image (Figure 3.9c). However, another limitation was aroused where the conductive microelectrodes are charged due to the electron beam leaving a blind spot above it (Figure 3.9a and b) after using a beam voltage of 3 kV. Although lowering this beam voltage value could solve the charging effect, image with the desired magnitude was somehow difficult. For example, as shown in Figure 9a, here is a zoomed-out image of all the microelectrodes (1 mm square) with 1 kV beam voltage without charging effect, and by increasing beam voltage to 3 kV (desired voltage for zoomed-in imaging) we can see the appearing of charging effect on top of the microelectrodes.

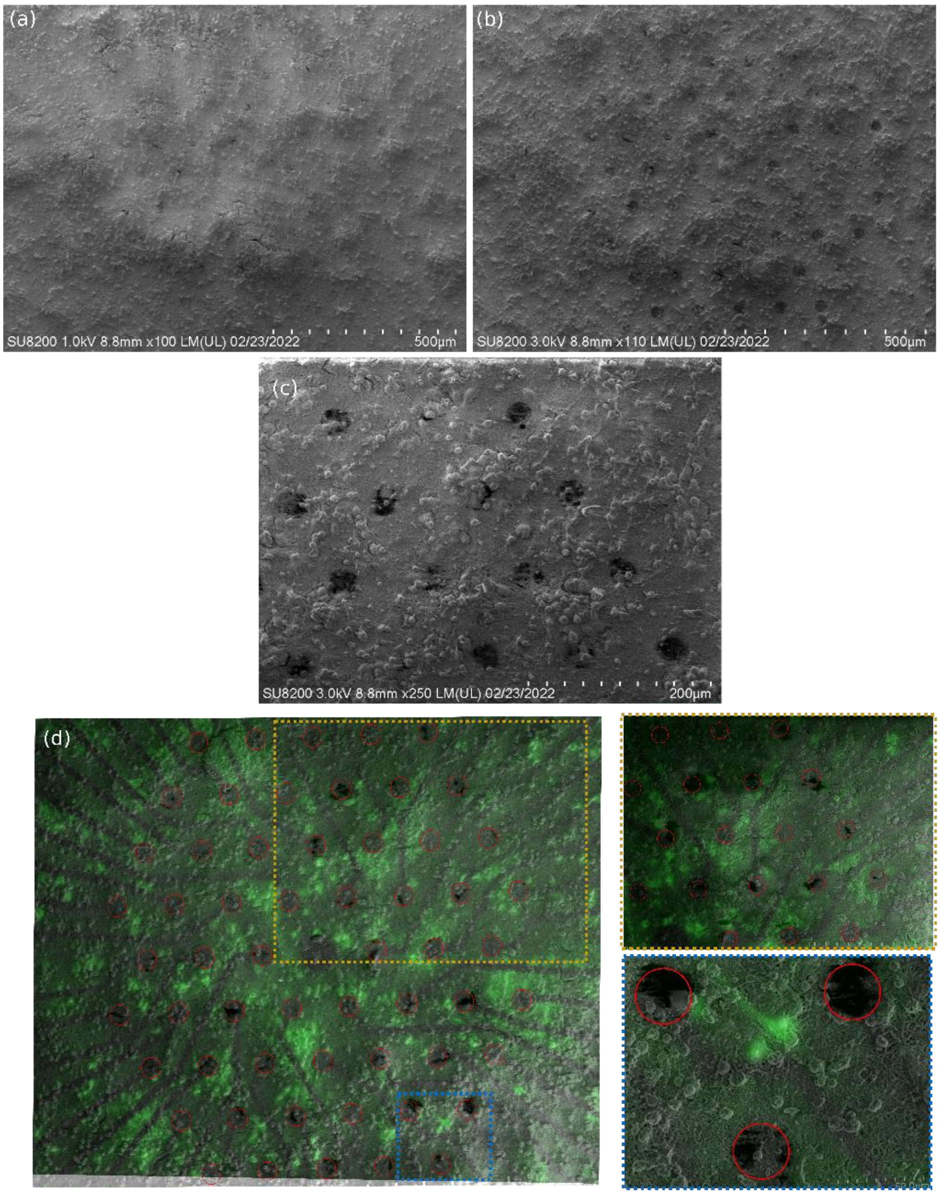

Figure 3.9 (a) SEM images of the 58 microelectrodes (zoomed-out) at 1 KV and (b) 3 KV beam voltage. (c) the zoomed-in case SEM imaging with 3 KV beam voltage. (d) Superposition of SEM and Fluorescent images. Red circles are the positions of the electrodes

Consequently, in Figure 3.8d, we naively compared the average distances between the estimated positions and the nearest cell bodies, for all recordings we had. As one can see, while the monopolar method provided slightly better results, this was not drastically different. However, this is mostly because of many "blind" neurons that can not be imaged, the method is biased towards finding matches that might be artificially far. So to compensate for this problem, we established a cut-off distance: any matches further away from that a given radius (here 50 µm) would be discarded. By doing so, we can see in Figure 3.8e that the results are much better for the monopolar estimation, with a much stronger effect. This allowed us to localize active neurons near a microelectrode with a maximum error of 25-µm from the real physical position (representation in figure 3.10). This will aid in understanding more the signal we are recording from a microelectrode: Am I recording from a neuron on top of the microelectrode? Near it? Or from far away? All of these will help us understand more the coupling between a microelectrode and a neuron. For example, going back to Maxwell equation and the neuron-electrode analogue electrical circuit, being able to estimate accurately the distance between an active neuron that we are recording and the microelectrode will help us quantify some electrical parameters, such as the most important one for recording: $R_{seal.}$ Understanding more about the functional relationship between microelectrodes and the neural network will help decoding better its electrical activity, but also will give better information about the interface that will help us while proposing new material or even new sensing technology (i.e. transistor) due to the pre-understanding of the neuron-device interaction. Comparing to similar work in literature, Aqrawe et al.[171] proposed a system records from neurons both electrically, through MEA (modified with PEDOT:PSS), and optically via voltage-sensitive dyes (VSDs) and camera (visualize the change in neuron's potential changes), and correlates between both types of recordings to test a proposed performance factor of different electrode material. Due to the correlated electrical/optical recordings, they could identify the distance between the recorded neuron and the electrode. Their performance metric is determined by the expected potential at the electrode (Using the Maxwell equation) divided by the actual recorded potential. Similar to the aim of our approach, the presented method allows for the incorporation of neuron distance from the electrode, aiming for more reliable quantification or comparison of performances. Our approach will be used as a tool to validate and compare performances of different electrode materials in *chapter IV.* Although the system proposed by Aqrawe et al. showed simultaneous optical and electrical recordings, which was not the case in our case; however, they were facing spatial challenges due to the limited magnification of the used camera. For example, several spikes were identified electrically through MEA and not optically due to different firing neurons at a distant location and not within the camera's field of view. Although our optical/electrical recordings were not simultaneous, we were able to cover all the microelectrodes and the active neural area. In addition to performance validation possibilities, our system was also used to validate spike sorting techniques, which proposed an interesting future perspective goal in the mentioned literature work.

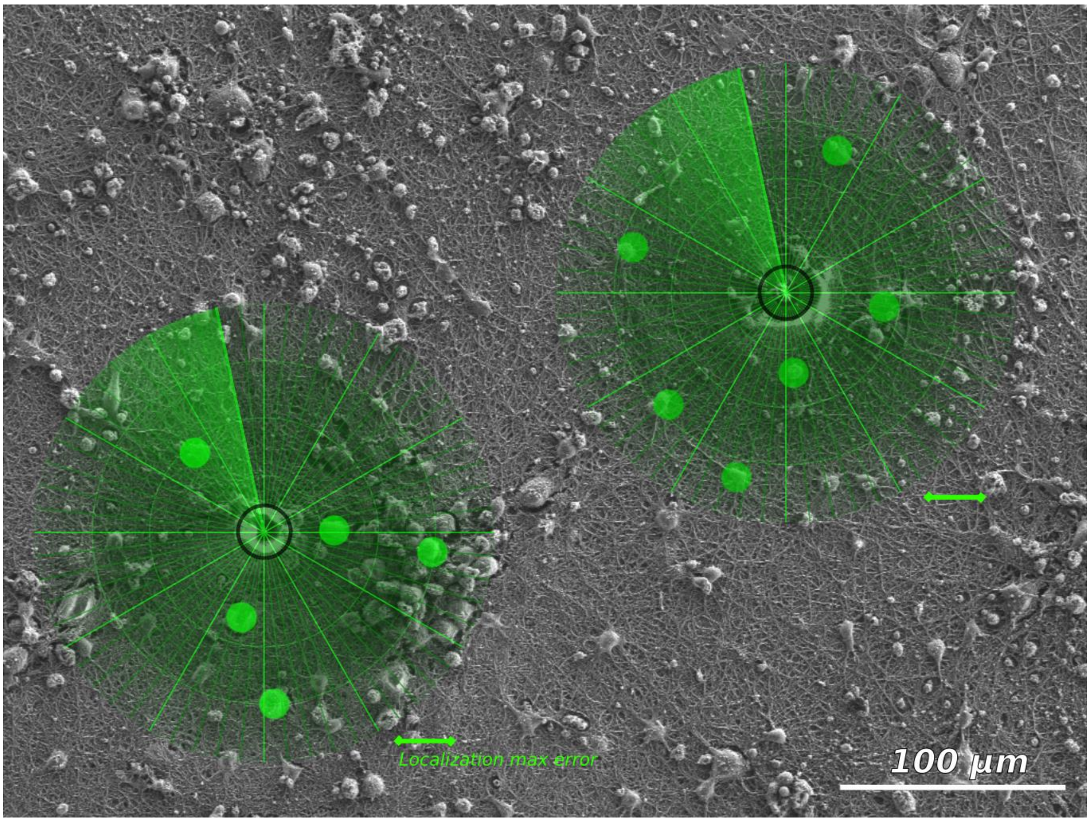

Figure 3.10 Modified and colorized SEM image as TOC figure of the work of this section

Try out experiment for future perspective: In-situ polymerization of PEDOT around neural cells

We demonstrated above how the material of the microelectrode, such as PEDOT enhances the quality of the recordings positively. This is due to the enhancement of the neuron-electrode interface coupling. In 2006, David C. Martin and his colleagues launched the idea of electropolymerizing *in-situ* PEDOT around neuronal living cells *in vivo* [172,173] and *in vitro* [153] (Figure 3.11). The idea behind that is to engulf neurons by the conducting polymer that increases the contact surface area between electrode and neuron with PEDOT, which will theoretically be supposed to enhance the coupling (increase seal resistance) greatly. For the *in vitro* experiments [153], they were able to demonstrate the process of polymerizing PEDOT around neuron cells. They mainly investigated the cytotoxicity of the monomer, the effect of polymerization on the cell plasma membrane of the neuron, and the effect of the process on the electrical parameters of the electrode (impedance). For the *in vivo* experiments, they show that with post-polymerization they maintained lower impedance and lower RMS noise values of LFP recordings from rat brains [172]. In another study, they showed that this polymerization around the living neuronal tissue does not negatively affect the performance of the hippocampal function (performance of the delayed alternation (DA) task) [173]. In their *in vitro* work, they performed the process on macroscale electrodes demonstrating cell attracting, biomimetic, neuron-template coating [153]. However, the extent to which this new process can be used on commercial-like MEA chips and its effect on the electrical recordings of neurons *in vitro* remains unexplored.

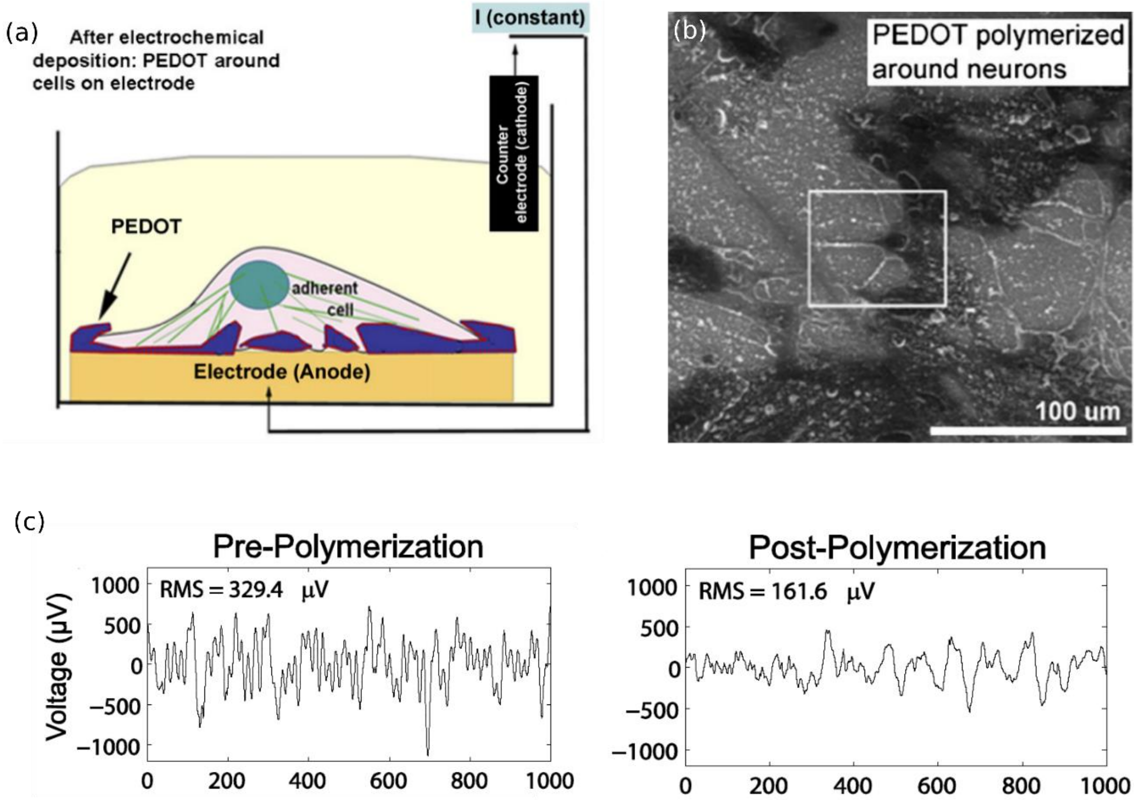

Figure 3.11 In situ electropolymerization around neurons examples from literature (David Martin group work). (a) Schematic representing PEDOT polymerized around living cell [153]. (b) SEM image showing PEDOT polymerized in the presence of neurons [153]. (c) LFP recorded *in vivo* from an electrode Pre-polymerization and Post-polymerization showing the decrease in the noise RMS value after polymerization [172].

During my thesis work, the idea was to try this process on our MEAs and check the effect of engulfing neurons on the *in-vitro* extracellular performance of a microelectrode. Firstly, we wanted to check the possibility of electropolymerizing while mixing the EDOT with PBS (ionic media). To do so, we performed *in-situ* electrochemical impedance spectroscopy (EIS) during the potentiodynamic electropolymerization experiment. This allowed us to show the possibility of the process in PBS and then identify the oxidation potential. Starting with 1:5 (EDOT : PBS) volume ratio of the solution, with an oxidation voltage less than or equal to 1V (for not killing the cells) no electropolymerization occurs until reaching 1:2 ratio (i.e. 200 µL EDOT + 400µL PBS) (Figure 3.12a). As shown in Figure 3.12a, using this ratio, after exceeding V_{IN} of 1V, the Bode's modulus graph shows a gradual decrease of the impedance modulus of the electrode, suggesting an incremental growth of the conducting monomer on top of the gold surface. This was supported by appearing a light blue color on top of the gold microelectrode. Suggesting oxidation potential equals 1V, we performed potentiostatic electropolymerization with V_{IN} = 1V. As we can see in Figure 3.12b to reach the maximum coating possible (no decrease in |Z|), it took around 500 seconds which is relatively long. Although the reduction of impedance was not significant (suggesting a lower amount of deposited material), however, it gives ineligible preliminary results showing the ability of electropolymerizing in salty aqueous environments. In real biological experiments, the electrolyte is filled with cell culture medium (see Methods) and not only saline solution (PBS). Usually, cell culture medium is a solution that contains optimized mixtures of nutrients, salts, proteins and vitamins to support primary neural cell and neuronal cultures. We tried to perform electropolymerization while mixing EDOT with the cell culture medium. In our MEAs, the well (molded glass ring) fits a volume of a maximum 1.2 mL. The volume of cell culture used during *in-vitro* cell culture and recording is 1 mL (see Methods). Hence, in order to not affect the cell culture protocol, at the first step we tried to perform electropolymerization after adding just 200 µL of EDOT for not exceeding 1.2 mL volume of the well (1:5 ratio). As shown in Figure 3.12c, we monitored a decrease in the impedance bode plot after exceeding 1.35 V input voltage. This may suggest the ability of electropolymerization, paving the way for exploring this technique more and conducting it with electrical recordings from microelectrodes.

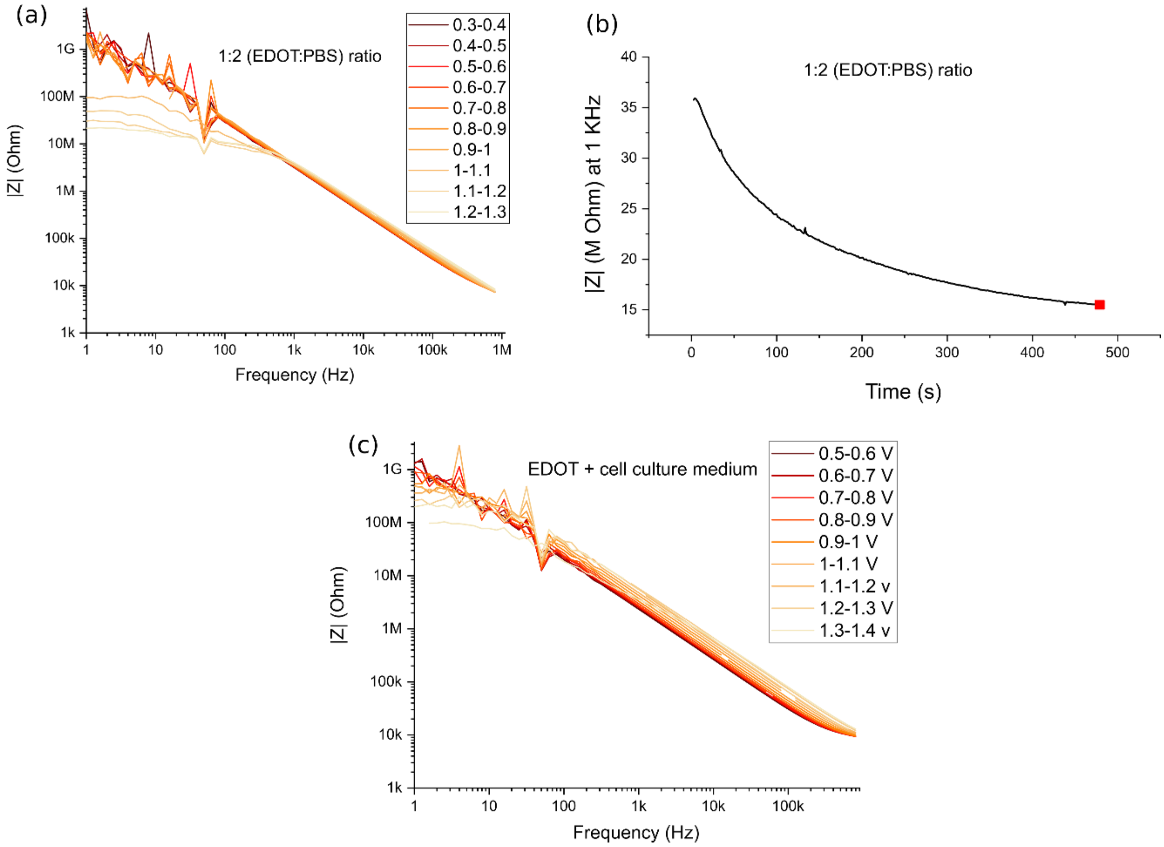

Figure 3.12 (a) Bode's diagram graph for in-situ electrochemical impedance spectroscopy (EIS) during the potentiodynamic electropolymerization experiment of the electrodes in presence of 1:2 EDOT:PBS ratio as an electrolyte. (b) graph showing the impedance value of and electrode at 1 KHz while performing potentiostatic electropolymerization with 1:2 (EDOT:PBS) ratio as an electrolyte. (c) is same as (a) but with electrolyte contains the mix between EDOT and cell culture medium.

To continue this study, we should overcome some limitations by these proposed steps:

- Study the toxicity of the different monomers and other additives with different mixing ratios within the cell culture medium.
- Find an optimum ratio where we can electropolymerize with a voltage equal to or less than 1 V and still not cytotoxic to neurons.
- Implement a technical setup where we can add monomer during recording, electropolymerize, and then recycle the electrolyte with a new cell culture medium to maintain a better biocompatible environment for long-term recordings. The schematic shown in Figure 3.13 could be a proposed setup for this future experiment. As shown in the schematic, the inlet of new cell culture medium is to add a add cell culture medium, the pipet is to add EDOT solution into the electrolyte, and after electropolymerization experiment we can recycle the medium that contain

cell culture medium mixed with EDOT and finally we can insert through the inlet again fresh cell culture medium.

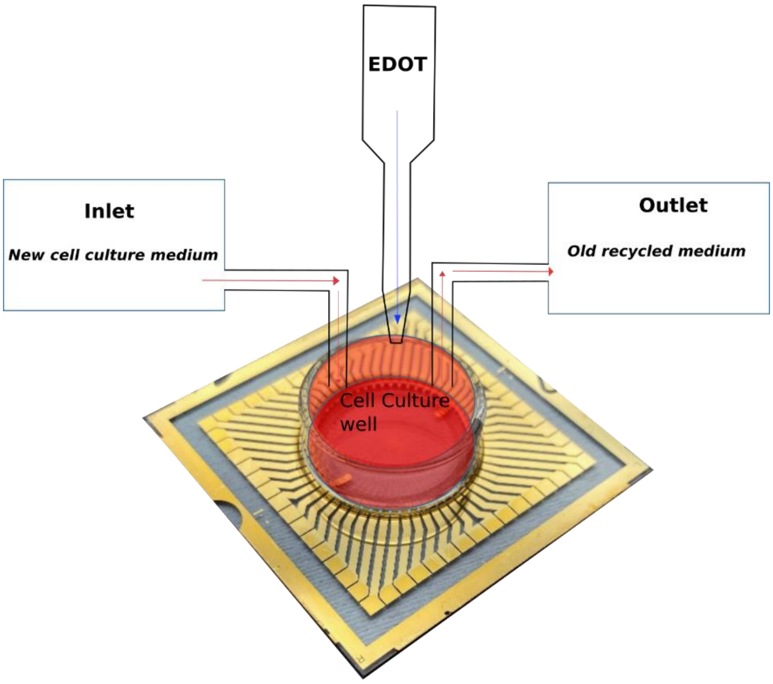

Figure 3.13 A schematic showing the proposed setup for in situ electropolymerization with neurons on top

Engulfing neurons or *in situ* electropolymerization with conductive polymers would open interesting opportunities for both *in vivo* and *in vitro* applications. For 2D cell culture, it can be used to connect « on demand » two disconnected 2D neuronal networks by appropriate electrical pulses, employed as a bidirectional bridging, which can be used in the future to reinforce neural connectivity. In our project, we worked on growing artificial dendritic structures by electropolymerization for 3D neuromorphic engineering that were able to mimic biological neural networks [154]. Exploring the possibility of growing these polymeric dendrites *in situ* would open great possibilities to replace the activity of a biological neural module with a real-time artificial hardware neuromorphic neural network that can be dedicated to neuromorphic prosthesis applications[20], for example. For *in vivo* applications, this technique could be used as a tool to repair some brain tissue, to reconnect some cut sections in specific nerves. Neural regeneration after lesions is still limited by several factors and new technologies are developed to address this issue. With further development and future work, this technique could be dedicated for axonal regeneration across a nerve gap through growing PEDOT:PSS *in situ* and on demand by using passive microelectrodes, simultaneously with functional analysis, comprising electrophysiological tests and through these microelectrodes to validate any enhancement in the electrical activity in parallel. At the bio-nano interface level, this technique will strengthen the adhesion between the neuron and the microelectrode by increasing its contact area, which could lead to superior performances for both *in vivo* and *in vitro* applications.

3.5 Conclusion

In this work, we explored the possibility of properly estimating the positions of cell bodies in neuronal cultures when extracellular recordings are performed via PEDOT-coated multi-electrode arrays. Being able to estimate accurately enough the positions of the somas from the extracellular signals might open new possibilities in order to better understand the relationships between functional responses and morphologies of the cells. Firstly, we showed that using PEDOT coating compared to gold led to a better signal-to-noise ratio on the recording channels, and to more cells that could be spike sorted in the vicinity of these channels. Secondly, we showed that by using these low-noise recordings for spike sorting, i.e. to isolate and detect the activity of individual neurons, we could use a monopolar approximation to estimate, from the extracellular waveforms triggered on the recording devices, the putative positions of the cells. Assuming cells were behaving as monopoles allowed us to get biologically plausible positions that seem to be more in line with the real positions of the cells. This result was verified with 2D cell cultures where the physical positions of the fluorescent cells were compared to the estimated positions.

Chapter IV. Electro-co-Polymerization of side chain engineered Electro-Active Polymer on Micro-Electrode-Arrays and Spike-Throughputs Assessment on a Neural Culture

4.1 Introduction.

In order to improve the neuron-electrode interface, there is a great effort to add an increased bio functionality property of PEDOT:PSS. Such additives can include proteins and peptides to direct aon growth and encourage the adhesion of cells on the microelectrode. As the electrochemical impedance of such micro-electrodes is governed by the accumulation profile of the ionic space-charge on the electrode electroactive coating, controlling the iono-molecular interaction at the electrolyte/electrode interface is crucial for optimal signal transduction. As cations are responsible for the doping level modulation of PEDOT-coated microelectrode, tuning the conducting polymer's chemistry according to the molecular affinity of alkali cations to the polymer backbone is necessary for optimizing the transduction. Another effective method to improve the biocompatibility properties of PEDOT films is to perform lateral side chain engineering of PEDOT by the inclusion of hydrophilic molecules. One example was the use of EDOT-acid (carboxylic-acide substituted EDOT monomer) to create EDOT/EDOT-acid copolymers with systematic variations in surface wetting (Figure 4.1a) [174]. Reynolds and Martin [175,176] were the first to use side chain engineering technique of PEDOT for coating microelectrodes in neural interface applications. In their work, a hydroxyethyl group (EDOT-MeOH)[175] and sulfonatoalkoxy group (S-EDOT)[176] (Figure 4.1b) were added as side chain to the EDOT, resulting in a polar monomer with higher solubility in water. The enhanced water solubility of EDOT-MeOH allowed deposit PEDOT-MeOH: nonapeptide CDPGYIGSR from aqueous solutions without introducing aqoues solution [175] (Figure 4.1c). A follow-up work continued this study and showed more growth of SH-SY5Y cell line grew on nonapeptide CDPGYIGSR compared to uncoated gold electrodes [177].

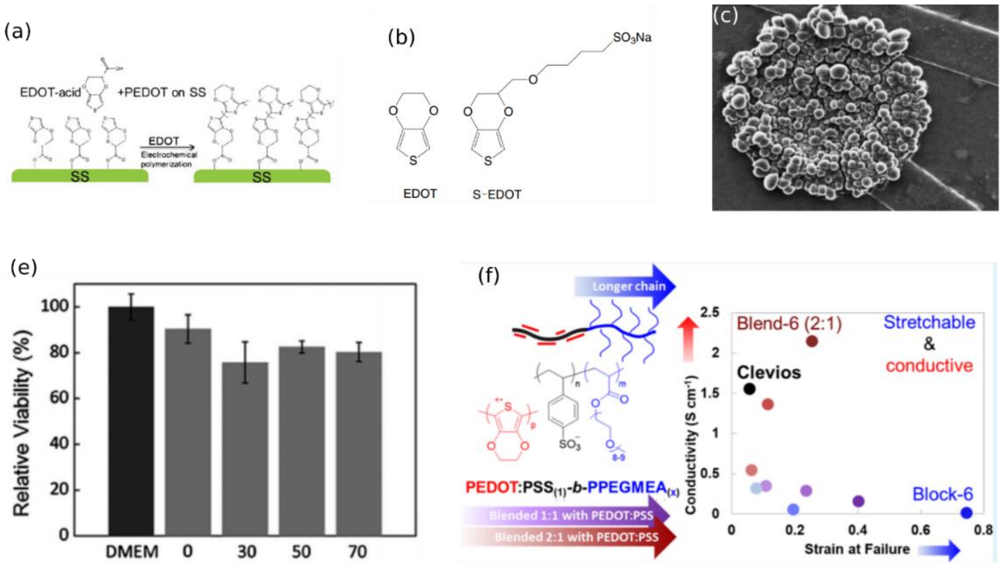

Figure 4.1 (a) Schematic of EDOT/EDOT-acid copolymers for systematic variations in surface wetting [174]. (b) Chemical structure of EDOT and s-EDOT (we can see the lateral side chain) [176]. (c) Microelectrode with deposited PEDOT-MeOH: nonapeptide CDPGYIGSR [175]. (d) Histogram showing the cell viability on top of different PEG concentration. This result shows the good biocompatibility of PEG [174] (DMEM : Dulbecco's Modified Eagle Medium). (f) Addition of PEG to PEDOT yielded in improving conductivity [178]. (Clevios: trade mark of PEDOT:PSS formulation. PPEGMEA: poly(poly(ethylene glycol) methyl ether acrylate)

In this way, the use of polyethylene glycol (PEG)-like molecules has been shown as an efficient approach towards the formation of biocompatible PEDOT films. For instance, the incorporation of fluorescent proteins onto the functionalized PEDOT films via carboxyl moieties of PEG(COOH) enhanced its biocompatibility [174]. Further, adding PEG to PEDOT improved conductivity, making it an interesting material as channel material for organic transistors [179] (Figure 4.1f). Interestingly, much effort has been made in this direction of functionalizing polythiophenes with oligoethylene glycol (OEG) side chains to increase the polymer affinity with cations [175,178]. This strategy has demonstrated great promises to enhance the hydrophilicity of neutral polythiophenes and promote cation penetrations to modulate the doping level in the material [179]. Although the lateral side chain (i.e. OEG) approach showed efficient results in engineering PEDOT for better biofunctionality performances, the extent to which these interfaces can help microelectrodes in extracellular recording applications remains unexplored.

Here, we investigate on electro-co-polymerization of EDOT with its triglymated derivative to control valence between monomer units and hydrophilic functions on a conducting polymer (Figure 4.2). Due to its additional hydrophilicity property, the rationale behind using this lateral side chain in our work is to enhance the affinity (R_{seal}) between the microelectrode and neurons and thus positively affecting the quality of the recording. It is worth mentioning that here the role of oligo ethylene glycol as a side-chain is significantly different to the one of ethylene glycol introduced as co-solvent for the formulation of wet-processable PEDOT:PSS aqueous suspensions. In case of electro-*co*-polymerization, oligoethers are not introduced as a flocculent to segregate high conductivity PEDOT-rich domains from the insulating PSS dopant to promote materials conductivity. Instead, in our approach, oligoether side chains are covalently bound to each PEDOT chain and promote cation conductivity all along it, which does not directly promote PEDOT’s electrical conductivity, *a priori*. Our chemically glycolated EDOT monomer has been synthesized (see Methods chapter) choosing 3 ethylene glycol unit (EDOT-g_4) instead of any longer or shorter chains as it shows the optimum value for better solubility and more favorable microstructure as reported lately [180]. Moser et al. [180] reported that while minimizing the ethylene glycol side chain length appears to boost both the capacitive and charge carrier transport properties of the polymers, the chosen ethylene glycol side chain length must be kept sufficiently long to induce solubility for processing, and allow for the necessary ion interactions with the conjugated polymer backbone.

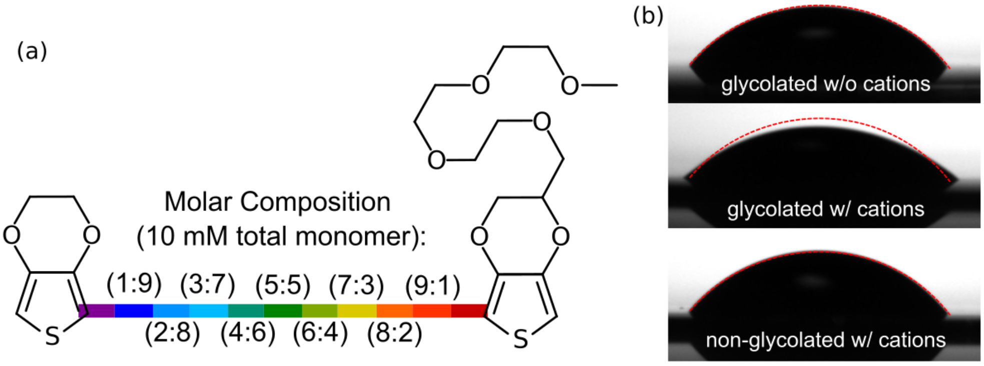

Figure 4.2 Electro-co-Polymerization of EDOT and its (Triglymated) OEG Derivative and Stability Assessment. (a) Schematic showing the chemical structure of EDOT and glycolated-EDOT (different ratios of EDOT and triglymated EDOT formulated and used in this study). (b) Water contact angle measurement of 5:5 EDOT-g$_4$ (top and middle) or non-glycolated (0:10 – bottom) electropolymerized gold coverslips, wetting a drop of either deionized water (top) or 100 mM NaCl (middle and bottom).

Thanks to electropolymerization technique, we were able to fine tune the glycolation of the polymer by mixing different volume ratios of EDOT with EDOT-g$_4$ in the electrolyte (Figure 4.2a). While performing voltage ramp impedance spectroscopy on gold microelectrodes with different ratio of monomers, we observed that the impedance modulus at 1 kHz of the electrodes stays low only if less than 80% of the hydrophilic EDOT-g$_4$ monomer is introduced in the electrolyte. That is, the contribution of the conducting polymer glycolation on the cation affinity can favor either interchains interactions in the conducting polymer (low glycolation) or intrachain interactions that promotes dissolving polythiophene chains in the water-based electrolyte [180]. Accordingly, we continue our work by not exceeding 70% of EDOT-g$_4$ monomer introduced in the electrolyte such that it still can maintain its hydrophilic property without dissolving in water.

Table 4.1 Static water contact angle static measurement on electro-co-polymerized surfaces from electrolytes containing different ratios of EDOT and EDOT-g$_4$ monomers

	EDOT (0:10)	**Glycolated (3:7)**	**Glycolated (5:5)**	**Glycolated (7:3)**
Deionized water	50°	50°	58°	55°
100 mM NaCl$_{(aq)}$	52°	55°	39°	39°

Impacts of such ion affinity with the polymer side-chains has been characterized by water contact angle measurements on surfaces containing glycol-free ePEDOT and glycolated-ePEDOT deposited on cover-slips gold surfaces (see Figure 4.2b and Table 4.1). In the case of electropolymerization of EDOT, water contact angle values equal 51°±1° in both cases for deionized water and for 100 mM NaCl$_{(aq)}$. However, when oligo ethers are grafted to the conducting polymer by mean of electro-co-polymerization of EDOT with EDOT-g$_4$, the water contact angle on the electropolymerized surface depends on both the monomer glycolation ratio (in each case, concentration of monomer units in the electrolyte is equal, under the same electrochemical conditions) and on whether the water drop contains the alkali electrolyte or not.

With the presence of $NaCl_{(aq)}$, the water contact angle on a glycolated conducting polymer tends to diminish from 54°±4° down to 39°, suggesting that the presence of sodium cations tends to increase the hydrophilicity of the conducting polymer, exclusively in cases EDOT-g_4/EDOT ratio is sufficiently high (Table 4.1 shows no noticeable effect in the case of 30% EDOT-g_4). To explain, the PEG chains are embedded within the PEDOT film in the dry state and even after deionized water droplet deposition. In the presence of the cations (Na^+), the side chain of the glycolated PEDOT material comes out, leading to a decrease of the water contact angle and, thus, to a better electrolyte infiltration within the film (better swelling behaviour).

Material hydrophilicity is known to have a reflection on cellular attachment and activity, and static water contact angle study is a useful evaluation to predict cell interaction with the substrate. Several studies showed that enhancing the hydrophilicity of the electrode's material will enhance or promote cell growth [169,181,182], highlighting a very interesting advantage of the EDOT-g_4 material for *in vitro* extracellular recordings from neurons.

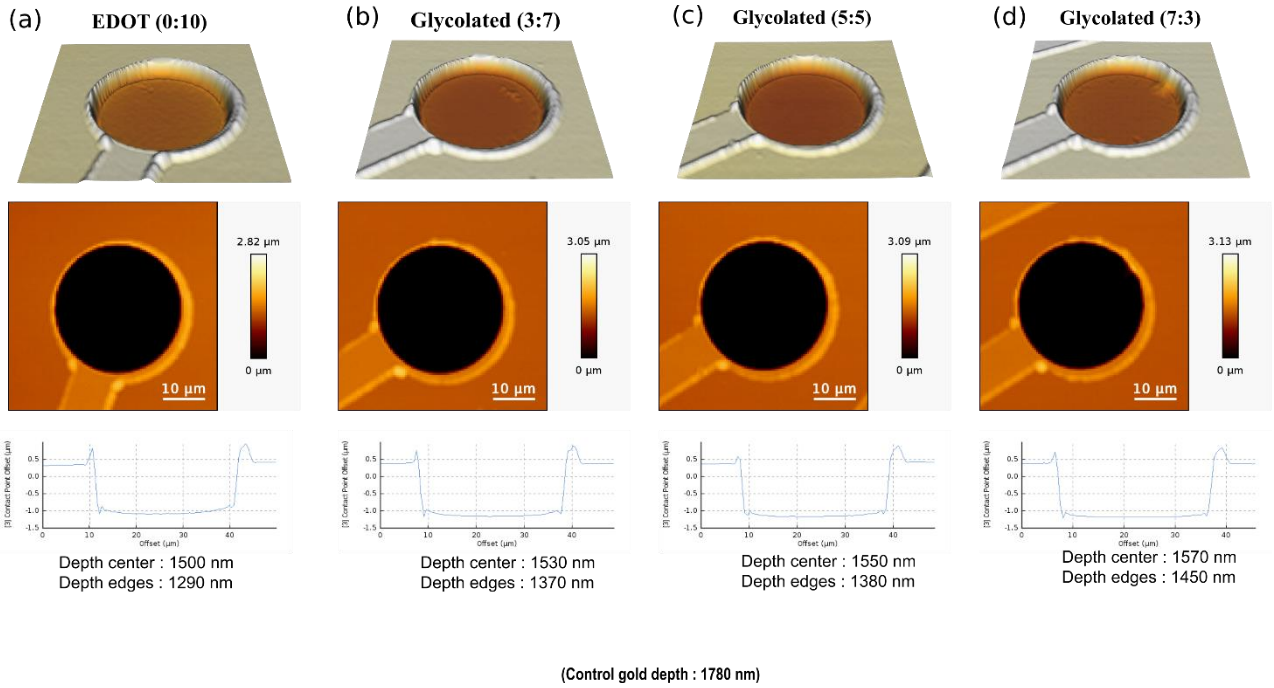

Figure 4.3 (a) Topography and profilometry experiments of a micro-electrode coated with (a) ePEDOT, (b) glycolated ePEDOT (3:7), (c) glycolated ePEDOT (5:5) and glycolated ePEDOT (7:3) at 1.4 V_{DC} for 8 seconds, recorded by Atomic Force Microscopy (AFM) in Phosphate Buffer Saline (PBS). Control depth of gold microelectrode: 1780 nm. This control will be used to calculate the thickness of each material (Table 4.2).

Our study is focused on coating the gold micro-electrodes with a chemically functionalized thin film glycolated-ePEDOT material to enhance its neuronal interface performances. However, this work was not dedicated to explore an additional 3D morphological optimization procedure by electropolymerizing thick bulk material that can form a 3D shape above the microelectrode's passivation layer (parylene C). Therefore, the electropolymerized materials were deposited by a correlation between voltage and time applied for forming a thin film coating on top of the gold micro-electrode with the same potentiostat electropolymerization parameters performed in the previous chapter. One hypothesis could be that it is not sure if the EDOT/EDOT-g_4 volume mixing ratio in the electrolyte would be the exact ratio in the electropolymerized film. However, the glycolation of EDOT did not alter the electropolymerization technique parameters, such that electropolymerization was done successfully with the same V_{IN} voltage used for pure EDOT . This highlight the fact that they still have the same physiochemical properties even with the maximum glycolation ratio.

Table 4.2 Thickness measurements extracted from the AFM and topography images in Figure 4.3 for the different electropolymerized materials

	EDOT (0:10)	**Glycolated (3:7)**	**Glycolated (5:5)**	**Glycolated (7:3)**
Center thickness (nm)	280	250	230	210
Edge thickness (nm)	480	410	400	330

Figure 4.3a shows the height profiles image recorded by Atomic Force Microscopy (AFM) in PBS for a microelectrode of ePEDOT, (3:7) glycolated-ePEDOT, (5:5) glycolated-ePEDOT and (7:3) glycolated-ePEDOT at 1.4 V_{DC} for 8 seconds. The topography analysis of the coated microelectrode (Figure 4.3 and Table 4.2) evidenced non-flat topographies for the coatings, with different thicknesses at the center from at the edges of the opening. Looking at Table 4.2, there was no huge relative significant difference in the thickness of pure EDOT glycolated EDOT with the same electropolymerization voltage and time. Interestingly, the surface tends to be flatter with glycolation, such that the difference between the edge and center thickness decreases with the increase of glycolation, assuming a more homogenous deposition with the presence of OEG in the electrolyte.

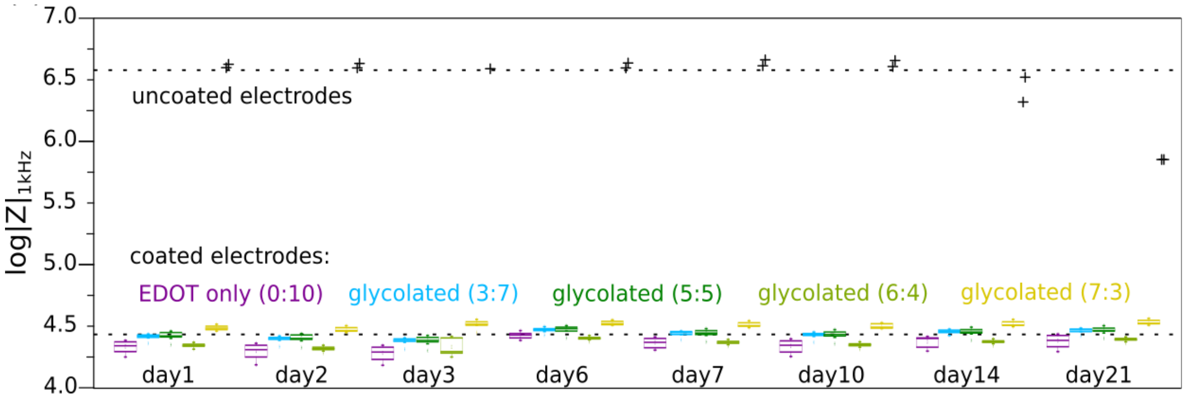

Figure 4.4 Log impedance modulus variation over incubation time in PBS at 40±2°C of micro-electrodes (10 electrodes per box), coated with different glycolated polymers, showing substantial impedance stability over 21 days of incubation (This measurement done by Najami Ghoudbane and co-supervised by me).

As the electrochemical growth on micro-electrodes does not lead to stable coating in cases >70% EDOT-g_4 observed *in operando* via voltage ramped impedance spectroscopy, we investigated the long-term stability of lower glycolated electrodes in a phosphated buffer or PBS (see Figure 4.4). One micro-electrode array with 60 electrodes individually electro-*co*-polymerized at five different ratios of EDOT/EDOT-g_4 monomers was immersed in 1×PBS for 21 days in a sealed chamber at 40±2°C. The five populations of 10 microelectrodes show remarkable stability over the days in the impedance modulus at 1 kHz measured in medium, compared to uncoated microelectrodes on the same MEA.

Thanks to this bottom-up strategy, local surface modification on each individual electrode allowed us investigating properties of different materials on a same substrate experiencing exactly the same environmental stresses. This is a key advantage for material engineering to establish structure property relationships that are not biased by the environment variability nor experimental reproducibility. The lack of impedance drift over 21 days shows that, up to 70% of EDOT-g_4, the electro-*co*-polymerization of EDOT and EDOT-g_4 leads to stable coating on a MEA for incubation till DIV21. Here, we presented a new chemically synthesized polymer showing interesting characteristics in hydrophilicity which is a key parameter for better adhesion with neurons. Additionally, we showed that these materials, when deposited on microelectrodes seem to be stable after incubation which makes it an interesting material to investigate its morphological characterization and validate its performances for extracellular recordings from neurons.

4.2 Material and surface Characterization of Glycolated-PEDOT:PSS and impact on micro-Electrodes.

As explained previously, the degree of the EDOT glycolation is a compromise between its interchain interactions and its stability (hydrophobic backbone suspension in water). The glycolated ePEDOT materials revealed higher hydrophilicity in ionic water and five different ratios of electro-co-polymerized EDOT/EDOT-g_4 monomers on microelectrodes showed stability in water. Hence, quantifying the degree of glycolation and getting more insight about the surface and material characteristics of each material is essential.

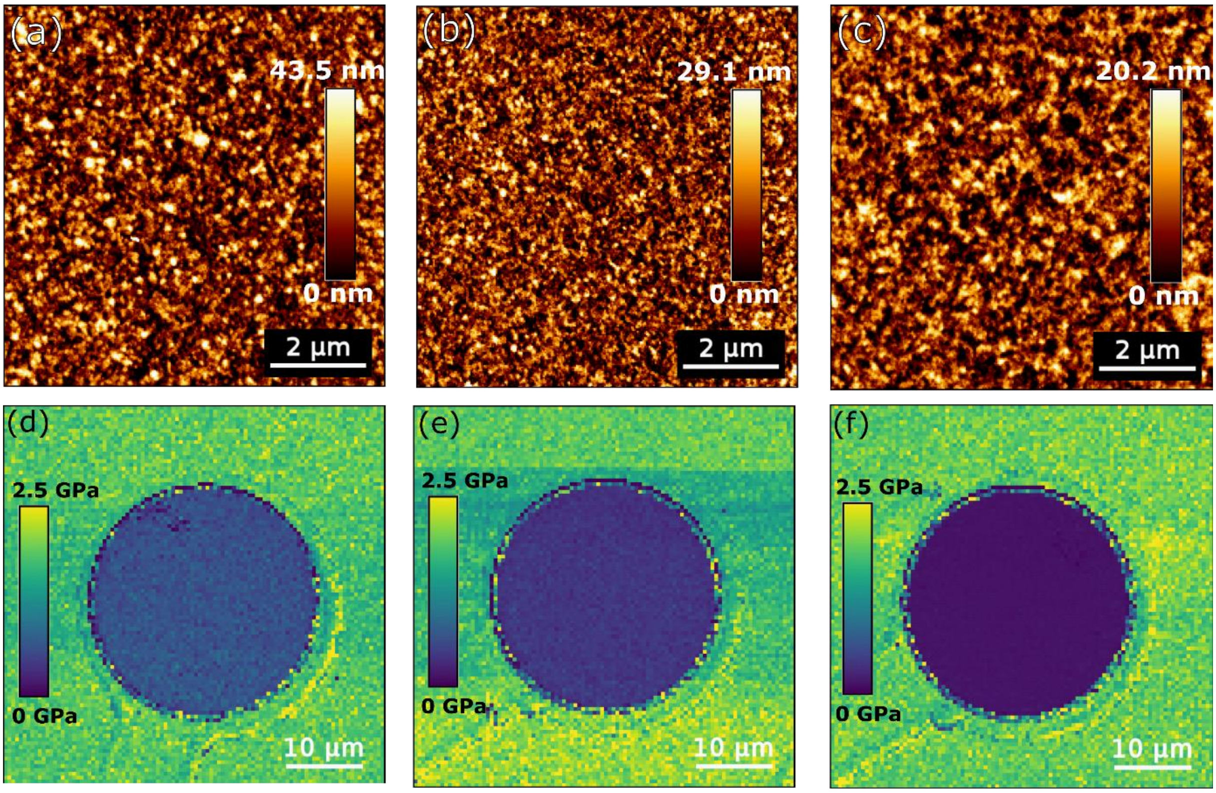

Figure 4.5 Microscaled topographies for micro-electrodes coated with different ePEDOT: unglycolated (a), 5:5-glycolated (b) and 7:3-glycolated (c), recorded by AFM in PBS. (d-f), Local Young modulus for micro-electrodes coated with different ePEDOT: unglycolated (d), 5:5-glycolated (e) and 7:3-glycolated (f), recorded by AFM in PBS, evidencing different stiffness with the glycolation degree.

To investigate the morphology of these materials, performing AFM experiment in liquid phase for the different coated microelectrodes, will give us better insight on their morphological properties. Figure 4.5a-c shows the AFM topography images of the ePEDOT unglycolated, 5:5-glycolated and 7:3-glycolated microelectrodes. Young modulus (elasticity) images for the same materials were also measured (Figure 4.5d-f). Statistical analysis of these AFM images revealed the surface roughness and elasticity of these materials. Correspondingly, the AFM height images showed a gradual decrease of the surface average roughness with glycolation from 9.9 nm for ePEDOT down to 6.6 nm and 4.6 nm for the 5:5-glycolated and 7:3-glycolated ePEDOT, respectively. Moreover, the Young modulus AFM images show a decrease from 651 ± 77 MPa for ePEDOT to 408 ± 42 MPa and 135 ± 9 MPa for the hemiglycolated and 70:30-glycolated ePEDOT, respectively. The polymer tends to be more elastic (soft) gradually with the degree of glycolation which makes the electrode mechanically closer to the Young modulus of the living tissue (1-100 kPa) [46].

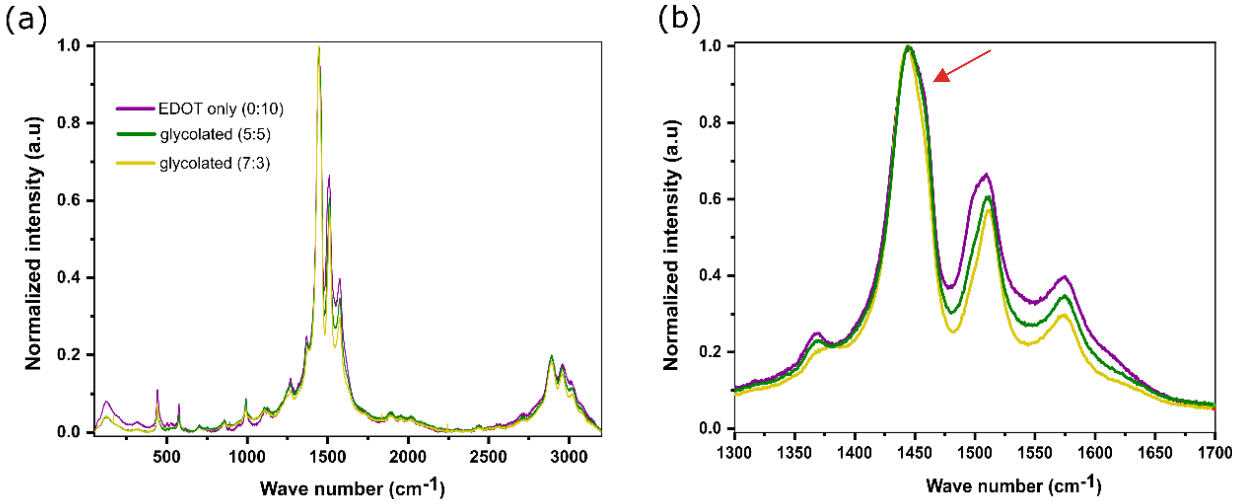

Figure 4.6 (a) μ-Raman spectra (λexc = 477 nm) on electropolymerized micro-electrodes, evidencing different inter-macromolecular packing for the polymer chains with different glycolation. (b) displays the region between 1300 and 1700 cm-1).

To correlate the AFM imaging results with the morphological characterization of our electrodes, we present in Figure 4.6 the Raman spectra of ePEDOT: unglycolated, 5:5-glycolated and 7:3-glycolated microelectrodes on a same MEA. The bands assignment is presented in Table 4.3. The PEDOT:PSS spectrum was comparable to the one's shown in the literature [123]. The monotonic changes in the glycolated EDOT spectra appeared with the increase of the concentration of OEG which indicates both (i) the integration of OEG in the PEDOT:PSS and (ii) the correlation between the concentration of OEG and the changes in the spectra, and thus the overall modification of the material. For the most intense peak at 1444 cm^{-1}, assigned to $C_α$=$C_β$ symmetric vibrations, we noticed a narrower peak for higher concentration of OEG (~20% smaller FWHM for the glycolated (7:3)) EDOT compared to unglycolated ePEDOT). Moreover, the shoulder at 1455 cm^{-1} for the PEDOT:PSS curve disappeared gradually with higher concentration of OEG (red arrow in Figure 4.6b). A lower intensity and broader peak at 1366 cm^{-1} ($C_β$–$C_β$ stretching vibrations) was also observed. It is well known that both benzoid and quinoid tautomeric structures exist in PEDOT:PSS films [183]. Here, the changes appearing while increasing the concentration of OEG indicated the formation of higher concentration of quinoid structures in the polymer films (linear conformation of structure). Linear structure suggested that the two EDOT rings were almost in the same plane which in turn implied that it was easier to delocalize the π-electrons. Additionally, the additive glycol in the liquid state may give space for the reorientation of the polymer chains. Furthermore, we observed a monotonic decrease in the C-H vibration intensity in the region of 2700-3200 cm^{-1}. In previous studies the intensity of the ratios $I_{2887/2957}$ was found to be sensitive to the intermolecular interactions [184] . In our measurements, this ratio decreased around 10% while adding OEG, alongside with the disappearance of the peak at 1126 cm^{-1} ($C_β$-H Band). This result suggested a reduce intermolecular interaction for glycolated (7:3) EDOT compared to pure PEDOT:PSS. Accordingly, from all these measurements, we can reveal that on the one hand, we have modification in the organization and the conformation of the polymer and on the second hand, we expect to have a more relaxed film and softer material with the degree of glycolation. The softness of glycolated ePEDOT enhances the adhesion between the neuron/electrode interface thus establishing better conformal interaction between the neuron and the electrode. Concsequently, this will increase R_{seal} due to the neuron-electrode affinity improvement which is the crucial point for better electrical signal transmission [14,29].

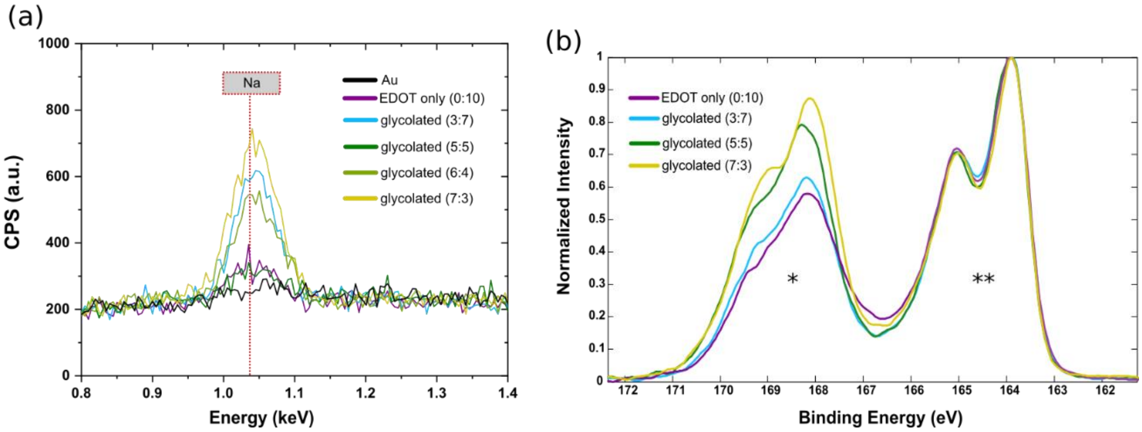

Figure 4.7 (a) EDX analysis of different electropolymerized micro-electrodes on a same MEA, after dipping in NaCl aqueous solution, where different Na^+ retention is evidenced on the different glycolated polymer electrodes (sodium peak marked by the red line). (b) High resolution XPS S_{2P} spectra obtainedon different electropolymerized polymers that evidences PSS^- moiety evolution while introducing glycolated EDOT PSS S_{2p}peaks are marked by "*" and PEDOT's with "").**

To investigate the different material interactions between its OEG chains and sodium ions, EDX analysis was performed. For more systematic study, EDX experiment was done on microelectrodes from the same MEA by first depositing a drop of $NaCl_{(aq)}$ solution and letting it in air for ten minutes until it dries. By looking to Figure 4.7a, we can see the rise of the Na^+ peak for the electropolymerized glycolated monomers comparing with the commercial ePEDOT, was enhanced by increasing the EDOT/-g4 part. That confirmed the capture of sodium ions on the OEG chains of the glycolated ePEDOT microelectrodes. In addition, XPS study has been conducted for the same materials electropolymerized on gold cover slips. As displayed in Figure 4.7b, we observed that, without glycol, the ratio of EDOT monomer unit/PSS unit, calculated from the high resolution XPS S_{2p} signal, is 1.5. However, this ratio tends to decrease monotonically with the degree of glycolation to reach 1 at 7:3 glycolation degree. The decrease of the ratio closer to one explained that due to the OEG chains, the Na^+ ions stay on the OEG chain pulling extra PSS^- into the glycolated PEDOT:PSS. Yet, this does not mean that this strategy increased PEDOT's capacitance (no change in impedance values shown in Figure 4.4). A different mechanism from what is reported when adding ethylene glycol to the commercial PEDOT formulations could be expected. Here, we rather maintain a different intermolecular organization by having glycol moiety on each EDOT. The positively charged surface of the OEG tends to be more hydrophilic and may enhance the adhesion of neurons. Hereby, in addition to the softness of glycolated materials, this aspect will enhance the affinity between the microelectrode and the neurons should increase the seal resistance between the cell and the electrode.

Table 4.3 Assignments of the Raman bands shown in Figure 4.6

ν (cm^{-1})	Absorption band
440, 574, 990	Oxyethylene ring deformation
700	C-S-C symmetric deformation
1106	C-O-C deformation
1126	C_β-H Bend

1266	C_{α}-$C_{\alpha'}$ inter-ring stretching
1366	C_{β}-C_{β} stretching
1444	C_{α}=C_{β} symmetric vibrations
1508-1570	C_{α}=C_{β} asymmetric vibrations
2750-3100	C-H stretching

4.3 *In Vitro* extracellular recording from primary neuronal cells by glycolated-ePEDOT based microelectrodes

Previously, we presented a new chemically synthesized polymer (glycolated-ePEDOT) material for coating microelectrodes. These materials showed impressive morphological characteristics that are promising for neurosensing applications. Here, the glycolated electropolymerized microelectrodes performances were validated with *in vitro* experiment. We will exploit the accurate neuronal localization results of previous chapter to help in validating the superiority of the performances of these materials.

Primary neurons were cultured on top of a MEA presenting ePEDOT and glycolated ePEDOT with the different glycolation degrees. As a reference, primary neuron cells were cultured on top of TiN commercial MEA with the same cell culture protocol used for our MEA (see material and methods chapter). As shown in Figure 4.8a, the different materials were coated randomly on the different micro-electrodes to diminish the impact of the cell culture heterogeneity and to not misinterpret any property enhancement/diminution due to both the coating materials on the electrodes and the presence or absence of healthy cells clusters as observed in Figure 4.8b.

We performed *in vitro* recordings for both MEAs (TiN commercial and our MEA) for five minutes at 21 *days in vitro* (DIV21). Figure 4.8c, presents a time series showing spontaneous burst-spike activity of the neural culture from TiN electrode from the commercial MEA and from non-glycolated and (7:3)-glycolated electrodes from the same MEA shown in the fluorescent image (Figure 4.8b). Since the impedance of the gold electrodes of our MEA was much higher than the ePEDOT microelectrodes, we benchmarked the glycolated ePEDOT microelectrodes by comparing it to the pure ePEDOT. Spike-burst analysis is presented in Figure 4.8d. As shown in the number of spike curve, the number of spikes detected by all the glycolated electrodes was notably higher than that from the non-glycolated electrodes. For instance, the mean average of the number of spikes detected during three minutes of recording by non-glycolated electrodes was 347 spikes much less comparing with that of the (7:3) glycolated electrodes with 1150 spikes. This can be clearly visualized in Figure 4.8c where the chosen electrodes are representative from the mean-value of the spike count statistics curve. The synchronized burst rate (burst/min) was almost the same for the glycolated and the non-glycolated electrodes. However, it is well known that the synchronized burst rate is a phenomenon of the activation patterns of neurons in the neural network and depends on topology and the maturation state of the network more than the interaction of single neurons with the electrode [185]. Finally, the signal-to-noise ratio (SNR) was calculated statistically from the unglycolated ePEDOT and the different glycolated ePEDOT channels.

Remarkably, the mean average SNR value of the recorded electrodes increased gradually from 29 dB for unglycolated electrodes to 31, 33, 38 and 36 dB for (3:7), (5:5), (6:4) and (7:3) – glycolated, respectively thus reaching the highest value of SNR ~ 45 dB with the glycolated electrodes.

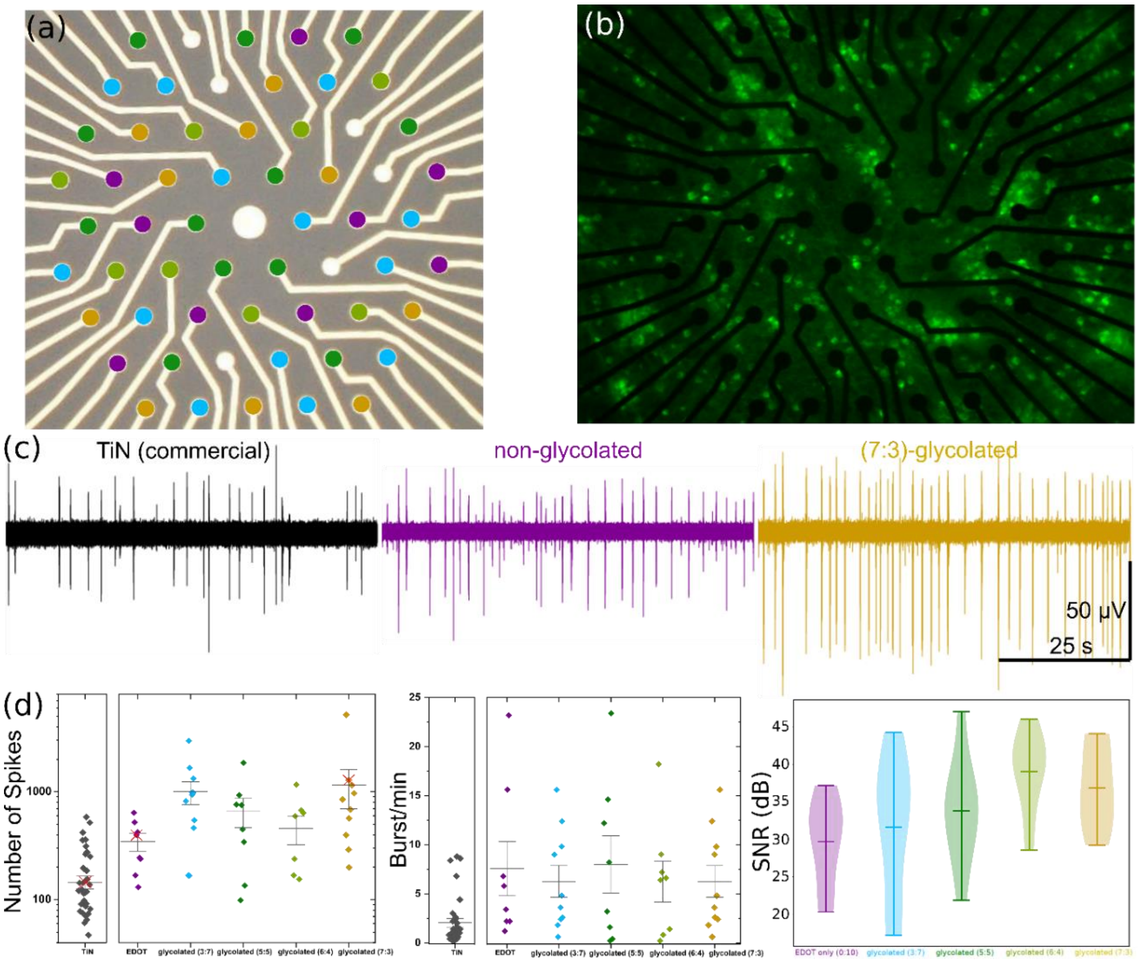

Figure 4.8 SNR and Spike Counting on Glycolated-PEDOT:PSS Micro-Electrodes. (a) Colorized microscopic image showing the random distribution of the different glycolated ePEDOT on the micro-electrodes of an array (MEA) used for *in vitro* extracellular recordings. (b) Live-imaging of primary cortical neurons on top of the MEA, after 21 days in vitro (DIV21). Note that the fluorescent probe we used detects only live neurons. (c) Time series showing spontaneous burst-spike activities of a neural culture at DIV21 on a commercial MEA (TiN electrode), compared to recording performed on the culture displayed in (b) (same conditions) on gold electrodes coated with unglycolated ePEDOT and (7:3)-glycolated ePEDOT. The chosen electrodes are representative from the mean-value statistics displayed in (d). (d) Number of spikes recorded (during 5 min) and bursts recorded per minutes for the commercial TiN MEA and the other MEA that contains the different investigated monomers (Red crosses in the first curve indicates the representative devices displayed in (c)). Signal-to-noise ratio (SNR) of the recorded channels from the same MEA, with the unglycolated ePEDOT and the different glycolated ePEDOT (Represented in violin plot chart, where each material group's SNR distribution is indicated by density curve)

Table 4.4 summarizes the comparison of performances of these glycolated-ePEDOT based microelectrodes in the literature, mainly in terms of SNR the recordings of spontaneous electrical activity coming from 2D neural culture (no stimulation and no electroporation to record intracellular activity in the case of 3D microelectrodes). The SNR parameter incorporates the signal's noise and peak amplitude in the quantification of performances, and not the coupling coefficient presented in *chapter I*, which considers just the recorded amplitude value compared to the neuron intracellular potential. As shown in Table 4.4, the SNR of the recordings detected by the glycolated-ePEDOT microelectrodes was superior to the SNR for state of art PEDOT:PSS planar microelectrodes reported previously for *in vitro* extracellular recordings from primary neuron culture. Additionally, to my knowledge, the SNR of these glycolated-ePEDOT microelectordes was higher than the reported planar electrode (Table 4.4). Furthermore, such SNR values were close to state-of-art 3D morphological microelectrodes (Table 4.4).

Table 4.4 A summary of performance (SNR) comparison between glycolated-ePEDOT microelectrodes and other comparative reported microelectrodes with different material, geometry, dimensions and impedance for *in vitro* extracellular recordings from neurons. “N/A” indicates that the associated data are not available. “a : SNR is reported in the paper, b: SNR values estimated from the paper data (noise and signal reported) such that SNR= 20log10 (peak amplitude/noise(std or rms).

Electrode material	Geometry / Morphology	Electrode dimensions	Impedance (at 1 kHz)	SNR (dB)	Ref.
SiO2 core coated with titanium/platinum	3D Vertical nanowires	Diameter = 150 nm Height = 3µm	120 MΩ	**60** [a]	[186]
Silicon converted into poly-crystalline platinum alloy	3D Nanowire based bioprobes	Diameter= 200 and 300 nm Height = 3 µm	48 MΩ	**66** [a]	[30]
Platinum	3D tip	Diameter = 60 µm Height = 50 – 70 µm	400 kΩ	**10 – 40 (min – max)** [b]	[187]
PEDOT:PSS - coated gold	3D Mushroom	Diameter= 1 µm Height = 2 µm	1 MΩ	**12 – 38** [b]	[188]
Gold	nanoflake	30 µm diameter	30 kΩ	**29 – 38** [b]	[189]
Gold	Fractal morphology	65 µm diameter	36 kΩ	**14 – 30** [a]	[40]
Gold	Planar	30 µm diameter	300 – 1000 kΩ	**14 – 22** [a]	[190,191]
Iridium-oxide	Planar	30 µm diameter	450 kΩ	**20 – 26** [b]	[192]
Carbon nanotube	Planar	80 µm diameter	N/A	**44 dB** [b] **(maximal)** **Average: N/A**	[43]
Graphene	Planar	10 – 20 µ diamater	3 – 4 MΩ	**26 – 37** [a]	[47]
PEDOT:PSS	Planar	30 µm diameter	22 kΩ	**17.7** [a]	[151]
PEDOT:PSS/Aliginate – coated platinum	Planar	30 µm diameter	3 kΩ	**16.5 – 18.2** [b]	[65]
glycolated-ePEDOT on top of gold	Planar	30 µm diameter	30 kΩ	**Maximal: 43 – 47** **Mean: 32 – 40**	**This work**

Figure 4.9 summarizes Table 4.4 scaling the mentioned SNR performances with the complexity of fabrication, time, and cost of the different geometries/materials. The high-quality performances of the 3D microelectrodes are in tradeoff with the complexity, time and, cost demanded for its fabrication. Polymer-based or specifically PEDOT:PSS-based microelectrodes have relatively lower fabrication complexity, time, and cost scale compared to the different materials used in planar microelectrodes. However, it is still limited in terms of SNR performances. Interestingly, our proposed materials offer a great comprise between the performances of the 3D microelectrodes and the fabrication simplicity, short time, and very low cost of PEDOT-based electrodes, which lies in the desired area in Figure 4.9 (high SNR with low fabrication complexity, time, and cost).

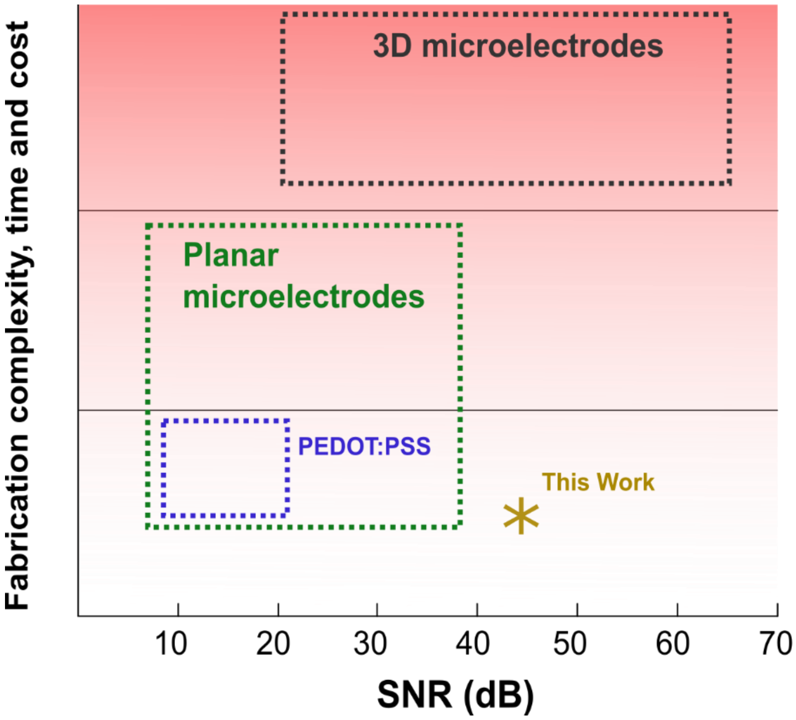

Figure 4.9 Representative graph showing the performance of different microelectrode technologies (from Table 4.4) in terms of SNR with their fabrication complexity, time and cost

There are two hypotheses that could explain the better performances in terms of SNR of the recordings: either (i) there is more cells on top or around the glycolated microelectrodes, or (ii) discarding the number of cells, there is better coupling between the neurons and the glycolated-ePEDOT due to the morphological characteristics of the glycolated-ePEDOT. To rationalize the hypothesis behind that, here comes the advantage of spike sorting accurate localization of cells that has been investigated in the previous chapter. Here, we used the monopolar estimation to identify the number of cells detected by ePEDOT and glycolated-ePEDOT electrodes. We estimated the number of detected cells of each electrode in a radius of 15 µm (on top of the electrode) and radius of 30 µm (around the electrode). More far distances have not been considered to avoid the interference of the number of cells detected between two adjacent electrodes (i.e. one cell will be counted twice). As shown in Figure 4.10, the mean average of the number of cells detected by ePEDOT or glycolated-ePEDOT microelectrodes is approximately equal in both cases of 30 µm and 15 µm radius. In addition to the number of neurons, here we also incorporated the distance between neurons and our microelectrode by showing the number of nearby neurons in terms of distance radius. With approximately similar distances and numbers, our quantification of recording performances could be more reliable in validating the higher SNR values of glycolated-ePEDOT microelectrodes. This points out that these materials maintain a very good affinity with neurons that explains the superior performances in their recordings.

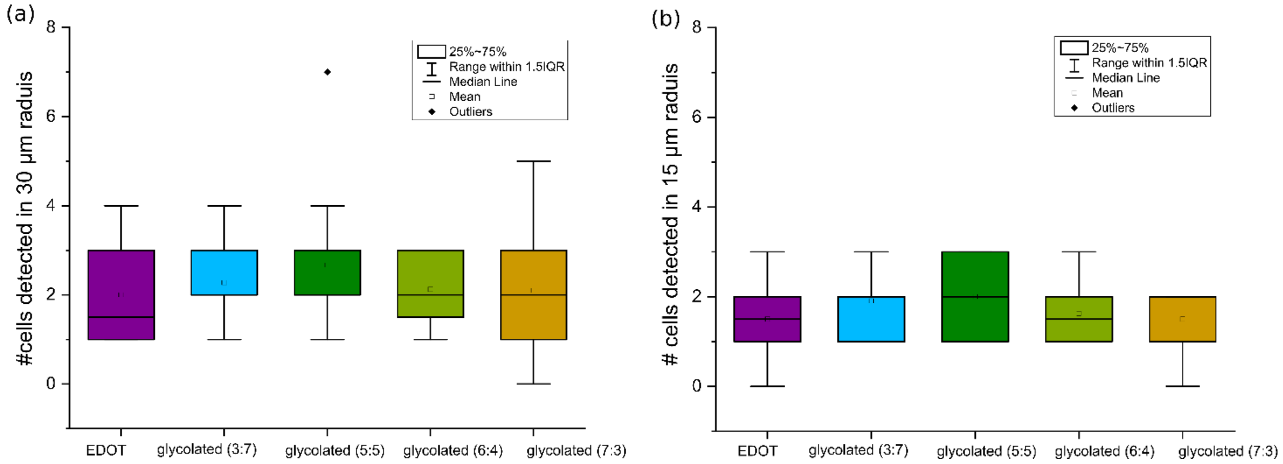

Figure 4.10 Box chart showing the number of cells detected after spike sorting whose template peaks are on ePEDOT or glycolated - ePEDOT channels in (a) 30-µm radius and (b) 15-µm radius around each microelectrode.

Two characteristics could explain the higher affinity between neurons and electrodes: the mechanical softness of the glycolated ePEDOT and higher hydrophilicity of the surfaces. Firstly, cell/electrode interfaces with higher affinity tend to form tighter gap junction and increase $R_{seal.}$ This increase in the seal resistance directly increases the SNR of the recording. Secondly, cells with higher affinity with a surface may tends to increase their total surface contact area, thus increasing the junctional membrane capacitance of the neuron. This second effect will also tend to increase the SNR of the recordings. In-operando AFM imaging to investigate the extension of the membrane of the neurons on these materials could help in the future to better explain the increase of the quality of the signal we are recording with glycolated-ePEDOT microelectrodes. Several study reported the use of AFM imaging as an effective tool to monitor architectures and topography of cells while living cells can be analysed in almost physiological conditions [193] . Hair-like extensions of the membrane along the walls of neuritic processes that shift in shape and density have been observed and reported [130]. This opens an important future objective could be done to explain more the enhancement of the neuron-microelectrode coupling at the micro/nanoscale level.

Regarding the more spikes detected from glycolated-ePEDOT microelectrodes, and since the number of cells is equal near all the microelectrodes, then it could be explained by two hypotheses. (i) Better neuron-electrode affinity, or (iii) the PEG chains are stressing the neuron leading to significant changes in its electrical activity. For the first hypothesis, the hydrophilicity and the low Young modulus of the glycolated-ePEDOT microelectrodes may create a better adhesion environment for the neuron to be more active regarding the number of spikes. For the second hypothesis, previous studies reported that *in vivo* and *in vitro* impedance measurements and neural tissue responses suggest that PEG coatings possess anti-biofouling properties which prevent glial cell adsorption and reduce astrocytic recruitment around the microelectrode [194–196]. Some types of astrocytes can respond to synaptic stimulation and interact with neighboring neurons, and this organization might play a functional role in the modulation of spiking activity [197]. Therefore, we can claim that the increased number of spikes coming from glycolated-ePEDOT microelectrodes could be due to the affected nearby glial cells or astrocytes by the PEG chains. Interestingly, this can be used to modulate cellular responses to microelectrodes *in vitro* which can be dedicated for information processing and learning applications in 2D cultures. Additionally, modulating the astrocytes or the electrical activity can present an essential target for possible therapeutic approaches for implantable microelectrodes (i.e. Disturbances in astrocytes' function may affect the pathomechanism of absence seizures [197]). Definitely, we should perform more reproducibility and perform these experiments on more MEAs with different cell culture mediums. This will strengthen more our claims and betting on the advantages of these promising materials to be conducted into a real-life applications.

4.4 Conclusion

In this work, we report the use of electropolymerization as a post-fabrication material engineering technique for MEAs by coating chemically synthesized glycolated-PEDOT on top of gold metallic microelectrodes with fine control of the glycolation degree of the electroactive PEDOT polymer. Molecular packing, cation complexation, dopant stoichiometry are governed by the glycolation degree on the electro-active coating on micro-electrodes. Optimal monomer ratio allows fine tuning electro-active materials' hydrophilicity and biocompatibility without affecting microelectrodes' electrochemical impedance nor their physio-chemical stability with a neural cell culture. The glycolated-ePEDOT microelectrodes show better neuron-electrode coupling due to its hydrophilic positively charged surfaces (OEG) compared to commercial ePEDOT in addition to its softer morphology. In *in vitro* extracellular recordings from primary neuron network were performed where the glycolated-ePEDOT microelectrodes displayed superior performances compared to the commercial ePEDOT microelectrodes. Indeed, from the same neural culture, glycolated-ePEDOT microelectrodes were able to detect higher number spikes (higher by ~250%) while presenting better SNR of the recordings. Our new synthesized polymer-based microelectrodes showed higher coupling parameters, superior performances and signal-to-noise ratio (SNR) to state-of-art PEDOT microelectrodes for in-vitro extracellular recordings from neurons. Such SNR values were close to that of state-of-art 3D morphological microelectrodes with lower cost and less complex fabricated microelectrodes. The new glycolated-ePEDOT material's output from the extracellular recording ensures their capability of releasing an advantageous materials to be used in coating cutting edge devices such as stretchable microelectrodes used for *in vivo* applications, and pushing further in enhancing the performances of other neurosensing devices used for wider applications in the electrophysiology application field.

Chapter V. Bio-inspired adaptive sensing through electropolymerization of organic electrochemical transistors (OECTs)

5.1 Introduction

In *chapter I*, we introduced several parameters that can impact the quality of the extracellular recordings from transistors; (i) transconductance which characterizes the signal amplifications of a transistor, by converting the variation of the gate from a biological process into modulation of the output source-drain current (ΔI_d). (ii) Capacitance of the gate oxide (C_{ox}) and geometry of the transistor (width (W) and length (L) values) that can directly influence the noise of the output drain current (higher C_{ox} or higher

WL leads into lower RMS noise values (*chapter I*)). (iii) The affinity and the contact area between the transistor and the cell, which is represented by R_{seal}.

Fromherz brought numbers of results on the interaction and the transistor by showing how the neuron ionic current is transformed to an extracellular voltage between the gate oxide and membrane that controls the electronic current in the semiconductor [92,93,102,198]. In most of his investigations, he reported the importance of the junction between the cell and transistor, by showing through simulations and experimental recording how better affinity is the key parameter to have higher extracellular amplitude (V_j) [101]. Compared to his first generation of FET-based systems, later he investigated low-noise level FET-based systems by enlarging the dimensions of the transistor. Implementation of low-noise transistors permits recording electrical activity from cortical or hippocampal mammalian neurons with RMS of noise lower by a factor of three. The equation of S_{Ves} the power density of the low-frequency noise in FETs is $S_{Ves} = \frac{k_B.T.e_0^2.\lambda_T.N_T}{C_{ox}^2.W.L}.\frac{1}{f}$,

where $k_B.T$is the thermal energy, elementary charge e_0, tunneling distance λ_T, width W, length L and C_{ox} dieletric capacitance. We can see that the low frequency noise is inversely proportional to the active area of the transistor (WL) and to the capacitance (C_{ox}). Transistors with large gate area W.L yield to a low noise level, but the probability for a direct interfacing between neurons and the transistor for a sparse neural culture are low leading, into lower seal resistances values [102]. Devices and techniques that can lower the noise of the recordings while keeping small geometries would be crucial for solving this bottleneck. Here comes the importance of having higher capacitance values of the capacitors. Although it has been shown that high values of capacitance (*Chapter I*) could lower the coupling coefficient ratio at higher frequencies, the bandwidth of the capacitance effect also depends on Rseal (*Chapter I and VI*). This leaves the negative effect of higher capacitances vague and still not clear. Like passive microelectrodes, increasing the capacitance of the interfacing electrode by lowering its impedance may be important for improving its electrochemical properties and reducing the influence of shunt capacitance or the external amplifier circuit on the recorded signal. Despite the importance of the amplification figure-of-merit g_m, Fromherz did not investigate its effect yet; however, other studies showed its importance in determining the quality of the recordings from electroactive cells [99,104]. For example, in [104] , by varying the gate voltage of a transistor change the maximum g_m value, they showed that the highest the gm values, the better the quality of *in vitro* recording from HL-1 cells. This highlights the necessity of maintaining better devices sensitivity (g_m) for better recordings. Hence, all of these discussions gave us the importance of g_m, R_{seal} and impedance of the transistor.

As bio-sensors, OECTs offer very attractive solutions for converting ionic signals into electronic ones thanks to the unique property of organic mixed ionic-electronic conductors (OMIECs).[199] Ionic concentration from an analyte or ionic currents from electroactive cells can be efficiently probed and amplified, thus making OECTs attractive sensors [139]. The organic polymer (PEDOT:PSS) materials used for OECT channel showed good biocompatibility and maintained good affinity with neurons (*see Chapter III*) which makes OECT's material very competitive for increasing the seal resistance. A critical parameter that characterizes the signal amplification of OECTs is the transconductance (g_m) which couples ionic signals to electronic ones[200]. Transconductance can be well described by the coupling between (i) volumetric ionic capacitance allowing for very large effective surface of interaction between the analyte and the polymer and (ii) efficient electronic transport along the π-conjugated organic chains ($g_m \propto \mu.C^*$). Hole mobility μ is the effective mobility of electronic carriers along the π-conjugated system and results from both delocalized states (i) intra-macromolecular π-σ-π electron delocalization along the thiophene backbone or (ii) hoping from π-π -stacked intermolecular thiophene rings (iii) intermolecular hoping between two PEDOT macro-molecules that are adjacent to a same PSS macromolecular chain.[201] Intermolecular hoping is the most limiting mechanism that largely defines the effective mobility of electronic carriers through the material. Volumetric capacitance C* is describing the permeability of PEDOT:PSS to ions allowing positively charged ions to interact with PSS^- fixed charges in the bulk of the material.[202,203] Direct correlation between g_m and both μ and C* justifies why transconductance is the main figure of merit describing both ionic and electronic properties of OMIECs[204]. It turns out that improving transconductance has been realized following either volumetric capacitance or electronic mobility tuning. Several works have demonstrated routes for optimizing transconductance through either volumetric capacitance or electronic mobility tuning.[121,122] Notably, side-chain engineering on the conductive backbone of the polymer have been recently proposed as a promising chemical engineering route [205]. Here, we show how electropolymerization can be used to adapt both properties simultaneously and independently via post-fabrication approach. This solution is opening new perspectives for engineering OECTs where transconductance and impedance can be finely adjusted. In terms of recording from electroactive cells, there is no still definitive decision of which parameter is the optimum one between these two (g_m or capacitance); hence, an in-situ post-fabrication technique that can finely adjust and optimize these two parameters simultaneously and independently is in great interest. We will also show how this technique will consequently improve the response time of an OECT which is one big challenge that has been facing OECTs in electrophysiological applications. These material aspects are then employed to show how transconductance of OECTs from a multi-sensor array can be adapted on-demand to an optimal transconductance value, which mimics the long-term potentiation process in biological synapses. We further demonstrate how tuning OECTs intrinsic properties can result in tunable frequency filters, which provides a unique opportunity for processing spike-based signals equivalently to short-term plasticity effects as a memory mechanism enabled in biological synapses.

5.2 Results and Discussions:

For spin-coated PEDOT:PSS, improving volumetric capacitance has been realized by material engineering routes consisting in addition of hydrophilic chains and molecules[206,207] to the spin-coated solution that results in larger volumetric capacitance values of up to 40 F/cm^3. A more straightforward solution is to increase the total thickness of PEDOT:PSS in order to increase the total capacitance of the OECT.[208] This technique has resulted in record transconductance of ~4000 µS. Nevertheless, as a soft fabrication process, spin-coating by itself does not allow adjusting the volumetric capacitance. Successive spin-coating steps are required and lead to a poor control over the total material thickness and variability. This holds also for the control of the effective mobility (i.e. organization of the π-conjugated system in PEDOT:PSS) that is mostly defined by chemical interaction of the polymer in its solution and its kinetics for drying upon a specific process. Notably, PEDOT polymer formulations have been reported to organize along the PSS chains resulting in fiber-like structure.[201] Addition of heterogeneous elements (additives) in the solution have demonstrated improved mobility of spin-coated PEDOT:PSS.[209] Recently, effective mobility improvement was obtained by mechanical-stress engineering in PEDOT-PSS fibers resulting in improved organization of the π-conjugated system along the fiber with effective mobility as high as 12.9 cm^2.V^{-1}.s^{-1}.[210] It turns out that both capacitance and effective mobility improvement for high transconductance are only accessible via various material synthesis and engineering techniques that cannot be necessarily combined. This lack of engineering flexibility represents a strong limitation for future development of OECTs applications.

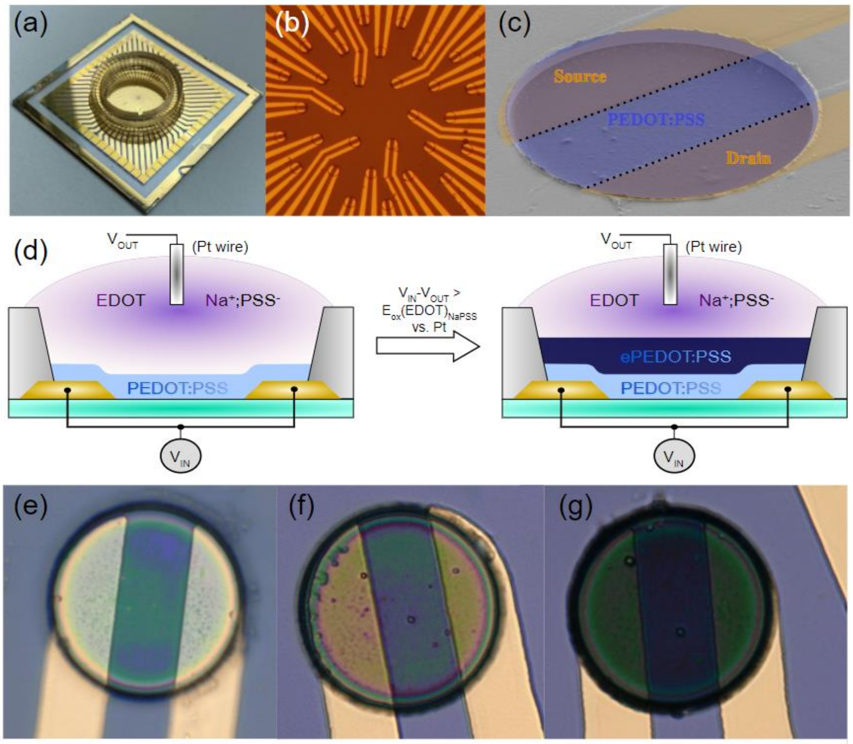

Figure 5.1 Electropolymerization technique for OECTs. (a) OECT glass chip. (b) Microscopic image of the array of 30 OECTs. (c) Colorized SEM image for a PEDOT:PSS OECT. (d) Schematic representation showing the experimental setup to perform potentiostatic electropolymerization of EDOT on top of spin-coated PEDOT:PSS OECT. (e-g) Microscopic images (from left to right) of spin-coated PEDOT:PSS OECT, spin-coated and electropolymerized PEDOT at 0.6 V , spin-coated and electropolymerized PEDOT at 0.7 V. [Figure published in Ghazal et al. Adv Electron Mater 8(3), 2100891 (2022)].

Here, the conductive material that was used as anode is no clean gold, as the case of MEA in the previous section. As a result, different voltage bias could have been expected for electropolymerization (EP) due to the higher conductivity of the PEDOT:PSS anode that will need lower applied voltage to maintain electron transfer for oxidizing EDOT monomers . EP configuration as shown in Figure 5.1d with S and D as anode (V_{IN}) and Pt wire as cathode (V_{OUT}) dipped into the electrolyte that contained the monomer (0.01 M EDOT + 0.1 M NaPSS). EP was realized on top of a standard spin-coated layer of a PEDOT:PSS (see experimental methods chapter) As done in previous sections, firstly, we performed *in-situ* potentiodynamic electropolymerization to determine the minimum oxidation voltage by monitoring the decrease in the impedance modulus curve. As shown in Figure 5.2a, the impedance modulus started to decrease after exceeding approximately V_{IN} = 0.55 V, as the minimum oxidation voltage bias. The potentiodynamic EP experiment was stopped after exceeding V_{IN} = 0.7 V where we started to see an increase in the impedance modulus. Here the aim was to determine an interval where we can electropolymerize since our approach combines spin-coating with electropolymerization to gain an additional level of freedom in adjusting ionic and electronic properties of OECTs. Consequently, another higher or lower input DC voltage bias have not been investigated. The effect of this EP on the transconductance (g_m) was inspected. In Figure 5.2b, the increase in the g_m curve after EP was satistying for investigating this process further to improve g_m. A more systematic study was realized on potentiostatic EP by investigating three different electropolymerization DCvoltage bias (V_p), 0.6 V, 0.65 V and 0.7V.

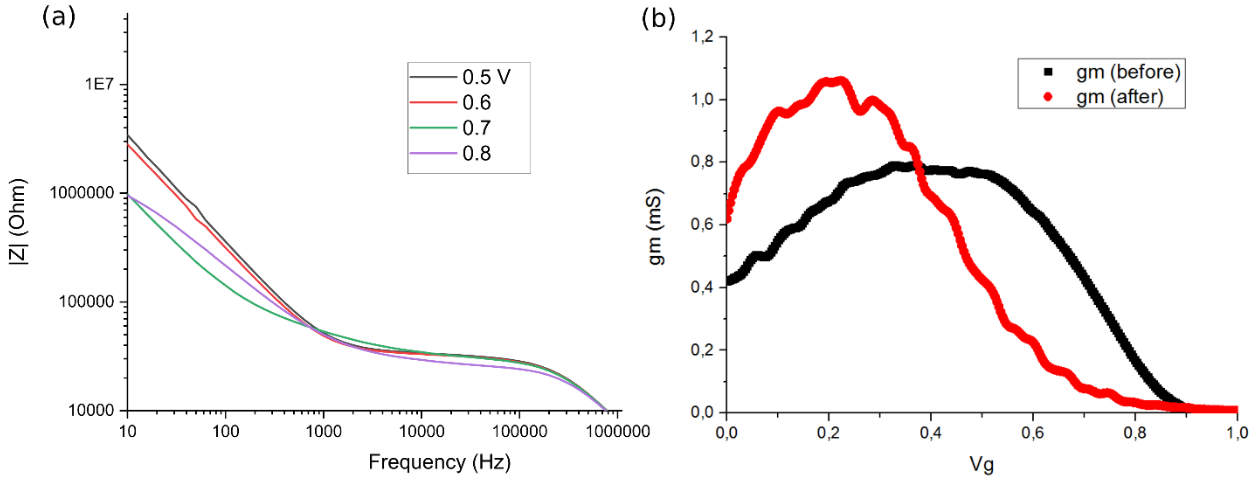

Figure 5.2 (a) In-situ electropolymerization of 10 mM EDOT in 100 mM NaPSS upon voltage ramped impedance spectroscopy (0.5 to 0.6 V), displaying a gradual change in the impedance modulus. (b) transconductance curve showing the evolution in the gm value before and after EP

5.2.1 Microstructural analysis of electropolymerized PEDOT:PSS

A fiber-like structure was obtained for spin-coated PEDOT and granular structure was obtained for electropolymerized materials as shown in the SEM and AFM images of Figure 5.3 statistical analysis of these AFM images was realized to reveal the grain size and overall morphology of the deposited polymer, the surface roughness and thicknesses of the electropolymerized thin films. For 0.6 V EP potential, AFM images showed granular growth with a grain size of ~5 nm whereas grains of ~9 nm were formed for 0.7 V potential. An averaged surface roughness increased from ~3 nm, ~ 4 nm and ~8 nm for the spin-coated, 0.6 V and 0.7 V electropolymerized PEDOT films, respectively. A clear relation between grain size and roughness can be drawn from these measurements with similar ratios of ~ 1:2 for both 0.6 V and 0.7 V EP potentials. Moreover, height profiles of AFM images before and after EP revealed electropolymerized thin films of (100 ± 4) nm and (200 ± 8) nm for 8 s of EP at 0.6 V and 0.7 V, respectively. The thickness of the two thin films presented a ratio of 1:2, which might explain the increase of the roughness and the creation of less organized surface for higher deposition rate. More interestingly, EP gave us access to various thin-film microstructures that should relate to different electrical properties of the materials.

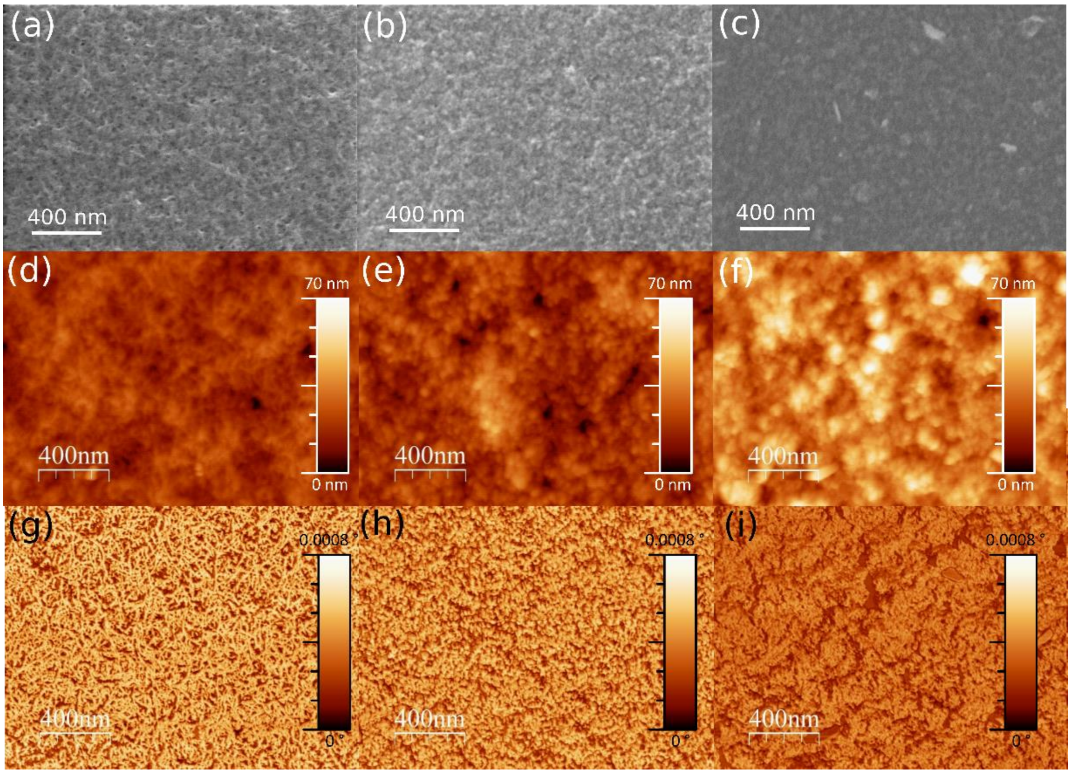

Figure 5.3 Impact of electropolymerization on PEDOT:PSS morphology. (a-c) SEM images of the channel material for spin-coated PEDOT:PSS, electropolymerized PEDOT at 0.6V and electropolymerized PEDOT at 0.7V OECTs. (d-f) AFM topography images of the channel's material for spin-coated PEDOT:PSS, electropolymerized PEDOT at 0.6V and electropolymerized PEDOT at 0.7V OECTs. (g-i) AFM phase images of the channel material for spin-coated PEDOT:PSS, electropolymerized PEDOT at 0.6V and electropolymerized PEDOT at 0.7V OECTs. [Figure published in Ghazal et al. Adv Electron Mater 8(3), 2100891 (2022)]

Figure 5.4a shows the Raman spectra of PEDOT:PSS grown by spin-coating (black line) and by EP at 0.6 V (green line) and at 0.7 V (blue line) potentials. These spectra are typical of the ones shown in the literature for PEDOT:PSS.[211–213] The bands assignment are presented in Table 5.1 From these measurements, we identified different orientations of polymer chains deposited on the surface and doping levels among the three different deposition conditions. Concerning the doping level, the peak for the $C_{\alpha}=C_{\beta}$ symmetric vibrations shifted from 1439 cm^{-1} for the spin-coated PEDOT to 1444 cm^{-1} for both electropolymerized PEDOT. This shifts indicates a higher level of oxidation for the polymer[211,213–218] in correlation with the peaks at 1266 cm^{-1} that corresponded to the oxidized state of PEDOT.[211,213–218]In addition, these blue-shifts (i.e. to higher wavenumbers) could be associated to oxidized states with quinoid form of polymer chains, which may have a key role to play on the conductivity of the polymers.[216] Moreover, electropolymerized PEDOT at 0.6 V presented the narrowest peak at 1444 cm^{-1} which suggested a larger rate of π-σ-π conjugation and thus higher crystallinity and conductivity as shown by Zhao et al. [214],[219] On the other hand, the decrease in the intensity of the peaks in the 400-1000 cm^{-1} region (dioxyethylene ring deformation) whereas an increase is observed at 1450-1650 cm^{-1} ($C_{\alpha}=C_{\beta}$ vibrations region) for both electropolymerized PEDOT relatively to spin-coated PEDOT indicated a perpendicular orientation of the thiophene rings with respect to the surface and thus an edge on growth of PEDOT:PSS on the surface.[215,220–222] To complete the discussion on the Raman measurements, electropolymerized PEDOT at 0.6 V and 0.7 V showed different intensity peaks in the 1300-1600 cm^{-1} region for the C_{β}-C_{β} stretching and the $C_{\alpha}=C_{\beta}$ asymmetric vibrations. These differences in relative intensities also indicated a different structure orientation of the polymer chains with respect to the surface, and thus different electrical properties. As illustrated in the schematic of Figure 5.4b, the relative orthogonality of thiophene rings organization to the substrate plane leads to a higher rate of in-plane π-π stacking which in turn increases the mobility in the thin films. In agreement, narrower peaks for PEDOT at 0.6 V indicate better crystallinity and thus better conductivity. Wu and coworkers[222] showed that a π-π stacking order in a lamella inter-chain stacking structure for an edge-on PEDOT orientation increased the conductivity of the thin-film polymer. Therefore, we can expect here a better crystallinity structure for PEDOT grown at 0.6 V with the latter ordering, which led to a better conductivity of the thin film polymer.

Table 5.1. Assignments of the Raman bands shown in Figure 5.4

ν (cm^{-1})	Absorption band
440, 574, 990	Oxyethylene ring deformation
700	C-S-C symmetric deformation
1106	C-O-C deformation
1266	C_α-$C_{\alpha'}$ inter-ring stretching
1366	C_β -C_β stretching
1444	C_α=C_β symmetric vibrations
1508-1570	C_α=C_β asymmetric vibrations

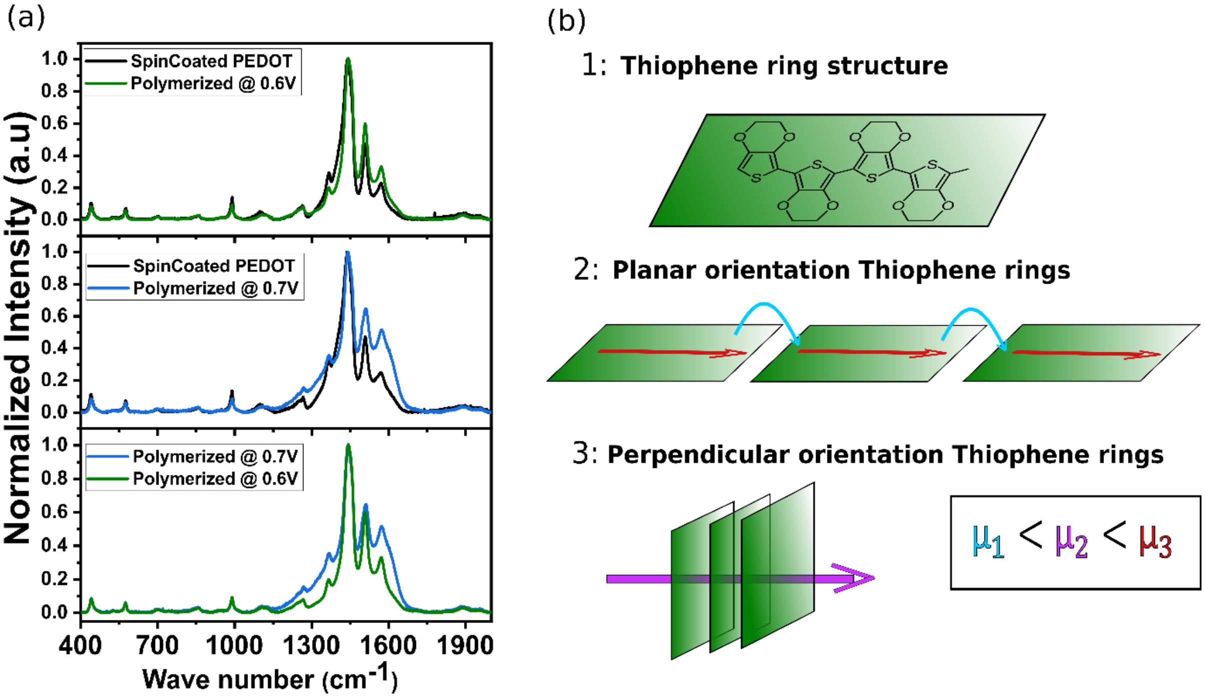

Figure 5.4 Impact of electropolymerization on PEDOT:PSS microstructure. (a) Typical Raman spectra (λ_{exc} = 477 nm) of spin coated PEDOT:PSS (in black), electropolymerized at 0.6 V (in green), and electropolymerized at 0.7 V (in blue). (b) Schematic representation of the PEDOT thiophene ring structure and its planar and perpendicular orientation structure. [Figure published in Ghazal et al. Adv Electron Mater 8(3), 2100891 (2022)]

From a structural and organizational standpoint, the Raman and AFM results correlated. The results were in agreement with a smoother and more organized PEDOT:PSS chains for the 0.6 V EP. These different growth characteristics (thickness, organization) revealed by AFM and Raman might give us a hint on the electrical properties of the PEDOT:PSS thin films. The growth at 0.6 V potential is expected to present a better conductivity while the growth at 0.7 V is expected to present higher capacitance.

These findings suggest that electrical properties can be tuned by applying different conditions of electropolymerization.

5.2.2 Transconductance and impedance evaluation

Combination of spin-coating with EP is offering an interesting option for accessing different material microstructures. Different microstructures are affecting the transconductance through a change either in capacitance or in electronic mobility. To access the ionic and electronic properties of the film, we conducted both DC electrical characterization of the OECTs and electrochemical impedance spectroscopy for various EP conditions. EP was realized sequentially on the same OECTs by steps of 2 seconds. Pt wire was used in EP for its inert electrochemical properties. Despite the large difference in size between the OECT and the gate, former studies showed that this material choice for a gate electrode is rather a limiting depletion.

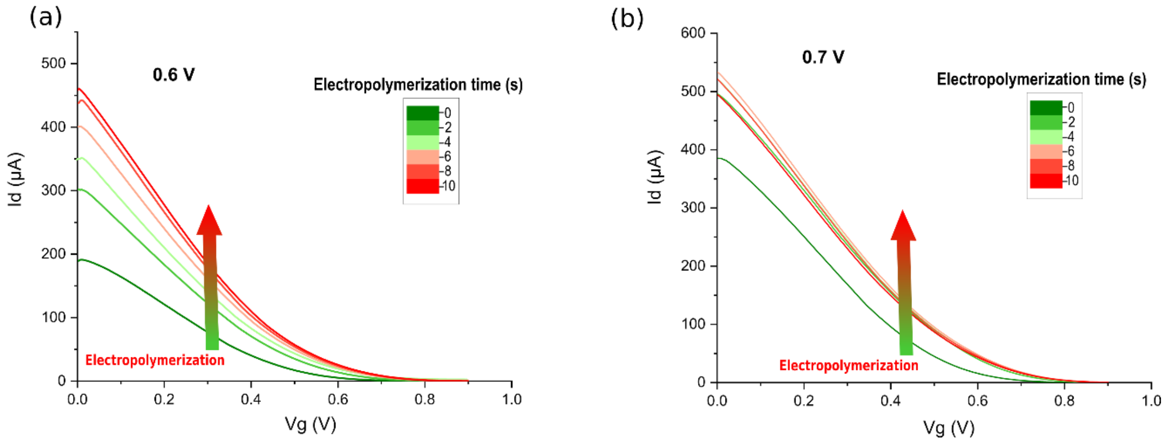

Figure 5.5 Evolution of transfer characteristic curves of OECTs electropolymerized at (a) 0.6 V and (b) 0.7 V

Figure 5.5 presents the evolution of transfer characteristic for potentiostatic EP on top of spin-coated PEDOT:PSS at $V_p = 0.6$ V and 0.7 V. Transfer characteristics provide a direct access to transconductance through $g_m = dI_{ds}/dV_g$, with I_{ds} the channel current and V_g the gate voltage where it is shown in Figure 5.6. As we can see for both cases the increase in the g_m curve after each electropolymerization step. In the case of 0.7 V, the g_m curve started to decrease after reaching 8 s. Figure 5.6 shows the evolution of impedance for potentiostatic EP on top of spin-coated PEDOT:PSS at $V_p = 0.6$ V and 0.7 V.

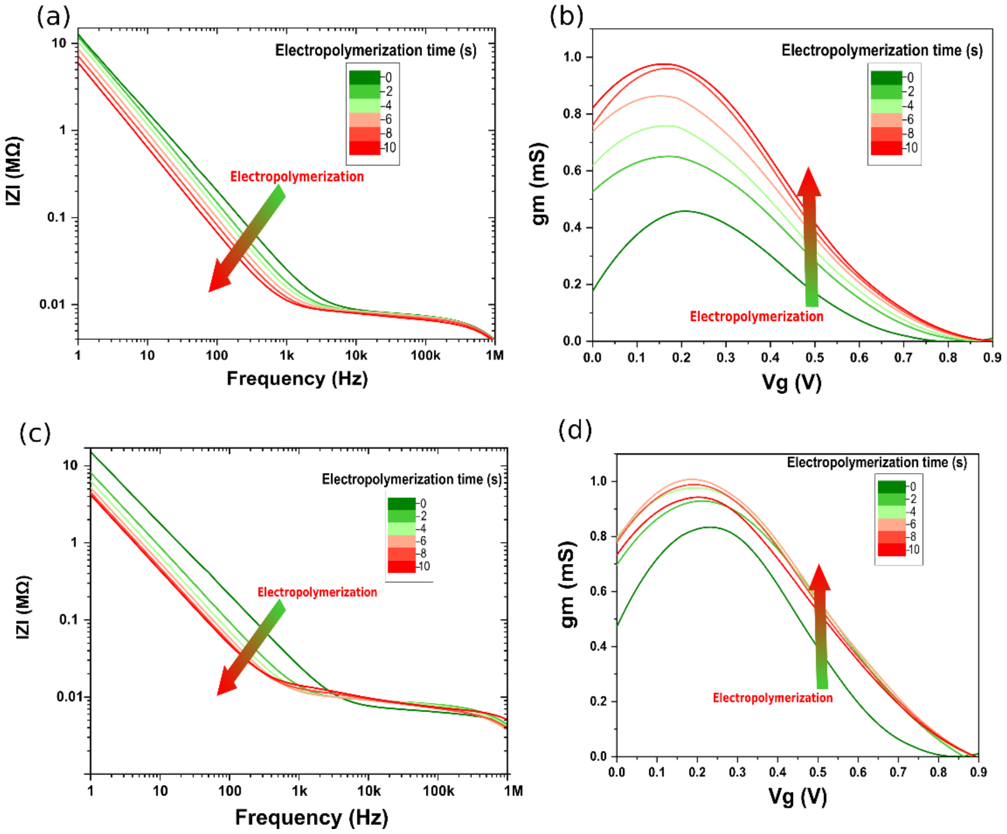

Figure 5.6 Impact of electropolymerization on OECTs' electrical properties. Bode's diagram of the impedance spectroscopy for an OECT during successive EP steps of 2 s at (a) $V_p = 0.6$ V and at (c) $V_p = 0.7$ V on top of spin-coated PEDOT:PSS. (b,d) Effect on the transconductance for the same devices as in (a,c) respectively. [Figure published in Ghazal et al. Adv Electron Mater 8(3), 2100891 (2022)]

The impedance modulus decreased gradually with EP in both $V_p = 0.6$ V and 0.7 V cases. Impedance spectroscopy was modeled with an equivalent electrical circuit (Figure 5.7) giving access to the total capacitance of the OECT (C_p). As shown in Figures 5.7b and c, the low pass filter shown in the first part of the impedance modulus (1 Hz to ~ 1 kHz) is modeled by Resistor-Capacitor circuit (C_p and R_p), representing the capacitance and the resistance of the OECT. The quasi-plateau between 1 kHz and 100 kHz represents impedance of the electrolyte resistance R_e, and the low pass filter shown at high frequencies modeled by Resistor-Capacitor circuit (C_g and R_g) representing the capacitance and the resistance of the gate-electrolyte interface. We conducted the same experiment for various potentiostatic conditions.

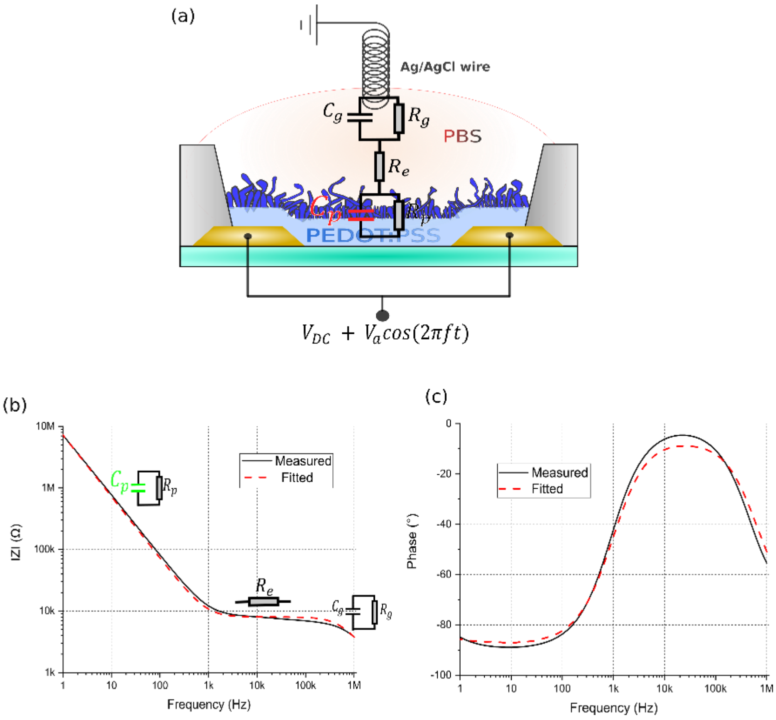

Figure 5.7 (a) Equivalent electrical circuit used to extract the total capacitance C_p of the OECT. (b,c) Bode's and Phase diagram of the impedance spectroscopy of an OECT showing the measured and fitted examples. [Figure published in Ghazal et al. Adv Electron Mater 8(3), 2100891 (2022)]

Figure 5.8 presents the relative change of maximum transconductance as a function of the relative change of capacitance. Considering a linear relationship between capacitance and transconductance [208], the dashed line in figure 5.8 presents expected trend in the case of a simple increase of a homogeneous material thickness. In this scenario, an increase of g_m is solely related to an increase of volume leading to higher capacitance. Interestingly, we observed that 0.6 V EP condition led to an evolution above this unity line while larger potential led to an evolution below it. Since transconductance depends on capacitance, mobility and threshold voltage[20], these deviation from the unity line indicates that EP should also affect mobility μ and/or threshold voltage V_{th} of the OECT.

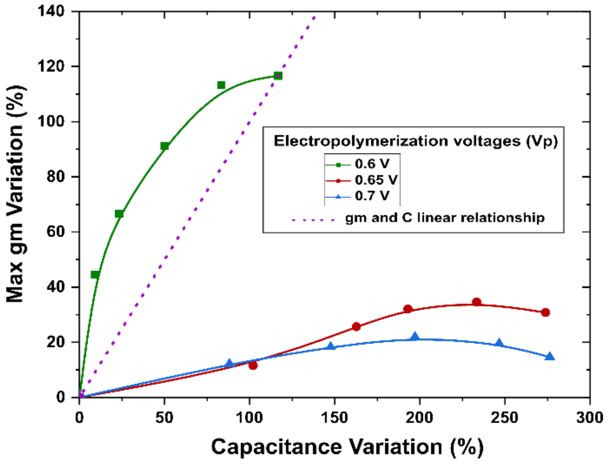

Figure 5.8 Correlation graph between the equivalent capacitance (from the impedance spectrogram fitting) and the device transconductance (from the OECT transfer characteristics) for different EP voltages. Each point from a line is obtained by repeating the same EP conditions for 2s. [Figure published in Ghazal et al. Adv Electron Mater 8(3), 2100891 (2022)]

Combining I_D-V_G with capacitance measurement, we extracted hole mobility μ ranging from 0.3 to 1.1 $cm^2.V^{-1}.s^{-1}$. Mobility was extracted from the I_d-V_g current-voltage relationship from [208] in the linear regime:

$$I_d=(W\cdot d/L)\cdot\mu\cdot C * [V_{th} - V_G + V_d/2]\cdot V_d$$

By calculating the slope of the Id-Vg curve in the linear regime, we get: $\mu = \frac{L^2.S}{CV_D}$, with S the slope, L the channel length, C the total capacitance obtained from the impedance measurement and V_d the SD voltage bias (see Table 5.2 for the absolute values). A clear increase of transconductance was observed as well as a clear increase in the capacitance (*i.e.* shift of the -1 slope part of the impedance modulus spectrum below 1 kHz).

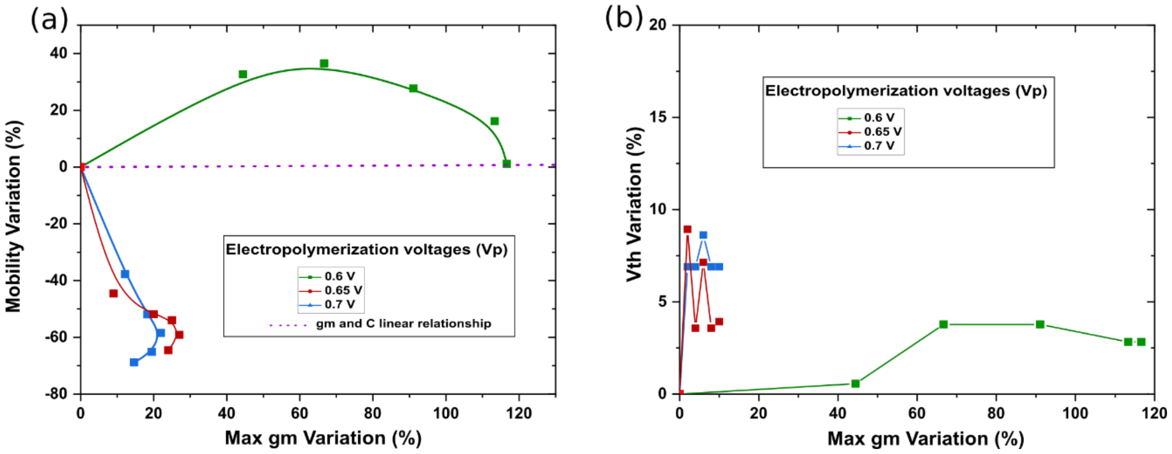

Figure 5.9 (a) Relative evolution of mobility and (b) threshold voltage as a function of the relative change in transconductance. A weak dependency of V_{th} is observed whereas mobility is clearly affected by the EP conditions. [Figure published in Ghazal et al. Adv Electron Mater 8(3), 2100891 (2022)]

We report in figure 5.9 the relative change of μ and V_{th} as a function of the relative change of g_m. V_{th} showed only a weak variation (below 10%) whereas μ showed a clear dependency with g_m for the different EP conditions. Low EP potential of 0.6 V led to higher mobility material and higher EP potentials of 0.65 V and 0.7 V led to lower mobility material with respect to spin-coated PEDOT:PSS (note that we can only access the average mobility of both spin-coated and electrodeposited PEDOT:PSS). In other words, EP provides a versatile technique that can be used to tune both electronic mobility and ionic capacitance, and this without changing the monomeric nature of the electropolymerized material on top of the spin-coated one (it is worth mentioning that different monomers can be electropolymerized on different spin-coated conducting materials as well). Note that although ionic diffusivity through PEDOT:PSS couldn't be directly evaluated on this electrical measurement protocol, EP should also modify its value the due to the different morphologies observed in Figure 5.8. Overall, a 120% increase in the peak transconductance and 40% increase in mobility with potentiostatic EP of PEDOT:PSS OECTs is demonstrated.

Table 5.2 Evolution of the electrical parameters of the three different devices used in Fig5.8 during EP at different potentials

OECT Electropolymerized at 0.6 V	Electropolymerization time (s)	Max gm (mS)	Capacitance (nF)	Mobility $(cm^2/V.s)$	Threshold Voltage (V)
	0 (Before)	0.45	12	0.52	0.53
	2	0.65	13.1	0.69	0.533
	4	0.75	14.8	0.71	0.55
	6	0.86	18	0.664	0.55
	8	0.96	22	0.604	0.545
	10	0.975	26	0.526	0.545
OECT Electropolymerized at 0.65 V					
	0 (Before)	0.78	9.9	1.1	0.56
	2	0.87	20	0.61	0.61
	4	0.98	26	0.53	0.58
	6	1.03	29	0.506	0.6
	8	1.05	33	0.45	0.58
	10	1.02	37	0.39	0.582
OECT Electropolymerized at 0.7 V					
	0 (Before)	0.82	10	1.06	0.58
	2	0.92	19	0.66	0.62
	4	0.97	25	0.51	0.62
	6	1	30	0.44	0.63
	8	0.98	35	0.37	0.62
	10	0.94	38	0.33	0.62

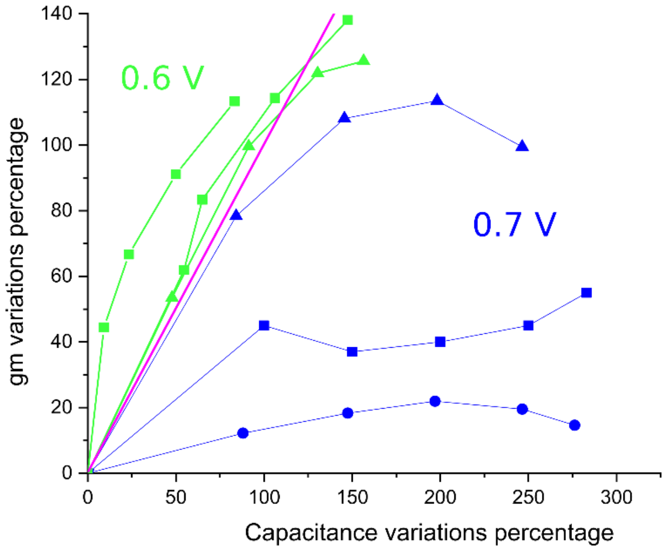

Figure 5.10 Figure showing the variation in reproducing the correlation between the equivalent capacitance and the device transconductance for different EP voltages.

One of the challenges was from this approach the ability/possibility of having same transcoductance evolution with respect to the capacitance evolution especially in the case depositing higher mobility PEDOT ($V_p = 0.6$ V) as shown in Figure 5.10. This may rise some interrrogations about adapting and controlling the setup more; i.e. decreasing more the EP step time and check more the systematic evolution of this mobility. Another hypothesis is that this variability could come from experimental or practical residues resulting from microfabrication step, rinsing or lab residues.

5.2.3 Effect mobility tuning for faster OECT response time:

The transient behavior of an OECT is critical for its electrophysiological applications. For example, 10 – 1000 kHz operation is essential for high-accuracy resolution of neuron action potential [223]. Unfortunately, OECTs are considered slow devices with time constant on the order of 1-100 ms [223].

Two parameters determine the response time of the OECT: ionic time response τ_i and electronic time response τ_e. As presented in *chapter I*, $\tau_i \sim \frac{l}{{C_o}^{1/2}}$ and $\frac{\tau_e}{\tau_i} \sim \frac{lL^2}{\mu V_d}$, the electronic transient response can be tuned by modulating the channel length or drain voltage value. However, in electrophysiological applications, it is preferable to keep biasing voltages as low as possible, and decreasing the channel length would limit the g_m values.

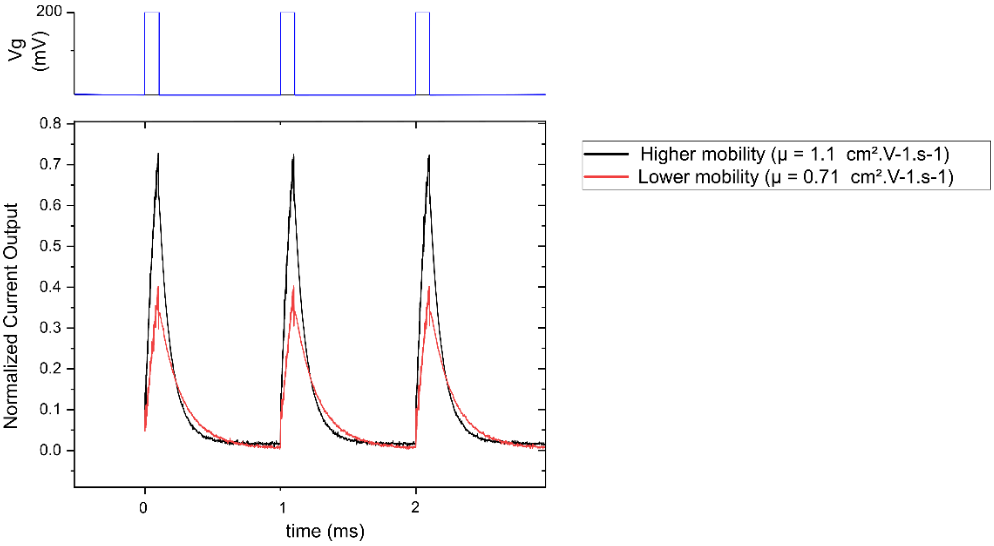

Figure 5.11 Current output response to a train of 100 µs and 200 mV pulses on the gate electrode at 1 KHz of an OECT before (lower mobility) and after mobility tuning by EP (higher mobility)

The time constant of the ionic transport in the electrolyte τ_i is defined by the solution resistance and the ionic double layer. Using the Gouy-Chapman theory: $\tau_i \sim \frac{l}{{C_o}^{1/2}}$ (l is the electrolyte double-layer and C_o is the ion concentration) [199], this time constant can be linked with physical parameters of the OECT. For example, the device ionic response can be tuned by decreasing the distance l or by increasing the electrolyte concentration. Considering the ratio expression: $\frac{\tau_e}{\tau_i} \sim \frac{lL^2}{\mu V_d}$, the electronic transient response can be tuned by modulating the electrode position, the channel length or the drain voltage value. Similarly, lowering mobility ($\mu = \frac{L^2.S}{CV_D}$) by decreasing the thickness of the channel's polymer (lower C) increases switching speed but causes a proportional decrease in transconductance. Here, using this technique, we were able to tune the mobility values to increase the response speed of the OECT without changing its geometrical parameters and decreasing its g_m; or even supported with further advantage by increasing g_m.

Figure 5.11, shows transient response of two OECTs with different mobility values to a 100 mV and 100 µs pulses at their gate. Here bottom-up tuning of OECTs mobility showed how an additional degree of freedom to change response time can be obtained with EP. Figure 5.11 compare the response to a train of 100 µs pulses before and after EP, respectively. After EP at 0.6 V, the mobility of the OECT

was increased from 0.72 to 1.1 $cm^2.V^{-1}.s^{-1}$ with a slighter change in its capacitance. As shown in the figure, in the case of lower mobility, the drain current exponentially relaxes to steady-state in ~ 1 ms, but for the device with higher mobility, the change in drain current settles to steady-state in ~650 µs.
The fast transient behavior of the OECT is critical in several applications. In neuromorphic applications, the response speed following a pulse voltage across the gate determines the learning speed, and in digital logic circuits transistor speed and bandwidth is an essential performance specifications [223]. Similarly, fast OECT response is critical for electrophysiological applications. The spiking activity of the neurons resides in the 0.1-7 kHz frequency intervals (*chapter I*); however, 0.1-100 kHz operation is necessary for high-accuracy resolution of neuron AP. Unfortunately, OECTs considered as slow devices with time constants on the order of 1-100 ms [223–225] and sometimes reaching values larger than 1 s [226,227]. In the case of having time constants above 1 ms, the devices will be either slow to catch APs or with low-accuracy resolution recordings. Indeed, a post-fabrication technique that enhance the time response down to ~ 650 µs is in great interest for overcoming a very important limitation for OECTs that is the slow operation performances

5.2.4 Capacitance and tuning for reduced noise

This section will be dedicated to the investigation of the effect of channel thickness on noise by using noise equations interpreted at the work of Polyravas. et al [228]. Their work showed lower noise achieved by increasing the channel distance during microfabrication.
The noise behavior of electrolyte-gated transistors including OECTs, is usually discussed in the context of the charge noise model [228]. The model suggests that flicker noise (low frequency noise for which the noise power is inversely proportional to the frequency) originates from fluctuations in the number of charge carriers in the transistor's channel. It suggests that the normalized power spectral density current is linked to the power spectral density of the gate voltage as:

$$\frac{S_{Id}}{Id^2} = \frac{g_m^2}{I_d^2} * S_{Vg}$$

, such that: $S_{Vg} = \frac{s_q}{C^2}$, where s_q is constant for given frequency and channel dimensions, meaning that relative noise scales as $\frac{1}{C^2}$.
Taking the case of two OECTs described previously, electropolymerized at 0.7 V (tunning mostly C) from the curve in Figure 5.8. Before EP, the capacitance was 10 nF and increases to 30 nF after EP (~300% relative variations). Using the relative noise formula presented, the EP should result in decreasing the noise relatively by 88% from its initial value.
In their work, they showed that the relative noise in OECTs decreases polymer thickness. Choice for polymer thickness in an OECT is usually made for maximizing transconductance while maintaining an acceptable cut-off frequency. This step is performed during microfabrication with limited flexibility. Here, EP is studied to find an appropriate capacitance value in order to adapt noise and suitable cut-off frequency, aspost-fabrication technique providing a higher degree of flexibility.

5.2.5 Capacitance and effective mobility tuning for adaptive OECTs sensors.

In the perspective of neuromorphic engineering, OECTs are capitalizing on the possibility to engineer devices where ion-electron coupling can be used to implement various synaptic plasticities, from short-term to long-term memory effects.[229–233] These two aspects have been so far mostly developed independently from each other. In contrast, synapses in biology are combining sensing capabilities with versatile plastic properties to provide some essential aspects of bio-computing. Through their adaptation, synapses are enhancing/depressing signals from neurons by relevance for information sorting. To do so, neural cells gather voltage non-linearity to process spike signals from.[234] As an element sensitive to its local chemistry, synapses are converting chemical signals from sensed neurotransmitters into transduced post-synaptic electric signals as ionic concentration modulation. Such ambivalence existing in biology is the natural example of a non-Von Neumann computing architecture that embeds highly complex biochemical sensing at all nodes in its network to ensure that computational tasks and data storage are both performed in place in the memory itself, and demonstrates reciprocally the power of local adaptation of a sensing array that programs according to its environment.

Versatility of electropolymerization is an attractive solution to engineer post-fabrication ionic and electronic properties in OMIECs. Having independent control over OMIECs capacitance and mobility can be used to adapt OECTs responses depending on the targeted application. In biological neural networks, synapses are experiencing long-term modification of their synaptic weights through learning to process efficiently bio-signals. This property is extensively used in artificial neural network through supervised training of networks to implement fundamental tasks such as signal classification or feature extraction.

Equivalently, tunable OECTs sensors with adaptive transconductance could be used to sort important features in the biological signal by weighting the transconductance of each sensor individually. Figure 5.12a presents the evolution of peak transconductance when successive electropolymerizations were realized to reach a 1 mS transconductance value. In our experiment, the transconductance was recorded after every 2 seconds of EP. When transconductance of more than 1 mS was reached or EP time was larger than 10 s, the transconductance tuning was stopped. In addition to a mean transconductance value of 0.98 mS (i.e. 2% deviation from the targeted value) a large decrease of standard deviation in transconductance from 0.24 to 0.086 mS was obtained for a batch of 30 devices belonging to the same array. Figure 5.12b shows the evolution of the capacitance for the same experiment. The low initial variability in capacitance associated to the large initial variability in transconductance of spin-coated PEDOT:PSS points to variability in mobility rather than variability in capacitance as the initial source of variability in transconductance. The increase in capacitance variability after EP suggests that variability in transconductance was reduced by adjusting capacitance rather than mobility. It is to note that transconductance tuning could be optimized further by using automated setup that could allow fine-tuning over time by combining EP and transconductance measurements in the same environment. In our case, the setup was limited by the manual control. Also, this demonstration implemented only long-term potentiation effects (i.e. increase of the transconductance). As suggested by the decay of transconductance for long EP time, long-term depressions (LTD) should be also available. Origin of LTD could be explained by either (i) a degradation of mobility of the previously deposited material by decreasing thiophene rings organization when more material was added or (ii) ions diffusivity limitation when too thick materials are deposited. Further investigations are required to conclude on this aspect. We also note that both LTP and LTD are irreversible mechanisms. By analogy with biological cells, which show different forms of plasticity, combining these structural modifications with long-term doping / de-doping of the PEDOT:PSS could offer more flexibility for OECT programming in the context of adaptive and plastic sensors.

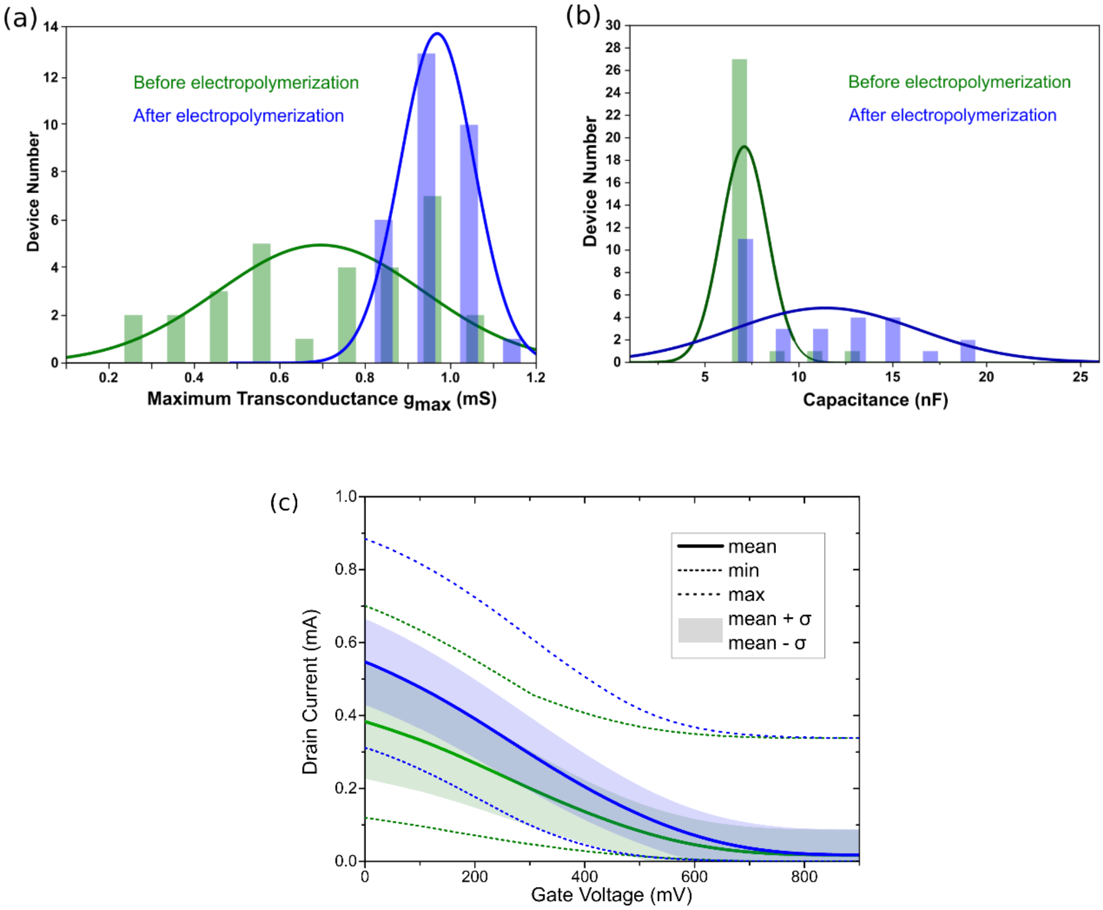

Figure 5.12 Adaptive OECT implementation with EP. (a) green: distribution of the maximum transconductance (mS) for an array of 30 OECTs . An adaptation procedure with target of 1 mS is used to gradually change the transconductance of each OECT sequentially. (blue) Final transconductance reach after device adaptation. (b) Distribution of the capacitance before (green) and after (blue) OECT adaptation. Lines are the Gaussian fitting of the histograms. (c) Transfer characteristic curves before (green) and after (blue) OECT adaptation. [Figure published in Ghazal et al. Adv Electron Mater 8(3), 2100891 (2022)]

A second bio-inspired feature available with adaptive OECTs is to implement Short Term Plasticity (STP). Here we capitalized on the bottom-up tuning of OECTs capacitance to show how an additional degree of freedom can be obtained with EP. Figures 5.13a and 5.13b compare the response to a train of 100 µs pulses at 1 kHz and 8 kHz before and after EP, respectively. STP effect results from the balance in between the ions charging during the 200 mV pulse and discharging during the 0 V inter-pulse moments. After EP at 0.7 V, the capacitance of the OECT was increased from 10 nF to19 nF, thus increasing the time constant of the equivalent Resistor-Capacitor circuit. Before EP, OECTs response presented higher modulation than after EP at low frequency. Note that in this low frequency regime, charge and discharge were completely balanced. At high frequency, both devices reached an equivalent saturation regime corresponding to the maximal accumulation of positive ions. In this latter case, charging was not balanced by discharging due to short inter-pulse interval and current reached the saturation level. Comparison between the two responses demonstrates the possibility to tune the high-pass filtering property of the OECT with EP. For instance, OECT after EP can discriminate the low frequency signals from the high frequency one whereas it cannot before EP. It was recently proposed that STP effects in neural networks can be modeled as a combination of various frequency filters.[235] Here, the adaptive property of OECTs with in-situ EP represents an attractive feature for neuromorphic synapses engineering that could allow to reproduce complex STP mechanisms.

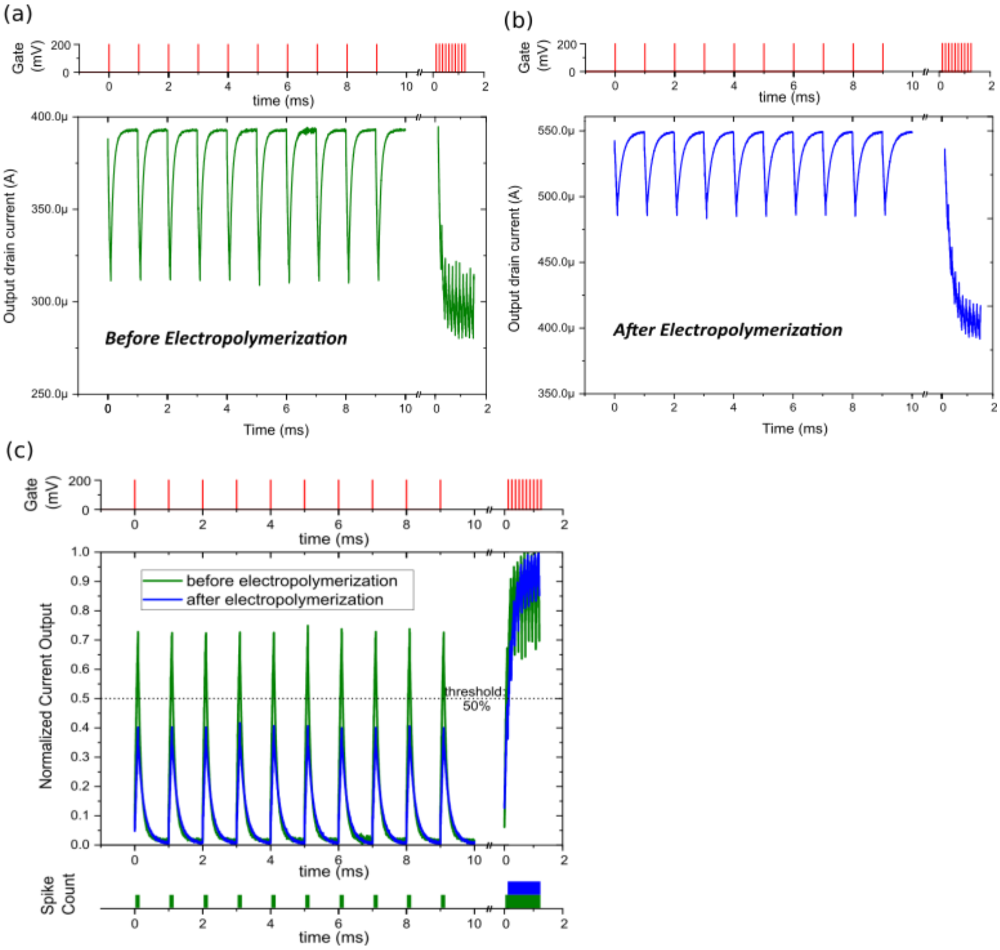

Figure 5.13 Capacitance tuning for adaptive OECTs sensors. Current output response to a train of 100 µs and 200 mV pulses on the gate electrode at 1 kHz and 8 kHz of an OECT before (a) and after (b) capacitive tuning by EP. EP allows tuning the frequency response of the OECT with a clear discrimination of the low / high frequency signal after EP and a low discrimination before EP. (c) The normalized current output response to a train of 100 µs pulses at 1 kHz and 8 kHz of an OECT before (green) and after (blue) capacitive tuning by EP. Spike-count graph counts the pulses that cross the defined threshold line (50% of output modulation). [Figure published in Ghazal et al. Adv Electron Mater 8(3), 2100891 (2022)]

As shown in Figure 5.13 we projected this experiment to highlight on signal processing application; on-chip spike detection at the interface (considering the gate voltage is mimicking spikes coming from biological medium). For instance, after performing capacitive tuning of the OECT, its response could discriminate the low frequency signals if a threshold of 50% of the signal was applied. Hence, this technique give the possibility of implementing an array adaptively with devices with different tunable parameters (i.e capacitance) that have the ability to sense and assist in processing data in parallel. For future work, the idea could be to design a matched filter for every identified neuron or population of neurons, which maximizes the output of the signal of the targeted signal (i.e. high frequency signal), and at the same time, minimizes the output for undesired signals, which includes spikes from other neurons and noise. Using on demand optimal filters represents a promising method for real-time spike sorting that may solve several data processing issues (i.e. overlapping spikes)

5.3 Conclusion

This chapter details on EP as *in-situ* technique for tuning the iono-electronic properties of OECTs. OMIEC optimization has been largely proposed with either volumetric capacitance or effective mobility tuning. EP allows controlling both properties simultaneously. This strategy opens new perspectives for

OECTs engineering where transconductance and impedance can be finely and independently adjusted. More fundamentally, this work is showing how ionic and electronic properties are governing the OECTs responses, which contributes to a better understanding of mixed ionic electronic processes in OMIECs.

Along this line, an important bottleneck of OECTs development as bio-sensors is associated with the large variability of soft technologies when circuits and systems need to be designed. Spin-coating as well as inkjet printing, which are the most popular OMIECs fabrication routes, are room-temperature and ambient atmosphere deposition conditions that are prone to large number of defects in the OMIECs. EP can offer an interesting alternative to adjust the iono-electronic properties of the material post-fabrication to match a tolerable range of variability in these properties. Notably, we showed that standard deviation in transconductance can be reduced by 60%.

This technique can adjust and optimize two important parameters for electrophysiology: response time and noise. It increased the response time of an OECT by 65% and lowered noise relatively by 88%. Both parameters can be optimized post-fabrication or in-situ in case device's performance did not match the electrophysiological application requirements after fabrication.

This approach is also offering a new strategy for the development of adaptive sensors that can adapt to their sensing environment. For instance, electrophysiological recording could benefit from sensor arrays that could be adapted to the specific organization of the biological neural network. Equivalently to learning, adaptive protocols could be designed to adjust OECTs response to match biological neural network organization. It has to be noted that EDOT molecules are non-cytotoxic[236,237] - at least in the range of concentration reported in this study – and PSS:Na is non acidic. Future work could consider in-situ EP with living cells in the medium. In addition, since electro-active cells / electrode coupling is based on capacitive effect, OECTs fine-tuning can be used to optimize cells / OECTs coupling or to adjust the filtering of complex bio-signals. Finally, EP can also open new perspectives for the development of non-standard OECTs structures that are not bounded to standard top-down design technics. Along this line, electropolymerized dendritic OECTs are emerging as a new direction for bio-inspired computing deployment.[154,238]

Chapter VI. Interfacing neurons with OECT *in vitro*

6.1 Introduction

OECTs has been already used for electrophysiological recordings such as electrocorticography (ECoG) [96], electro-oculogram (EOG) [137], electroencephalography EEG [137] and electrocardiogram (ECG) [138]. For *in vitro* recordings, OECTs have been reported for recording cardiac cells [140–143] for applications in medical health and pharmacological industries. These studies have shown proof of concept of *in vivo* and *in vitro* recording by using OECT. In order to better understand the coupling between an OECT and cells, *in vitro* 2D neural culture is an important and beneficial platform to use to understand in detail the coupling between a neuron and an OECT. Contrary to cardiac cells, primary neural culture network is more complex in terms of structural variability and electrical activity, making them a complicated system to interface. Here, systematic electrical and morphological characterization of OECTs were performed *in vitro* with primary cortical cells. We investigated the effect of neural growth on OECTs' electrical characteristics. The optimal voltage biasing has been determined for maintaining the best transduction from the device, while keeping the environment under the lowest electrochemical stress. *In situ* electrochemical impedance spectroscopy (EIS) of the device with neurons seeded on top of it has been compared to compact models and their simulations to identify parameters that yield the neuron coupling. Finally, preliminary results are shown for *in vitro* recording of primary neurons with OECTs. These experiments allowed identifying several critical challenges for the use of transistors in general and OECT in particular for *in vitro* recordings.

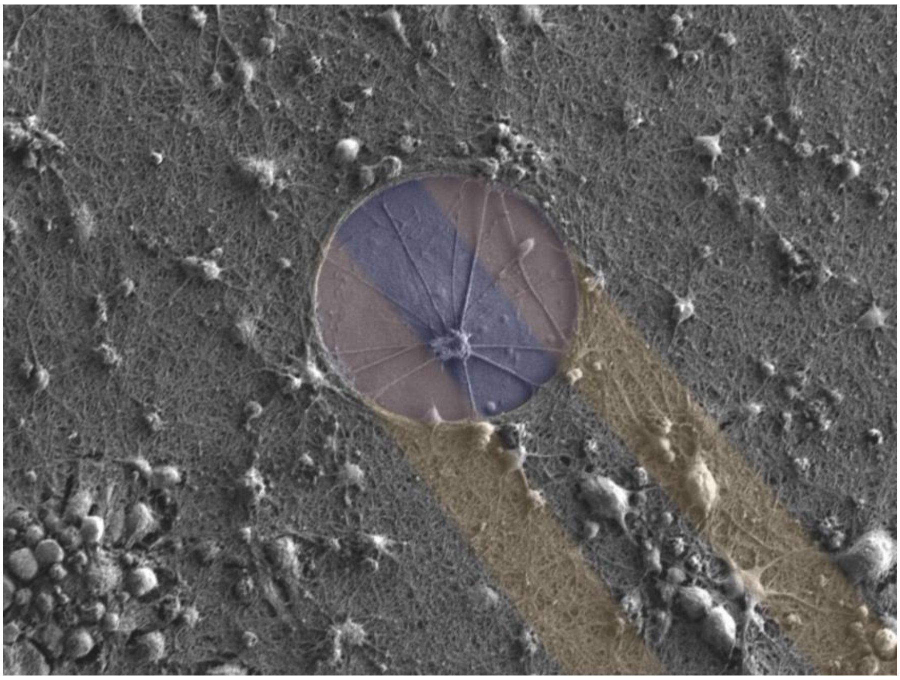

Figure 6.1 Colorized SEM image of 2D primary neural culture interfacing an OECT: The blue shaded area defines the coverage in PEDOT:PSS material beneath the cell culture, and the yellow ones for the metal contacts beneath PEDOT:PSS and Parylene C.

6.2 Effect of cell adhesion layer on electrical performances

Before seeding neurons on top of the OECT patterned substrate, its surface has been covered with a layer of poly-D-lysine (PDL) and Laminin (see Methods) to promote neuronal adhesion. Cell attachment is favored by the interaction between the positively charged polymer coating (polylysine) and negatively charged cells on the membrane proteins. While they are crucial for neuron cultures, they could affect the electrical property of the active sensor due to its charged interface and may partially screen the electrolyte. To estimate the effect of the adhesion layer on the sensor performance, DC electrical characterization (i.e. transconductance) and electrochemical impedance was performed for the same OECTs before and after covering the chip with the PDL+Laminin layer, in PBS as electrolyte. This type of investigation was conducted for the first time and it represents a significant step toward the widespread introduction of these devices to the *in vitro* recording from neurons applications.

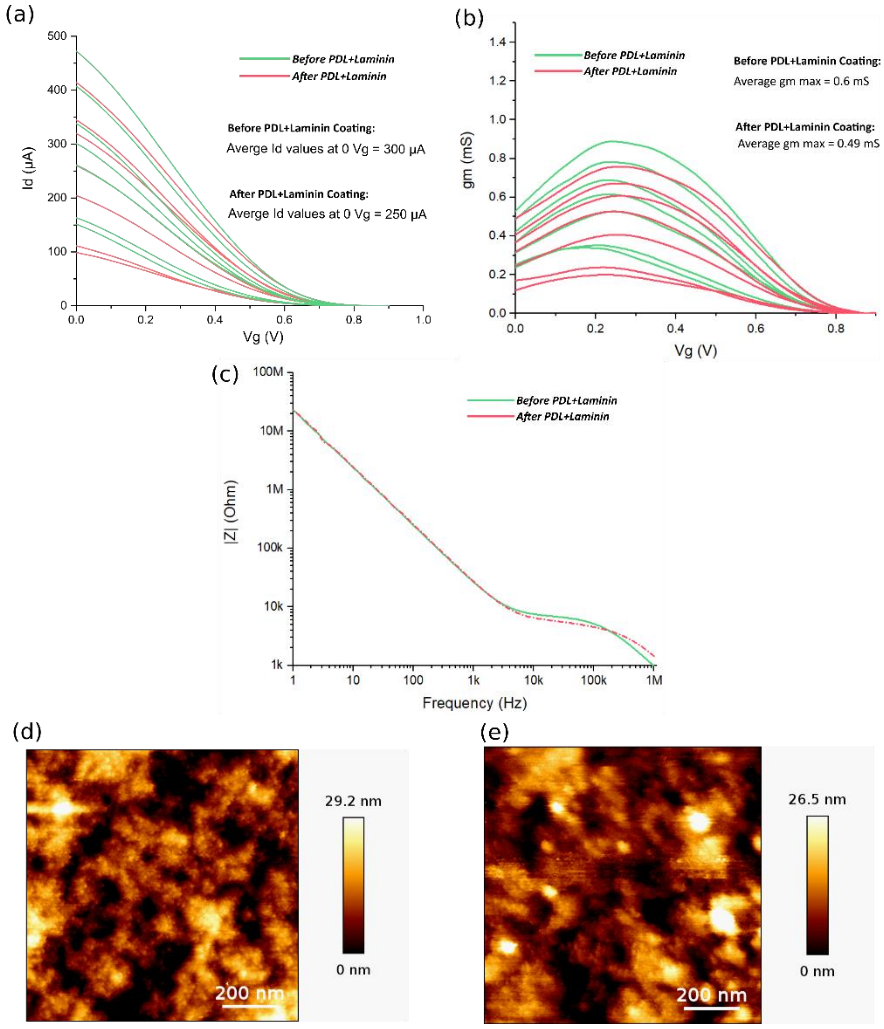

Figure 6.2 Effect of adhesion layer. (a) Transfer characteristic (I_d - V_g) curve of OECTs before and after coating PDL+Laminin (n=7). (b) Transconductance curve of OECTs before and after coating PDL+Laminin (n=7). (c) Bode's diagram of the impedance spectroscopy for an OECT before and after coating PDL+Laminin. AFM topography images of the channel's material (d)before and (e) after coating PDL+Laminin

These preliminary measurements evidence a minor change in the transistor properties. Figure 6.2a shows the transfer characteristic curve for multiple OECTs from the same array (measured in the same environment) before and after coating. The adhesion layer leads to an average of ~17 % decrease in the conductance values (I_{ds} values at $V_g = 0$ V) reproducible on all the OECTs. This decrease could be attributed to the positive net charge of the coating's molecules that may better favor the reduced (de-doped) state of the PEDOT film and decrease its conductivity. Additionally, the coating leads also to an average of ~18% decrease in the maximum g_m values reproducible on all the OECTs, which can attributed to the decrease in its conductivity (same relative decrease between I_{ds} values and g_m). Some polycations (e.g. Polyethylenimine (PEI)) have been used to fabricate OFF-state transistors where the redox state of the semiconductor material is controlled due to the doping capability of the polycations in the channel [239,240]. In our case, the PDL polycations could induce lower capabilities of doping than, for example, PEI, which could explain the slight decrease in the conductivity and transconductance values. We performed electrochemical impedance spectroscopy for an OECT before and after the adhesion coatings, as shown in Bode's diagram in Figure 6.2b. As we can see, there was no significant change in the impedance. Electrical modeling has been performed (similar to the OECT model introduced in *Chapter V*) to quantify the capacitance of the OECT, showing no change in its value (C =

6.9 nF) after the adhesion layer coating. This assures that the volumetric capacitance did not change after the coating, which suggests that the effect of the coating layer (lower g_m, same capacitance) does not alter the electrochemical coupling of the conducting material with electrolyte, but the effect of the latter one on the in-plane material conductance. Figure 6.2c and d show AFM images of the same OECT channel scanned exactly on the same position before and after coating the adhesion layer. Different morphology between the two images can be observed, such that the RMS value of the surface roughness decreased from 8.6 ± 3.6 nm to 6.9 ±2.1 nm after coating, which could be due to the morphology of the PDL+Laminin layer (i.e. protein/peptide distribution on the surface). This confirms that PDL+ Laminin promotes neuronal growth on PEDOT:PSS-based OECTs for *in-vitro* recordings,without drastically affecting the sensing performance of the device

6.3 OECT electrical characteristics during neural culture

In the previous chapter,the electrical characterizations were performed in the presence of saline solution to determine OECTs performances. We show above the non-significant effect of the adhesion layer on the electrical performances of OECTs; In this section, the effect of the culture on the electrical performances of the OECT is studied.

Figure 6.3 shows the OECT characteristics before and after cell culture, with 21DIV neurons grown on top of the devices. The OECTs were first characterized by measuring the output and transfer characteristics in PBS. After culture, a 50% relative decrease in the OECT conductivity was observed. Relatively, the PDL + Laminin coatings, as investigated previously could cause around 20% of this decrease, leaving about 30% induced by the culture itself. Looking at the transfer characteristic curve in Figure 6.3b, we can see a largehysteresis in the drain current between closing and re-opening the channel (75% relative difference at V_g = 0 V). This hysteresis was not monitored in the measurements before neural culture (red curve). Another experiment has been performed for another OECT with two consecutive rounds of I_D-V_G experiment showing reproducible results (approximately 85% relative difference at V_G = 0 V) to what is shown in Figure 6.3c. In the 2nd round curve (Figure 6.3d), we monitored a decrease in the hysteresis effect to approximately 40% relative difference at V_G = 0 V.

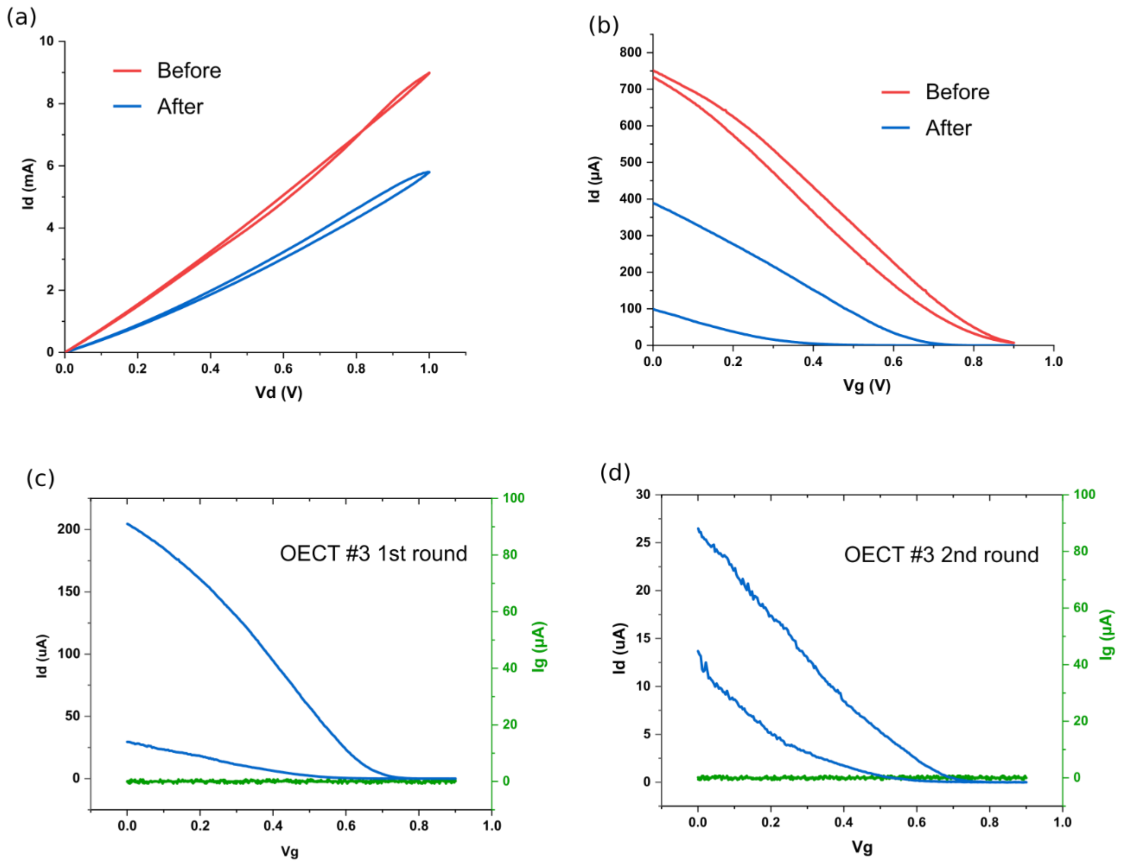

Figure 6.3 Effect of neural culture. (a) Output characteristics curve and (b) transfer characteristic curve of an OECT before and after neural culture. (c) Transfer characteristic curve of another OECT after neural culture. (d)Transfer characteristic for the 2nd round of Id-Vg after performing Id-Vg in (c) for the same device.

Figure 6.4 shows the transfer characteristics for one OECT in accumulation and depletion mode at different gate voltage intervals, to evaluate the effect of the gate voltage on the hysteresis. In each round, dedoping (positive V_G) was initiated, followed by a reversed redoping stress (negative V_G). Noticeably, the hysteresis increases with the increase of positive gate interval. Additionally, whenever the channel is reduced, it is not reversibly oxidized back by applying negative gate voltage of a same amplitude as a previous cathodic stress (for stresses higher than 0.6 V in amplitude).

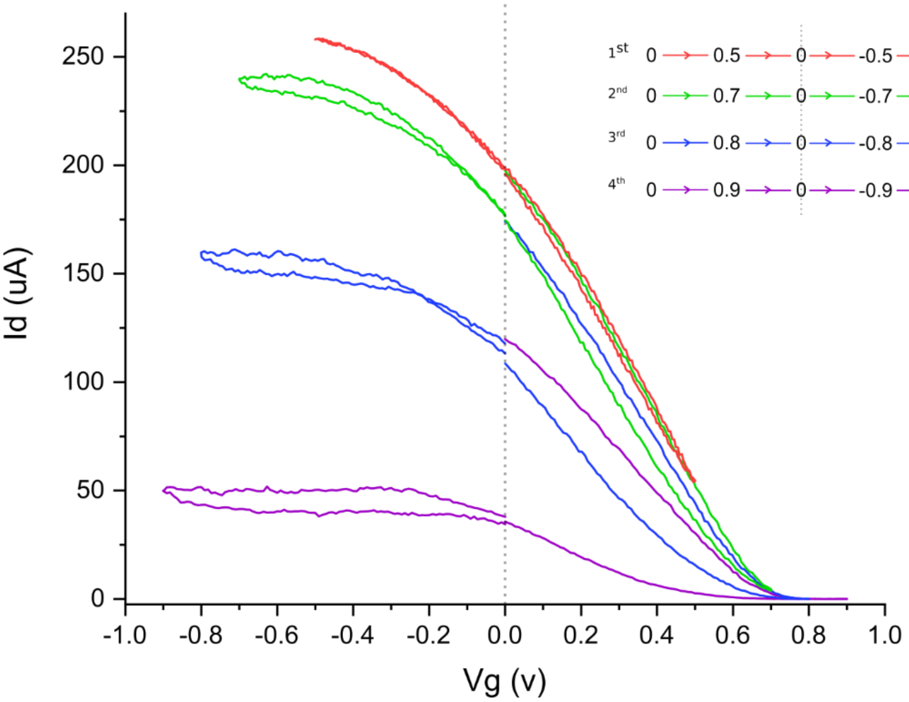

Figure 6.4 Transfer characteristic curve with different gate voltage interval. Each color represent a gate voltage interval.

One hypothesis to explain this irreversible diminishing of the channel conductance is that the thick and very dense neural network layer maintains a mechanical shield for the OECTs to interact with the ions from the electrolyte. We performed different neural growth densities, as shown in Figure 6.5. The SEM images in Figure 6.5a and b, show a very thick and dense culture, while the SEM images in Figure 6.5c and d show another OECT array with a sparse network. Figure 6.6 shows microscopic and fluorescent images of the array with sparse neural network. The hysteresis effect was reproducible in both neuronal growth density cases, as shown in Figure 6.4 with the sparse neural network (the same OECT device shown in SEM image in Figure 6.5d), and in Figure 6.3 with the dense network (OECTs from the array shown in Figure 6.5a and b)

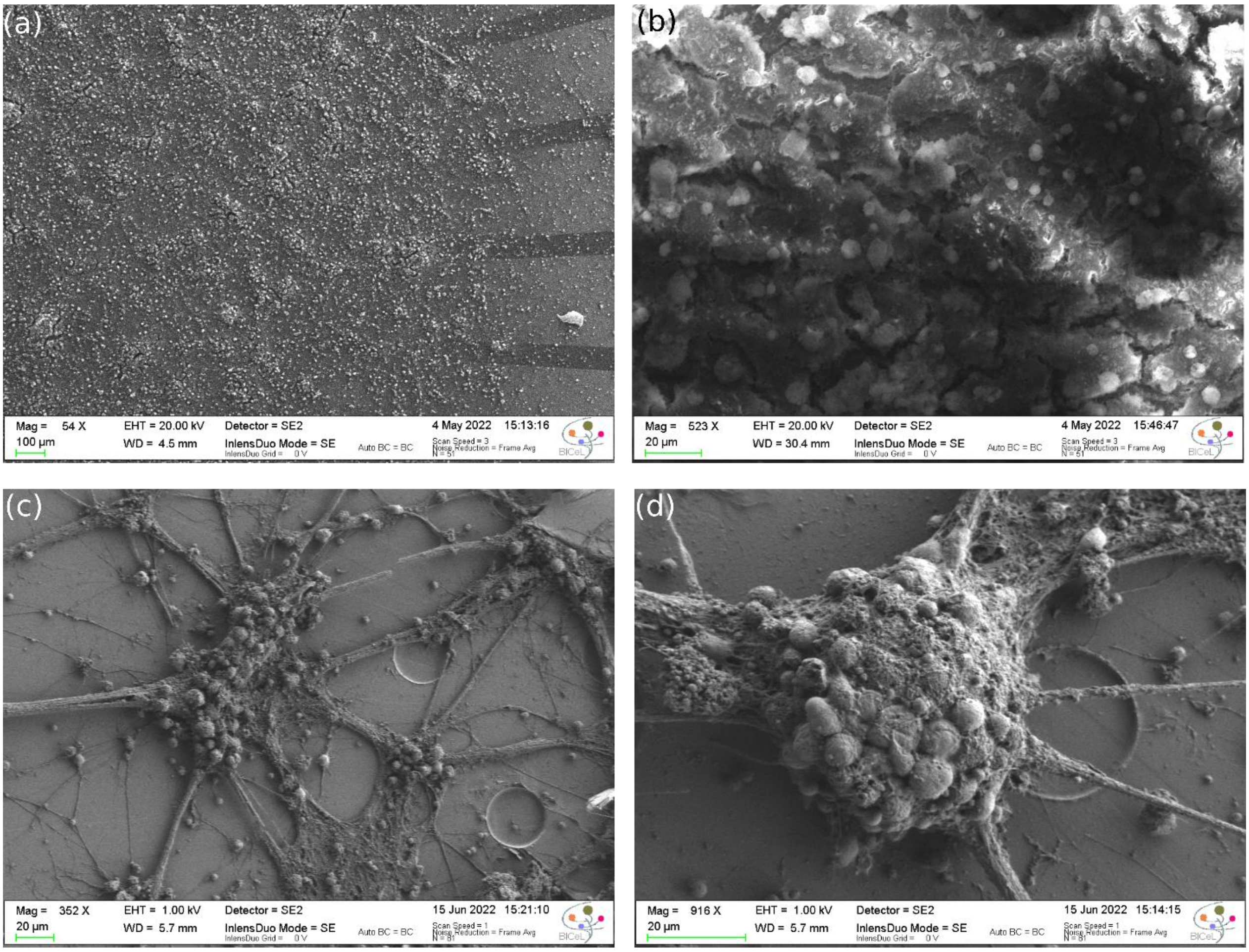

Figure 6.5 SEM images showing variable neural network densities. (a, b) OECT array with very dense network. (c, d) OECT array with sparse neural network. All images were taken at DIV 21. The difference in the neural network densities is due to less amount of cells deposited during cell culture.

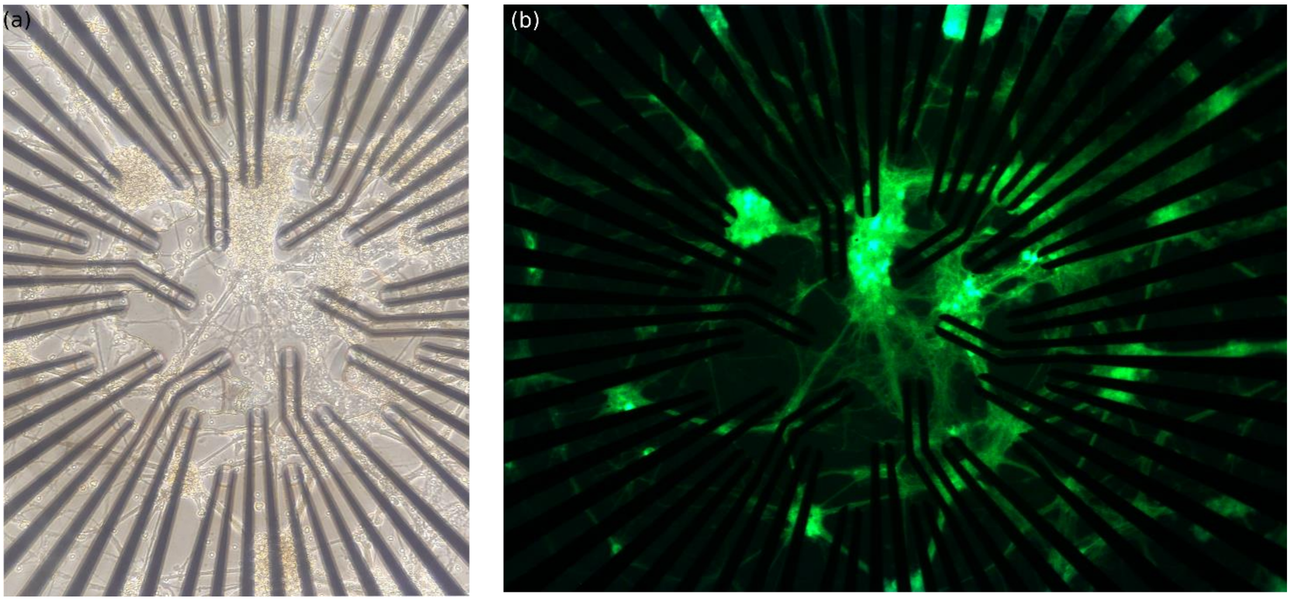

Figure 6.6 (a) Microscopic and (b) Fluorescent images for the OECT array with the sparse network.

Another hypothesis to explain this effect lies in the potential electroactive neurotransmitters secreted the neurons. Several studies showed that by using micro/nanoelectrodes, the electrochemically active neurotransmitters, such as dopamine (DA), epinephrine, and norepinephrine, can be directly detected using neurochemical electrodetection techniques (i.e. Cyclic Voltematery). Inspired by biology, electropolymerization of dopamine under alkaline conditions (PH ~8) has been proven to be a simple and effective method for surface modification of biomaterials [241–243]. In our case, to get more insight into redox processes at the OECT interface, we performed CV experiments such that the working electrode (WE) is the addressed OECT, counter electrode (CE) is the Ag/AgCl gate wire, and reference electrode (RE) is another OECT in the array. Looking at our CV curve in Figure 6.7, we can see that current decreases with the increase of the scanning potential while no reduction occurs when applying negative voltage. This oxidization without the ability to reduce back is correlated with the transfer characteristics curves shown previously (Figures 6.3 and 6.4). Additionally, these CV measurements highlight that either, the PEDOT:PSS is electrochemically reduced with < 0.6 V voltage stress, supported by the analytes (i.e. electroactive neurotransmitters) present in the culture, or PEDOT:PSS gets passivated by an electrochemically generated insulator (presumably such as polydopamine as reported by Wang et al. [242]) . AFM and SEM imaging of the OECT's channel before and after characterization could help correlating morphological changes with electrical characteristics in the case of electrochemically generated insulator on top of PEDOT.

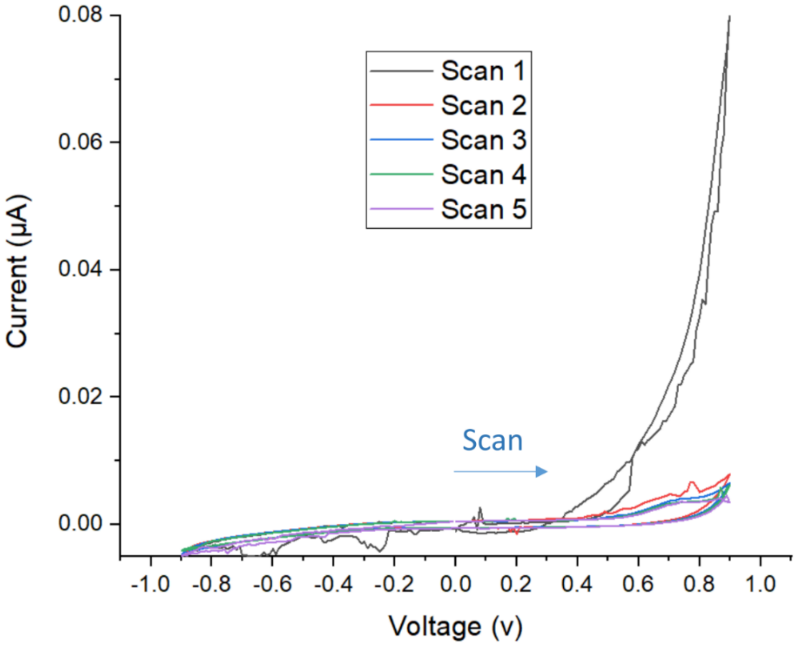

Figure 6.7 In situ cyclic voltammetry measurements performed while neurons cultured on top of an OECT. (Five scans)

Even without explaining the cause yet, we know now that after exceeding V_G = 0.6 V while characterizing the OECTs in the presence of neurons, we will negatively influence the performances of the OECTs. Therefore, for characterizing OECTs for future *in vitro* recording experiments, we used a gate voltage interval between zero and 0.6 V, as shown in Figure 6.8.

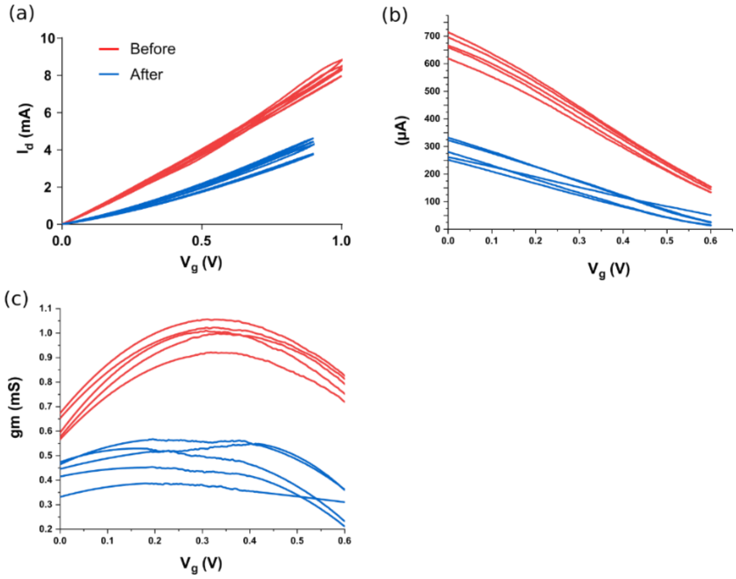

Figure 6.8 Biasing interval of OECTs for in vitro recordings. (a) Output characteristics, (b) transfer characteristics, and (c) gm curves for several OECTs (n=6) before and after neural culture for maximum Vg applied is 0.6v.

6.4 Impedance measurement during neural culture and device performances

Electrochemical impedance spectroscopy (EIS) measurements in neuroscience have been used to monitor cell growth, cell adhesion, and morphological changes during neuronal differentiation, to track cell apoptosis, and neural degeneration, and to distinguish among specific types of cells [244]. To get insight into the physical and electrochemical properties of the device during the interaction with the neural network, *in-situ* electrochemical impedance spectroscopy (EIS) was performed with 2D primary neurons cultured on top of the OECTs. Figure 6.9 shows the Bode's modulus plots of the impedance spectra measured from 1 Hz to 1 MHz. As shown in Figure 6.9 there is a clear change in the device's impedance behaviour after culturing neurons. Notably, the difference in the shape and amplitude of the impedance is above 250 Hz. Zhao et al. [245] reported monitoring the differentiation of neural stem cells derived from rat embryos through the changes in the electrical parameters using a microfluidic platform. The impedance values at two definite frequencies were collected: the impedance data at 1 kHz were used to determine the sealing properties of cells with the walls of the channel, while the impedance data at 100 kHz were used to quantify equivalent cellular membrane capacitance and cytoplasm resistance. This could be correlated to the changes in our impedance bode's diagram after seeding neurons. The difference in the impedance modulus around 1 kHz could be related to the sealing of neurons on top of the OECT. Additionally, we can see a decrease in the impedance at 100 kHz and above, representing more conductivity, which can be due to the cellular membrane capacitance. Interestingly, we can see higher instability of the impedance measurement, particularly at the interval 1 – 10 kHz interval, which could be attributed to the electrical activity of the active neurons affecting the measurements. EIS measurement requires linearity on passive elements, and although primary neural cell culture cannot be considered as a power supply but one hypothesis of the insatiability at the interval 1 – 10 kHz could be due to the electrical activity of the neurons (same effect shown in the phase plot in Figure 6.10d). This interval is in agreement with the frequency interval of the spiking activity (1ms). One hypothesis could be that this instability could come from a noise effect; however, it seems to be local at the specific interval, which supports the hypothesis that it is due to the neuronal electrical activity. Taking this possibility, it could be an interesting approach for future experiments to investigate more in detail with more systematic and reproducible experiments. This would propose EIS as a tool for sensing the spectral density of the neurons (sensing at frequency regime).

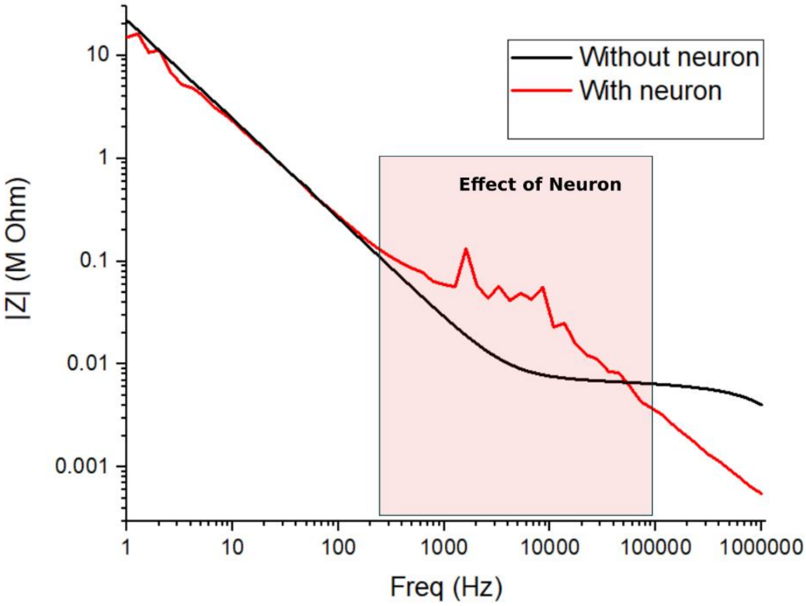

Figure 6.9 Bode's diagram of the impedance spectroscopy for an OECT before (without) and after neural culture (with) taken from the same chip.

EIS modelling was systematically made according to the equivalent circuits shown in Figure 6.10 to analyse the change of the electrode's electrical arameters in the presence of neurons on top. In Figure 6.10a the equivalent circuit use for device electrical modeling in previous section is depicted. As shown in Figure 6.10a, the low-pass filter shown in the first part of the impedance modulus (1 Hz to ~ 1 kHz) is modeled by the Resistor-Capacitor circuit (C_p and R_p), representing the capacitance and the resistance of the OECT. The plateau between 1 kHz and ~100 k Hz R_e represents the resistance of the electrolyte, and the low-pass filter show at high frequencies modeled by Resistor-Capacitor circuit (C_g and R_g) represents the capacitance and the resistance of the gate-electrolyte interface. Figure 6.10b shows the equivalent circuit for the measured device after culturing neurons. The model has been done referring to the neuron/microelectrode electrical analog circuit model from literature [14]. C_g and R_g represent the capacitance and the resistance of the gate-electrolyte interface, R_e represent the resistance of the electrolyte, C_{nj} and R_{nj} represent the non-junctional membrane of the neuron, $C_{membrane}$ and $R_{membrane}$ represent the junctional membrane facing the device, R_{seal} is the cleft resistance and C_{OECT} and R_{OECT}, represent the capacitance and the resistance of the device.

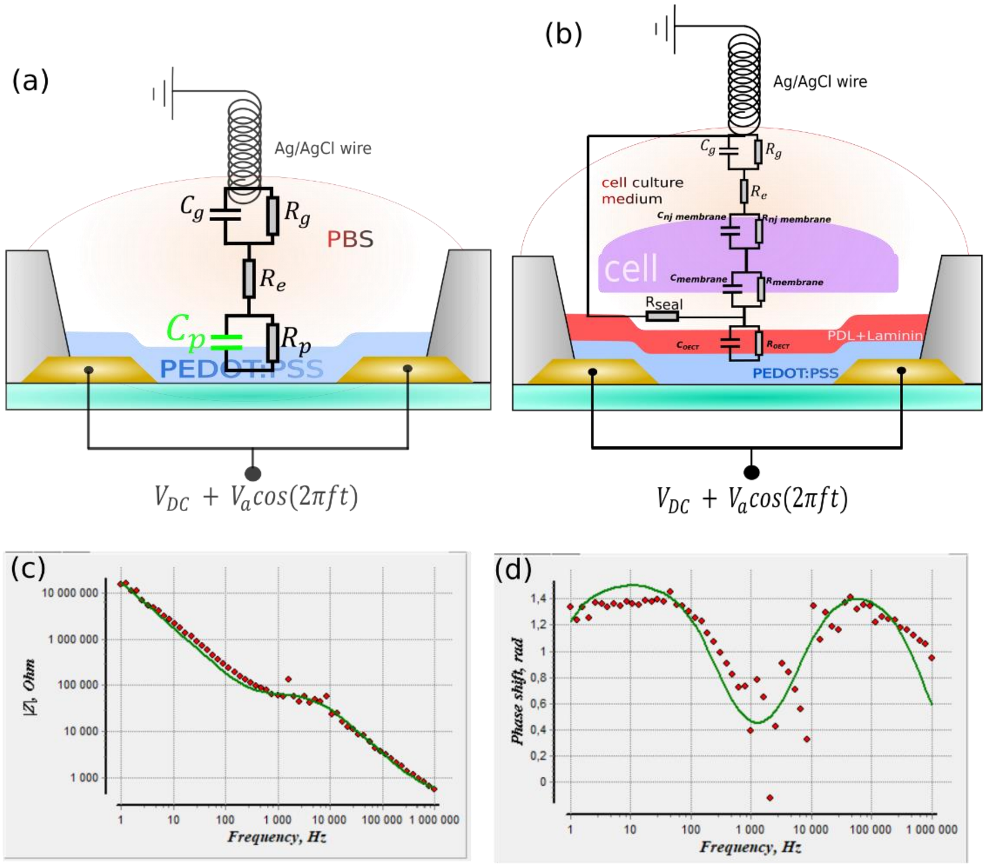

Figure 6.10 Equivalent electrical circuit for an OECT (a) without and (b) neuron cultured on top. (c, d) Bode's and Phase diagram of the impedance spectroscopy of an OECT with cultured neuron (for the case in (b)) showing the measured and fitted examples. Red: Measured, green: fitted.

Table 6.1 shows the values of the electrical parameters of the model. As shown in the table, the values of the R-C elements of the device, electrolyte, and gate did not change significantly, which is interesting to have a systematic modeling study for determining the effect of the additional parameters (i.e. neuron) on the impedance. Surprisingly, the value of the seal resistance is considered to be very low (60 kΩ); however, , the junctional membrane capacitance is considered high compared with the literature (1nF) [14]. The impedance measurement shown in Figure 6.9 is more complex than in the case of a single cell investigated in the literature [14]. So far, we have difficulty to evaluate how many cells are covering the device due to the limitation of mastering biology in terms of the density of the cultured neural network.

Table 6.1 Table showing the values of the fitted electrical parameters in Figure 6.10 for an OECT before and after culturing neurons

	R_{OECT}	C_{OECT}	C_g	R_g	R_e	R_{seal}	C_{nj}	R_{nj}	$C_{membrane}$	$R_{membrane}$
Before Neurons	80 MΩ	10 nF	40 nF	7,5 KΩ	500 Ω	*	*	*	*	*
After Neurons	80 MΩ	10 nF	200 nF	1 KΩ	500 Ω	60 KΩ	992 pF	0,47 MΩ	1 nF	3 MΩ

Figure 6.5 shows SEM images for different densities cultured on top of multiple OECT arrays. We can see that there are two kinds of growth: dense networks of cells (Figure 6.5a and b) or a sparse network (Figure 6.5c and d). Additionally, the size of cells in our neural cultures was <10 µm according to the SEM images shown in Figure 6.5, which highlights the fact that we could have multiple neurons on top of one OECT. This could alter the parameters R_{seal} and membrane capacitance differently from one single cell interaction reported in the literature. In the upcoming sections, by exploiting the impedance measurements and modeling, we performed electrical simulations to explain more the reason behind the R_{seal} and $C_{membrane}$ values and investigate its effect on the coupling coefficient between neuron and device.

We want to mention that according to our EIS measurement setup, this model in Figure 6.10b can be considered as a passive electrode in which we are wiring the source and drain and grounding the gate. Here we divided the simulations into two sections: (i) when considering the device as MEA, and (ii) as OECT. Surely, the values of the parameters extracted from the model are the same in both cases, and more explanations will be introduced below about the difference in both cases.

The master student *Mona Ghazal* performed the statistical electrical simulation graphs in Figure 6.13, Figure 6.14 and Figure 6.16 using Matlab.

(i) In case of passive MEA:

Figure 6.11 shows the circuit implemented for simulations where the electrical activity of the neuron is represented by AC voltage signal. For MEA case, an amplifier and stray capacitance circuits was added in series to the electrode. The output voltage has been measured at the electrode as what has been done in literature for modeling 3D MEA (*chapter I*) [14].

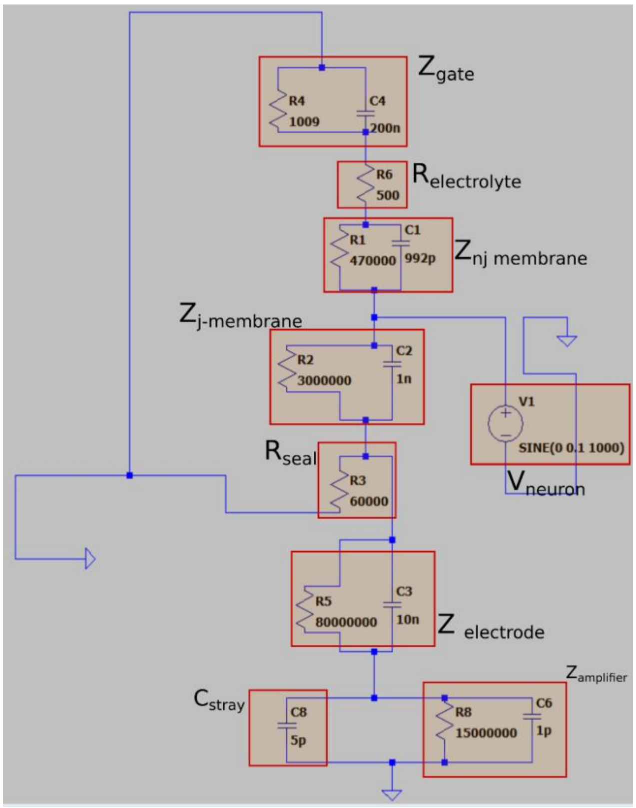

Figure 6.11 Electrical circuit for the "MEA" case used for the simulations

Figure 6.13, shows the coupling coefficient of the system that has been simulated with 4 different values of junctional membrane capacitance and, in each case, with 4 values of R_{seal} and 7 different values of electrode capacitance. Clearly, what impact the coupling coefficient value is R_{seal} and $C_{membrane}$ values. The higher their values, the more increased the coupling coefficient in agreement with[14]. The electrode impedance value showed opposite results from what is expected from the literature where decreasing impedance increase coupling. In the literature [14] (*chapter I*), the effect of impedance on coupling for electrode's impedance in monitored between 1 MΩ and 100 GΩ and from 1 to 1 kHz (Figure 6.12d).

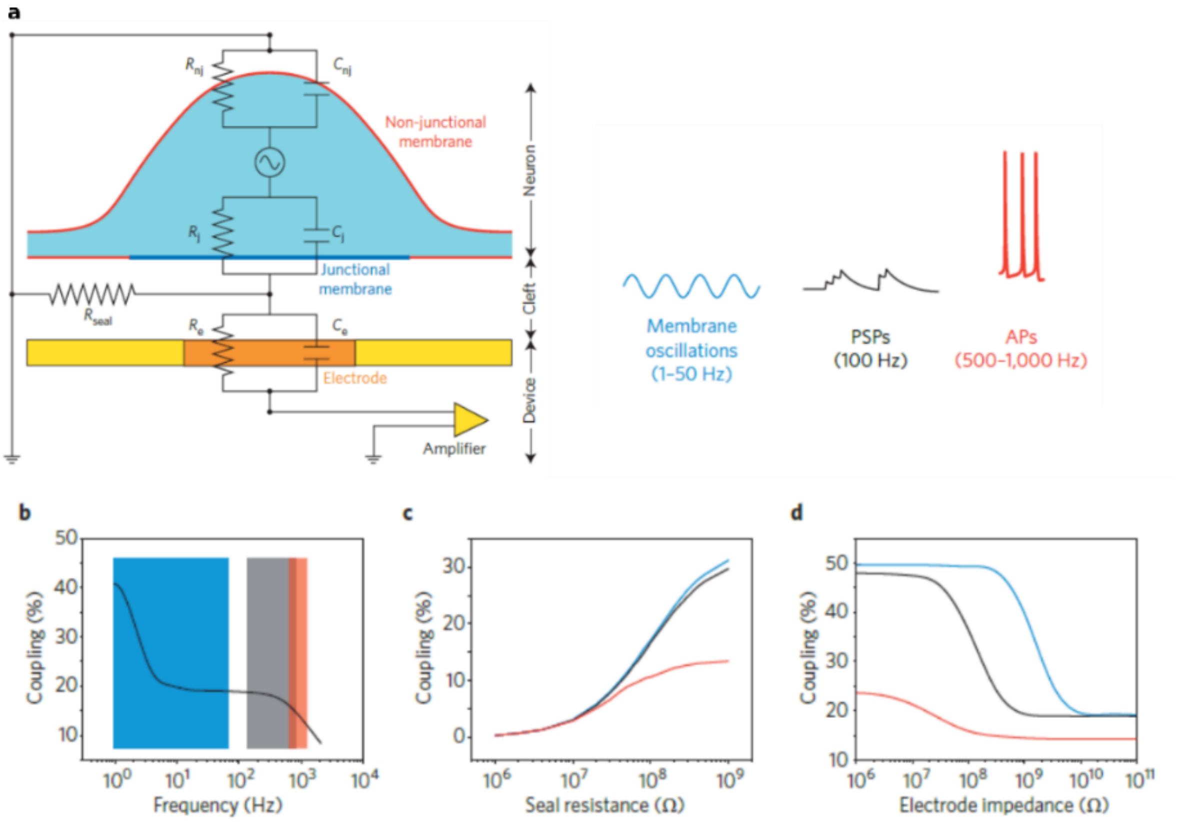

Figure 6.12 Neuron/electrode interface. (a) Left: schematic showing the analog electrical circuit of the neuron/electrode interface. Right: An illustration showing the different type of recorded signals such as low-frequency signals representing membrane oscillations, medium frequencies representing postsynaptic potentials (PSPs) and fast frequencies representing APs. The electrical coupling coefficient of the neuron/electrode as function of (a) type (frequency) of the signal, (b) seal resistance (b) and the electrode's impedance. Figure adapted from [14].

As shown in Figure 6.12d, the coupling coefficient starts to be constant with impedance after going lower than 10 MΩ. Hence, in our study, simulations by scanning different impedance values was performed (i.e. from 70 MΩ down to 1.5 kΩ at 1 kHz) and showed its effect on coupling for large frequency intervals from 1 Hz to 1 M Hz. At 1 kHz (APs we record after filtering), the impact of the electrode capacitance value is not significantly affecting the coupling coefficient at high $C_{membrane}$ values (i.e. 1nF and 100 pF). For lower membrane capacitance values (i.e. 10 pF and 1 pF) significant effect of electrode capacitance on the coupling coefficient was observed such that lower capacitances give higher coupling. This was particularly seen at high frequencies (above 100 kHz), not measured during *in-vitro* recording from neurons. For the recorded frequency interval (300-3000 Hz), the counterintuitive effect of capacitance has been shown only in cases with a coupling coefficient higher than 60% (very high R_{seal}), which is 60 mV of output voltage. This case could occur while using patch-clamp or nanowires, for example. These simulations could open new perspectives in re-thinking about choosing the values of impedance for microelectrodes, especially in high R_{seal} cases (i.e. 3D nanowires) by finding the optimum point between lowering impedance but also still in high coupling coefficient values (lower capacitance).

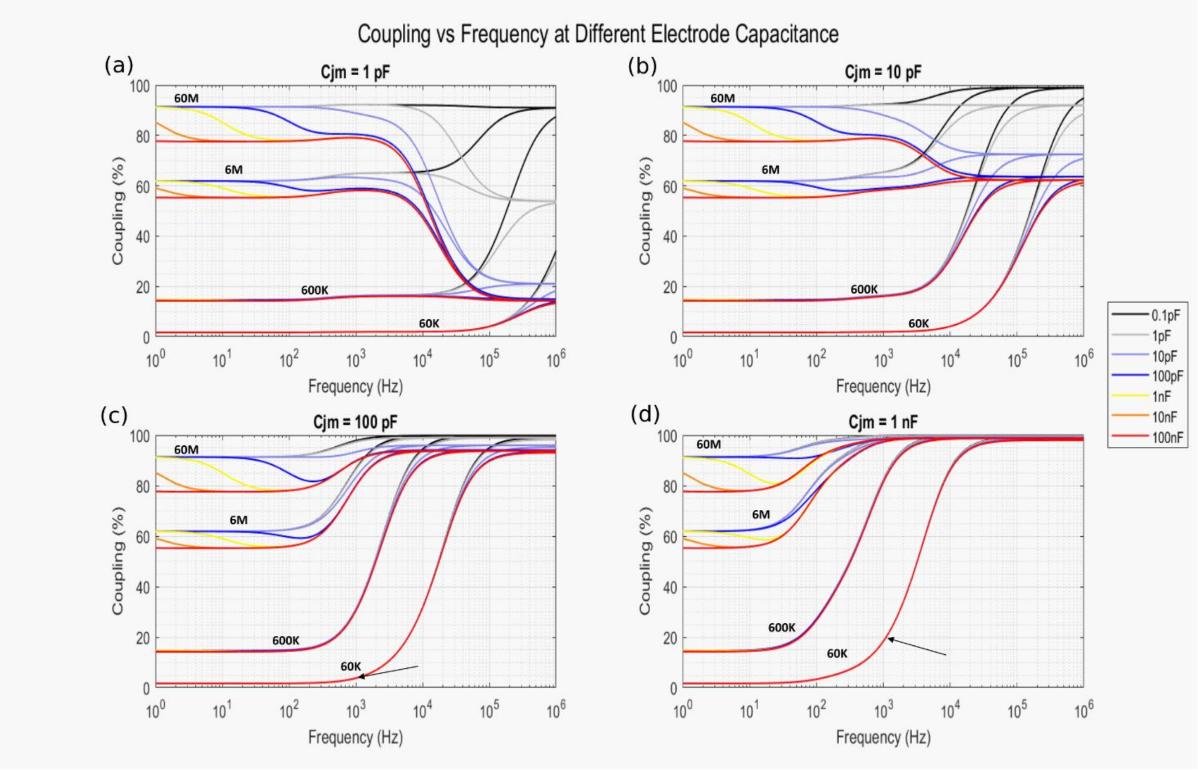

Figure 6.13 Simulation results for the case of MEA. The coupling vs frequency curve at different electrode capacitance and Rseal values such that the membrane capacitance equals (a) 1pF, (b) 10pF, (c) 100 pF and (d) 1nF. Black arrow in (c) and (d)) correspond to the black and red cross in Figure 6.14 respectively

Figure 6.14, shows extracted curves from Figure 6.13 taking into consideration one frequency value 1 kHz which contributed to the frequency of APs. This further analysis will simplify the analysis to concentrate on explaining the effect of R_{seal} and membrane capacitance in case of passive electrode. Performing simulations with the parameters extracted from the impedance model ($C_{electrode}$ = 10nF, R_{seal} = 60 kΩ, and $C_{membrane}$ = 1 nF) we can see that at 1 kHz, the coupling coefficient is 20% (red cross in Figure 6.14) corresponding to 20 mV output voltage amplitude which is not the case that we got from the passive MEA measurements from previous chapters. However, by looking at the fitted curves in Figures 6.10c and d, it seems that the fitting is correct, and consequently, we should expect valid values for the parameters. This supports the claim when we may consider multiple cells in our case during the EIS measurements. The values we get could probably correspond to the values where there are numerous cells on top of a device and not one single cell, which means that we are overestimating the cell junctional membrane value. Assuming we are overestimating by a factor of 10 by considering we have 10 cells on top of our device by changing the $C_{membrane}$ capacitance value from 1nF into 100 pF. Looking at the graphs in Figure 6.14 , the coupling coefficient decreased from around 20% to about 2.5%, which is a decrease by the same factor of reducing the cell capacitance (black cross). This supports the hypothesis that during the measurement, we are overestimating the values comparable with the model that supposes one cell, which will have much higher leakage. Here we are pointing toward the fact that these measurements have some limitations because we are measuring multiple cells simultaneously, which means that these limitations are significantly changing the R_{seal} values. If we correct this measurement by targeting one single cell for each device, it is a great possibility that the value of R_{seal} is different and would be comparable to the ones in literature with much higher values than 60 kOhm. Another limitation in our case for having this low value of R_{seal} is the use of spongy material. To explain, in the neuron/electrode electrical circuit model, the R_{seal} is calculated in around 2nm separation between the metallic electrode and neuron, while if having spongy material such as PEDOT could raise the question if we are really good for R_{seal} because we have plenty of room for the ionic current to flow out of the gap through the device. More systematic and statistical EIS measurements with neurons on top of the OECT/microelectrode are important in future work to give more solid explanations.

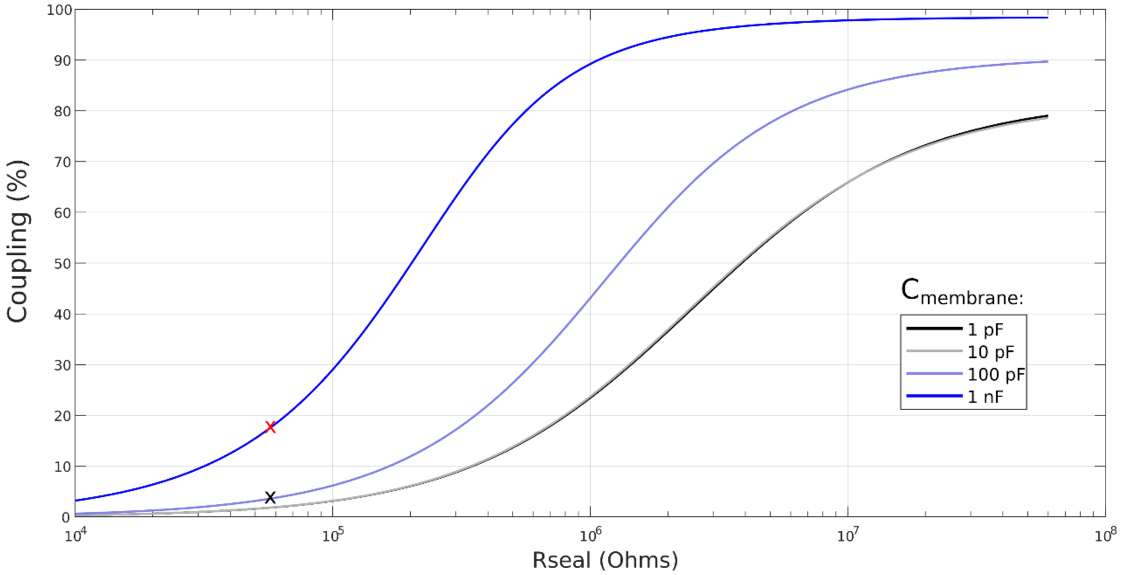

Figure 6.14 Simulation results for the case of a microelectrode ($C_{electrode}$ = 10 nF (the extracted from our model)) at 1 kHz. The coupling vs R_{seal} at different capacitance membrane values (1pF, 10pF, 100 pF and 1nF)

(ii) In case of OECT:

In MEA, the amplifier is separated from the electrodes, while in the case of transistor or OECT, the amplifier is considered the transistor itself; thus the amplifier and stray impedances from the model was removed. Unlike the MEA case, the capacitance of the OECT plays a significant role in changing the coupling coefficient at the recorded frequency (1 kHz), no matter membrane capacitance value (Figure 6.16). Hence, the effect is substantial even in the low coupling coefficient values (below 10% and even 1%), which we expect from planar geometry devices. In this case, the capacitance of the membrane and capacitance of OECTs are in series then the drop of voltage will go to the smallest capacitance. Here, if we want the highest values of coupling, we need the lowest values of capacitances as shown in all the graphs of Figure 6.16. As we can see in Figure 6.16, the device’s capacitance directly affects the amplitude and bandwidth of the coupling.

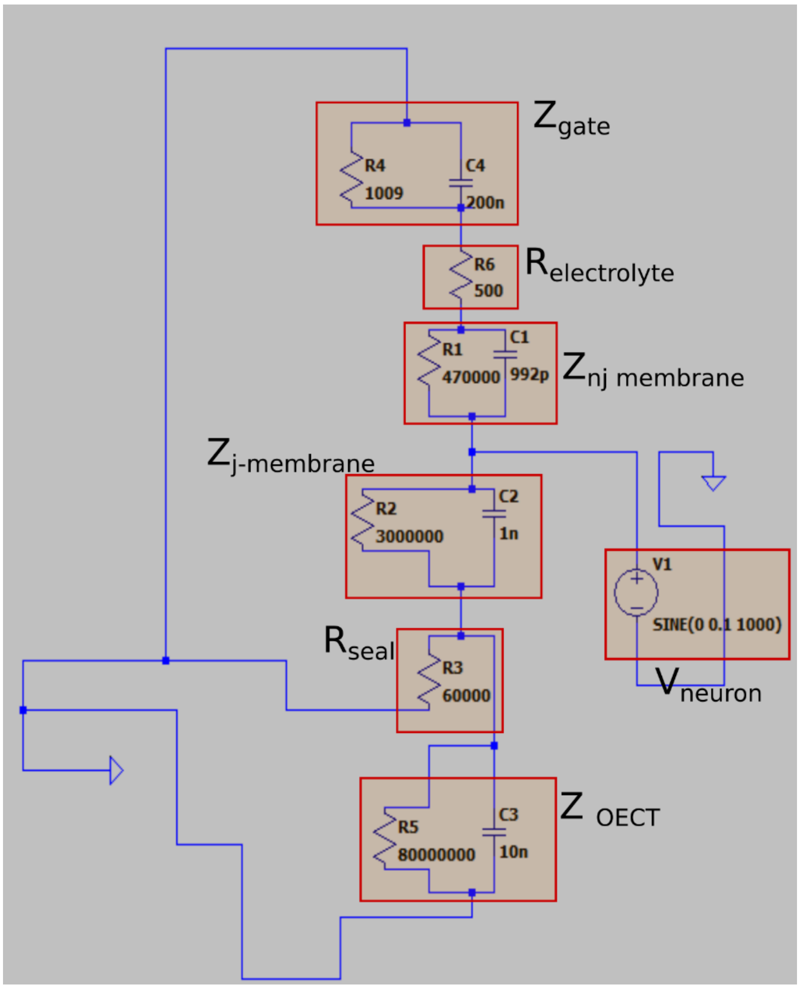

Figure 6.15 Electrical circuit for the "OECT" case used for the simulations. We can see that the amplifier and stray capacitance elements are removed.

For OECTs, these results are counter intuitive with the idea of increasing capacitance to increase the transconductance values, which is the amplifying performances of the recorded signal which seem that here it is not an attractive solution. Another important counter intuitive discussion is about the contribution of the device's noise to the measurements. As mentioned previously, the noise values are in function of the capacitance or the size of the device, where the larger devices (or higher capacitance), the lower the noise. Here are three parameters to optimize the recording from an active sensor or OECT but with counter intuitive effects. A more in-depth model analysis of statistical EIS measurements correlated with *in-vitro* recordings from different OECTs with different geometry, capacitance, and gm would help us to find an optimal point for fabricating devices with the best possible coupling, lower noise, and higher amplification.

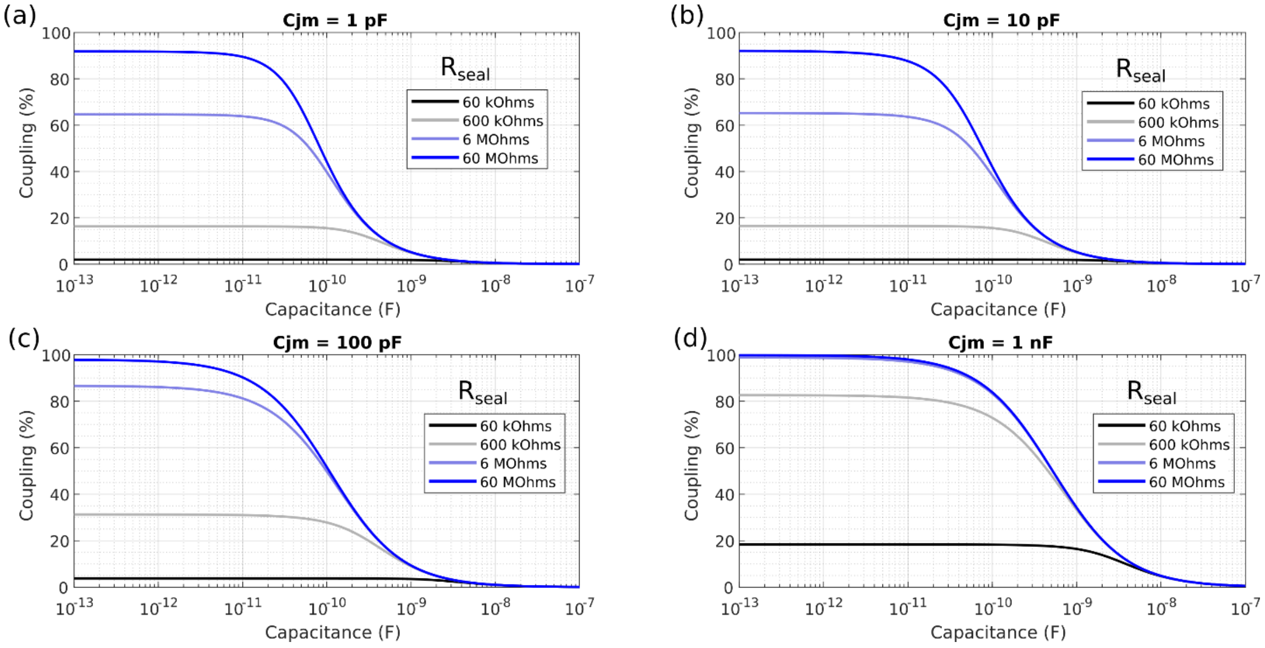

Figure 6.16 Simulation results for the case of OECT at 1 kHz. The coupling vs OECT capacitance curve at different Rseal values such that the membrane capacitance equals (a) 1pF, (b) 10pF, (c) 100 pF and (d) 1nF.

6.5 In-vitro recordings from primary neuron culture

After presenting the electrical behavior of an OECT in the presence of *in vitro* neural culture on top, *in vitro* extracellular recordings of a 2D cultured neural network by using OECT (active sensor) was performed. Primary neurons were cultured on top of an OECT array to do so.

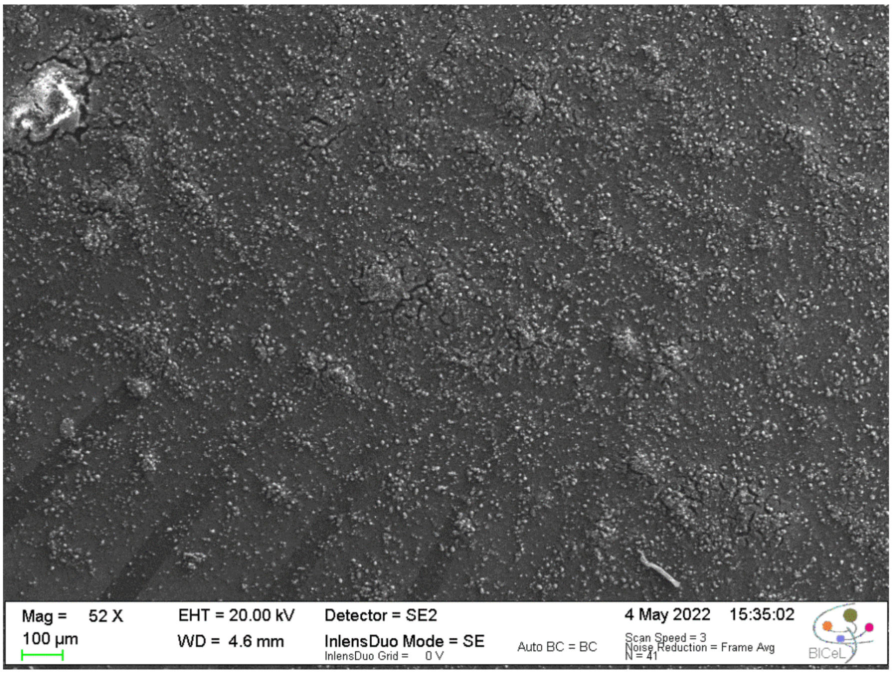

Figure 6.17 SEM image of dense neural network cultured on top of the OECT array for in vitro electrical recordings

To assess the culture viability, we first used the OECT array as a passive MEA (no drain or gate biasing). Each source and drain were stressed as single microelectrodes and we performed recording using the commercial Multichannel System setup (as used in passive MEAs chapters). Figure 6.18 shows one example of a time series for an OECT recorded as a passive microelectrode with spike-burst electrical activity presenting a mature and active neural network.

Figure 6.18 Recording of neuronal activity by using an OECT as a passive microelectrode.

Figure 6.19 shows the electrical characteristic of an OECT from an array interfaced to 20 DIV neural networks before and after culture. For *in vitro* recordings, the transistor was connected in series to a 500 Ω load resistance as a voltage divider setup to convert the output current into voltage to be monitored (see Methods) such that $V_{out} = R_l * I_{ds}$ or $\mathrm{V_{out}} = \left(\frac{\mathrm{R_l}}{\mathrm{R_l+R_{OECT}}}\right)\mathrm{V_{DS}}$, where $\mathrm{R_l}$ is the load resistance, I_{ds} is the output drain current and $\mathrm{V_{DS}}$ is the drain-source biasing voltage.

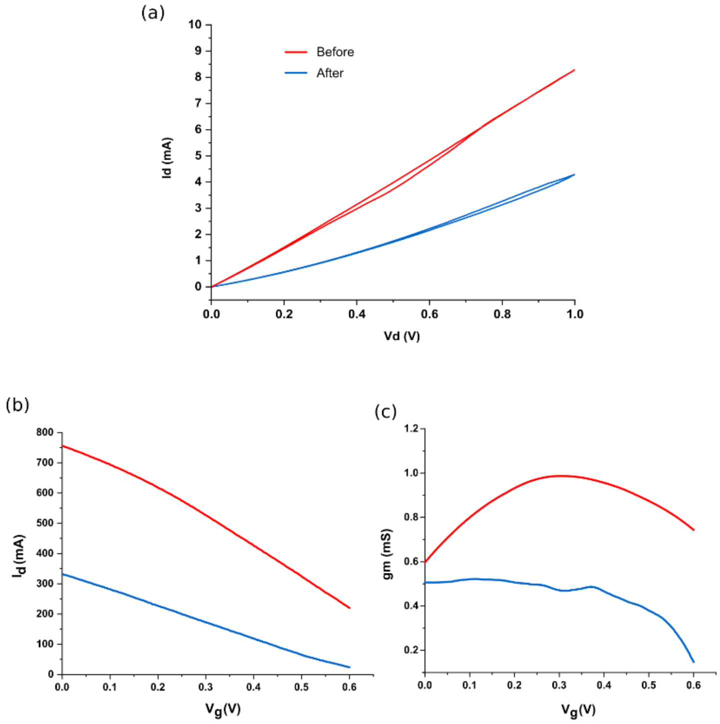

Figure 6.19 (a) Output characteristics, (b) transfer characteristics and (c) gm measurements for the OECT device used for in vitro recordings. Red: before neural culture. Blue: after neural culture.

For the detection of neural activity, the transistor's working point was set at the highest transconductance, and the source-drain current was recorded at constant $\mathrm{V_{DS.}}$ It is worth pointing out that the voltage applied across the drain and gate will not be directly the working point voltage. For example, to bias the source-drain with 100 mV (the voltage we use for all the DC electrical characteristic measurements), we apply drain voltage $\mathrm{V_D}$ to get $\mathrm{V_{DS}} = \left(1 - \frac{\mathrm{R_l}}{\mathrm{R_l+R_{OECT}}}\right)\mathrm{V_D} = 100\ mV$ where $\mathrm{R_l}$ is known and $\mathrm{R_{OECT}}$ is extracted from the output characteristic curve. Similarly, for choosing the $\mathrm{V_{GS,}}$ we apply gate voltage $\mathrm{V_G}$ to have the desired $\mathrm{V_{GS}}$ wanted such that $\mathrm{V_{GS}} = \mathrm{V_G}$ (applied) – $\mathrm{V_S}$ (extracted previously). Therefore, we avoided performing measurements by setting the $\mathrm{V_{GS}}$ at higher voltages (i.e. above 0.2 V) because it may demanded high values of $\mathrm{V_G}$ to applied which may stress the neurons.

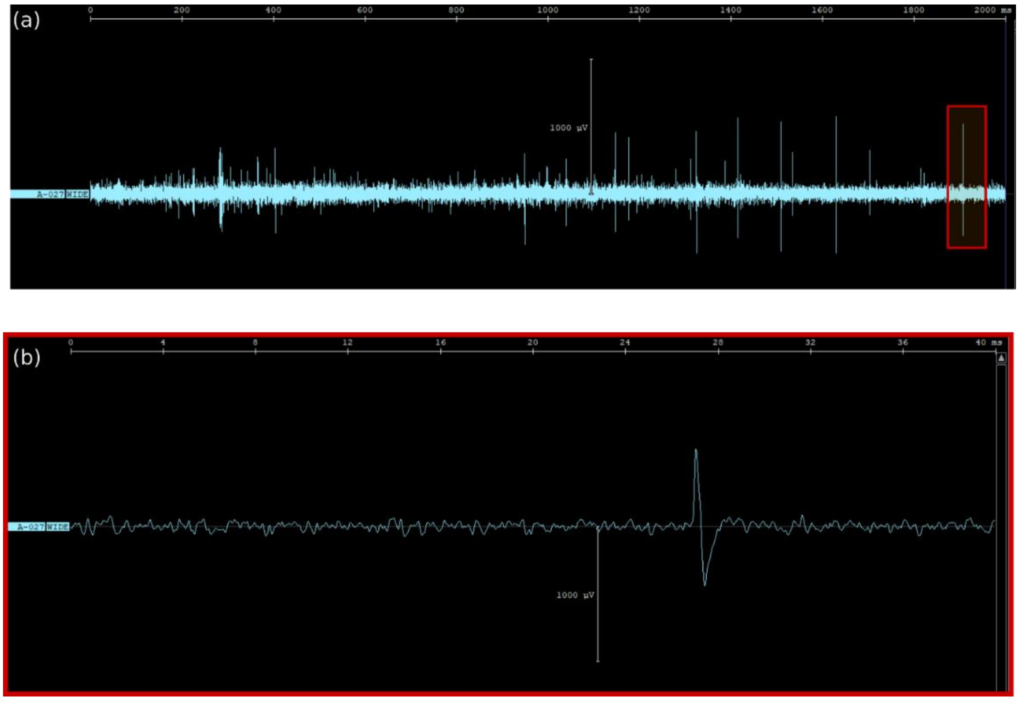

Figure 6.20 (a) Recording neuronal activity by using an active OECT at $V_G = 0$ ($g_m = 0.5$ mS), (b) Zoomed in window showing the spike marked with the red rectangle in (a).

Figures 6.20a and b, show time series showing spontaneous burst-spike activities of a neural culture at DIV21 from an OECT. The recorded trace (Figure 6.20) exhibits short negative and positive pulses, which can be attributed to short negative and positive pulses in the extracellular medium coming from the neuron. The polarity and the shape of the detected signals shown in the waveform in Figure 6.21a correspond to the expected extracellular potential spike. Looking into the interspike interval (ISI) histogram in Figure 6.21b, the shape of the distribution resembles to multiunit activity from neurons because more than 1% of the ISIs were less than 2.5 ms [246]. The ISI distribution coming from single-unit activity usually maintains a refractory period of 0% (or less than 1%) between 0 and 2.5 ms [246]. Since we did not perform spike sorting (1 OECT) to differentiate single unit activities, these waveforms and the ISI results are expected. Similar ISI distribution results we obtained from passive MEAs used and validated in *chapter IV* when we do not perform spike sorting (Figure 6.22).

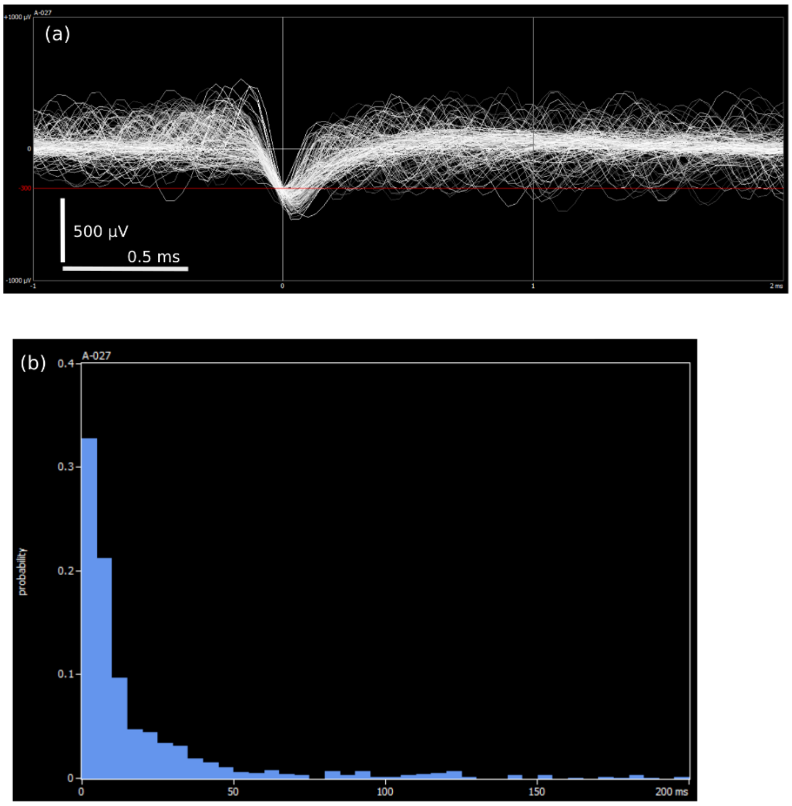

Figure 6.21 (a) Waveform showing the superposition of all detected spikes from Figure 6.20 using the INTAN RHX software after thresholding step (10*RMS of the background noise (red line)) (b) Histogram showing the distribution of the interspike interval (ISI).

Indeed, by looking at the recordings in Figure 6.20, we can see that there is a strong contribution of noise in the recordings with RMS ~ 30 µV, which makes it difficult to record low amplitude spikes. The contribution of low-frequency noise (flicker noise, see *chapter IV*) can be excluded from this case since these are recordings filtered by a 300 – 4000 Hz band-pass filter. Regarding the biological noise, as shown in the recordings from passive OECT (as a MEA) in Figure 6.18, we can see that the noise is very low ~ 3 µV, coming mostly from the culture itself and its environment. Accordingly, the high noise values obtained can be due to a non-shielded home-built PCB circuit that contains the leading wires and voltage divider setups. For future work and better recordings, it is essential to implement electrical circuit with more in depth noise experiments to neglect its effect on the recordings as much as possible similar to the commercial recording setups used for passive MEAs. This is considered an essential step for the future for a more reliable recording system by using transistors in general and specifically OECTs.

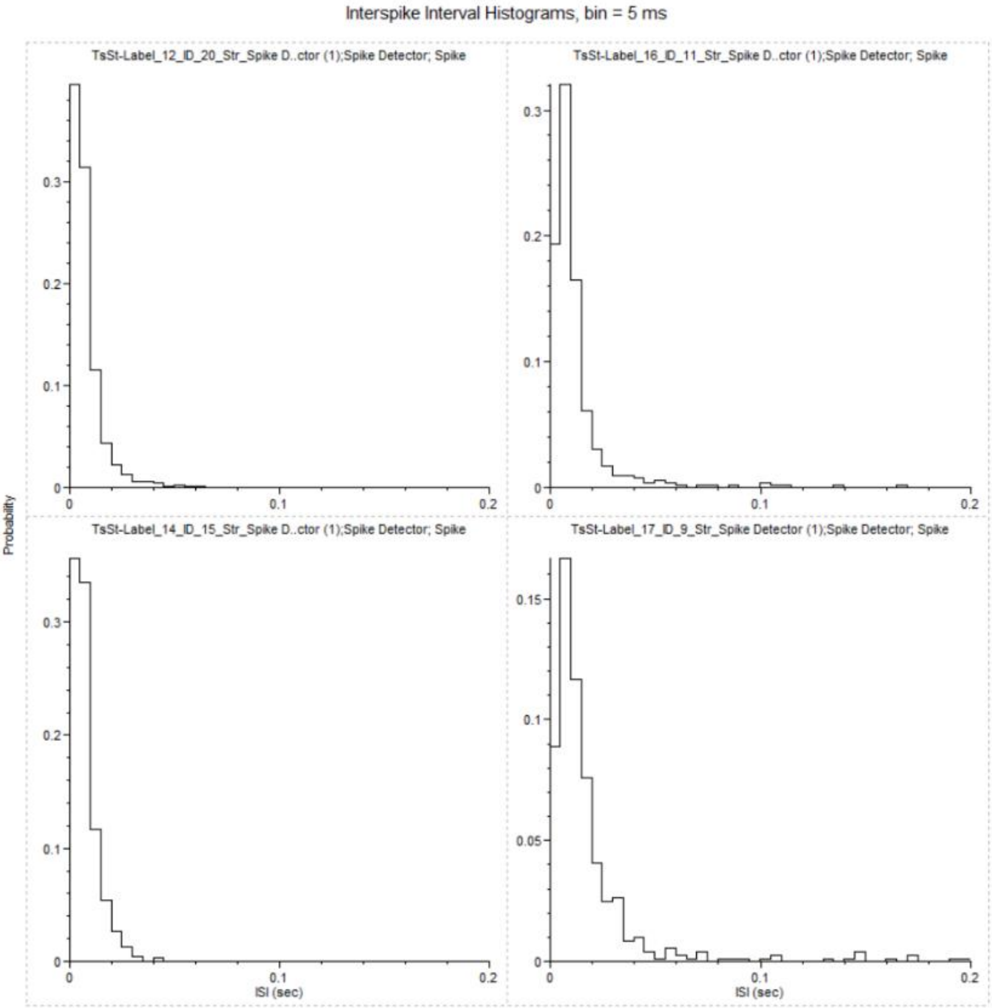

Figure 6.22 Histogram showing the distribution of the interspike interval (ISI) for recordings coming from four different microelectrodes from the MEA investigated in Chapter IV

Using the transconductance g_m at the set transistor working point V_{GS} = 0 V with g_m = 0.5 mS (Figure 6.19), the extracellular potential at the interface can be calculated to $V_{extra} = \frac{I_{ds}}{g_m}$ with transoconductance measured in presence of neurons. The output voltage amplitude (V_{out}) is around 400 ± 50 µV (Figure 6.21a), and spike duration t_{spike} = ~ 1 ms which is in agreement with the APs pulse width (Figure 6.21a). With R_l = 500 Ω, this makes the $\Delta I_{DS} = \frac{400\ \mu V}{500\ \Omega} = 800\ nA$ and thus $V_{extra} = \frac{800\ nA}{0.5\ mS} = 1.8\ mV$. Accordingly, the coupling coefficient would be 1.8% ($\frac{V_{extra}}{V_{in}} = \frac{1.8\ mV}{100\ mV} = 1.8$). The SNR maintained from this recording using an OECT is $20\log_{10}(\frac{V_{out}}{V_{noise}}) = 22.5\ dB$, which is considered lower than that from MEA due to the high noise contribution. Thus, the recording noise has to be further reduced by developing of adapted low noise amplifiers. To this end, if the noise coming from the recording setup is reduced to be similar to the one used for recording MEA, the SNR ratio of the recordings from OECTs could be significantly multiplied.

As shown in the transcoductance curve in Figure 19, the max g_m value is in constant between 0 and 0.4 V_{GS} values. Two different in vitro recording experiments has been done for the same device at V_{GS} =

0.1V and V_{GS} = 0.2 V (Figure 6.23) where the gm value did not change from 0.5 mS. Similar to the previous case where V_{GS} = 0V, the output voltage (V_{out}) is also around 400 V, which points out the effect of g_m on the output amplification (same g_m. same amplification). Definitely, comparing different OECTs with different g_m values from the same array and exposed to the same neural culture is very important for future perspective to investigate more the effect of gm in coupling.

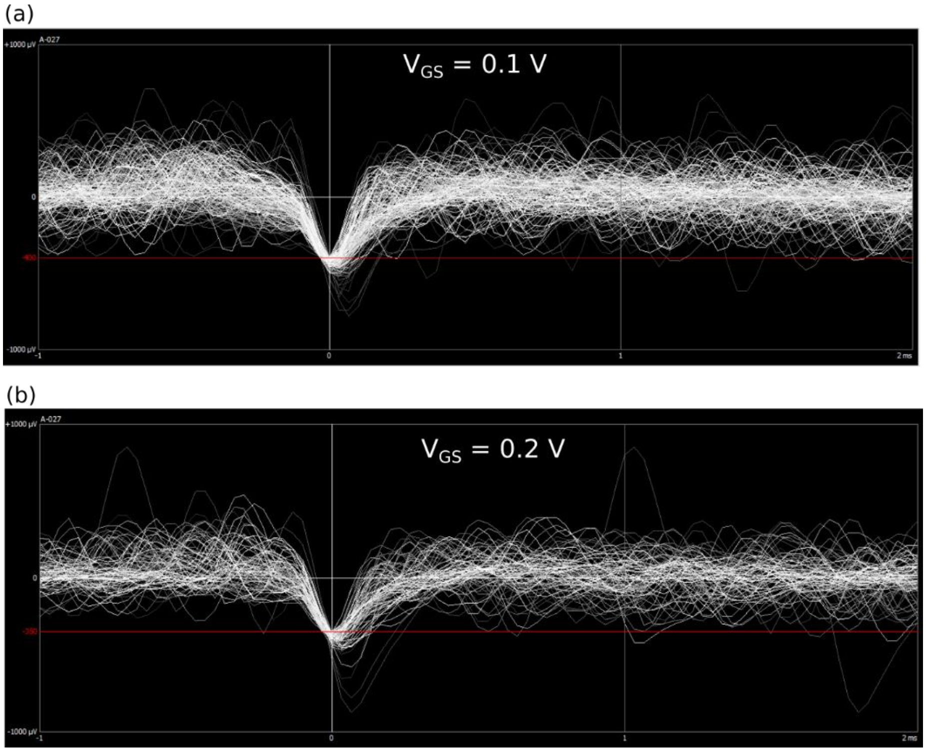

Figure 6.23 Waveform showing the superposition of all detected spikes from the recording of the same device shown at Figure 6.21 at (a) V_{GS} = 0.1 V and (b) V_{GS} = 0.2 V using the INTAN RHX software after thresholding step (10*RMS of the background noise (red line))

The rhythmic behavior of the electrical activity recorded by an OECT (active sensing) was clearly different from when it is recorded by a passive electrode (as a MEA). As a MEA, the electrical activity showed organized and repetitive rhythmic behavior, however, as an OECT the electrical activity showed random spike-burst behavior indicating long burst activities and single spike activity without specific rhythm (raster plot in Figure 6.24). One hypothesis could be related to what has been proposed by Fromhertz, such that the current flowing through the transistor beneath the neuron gives rise to an extracellular voltage where its stimulus can affect the cell membrane leading to opening the voltage-controlled ion channels, and thus AP may be elicited [100]. Therefore, the extracellular voltage arises from a superposition of all capacitive and ionic currents in the interface. The raster plot shown in Figure 6.24 clearly shows different behavior supporting this hypothesis.

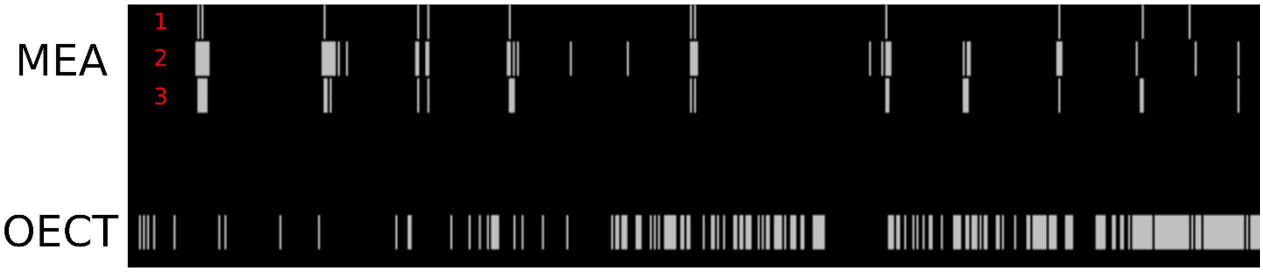

Figure 6.24 Raster plot showing the spiking activity of the same neural network while recording them as active OECT or passive microelectrodes. (As passive microelectrode, we showed 3 different devices)

Additionally, we investigated the effect of the DC bias of the gate on the rhythmic behavior of the electrical activity recorded by an OECT. Figure 6.25 shows a raster plot showing the spiking activity of the same OECT with different V_{GS} biasing values. We can see that the spiking activity of the neurons chamges with the different applied voltage. The different between the spiking activity at VGS = 0 V and VGS = 0.1 was not significantly different: ~550 spikes at VGS = 0 V and ~ 690 spikes at VGS = 0.1 V (1 minute of recordings). However, the clear change in the activity was when we applied a V_{GS} = 0.2 V, where the spikes number decreased notably from ~690 spikes at V_{GS} = 0.1 V down to ~ 70 spikes V_{GS} = 0.2 V for 1 minute of recordings. Several hypotheses can be proposed for this significant change: (i) we are stressing the neurons due to the higher V_G applied, in which the neuron's activity decreased. (ii) or it is the effect of the DC bias that controls the current value passing through the channel, which can affect the electrical activity, as explained in the previous paragraph. This would pave the way for an interesting approach for recording and stimulating the neural culture through the DC bias of the device rather than pulse stimulation approaches. One example of future approaches is to bias the OECTs in the array with different values to tune and control the electrical activity of the neural network that would be dedicated to learning and memory applications.

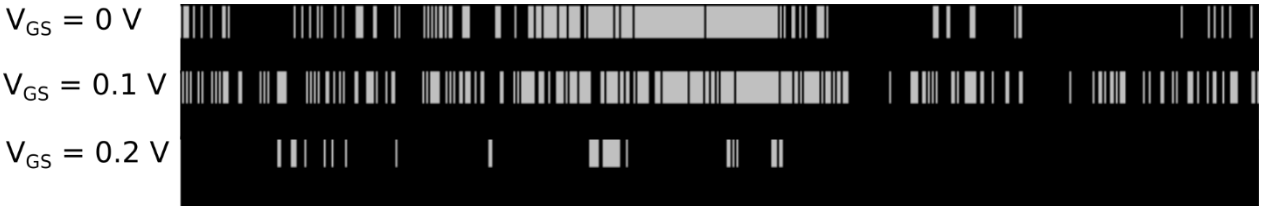

Figure 6.25 Raster plot showing the spiking activity of the same neural network while recording from same at three different applied V_{GS} values.

6.6 Conclusion

In this chapter, we reported the electrical characterization of an OECT in the presence of primary neural culture, *in situ* EIS measurements correlated with modeling, and *in vitro* extracellular recordings from neurons using OECTs. Bio-coatings are not significantly affecting the OECT performances. Investigation on the effect of the neural culture on the OECT electrical characteristics showed the effective biasing interval without negatively influences the performances. More insight was obtained into the electrochemical characteristics of the device in the presence of neurons by performing *in situ* EIS followed by electrical modeling. The correlation between fitted parameter values and electrical simulation revealed several limitations we will face while using transistors or OECTs for *in vitro* recordings. A very important point and main limitation is that we still need to find an optimum point between higher amplification (higher C higher g_m) and higher coupling (lower C) opposing the state-of-the-art direction of always lowering the device impedance. As shown in our analysis and the work from the literature it is still vague which direction we should take to have better recordings from a transistor. Do we concentrate on increasing capacitance for higher g_m and lower noise? On the other hand, we focus on decreasing capacitance to have a higher coupling coefficient with the neuron. Increasing the g_m of the device by electropolymerizing materials with higher mobility without tuning its capacitance, as shown in our technique in *chapter V* is an interesting and flexible solution in case increasing a lot the capacitance would cause some limitations. In this case, we agree that our approach is not universal, but we would like to emphasize that the methodology still applies to different reference electrode materials and devices geometries. Experimental parameters will need to be adjusted, but there is no blocking point in transferring this approach to other electrode materials.

Finally, we showed preliminary results of *in vitro* recordings from primary neurons using OECT. Such measurements have not been reported in the state-of-the-art yet; however more statistical and reproducible results are demanded. More optimization for the electronic recording setup needed to reduce the noise and maintain more reliable recordings.

Despite these encouraging results, we were always pointing out several challenges and limitations to face for addressing OECT for *in vitro* recordings of neurons.

Conclusion and perspectives

In this manuscript, several questions have been addressed for optimizing our capabilities to interface neurons at different levels, from circuitry to bio-nano interface levels. Here I will present the main results achieved, highlight its challenges, and give a global overview of its possible future work.

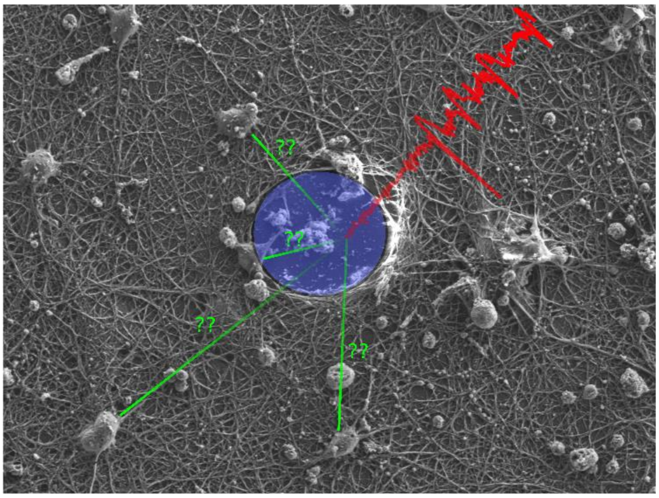

1) **Material level: how to improve planar classical MEA by addressing the bio-nano interface?**

Neural localization and coupling. We showed how EDOT electropolymerization could optimize the cell/electrode interface leading to a better signal-to-noise ratio on the recording and to more cells on the channel that could be spike-sorted in its vicinity. We explored the possibility of properly estimating the positions of cell bodies in neuronal cultures by using these enhanced recordings for spike sorting, i.e., to isolate and detect the activity of individual neurons correlated with optical imaging. Being able to estimate the positions of neurons from the sensor accurately might open new possibilities to understand better the relationships between the sensor and the neuron at the micro-scale level

Nevertheless, while our results indicate that the spatial precision of such localization methods is in the order of tens of microns (few somas' sizes), this spatial extent should be investigated more deeply. In a very dense neural network, the distance between adjacent neurons could be much lower than tens of microns; thus without a proper way to tag/identify the cells recorded via spike sorting and imaging, verifying the origin of the signal is not feasible. While the cultures in this study were also imaged via Electron Microscopy, it turned out that such an additional imaging technique did not help to identify the somas properly. It is worthwhile noting that our designed MEAs sparse array are quite common in culture recordings (100 µm spacing), which gave a poor spatio-temporal resolution for the extracellular waveforms triggered by the neurons when emitting action potentials. Increasing the density of the array will lead to a better resolution in estimating of the cell's positions. In addition, using a denser array could also have decreased the number of cells whose positions were detected just on the top of the electrodes. This was quite problematic because since electrodes are not transparent, the cells cannot be imaged accordingly while too close or over the recording sites, biasing the search of putative matches with the segmented fluorescent cell bodies. To perform such an unambiguous labelling, one solution could be to either go for very sparse/diluted cultures, controlling exactly the position of the cells on the substrate, and/or guide the process outgrowth of mammalian neurons via textural guidance cues. The drawback, however, is that such constrained cell morphologies might differ from what is observed in vivo, and thus results might only partially be generalized.

High-quality PEDOT-based MEA. A new chemically synthesized polymer based on the electropolymerization of glycolated-EDOT and introducing oligo ethylene glycol to the PEDOT side-chain. Thanks to the versatility of the electropolymerization technique, a highly controlled degree of glycolation was obtained to tune the morphological and electrochemical performance of the microelectrode finely. Contact angle and morphological measurements showed higher hydrophilicity to cations for glycolated-ePEDOT microelectrodes compared to the standard PEDOT one. AFM in saline experiments revealed the monotonic decrease in Young Modulus value with glycolation. High hydrophilicity to cations and low conformal properties are essential properties for better neuron-electrode coupling. *In vitro* extracellular recording from primary neurons showing superior performances of glycolated-ePEDOT electrodes compared to standard PEDOT electrodes exposed to the same neural network in terms of SNR and number of spikes detected. SNR values were close to the state-of-the-art 3D microelectrodes with lower cost and complexity in fabrication.

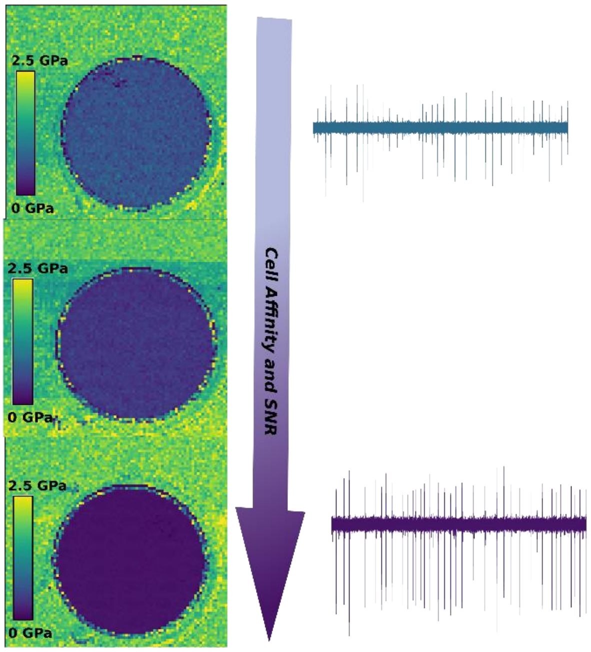

Despite the promising results for the performances of the glycolated-ePEDOT for in vitro recordings, these measurements were obtained from one single MEA without additional statistical experiments. The obtained recordings statistics (~8 electrodes per material) from the same neural correlated with the morphological investigations we relatively sufficient to show it as a proof of concept of its capabilities to be introduced as a powerful material for electrophysiological applications. At micrometer scale, more experiments could be conducted to rationalize the real cause behind this performance. For example, we performed AFM for the materials before coating the adhesion layer (PDL+laminin) before seeding cells. Doing same experiments after coating the adhesion layer gives us more insight into the interaction between the adhesion coating and the glycolated-ePEDOT. This could clarify if the soft property of the glycolated-ePEDOT were not altered due to the adhesion layer. A non-significant change in the Young Modulus will validate the effect of the softness of the material on the quality of the recordings. For further real-time application uses, long-term stability up to several months incubated with cell culture should be performed to investigate its ability to be an alternative material for implantable BCI interfaces.

2) **Device and circuit level: how does addressing active electrodes (OECT) will improve electrophysiology/cell interfacing?**

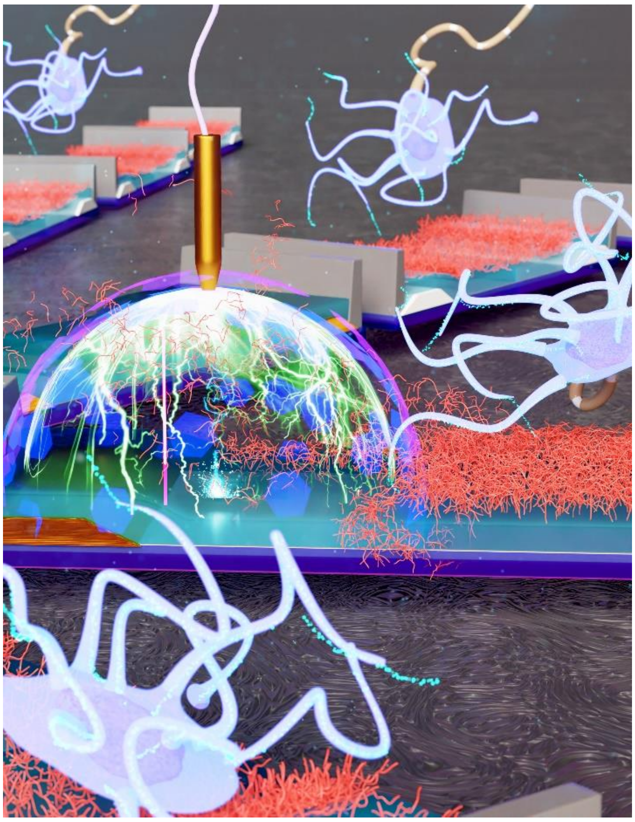

Adaptive Active Sensors. First, we have demonstrated how *in-operando* electropolymerization of organic electrochemical transistors can implement adaptive bio-sensors by tuning the iono-electronic properties of the material. This approach addresses the neuron/interface at the device and material level by engineering biocompatible and conformal materials to optimize active device's parameters considered as figure-of-merit for its sensing performances and additional features i.e., on-site signal amplification. This strategy exploits the concept of adaptive sensing, where both transconductance and impedance are tunable and can be modified on-demand to match different sensing requirements. Material investigation through Raman spectroscopy, atomic force microscopy and scanning electron microscopy reveal that electropolymerization can lead to a fine control of PEDOT microdomains organization, which directly affects the iono-electronic properties of OECTs. We further highlight how volumetric capacitance and effective mobility of PEDOT:PSS distinctively influence the transconductance and impedance of OECTs. This approach improves the transconductance by 150% while reducing their variability by 60% in comparison with standard spin-coated OECTs. The mobility adaptive tuning ability makes this technique a key solution for optimizing the speed operation of OECT devices, which is a main bottleneck for OECTs. Thanks to the capacitive tuning, we were able to decrease the noise of the OECT relatively by 88%, which is a crucial requirement for electrophysiology. Finally, we show how the technique can influence voltage spike rate hardware classification with a direct interest in bio-signals sorting applications.

One limitation we can highlight is that the absolute performances of OECT proposed in this work are below record performances obtained with optimized devices. However, the relative improvement of iono-electronic performances with the proposed approach is still appealing for improving and diversifying OECT from an applicative perspective. Indeed, using different counter electrodes will modify the potential distribution in the system electrode/electrolyte/OECT and will modify the absolute potential to be applied to electropolymerize EDOT. In this sense, this approach is still limited to be proposed as a universal technique, but we would like to emphasize that the methodology is still applicable to different counter electrode materials. Additional electrical and morphological characterization should be done and experimental parameters will need to be adjusted but there is no blocking point in transferring this approach to other electrode materials. Capacitive tuning by electropolymerizing at 0.65 or 0.7 V seemed to be more reproducible than the effect mobility tuning (electropolymerization at 0.6 V), which could need more systematic characterization achieved to bypass this bottleneck. Decreasing the electropolymerization time interval to monitor slowly the mobility *change could be a proposed solution in addition to more statistical experiments. The investigated electropolymerization technique permits us to try electropolymerizing different monomers with better electrical or bioactive performances paving the way for an interesting, versatile approach for engineering OECT with on-demand characteristics.*

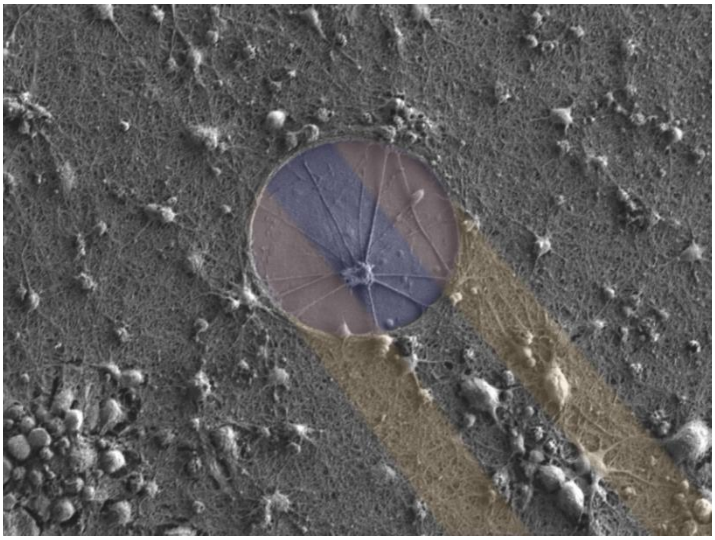

OECT/Neuron interface. To go further we performed in vitro extracellular recordings from 2D primary neuron culture using OECT. Before that, we characterized the performance of OECTs electrically after interfacing the adhesion layer and neural culture. OECT transconductance decreased by relatively 50% after culturing neurons on top of it. During transfer characteristics measurements, when the applied gate voltage exceeds 0.6 V, the OECT channel is oxidized and not reduced back, proposing the polymerization of dopamine on top. In situ EIS measurements have been performed while neurons were cultured on top; correlated with impedance modelling, we quantified expected values for the electrical parameters of the neurons. Combining modeling with electrical simulations allowed us to highlight the parameters that limit or enhance the neuron/OECT coupling such as seal resistance, membrane capacitance and OECT’s capacitance. Finally, we showed preliminary results for spiking activity of primary neurons recorded by an OECT.

In this part of the work, we faced many challenges starting from the electronic setup used to record the signal coming from the OECT down to the neuron-OECT interaction. The hypothesis of dopamine electropolymerization is very interesting, opening new perspectives on using OECTs for neurotransmitter sensing applications. However, no solid results have been shown to support this claim. Additional experiments by characterizing OECTs with dopamine solution without neurons is a proposed approach to ensure the dopamine sensing capability. Seal resistance and membrane capacitance values extracted from the model were contrary to the state-of-the-art results. One possible reason behind that could be the dense neural network and the small neuron size (<10 µm) that make the interface more complex than just a single neuron-OECT interface. Less dense neural culture could help in diminishing the effect of this issue. The output of the transistor or OECT is current and not voltage; one bottleneck for high-quality and reproducible in vitro recordings by using OECT was the home-built voltage divider electronic setup we used to convert current to voltage limited our parallel recordings ability and added large values of noise. Implementing a more advanced and low-noise electronic circuits embedded with the desired filters (i.e. for recording spikes) is essential for making a high-quality and user-friendly setup such as the commercial setups implemented for passive MEAs.

References

[1] E. C. Amerman, *Human anatomy & physiology*, **2019**.

[2] brain illustration, .

[3] S. Hwang, J. Chang, M.-H. Oh, J.-H. Lee, B.-G. Park, *Sci Rep* **2020**, *10*, 3515.

[4] https://neuralink.com/, .

[5] L. R. Hochberg, M. D. Serruya, G. M. Friehs, J. A. Mukand, M. Saleh, A. H. Caplan, A. Branner, D. Chen, R. D. Penn, J. P. Donoghue, *Nature* **2006**, *442*, 164.

[6] www.cochlear.com, .

[7] www.2-sight.com, .

[8] H. Bergman, T. Wichmann, M. R. DeLong, *Science* **1990**, *249*, 1436.

[9] A. De Luca, A. Bellitto, S. Mandraccia, G. Marchesi, L. Pellegrino, M. Coscia, C. Leoncini, L. Rossi, S. Gamba, A. Massone, M. Casadio, *Applied Sciences* **2019**, *9*, 2868.

[10] D. Ham, H. Park, S. Hwang, K. Kim, *Nat Electron* **2021**, *4*, 635.

[11] J. P. Donoghue, *Neuron* **2008**, *60*, 511.

[12] T. H. Bullock, *Proc. Natl. Acad. Sci. U.S.A.* **1997**, *94*, 1.

[13] A. Biasiucci, B. Franceschiello, M. M. Murray, *Current Biology* **2019**, *29*, R80.

[14] M. E. Spira, A. Hai, *Nature Nanotech* **2013**, *8*, 83.

[15] Z. Yu, J. K. Liu, S. Jia, Y. Zhang, Y. Zheng, Y. Tian, T. Huang, *Engineering* **2020**, *6*, 449.

[16] T. Baden, F. Esposti, A. Nikolaev, L. Lagnado, *Current Biology* **2011**, *21*, 1859.

[17] I. Lazarou, S. Nikolopoulos, P. C. Petrantonakis, I. Kompatsiaris, M. Tsolaki, *Front. Hum. Neurosci.* **2018**, *12*, 14.

[18] N. V. Thakor, *Sci. Transl. Med.* **2013**, *5*.

[19] D. Myers, *ALTEX* **2017**, 479.

[20] S. Buccelli, Y. Bornat, I. Colombi, M. Ambroise, L. Martines, V. Pasquale, M. Bisio, J. Tessadori, P. Nowak, F. Grassia, A. Averna, M. Tedesco, P. Bonifazi, F. Difato, P. Massobrio, T. Levi, M. Chiappalone, *iScience* **2019**, *19*, 402.

[21] K. Richetin, P. Steullet, M. Pachoud, R. Perbet, E. Parietti, M. Maheswaran, S. Eddarkaoui, S. Bégard, C. Pythoud, M. Rey, R. Caillierez, K. Q Do, S. Halliez, P. Bezzi, L. Buée, G. Leuba, M. Colin, N. Toni, N. Déglon, *Nat Neurosci* **2020**, *23*, 1567.

[22] V. Thakore, P. Molnar, J. J. Hickman, *IEEE Trans. Biomed. Eng.* **2012**, *59*, 2338.

[23] R. Schätzthauer, P. Fromherz, *European Journal of Neuroscience* **1998**, *10*, 1956.

[24] P. L. Nunez, R. Srinivasan, *Electric fields of the brain: the neurophysics of EEG*, 2nd ed., Oxford University Press, Oxford ; New York, **2006**.

[25] G. Buzsáki, C. A. Anastassiou, C. Koch, *Nat Rev Neurosci* **2012**, *13*, 407.

[26] M. E. J. Obien, *Frontiers in Neuroscience* 30.

[27] M. Dipalo, H. Amin, L. Lovato, F. Moia, V. Caprettini, G. C. Messina, F. Tantussi, L. Berdondini, F. De Angelis, *Nano Lett.* **2017**, *17*, 3932.

[28] A. Hai, J. Shappir, M. E. Spira, *Journal of Neurophysiology* **2010**, *104*, 559.

[29] F. A. Pennacchio, L. D. Garma, L. Matino, F. Santoro, *J. Mater. Chem. B* **2018**, *6*, 7096.

[30] A. Casanova, L. Bettamin, M.-C. Blatche, F. Mathieu, H. Martin, D. Gonzalez-Dunia, L. Nicu, G. Larrieu, *J. Phys.: Condens. Matter* **2018**, *30*, 464001.

[31] R. Liu, R. Chen, A. T. Elthakeb, S. H. Lee, S. Hinckley, M. L. Khraiche, J. Scott, D. Pre, Y. Hwang, A. Tanaka, Y. G. Ro, A. K. Matsushita, X. Dai, C. Soci, S. Biesmans, A. James, J. Nogan, K. L. Jungjohann, D. V. Pete, D. B. Webb, Y. Zou, A. G. Bang, S. A. Dayeh, *Nano Lett.* **2017**, *17*, 2757.

[32] J. R. Eles, A. L. Vazquez, N. R. Snyder, C. Lagenaur, M. C. Murphy, T. D. Y. Kozai, X. T. Cui, *Biomaterials* **2017**, *113*, 279.

[33] A. Markov, V. Maybeck, N. Wolf, D. Mayer, A. Offenhäusser, R. Wördenweber, *ACS Appl. Mater. Interfaces* **2018**, *10*, 18507.

[34] B. Van Meerbergen, K. Jans, J. Loo, G. Reekmans, D. Braeken, C. Seon-Ah, K. Bonroy, G. Maes, G. Borghs, Y. Engelborghs, W. Annaert, C. Bartic, In *2008 30th Annual International Conference of the IEEE Engineering in Medicine and Biology Society*, IEEE, Vancouver, BC, **2008**, pp. 1833–1836.

[35] Z. Aqrawe, J. Montgomery, J. Travas-Sejdic, D. Svirskis, *Sensors and Actuators B: Chemical* **2018**, *257*, 753.

[36] D. A. Robinson, *Proc. IEEE* **1968**, *56*, 1065.

[37] A. Khalifa, Z. Gao, A. Bermak, Y. Wang, L. L. H. Chan, *Sens. Bio-Sens. Res.* **2015**, *5*, 1.

[38] T. Gabay, M. Ben-David, I. Kalifa, Z. R. Abrams, R. Sorkin, E. Ben-Jacob, Y. Hanein, In *TRANSDUCERS 2007 - 2007 International Solid-State Sensors, Actuators and Microsystems Conference*, IEEE, Lyon, France, **2007**, pp. 1553–1556.

[39] S. Seyock, V. Maybeck, E. Scorsone, L. Rousseau, C. Hébert, G. Lissorgues, P. Bergonzo, A. Offenhäusser, *RSC Adv.* **2017**, *7*, 153.

[40] A. Koklu, R. Atmaramani, A. Hammack, A. Beskok, J. J. Pancrazio, B. E. Gnade, B. J. Black, *Nanotechnology* **2019**, *30*, 235501.

[41] R. Tang, W. Pei, S. Chen, H. Zhao, Y. Chen, Y. Han, C. Wang, H. Chen, *Science China Information Sciences* **2013**, *57*.

[42] A. Baradoke, J. Juodkazyte, I. Masilionis, A. Selskis, R. Pauliukaite, R. Valiokas, *Microelectronic Engineering* **2019**, *208*, 39.

[43] T. Gabay, M. Ben-David, I. Kalifa, R. Sorkin, Z. R. Abrams, E. Ben-Jacob, Y. Hanein, *Nanotechnology* **2007**, *18*, 035201.

[44] B. Sakmann, E. Neher, *Annu. Rev. Physiol.* **1984**, *46*, 455.

[45] J. T. Robinson, M. Jorgolli, A. K. Shalek, M.-H. Yoon, R. S. Gertner, H. Park, *Nature Nanotech* **2012**, *7*, 180.

[46] L. D. Garma, L. M. Ferrari, P. Scognamiglio, F. Greco, F. Santoro, *Lab Chip* **2019**, *19*, 3776.

[47] D. Kireev, S. Seyock, J. Lewen, V. Maybeck, B. Wolfrum, A. Offenhäusser, *Adv. Healthcare Mater.* **2017**, *6*, 1601433.

[48] G. G. M. Dimitrios A. Koutsouras Adel Hama, Jolien Pas, Paschalis Gkoupidenis, Bruno Hivert, Catherine Faivre-Sarrailh, Eric Di Pasquale, Róisín M. Owens, *MRS Commun.* **2017**, *7*, 259.

[49] C. Pitsalidis, A.-M. Pappa, A. J. Boys, Y. Fu, C.-M. Moysidou, D. van Niekerk, J. Saez, A. Savva, D. Iandolo, R. M. Owens, *Chem. Rev.* **2022**, *122*, 4700.

[50] B. Love, In *Biomaterials*, Elsevier, **2017**, pp. 205–238.

[51] P. Fattahi, G. Yang, G. Kim, M. R. Abidian, *Adv. Mater.* **2014**, *26*, 1846.

[52] G. Dijk, A. L. Rutz, G. G. Malliaras, *Adv. Mater. Technol.* **2020**, *5*, 1900662.

[53] N. K, C. S. Rout, *RSC Adv.* **2021**, *11*, 5659.

[54] P. Fattahi, G. Yang, G. Kim, M. R. Abidian, *Adv. Mater.* **2014**, *26*, 1846.

[55] D. Khodagholy, T. Doublet, M. Gurfinkel, P. Quilichini, E. Ismailova, P. Leleux, T. Herve, S. Sanaur, C. Bernard, G. G. Malliaras, *Adv. Mater.* **2011**, *23*, H268.

[56] M. Sessolo, D. Khodagholy, J. Rivnay, F. Maddalena, M. Gleyzes, E. Steidl, B. Buisson, G. G. Malliaras, *Adv. Mater.* **2013**, *25*, 2135.

[57] A. Susloparova, S. Halliez, S. Begard, M. Colin, L. Buée, S. Pecqueur, F. Alibart, V. Thomy, S. Arscott, E. Pallecchi, Y. Coffinier, *Sens. Actuators, B* **2021**, *327*, 128895.

[58] A. K. Waafi, N. Gaio, W. F. Quiros-Solano, P. Dijkstra, P. M. Sarro, R. Dekker, *IEEE_J_SENSOR* **2020**, *20*, 1150.

[59] R. T. Richardson, B. Thompson, S. Moulton, C. Newbold, M. G. Lum, A. Cameron, G. Wallace, R. Kapsa, G. Clark, S. O'Leary, *Biomaterials* **2007**, *28*, 513.
[60] F. Greco, A. Zucca, S. Taccola, A. Menciassi, T. Fujie, H. Haniuda, S. Takeoka, P. Dario, V. Mattoli, *Soft Matter* **2011**, *7*, 10642.
[61] Manifacturer: H.C. Starck Clevios GmbH, Leverkusen, Germany, www.clevios.com, .
[62] J. Rivnay, P. Leleux, M. Ferro, M. Sessolo, A. Williamson, D. A. Koutsouras, D. Khodagholy, M. Ramuz, X. Strakosas, R. M. Owens, C. Benar, J.-M. Badier, C. Bernard, G. G. Malliaras, *Sci. Adv.* **2015**, *1*, e1400251.
[63] A. V. Volkov, K. Wijeratne, E. Mitraka, U. Ail, D. Zhao, K. Tybrandt, J. W. Andreasen, M. Berggren, X. Crispin, I. V. Zozoulenko, *Adv. Funct. Mater.* **2017**, *27*, 1700329.
[64] Z. Aqrawe, B. Wright, N. Patel, Y. Vyas, J. Malmstrom, J. M. Montgomery, D. Williams, J. Travas-Sejdic, D. Svirskis, *Sensors and Actuators B: Chemical* **2019**, *281*, 549.
[65] L. Ferlauto, A. N. D'Angelo, P. Vagni, M. J. I. Airaghi Leccardi, F. M. Mor, E. A. Cuttaz, M. O. Heuschkel, L. Stoppini, D. Ghezzi, *Front. Neurosci.* **2018**, *12*, 648.
[66] M. Ganji, E. Kaestner, J. Hermiz, N. Rogers, A. Tanaka, D. Cleary, S. H. Lee, J. Snider, M. Halgren, G. R. Cosgrove, B. S. Carter, D. Barba, I. Uguz, G. G. Malliaras, S. S. Cash, V. Gilja, E. Halgren, S. A. Dayeh, *Adv. Funct. Mater.* **2018**, *28*, 1700232.
[67] M. Shur, F. Fallegger, E. Pirondini, A. Roux, A. Bichat, Q. Barraud, G. Courtine, S. P. Lacour, *ACS Appl. Bio Mater.* **2020**, *3*, 4388.
[68] J. Isaksson, P. Kjäll, D. Nilsson, N. Robinson, M. Berggren, A. Richter-Dahlfors, *Nature Mater* **2007**, *6*, 673.
[69] L. H. Jimison, A. Hama, X. Strakosas, V. Armel, D. Khodagholy, E. Ismailova, G. G. Malliaras, B. Winther-Jensen, R. M. Owens, *J. Mater. Chem.* **2012**, *22*, 19498.
[70] C. Saltó, E. Saindon, M. Bolin, A. Kanciurzewska, M. Fahlman, E. W. H. Jager, P. Tengvall, E. Arenas, M. Berggren, *Langmuir* **2008**, *24*, 14133.
[71] S. Middya, V. F. Curto, A. Fernández-Villegas, M. Robbins, J. Gurke, E. J. M. Moonen, G. S. Kaminski Schierle, G. G. Malliaras, *Adv. Sci.* **2021**, *8*, 2004434.
[72] P. Leleux, J.-M. Badier, J. Rivnay, C. Bénar, T. Hervé, P. Chauvel, G. G. Malliaras, *Adv. Healthcare Mater.* **2014**, *3*, 490.
[73] M. E. J. Obien, *Frontiers in Neuroscience* 30.
[74] G. W. Fraser, S. M. Chase, A. Whitford, A. B. Schwartz, *J. Neural Eng.* **2009**, *6*, 055004.
[75] S. Todorova, P. Sadtler, A. Batista, S. Chase, V. Ventura, *J. Neural Eng.* **2014**, *11*, 056005.
[76] R. Q. Quiroga, L. Reddy, C. Koch, I. Fried, *Journal of Neurophysiology* **2007**, *98*, 1997.
[77] B. Lefebvre, P. Yger, O. Marre, *Journal of Physiology-Paris* **2016**, *110*, 327.
[78] P. Yger, G. L. Spampinato, E. Esposito, B. Lefebvre, S. Deny, C. Gardella, M. Stimberg, F. Jetter, G. Zeck, S. Picaud, J. Duebel, O. Marre, *eLife* **2018**, *7*, e34518.
[79] J. Lee, C. Mitelut, H. Shokri, I. Kinsella, N. Dethe, S. Wu, K. Li, E. B. Reyes, D. Turcu, E. Batty, Y. J. Kim, N. Brackbill, A. Kling, G. Goetz, E. J. Chichilnisky, D. Carlson, L. Paninski, *YASS: Yet Another Spike Sorter applied to large-scale multi-electrode array recordings in primate retina*, Neuroscience, **2020**.
[80] A. P. Buccino, E. Hagen, G. T. Einevoll, P. D. Hafliger, G. Cauwenberghs, In *2018 40th Annual International Conference of the IEEE Engineering in Medicine and Biology Society (EMBC)*, IEEE, Honolulu, HI, **2018**, pp. 2627–2630.
[81] A. P. Buccino, S. Garcia, P. Yger, *Prog. Biomed. Eng.* **2022**, *4*, 022005.
[82] N. A. Steinmetz, C. Aydin, A. Lebedeva, M. Okun, M. Pachitariu, M. Bauza, M. Beau, J. Bhagat, C. Böhm, M. Broux, S. Chen, J. Colonell, R. J. Gardner, B. Karsh, F. Kloosterman, D. Kostadinov, C. Mora-Lopez, J. O'Callaghan, J. Park, J. Putzeys, B. Sauerbrei, R. J. J. van Daal, A. Z. Vollan, S. Wang, M. Welkenhuysen, Z. Ye, J. T. Dudman, B. Dutta, A. W. Hantman, K. D. Harris, A. K. Lee, E. I. Moser, J. O'Keefe, A. Renart, K. Svoboda, M. Häusser, S. Haesler, M. Carandini, T. D. Harris, *Science* **2021**, *372*, eabf4588.

[83] J. Boussard, E. Varol, H. D. Lee, N. Dethe, L. Paninski, *Three-dimensional spike localization and improved motion correction for Neuropixels recordings*, Neuroscience, **2021**.

[84] C. L. Hurwitz, K. Xu, A. Srivastava, A. P. Buccino, M. H. Hennig, **2019**.

[85] K. H. Pettersen, G. T. Einevoll, *Biophysical Journal* **2008**, *94*, 784.

[86] T. J. Blanche, M. A. Spacek, J. F. Hetke, N. V. Swindale, *Journal of Neurophysiology* **2005**, *93*, 2987.

[87] M. I. Chelaru, M. S. Jog, *Journal of Neuroscience Methods* **2005**, *142*, 305.

[88] M. Pachitariu, N. Steinmetz, S. Kadir, M. Carandini, H. Kenneth D., *Kilosort: realtime spike-sorting for extracellular electrophysiology with hundreds of channels*, Neuroscience, **2016**.

[89] G. Hilgen, M. Sorbaro, S. Pirmoradian, J.-O. Muthmann, I. E. Kepiro, S. Ullo, C. J. Ramirez, A. Puente Encinas, A. Maccione, L. Berdondini, V. Murino, D. Sona, F. Cella Zanacchi, E. Sernagor, M. H. Hennig, *Cell Reports* **2017**, *18*, 2521.

[90] H. G. Rey, C. Pedreira, R. Quian Quiroga, *Brain Research Bulletin* **2015**, *119*, 106.

[91] A. Hierlemann, U. Frey, S. Hafizovic, F. Heer, *Proc. IEEE* **2011**, *99*, 252.

[92] P. Fromherz, *Solid-State Electronics* **2008**, *52*, 1364.

[93] M. Hutzler, P. Fromherz, *Eur J Neurosci* **2004**, *19*, 2231.

[94] J. Dragas, V. Viswam, A. Shadmani, Y. Chen, R. Bounik, A. Stettler, M. Radivojevic, S. Geissler, M. E. J. Obien, J. Muller, A. Hierlemann, *IEEE J. Solid-State Circuits* **2017**, *52*, 1576.

[95] H. Kang, Y. Nam, In *Stretchable Bioelectronics for Medical Devices and Systems* (Eds.: Rogers, J. A.; Ghaffari, R.; Kim, D.-H.), Springer International Publishing, Cham, **2016**, pp. 275–291.

[96] D. Khodagholy, T. Doublet, P. Quilichini, M. Gurfinkel, P. Leleux, A. Ghestem, E. Ismailova, T. Hervé, S. Sanaur, C. Bernard, G. G. Malliaras, *Nat Commun* **2013**, *4*, 1575.

[97] D. Jackel, J. Muller, M. U. Khalid, U. Frey, D. Bakkum, A. Hierlemann, In *2011 16th International Solid-State Sensors, Actuators and Microsystems Conference*, IEEE, Beijing, China, **2011**, pp. 1200–1203.

[98] P. Bergveld, J. Wiersma, H. Meertens, *IEEE Trans. Biomed. Eng.* **1976**, *BME-23*, 136.

[99] F. Veliev, Z. Han, D. Kalita, A. Briançon-Marjollet, V. Bouchiat, C. Delacour, *Front. Neurosci.* **2017**, *11*, 466.

[100] P. Fromherz, *ChemPhysChem* **2002**, *3*, 276.

[101] R. Weis, P. Fromherz, *Phys. Rev. E* **1997**, *55*, 877.

[102] M. Voelker, P. Fromherz, *Small* **2005**, *1*, 206.

[103] M. Hutzler, A. Lambacher, B. Eversmann, M. Jenkner, R. Thewes, P. Fromherz, *Journal of Neurophysiology* **2006**, *96*, 1638.

[104] T. Cohen-Karni, Q. Qing, Q. Li, Y. Fang, C. M. Lieber, *Nano Lett.* **2010**, *10*, 1098.

[105] F. Patolsky, B. P. Timko, G. Yu, Y. Fang, A. B. Greytak, G. Zheng, C. M. Lieber, *Science* **2006**, *313*, 1100.

[106] T. Cohen-Karni, B. P. Timko, L. E. Weiss, C. M. Lieber, *Proc. Natl. Acad. Sci. U.S.A.* **2009**, *106*, 7309.

[107] M. V. Hauf, L. H. Hess, J. Howgate, M. Dankerl, M. Stutzmann, J. A. Garrido, *Appl. Phys. Lett.* **2010**, *97*, 093504.

[108] B. Tian, T. Cohen-Karni, Q. Qing, X. Duan, P. Xie, C. M. Lieber, *Science* **2010**, *329*, 830.

[109] X. Duan, R. Gao, P. Xie, T. Cohen-Karni, Q. Qing, H. S. Choe, B. Tian, X. Jiang, C. M. Lieber, *Nature Nanotech* **2012**, *7*, 174.

[110] T.-M. Fu, X. Duan, Z. Jiang, X. Dai, P. Xie, Z. Cheng, C. M. Lieber, *Proc. Natl. Acad. Sci. U.S.A.* **2014**, *111*, 1259.

[111] H. S. White, G. P. Kittlesen, M. S. Wrighton, *J. Am. Chem. Soc.* **1984**, *106*, 5375.

[112] J. Rivnay, S. Inal, A. Salleo, R. M. Owens, M. Berggren, G. G. Malliaras, *Nat Rev Mater* **2018**, *3*, 17086.

[113] D. A. Bernards, G. G. Malliaras, *Advanced Functional Materials* **2007**, *17*, 3538.
[114] P. R. Paudel, J. Tropp, V. Kaphle, J. D. Azoulay, B. Lüssem, *J. Mater. Chem. C* **2021**, *9*, 9761.
[115] P. R. Paudel, V. Kaphle, D. Dahal, R. K. Radha Krishnan, B. Lüssem, *Adv. Funct. Mater.* **2021**, *31*, 2004939.
[116] M. D. Angione, S. Cotrone, M. Magliulo, A. Mallardi, D. Altamura, C. Giannini, N. Cioffi, L. Sabbatini, E. Fratini, P. Baglioni, G. Scamarcio, G. Palazzo, L. Torsi, *Proc. Natl. Acad. Sci. U.S.A.* **2012**, *109*, 6429.
[117] S. Ranganathan, R. L. McCreery, *Anal. Chem.* **2001**, *73*, 893.
[118] J. Rivnay, S. Inal, A. Salleo, R. M. Owens, M. Berggren, G. G. Malliaras, *Nat Rev Mater* **2018**, *3*, 17086.
[119] A. Marks, S. Griggs, N. Gasparini, M. Moser, *Adv Materials Inter* **2022**, *9*, 2102039.
[120] D. Khodagholy, T. Doublet, P. Quilichini, M. Gurfinkel, P. Leleux, A. Ghestem, E. Ismailova, T. Hervé, S. Sanaur, C. Bernard, G. G. Malliaras, *Nat Commun* **2013**, *4*, 1575.
[121] P. R. Paudel, V. Kaphle, D. Dahal, R. K. Radha Krishnan, B. Lüssem, *Adv. Funct. Mater.* **2021**, *31*, 2004939.
[122] A. F. Paterson, A. Savva, S. Wustoni, L. Tsetseris, B. D. Paulsen, H. Faber, A. H. Emwas, X. Chen, G. Nikiforidis, T. C. Hidalgo, M. Moser, I. P. Maria, J. Rivnay, I. McCulloch, T. D. Anthopoulos, S. Inal, *Nat Commun* **2020**, *11*, 3004.
[123] S. Sakamoto, M. Okumura, Z. Zhao, Y. Furukawa, *Chemical Physics Letters* **2005**, *412*, 395.
[124] M. Ghazal, M. Daher Mansour, C. Scholaert, T. Dargent, Y. Coffinier, S. Pecqueur, F. Alibart, *Adv Elect Materials* **2022**, *8*, 2100891.
[125] E. Zeglio, M. Vagin, C. Musumeci, F. N. Ajjan, R. Gabrielsson, X. T. Trinh, N. T. Son, A. Maziz, N. Solin, O. Inganäs, *Chem. Mater.* **2015**, *27*, 6385.
[126] A. Giovannitti, D.-T. Sbircea, S. Inal, C. B. Nielsen, E. Bandiello, D. A. Hanifi, M. Sessolo, G. G. Malliaras, I. McCulloch, J. Rivnay, *Proc. Natl. Acad. Sci. U.S.A.* **2016**, *113*, 12017.
[127] Y. Kim, H. Noh, B. D. Paulsen, J. Kim, I. Jo, H. Ahn, J. Rivnay, M. Yoon, *Adv. Mater.* **2021**, *33*, 2007550.
[128] J. Y. Gerasimov, R. Gabrielsson, R. Forchheimer, E. Stavrinidou, D. T. Simon, M. Berggren, S. Fabiano, *Adv. Sci.* **2019**, *6*, 1801339.
[129] C. Liao, M. Zhang, L. Niu, Z. Zheng, F. Yan, *J. Mater. Chem. B* **2013**, *1*, 3820.
[130] H. Tang, P. Lin, H. L. W. Chan, F. Yan, *Biosens Bioelectron* **2011**, *26*, 4559.
[131] P. Lin, X. Luo, I.-M. Hsing, F. Yan, *Adv. Mater. Weinheim* **2011**, *23*, 4035.
[132] D. Khodagholy, V. F. Curto, K. J. Fraser, M. Gurfinkel, R. Byrne, D. Diamond, G. G. Malliaras, F. Benito-Lopez, R. M. Owens, *J. Mater. Chem.* **2012**, *22*, 4440.
[133] C. Liao, M. Zhang, L. Niu, Z. Zheng, F. Yan, *J. Mater. Chem. B* **2013**, *2*, 191.
[134] A. Spanu, L. Martines, A. Bonfiglio, *Lab Chip* **2021**, *21*, 795.
[135] F. Hempel, J. K. Y. Law, T. C. Nguyen, R. Lanche, A. Susloparova, X. T. Vu, S. Ingebrandt, *Biosensors and Bioelectronics* **2021**, *180*, 113101.
[136] J. Rivnay, M. Ramuz, P. Leleux, A. Hama, M. Huerta, R. M. Owens, *Appl. Phys. Lett.* **2015**, *106*, 043301.
[137] P. Leleux, J. Rivnay, T. Lonjaret, J.-M. Badier, C. Bénar, T. Hervé, P. Chauvel, G. G. Malliaras, *Adv. Healthcare Mater.* **2015**, *4*, 142.
[138] A. Campana, T. Cramer, D. T. Simon, M. Berggren, F. Biscarini, *Adv. Mater.* **2014**, *26*, 3874.
[139] C. Yao, Q. Li, J. Guo, F. Yan, I.-M. Hsing, *Adv. Healthcare Mater.* **2015**, *4*, 528.
[140] X. Gu, C. Yao, Y. Liu, I.-M. Hsing, *Adv. Healthcare Mater.* **2016**, *5*, 2345.
[141] X. Gu, S. Y. Yeung, A. Chadda, E. N. Y. Poon, K. R. Boheler, I.-M. Hsing, *Adv. Biosys.* **2019**, *3*, 1800248.
[142] F. Hempel, J. K.-Y. Law, T. C. Nguyen, W. Munief, X. Lu, V. Pachauri, A. Susloparova, X. T. Vu, S. Ingebrandt, *Biosensors and Bioelectronics* **2017**, *93*, 132.

[143] Y. Liang, M. Ernst, F. Brings, D. Kireev, V. Maybeck, A. Offenhäusser, D. Mayer, *Adv. Healthcare Mater.* **2018**, *7*, 1800304.
[144] A. Williamson, M. Ferro, P. Leleux, E. Ismailova, A. Kaszas, T. Doublet, P. Quilichini, J. Rivnay, B. Rózsa, G. Katona, C. Bernard, G. G. Malliaras, *Adv. Mater.* **2015**, *27*, 4405.
[145] L. K. Daniels, *Am J Clin Hypn* **1976**, *18*, 200.
[146] D. Nečas, P. Klapetek, *Open Physics* **2011**, *10*, 181.
[147] M.-C. Galas, P. Dourlen, S. Bégard, K. Ando, D. Blum, M. Hamdane, L. Buée, *Journal of Biological Chemistry* **2006**, *281*, 19296.
[148] A. P. Buccino, C. L. Hurwitz, S. Garcia, J. Magland, J. H. Siegle, R. Hurwitz, M. H. Hennig, *eLife* **2020**, *9*, e61834.
[149] Intan, .
[150] Z. Aqrawe, B. Wright, N. Patel, Y. Vyas, J. Malmstrom, J. M. Montgomery, D. Williams, J. Travas-Sejdic, D. Svirskis, *Sensors and Actuators B: Chemical* **2019**, *281*, 549.
[151] S. Middya, V. F. Curto, A. Fernández-Villegas, M. Robbins, J. Gurke, E. J. M. Moonen, G. S. Kaminski Schierle, G. G. Malliaras, *Adv. Sci.* **2021**, *8*, 2004434.
[152] L. Ferlauto, A. N. D'Angelo, P. Vagni, M. J. I. Airaghi Leccardi, F. M. Mor, E. A. Cuttaz, M. O. Heuschkel, L. Stoppini, D. Ghezzi, *Front. Neurosci.* **2018**, *12*, 648.
[153] S. M. Richardson-Burns, J. L. Hendricks, B. Foster, L. K. Povlich, D.-H. Kim, D. C. Martin, *Biomaterials* **2007**, *28*, 1539.
[154] K. Janzakova, M. Ghazal, A. Kumar, Y. Coffinier, S. Pecqueur, F. Alibart, *Advanced Science* **2021**, *8*, 2102973.
[155] M. Ren, H. Zhou, H.-J. Zhai, *J Mater Sci: Mater Electron* **2021**, *32*, 10078.
[156] S. Pecqueur, D. Guérin, D. Vuillaume, F. Alibart, *Organic Electronics* **2018**, *57*, 232.
[157] Z. Kerner, T. Pajkossy, *Journal of Electroanalytical Chemistry* **1998**, *448*, 139.
[158] L. Nyikos, T. Pajkossy, *Electrochimica Acta* **1985**, *30*, 1533.
[159] P. Córdoba-Torres, T. J. Mesquita, O. Devos, B. Tribollet, V. Roche, R. P. Nogueira, *Electrochim. Acta* **2012**, *72*, 172.
[160] C. Hitz, A. Lasia, *Journal of Electroanalytical Chemistry* **2001**, *500*, 213.
[161] A. Lasia, *Journal of Electroanalytical Chemistry* **1995**, *397*, 27.
[162] S. H. Liu, *Phys. Rev. Lett.* **1985**, *55*, 529.
[163] T. Pajkossy, D. M. Kolb, *Electrochimica Acta* **2008**, *53*, 7403.
[164] M.-L. Tremblay, M. H. Martin, C. Lebouin, A. Lasia, D. Guay, *Electrochimica Acta* **2010**, *55*, 6283.
[165] Z. Kerner, T. Pajkossy, *Electrochimica Acta* **2000**, *46*, 207.
[166] T. Pajkossy, *Solid State Ionics* **1997**, *94*, 123.
[167] P. Córdoba-Torres, T. J. Mesquita, R. P. Nogueira, *J. Phys. Chem. C* **2015**, *119*, 4136.
[168] T. Pajkossy, *Solid State Ionics* **2005**, *176*, 1997.
[169] M. Solazzo, K. Krukiewicz, A. Zhussupbekova, K. Fleischer, M. J. Biggs, M. G. Monaghan, *J. Mater. Chem. B* **2019**, *7*, 4811.
[170] M. L. Hines, N. T. Carnevale, *Neural Computation* **1997**, *9*, 1179.
[171] Z. Aqrawe, N. Patel, Y. Vyas, M. Bansal, J. Montgomery, J. Travas-Sejdic, D. Svirskis, *PLoS ONE* **2020**, *15*, e0237709.
[172] S. J. Wilks, A. J. Woolley, Liangqi Ouyang, D. C. Martin, K. J. Otto, In *2011 Annual International Conference of the IEEE Engineering in Medicine and Biology Society*, IEEE, Boston, MA, **2011**, pp. 5412–5415.
[173] L. Ouyang, C. L. Shaw, C. Kuo, A. L. Griffin, D. C. Martin, *J. Neural Eng.* **2014**, *11*, 026005.
[174] X. Strakosas, B. Wei, D. C. Martin, R. M. Owens, *J. Mater. Chem. B* **2016**, *4*, 4952.
[175] Y. Xiao, X. Cui, J. M. Hancock, M. Bouguettaya, J. R. Reynolds, D. C. Martin, *Sensors and Actuators B: Chemical* **2004**, *99*, 437.
[176] Y. Xiao, X. Cui, D. C. Martin, *Journal of Electroanalytical Chemistry* **2004**, *573*, 43.

[177] Y. Xiao, D. C. Martin, X. Cui, M. Shenai, *ABAB* **2006**, *128*, 117.

[178] R. Blau, A. X. Chen, B. Polat, L. L. Becerra, R. Runser, B. Zamanimeymian, K. Choudhary, D. J. Lipomi, *ACS Appl. Mater. Interfaces* **2022**, *14*, 4823.

[179] E. Tan, J. Kim, K. Stewart, C. Pitsalidis, S. Kwon, N. Siemons, J. Kim, Y. Jiang, J. M. Frost, D. Pearce, J. E. Tyrrell, J. Nelson, R. M. Owens, Y. Kim, J. Kim, *Advanced Materials* **2022**, 2202574.

[180] M. Moser, L. R. Savagian, A. Savva, M. Matta, J. F. Ponder, T. C. Hidalgo, D. Ohayon, R. Hallani, M. Reisjalali, A. Troisi, A. Wadsworth, J. R. Reynolds, S. Inal, I. McCulloch, *Chem. Mater.* **2020**, *32*, 6618.

[181] A. J. Ryan, C. J. Kearney, N. Shen, U. Khan, A. G. Kelly, C. Probst, E. Brauchle, S. Biccai, C. D. Garciarena, V. Vega-Mayoral, P. Loskill, S. W. Kerrigan, D. J. Kelly, K. Schenke-Layland, J. N. Coleman, F. J. O'Brien, *Adv. Mater.* **2018**, *30*, 1706442.

[182] A. M. Pappa, V. Karagkiozaki, S. Krol, S. Kassavetis, D. Konstantinou, C. Pitsalidis, L. Tzounis, N. Pliatsikas, S. Logothetidis, *Beilstein J. Nanotechnol.* **2015**, *6*, 254.

[183] S. Xiong, L. Zhang, X. Lu, *Polym. Bull.* **2013**, *70*, 237.

[184] M. Boussoualem, R. C. Y. King, J.-F. Brun, B. Duponchel, M. Ismaili, F. Roussel, *Journal of Applied Physics* **2010**, *108*, 113526.

[185] S. M. P. Daniel A Wagenaar Jerome Pine, *BMC Neurosci.* **2006**, *7*, 11.

[186] J. Abbott, T. Ye, L. Qin, M. Jorgolli, R. S. Gertner, D. Ham, H. Park, *Nature Nanotech* **2017**, *12*, 460.

[187] Y. Nam, B. C. Wheeler, M. O. Heuschkel, *Journal of Neuroscience Methods* **2006**, *155*, 296.

[188] P. D. Jones, A. Moskalyuk, C. Barthold, K. Gutöhrlein, G. Heusel, B. Schröppel, R. Samba, M. Giugliano, *Front. Neurosci.* **2020**, *14*, 405.

[189] J.-H. Kim, G. Kang, Y. Nam, Y.-K. Choi, *Nanotechnology* **2010**, *21*, 085303.

[190] Y. Nam, B. C. Wheeler, *Critical Reviews™ in Biomedical Engineering* **2011**, *39*, 45.

[191] C. D. James, A. J. H. Spence, N. M. Dowell-Mesfin, R. J. Hussain, K. L. Smith, H. G. Craighead, M. S. Isaacson, W. Shain, J. N. Turner, *IEEE Trans. Biomed. Eng.* **2004**, *51*, 1640.

[192] T. Ryynänen, L. Ylä-Outinen, S. Narkilahti, J. M. A. Tanskanen, J. Hyttinen, J. Hämäläinen, M. Leskelä, J. Lekkala, *Journal of Vacuum Science & Technology A: Vacuum, Surfaces, and Films* **2012**, *30*, 041501.

[193] C. Bustamante, C. Rivetti, D. J. Keller, *Current Opinion in Structural Biology* **1997**, *7*, 709.

[194] H. C. Lee, J. Gaire, S. W. Currlin, M. D. McDermott, K. Park, K. J. Otto, *Front. Neurosci.* **2017**, *11*, 513.

[195] S. M. Gutowski, K. L. Templeman, A. B. South, J. C. Gaulding, J. T. Shoemaker, M. C. LaPlaca, R. V. Bellamkonda, L. A. Lyon, A. J. García, *J. Biomed. Mater. Res.* **2014**, *102*, 1486.

[196] S. Sommakia, J. L. Rickus, K. J. Otto, *Front. Neuroeng.* **2014**, *7*.

[197] M. Ozgur, M. G. Özyurt, S. Arkan, S. Cavdar, *Annals of Neurosciences* **2022**, *29*, 53.

[198] P. Fromherz, A. Offenhäusser, T. Vetter, J. Weis, *Science* **1991**, *252*, 1290.

[199] D. A. Bernards, G. G. Malliaras, *Adv. Funct. Mater.* **2007**, *17*, 3538.

[200] D. Khodagholy, J. Rivnay, M. Sessolo, M. Gurfinkel, P. Leleux, L. H. Jimison, E. Stavrinidou, T. Herve, S. Sanaur, R. M. Owens, G. G. Malliaras, *Nat Commun* **2013**, *4*, 2133.

[201] M. N. Gueye, A. Carella, J. Faure-Vincent, R. Demadrille, J.-P. Simonato, *Progress in Materials Science* **2020**, *108*, 100616.

[202] C. M. Proctor, J. Rivnay, G. G. Malliaras, *Journal of Polymer Science Part B: Polymer Physics* **2016**, *54*, 1433.

[203] A. V. Volkov, K. Wijeratne, E. Mitraka, U. Ail, D. Zhao, K. Tybrandt, J. W. Andreasen, M. Berggren, X. Crispin, I. V. Zozoulenko, *Advanced Functional Materials* **2017**, *27*, 1700329.

[204] S. Inal, G. G. Malliaras, J. Rivnay, *Nat Commun* **2017**, *8*, 1767.

[205] A. L. Jones, M. De Keersmaecker, L. R. Savagian, B. T. DiTullio, I. Pelse, J. R. Reynolds, *Advanced Functional Materials* **2021**, *31*, 2102688.
[206] A. Giovannitti, D.-T. Sbircea, S. Inal, C. B. Nielsen, E. Bandiello, D. A. Hanifi, M. Sessolo, G. G. Malliaras, I. McCulloch, J. Rivnay, *PNAS* **2016**, *113*, 12017.
[207] P. Schmode, A. Savva, R. Kahl, D. Ohayon, F. Meichsner, O. Dolynchuk, T. Thurn-Albrecht, S. Inal, M. Thelakkat, *ACS Appl. Mater. Interfaces* **2020**, *12*, 13029.
[208] J. Rivnay, P. Leleux, M. Ferro, M. Sessolo, A. Williamson, D. A. Koutsouras, D. Khodagholy, M. Ramuz, X. Strakosas, R. M. Owens, C. Benar, J.-M. Badier, C. Bernard, G. G. Malliaras, *Science Advances* **2015**, *1*, e1400251.
[209] Y. H. Kim, C. Sachse, M. L. Machala, C. May, L. Müller-Meskamp, K. Leo, *Advanced Functional Materials* **2011**, *21*, 1076.
[210] Y. Kim, H. Noh, B. D. Paulsen, J. Kim, I.-Y. Jo, H. Ahn, J. Rivnay, M.-H. Yoon, *Advanced Materials* **2021**, *33*, 2007550.
[211] S. Garreau, J. L. Duvail, G. Louarn, *Synthetic Metals* **2001**, *125*, 325.
[212] S. Garreau, G. Louarn, J. P. Buisson, G. Froyer, S. Lefrant, *Macromolecules* **1999**, *32*, 6807.
[213] S. Sakamoto, M. Okumura, Z. Zhao, Y. Furukawa, *Chemical Physics Letters* **2005**, *412*, 395.
[214] Q. Zhao, R. Jamal, L. Zhang, M. Wang, T. Abdiryim, *Nanoscale Res Lett* **2014**, *9*, 557.
[215] E. Tamburri, S. Orlanducci, F. Toschi, M. L. Terranova, D. Passeri, *Synthetic Metals* **2009**, *159*, 406.
[216] W. W. Chiu, J. Travaš-Sejdić, R. P. Cooney, G. A. Bowmaker, *Synthetic Metals* **2005**, *155*, 80.
[217] P. V. Almeida, C. M. S. Izumi, H. F. D. Santos, A. C. Sant’Ana, *QuÃ\-mica Nova* **2019**, *42*, 1073.
[218] W. W. Chiu, J. Travaš-Sejdić, R. P. Cooney, G. A. Bowmaker, *Journal of Raman Spectroscopy* **2006**, *37*, 1354.
[219] J. L. Duvail, P. Rétho, S. Garreau, G. Louarn, C. Godon, S. Demoustier-Champagne, *Synthetic Metals* **2002**, *131*, 123.
[220] B. R. Moraes, N. S. Campos, C. M. S. Izumi, *Vibrational Spectroscopy* **2018**, *96*, 137.
[221] N. Sakmeche, S. Aeiyach, J.-J. Aaron, M. Jouini, J. C. Lacroix, P.-C. Lacaze, *Langmuir* **1999**, *15*, 2566.
[222] D. Wu, J. Zhang, W. Dong, H. Chen, X. Huang, B. Sun, L. Chen, *Synthetic Metals* **2013**, *176*, 86.
[223] J. T. Friedlein, M. J. Donahue, S. E. Shaheen, G. G. Malliaras, R. R. McLeod, *Adv. Mater.* **2016**, *28*, 8398.
[224] P.-O. Svensson, D. Nilsson, R. Forchheimer, M. Berggren, *Appl. Phys. Lett.* **2008**, *93*, 203301.
[225] P. Andersson Ersman, D. Nilsson, J. Kawahara, G. Gustafsson, M. Berggren, *Organic Electronics* **2013**, *14*, 1276.
[226] R. Porrazzo, S. Bellani, A. Luzio, C. Bertarelli, G. Lanzani, M. Caironi, M. R. Antognazza, *APL Materials* **2015**, *3*, 014905.
[227] G. Tarabella, G. Nanda, M. Villani, N. Coppedè, R. Mosca, G. G. Malliaras, C. Santato, S. Iannotta, F. Cicoira, *Chem. Sci.* **2012**, *3*, 3432.
[228] A. G. Polyravas, N. Schaefer, V. F. Curto, A. B. Calia, A. Guimera-Brunet, J. A. Garrido, G. G. Malliaras, *Appl. Phys. Lett.* **2020**, *117*, 073302.
[229] P. Gkoupidenis, N. Schaefer, B. Garlan, G. G. Malliaras, *Adv. Mater.* **2015**, *27*, 7176.
[230] X. Ji, B. D. Paulsen, G. K. K. Chik, R. Wu, Y. Yin, P. K. L. Chan, J. Rivnay, *Nat Commun* **2021**, *12*, 2480.
[231] J. Y. Gerasimov, R. Gabrielsson, R. Forchheimer, E. Stavrinidou, D. T. Simon, M. Berggren, S. Fabiano, *Adv. Sci.* **2019**, *6*, 1801339.

[232] S. Pecqueur, M. Mastropasqua Talamo, D. Guérin, P. Blanchard, J. Roncali, D. Vuillaume, F. Alibart, *Adv. Electron. Mater.* **2018**, *4*, 1800166.
[233] P. Gkoupidenis, N. Schaefer, X. Strakosas, J. A. Fairfield, G. G. Malliaras, *Appl. Phys. Lett.* **2015**, *107*, 263302.
[234] F. Zenke, E. J. Agnes, W. Gerstner, *Nat Commun* **2015**, *6*, 6922.
[235] E. M. Izhikevich, N. S. Desai, E. C. Walcott, F. C. Hoppensteadt, *Trends in Neurosciences* **2003**, *26*, 161.
[236] L. Ouyang, C. L. Shaw, C.-C. Kuo, A. L. Griffin, D. C. Martin, *J Neural Eng* **2014**, *11*, 026005.
[237] Poly(3,4-ethylenedioxythiophene) (PEDOT) as interface material for improving electrochemical performance of microneedles array-based dry electrode, *Sensors and Actuators B: Chemical* **2013**, *188*, 747.
[238] M. Cucchi, C. Gruener, L. Petrauskas, P. Steiner, H. Tseng, A. Fischer, B. Penkovsky, C. Matthus, P. Birkholz, H. Kleemann, K. Leo, *Science Advances* **2021**.
[239] C. Cea, G. D. Spyropoulos, P. Jastrzebska-Perfect, J. J. Ferrero, J. N. Gelinas, D. Khodagholy, *Nat. Mater.* **2020**, *19*, 679.
[240] A. V. Marquez, N. McEvoy, A. Pakdel, *Molecules* **2020**, *25*, 5288.
[241] S. Li, H. Wang, M. Young, F. Xu, G. Cheng, H. Cong, *Langmuir* **2019**, *35*, 1119.
[242] J. Wang, B. Li, Z. Li, K. Ren, L. Jin, S. Zhang, H. Chang, Y. Sun, J. Ji, *Biomaterials* **2014**, *35*, 7679.
[243] C. Song, Y. Yang, Y. Zhou, L. Wang, S. Zhu, J. Wang, R. Zeng, Y. Zheng, S. Guan, *Materials Letters* **2019**, *252*, 202.
[244] K. Krukiewicz, *Electrochemistry Communications* **2020**, *116*, 106742.
[245] Y. Zhao, Q. Liu, H. Sun, D. Chen, Z. Li, B. Fan, J. George, C. Xue, Z. Cui, J. Wang, J. Chen, *PLoS ONE* **2016**, *11*, e0158044.
[246] A. I. Kashkoush, R. A. Gaunt, L. E. Fisher, T. M. Bruns, D. J. Weber, *Sci Rep* **2019**, *9*, 2786.